ISSN 0915-6348

NATIONAL INSTITUTE FOR FUSION SCIENCE

Production and Physics of High Energy Density Plasma

T. Miyamoto and K. Takasugi (Eds.)

(Received - Sep. 4, 1997)

NIFS-PROC-36 Oct. 1997

This report was prepared as a preprint of work performed as a collaboration reserch of the National Institute for Fusion Science (NIFS) of Japan. This document is intended for infomation only and for future publication in a journal after some rearrangements of its contents.

Inquiries about copyright and reproduction should be addressed to the Research Information Center, National Institute for Fusion Science, Oroshi-cho, Toki-shi, Gifu-ken 509-5292 Japan.

RESEARCH REPORT
NIFS-PROC Series

NAGOYA, JAPAN

Production and Physics of High Energy Density Plasma

Edited by T. Miyamoto and K. Takasugi

January 9 – 10, 1997
National Institute for Fusion Science
Nagoya, Japan

Abstract

This is the Proceeding of "Symposium on Production and Physics of High Energy Density Plasma" held in National Institute for Fusion Science. Experimental and theoretical results on dense z-pinches, intense beams, diagnostics of dense plasma and technologies related with pulsed power systems are presented.

Keywords: high energy density plasma, z-pinch, plasma focus, high power ion beam, intense relativistic electron beam, pulsed power, high power microwave, x-ray radiation

Preface

This is the collected article of papers presented at the "Symposium on Production and Physics of High Energy Density Plasma" held at National Institute of Fusion Science on January 9 – 10, 1997. The main interests were concerned on the production and physics of high energy density plasma — z-pinches and high power particle beams. Various topics presented in the symposium are summerized as the following subjects:

- Dense z-pinches including plasma focus
- Intense pulsed ion beams
- Relativistic electron beams
- X-ray lasers
- Diagnostics of dense plasma
- Pulsed power technology

At the simposium, 24 papers were presented, and 39 scientists (including 6 attendants from foreign countries) attended from universities and institutes. Great achievements were obtained by this symposium through fruitful discussions among attendants.

Tetsu Miyamoto

Contents

List of Participants

Hidenori Akiyama	Kumamoto University
Tatsuyoshi Baba	Nihon University
Hidemoto Furuya	Tokyo Institute of Technology
Seizo Furuya	Tokyo Institute of Technology
Yoshikuni Goshima	Nihon University
Frank Hegeler	Kumamoto University
Makoto Horiuchi	Nihon University
Takehito Igusa	Nihon University
Juichi Irisawa	Nagaoka Institute of Technology
Shozo Ishii	Tokyo Institute of Technology
Kazutaka Jingushi	Tokyo Institute of Technology
Sunao Katsuki	Kumamoto University
Hiroyuki Kitaoka	Gunma University
Shinichi Kondo	Tokyo Institute of Technology
Igor Lisitsyn	Kumamoto University
Tomomitsu Masuda	Himeji Institute of Technology
Katsumi Masugata	Nagaoka Institute of Technology
Hidenori Matsuzawa	Yamanashi University
Tetsu Miyamoto	Nihon University
Alexander Muravich	Nihon University
Jun Nakamura	Nihon University
Nobuhiro Nishino	Hiroshima University
Koji Nishiura	Nagaoka Institute of Technology
Jun Ohrui	Nagaoka Institute of Technology
B. Rahmani	Tokyo Institute of Technology
Morihiko Sato	Gunma University
Tsuyoshi Sueda	Kumamoto University

Keiichi Takasugi	Nihon University
Mitsuru Tanigawa	Himeji Institute of Technology
Katsuhiro Tatsumi	Nihon University
Teruhiko Tazima	National Institute for Fusion Science
Osamu Tsuboi	Tokyo Institute of Technology
Wang Xiaojun	Nagaoka Institute of Technology
Toshikazu Yamamoto	Gunma University
Takeshi Yanagidaira	Gunma University
Kiyoshi Yatsui	Nagaoka Institute of Technology
Mitsuyasu Yatsuzuka	Himeji Institute of Technology
Hiroshi Yoshida	Kanazawa University
Qifeng Zhu	Nagaoka Institute of Technology

Basic characteristics of the multi−arc gap

J. Ohrui, S. Takano, T. Muso, N. Watanabe, S. Yoshida and J. Irisawa

Department of Electrical Engineering, Nagaoka University of Technology,

Nagaoka, Niigata 940−21,Japan

Abstract

Basic characteristics of multi arc gap,consist of 12 needle electrodes and a rod electrode of 160mm long, was investigated. Voltage rising rates about 12kV/ns, developed by a non−liniear coaxial cable type of ferrite shrapner, have been applied to the gap.As results, we obtaind the following:

- Being gap distance shorter or leadline length longer,appearance of arc channle was increased.
- Applying positive pulse to needle electrodes, number of channel appearance was larger than applying negative.
- Distribution of channel appearance had a maximum around 0.05Mpa.
- Using Ar, breakdown voltage higher than air, number of channle appearance was increased.

I Introduction

Multi−arc gap is one of the spark gap switch utilized in pulse power technology. Sparkgap is opearated by creating arc discharge between electrodes. There are many methods of creating arc discharge. Field distortinon trrigers are used in multi−arc gap. [1) 2) 3) 4)] The necessary condition acheaving the multi−arc operation of voltage rising rate of 5kV/ns was discribed by Neil et al. [5)] We obtained high dV/dt pulses using a nonlinear coaxial cable type of ferrite sharpner [6)].

Characteristics of the multi−arc gap have been made clear in a very high voltage, but it's unknown in a low voltage range. This papaer discribes the studies of self breakdown multi−arc switch's characteistics. The gap is consist of 12 steel needle electrodes separated by 10mm each and a 160mm long brass rod of 18mm diameter.

II Experimental Details

High rising rates of voltage were created by a ferrite sharpner whose main concept of non−linear coaxial line is shown in reference 6 and 7. A pulse generator circuit and its output waveform of open ended are shown in Fig.1 and Fig.2 ,respectively. Pulse generator is consist of voltage doubler and capacitor bank. Ferrite sharpner is connected at the of the pulse generator.

If the magnitude of output voltage of open ended set to 40kV, rising rate before traveling ferrite sharpner of 0.66kV/ns becomes 12kV/ns after traveled. The geometory of the switch,definition of feeder length are illustrated in Fig.3 and Fig.4, respectively. In our studies,voltages were measured by Tektronix high voltage probe: P6015A and Hewlett Packard digital Oscilloscope:HP54510A. A number of arc channels were detected by SONY CCD video camera:CCD−TR650.

50 shots at each experimental conditions were performed, then the data were handled by taking the mean. We had performed 4 experiments of the following.

(a) Parameter:Gap distance, Feeder length

Appearance of arc channel were measured by varying ① gap distance:1～6mm, ② feeder length:25mm,100mm,200mm,300mm. Other conditions of this experiment ③ pulse polarity : +,− ④ atomosphere : air 0.1MPa. Total 48 conditions were performed.

(b) Influcence of feeding point

Relation between feeding point and appearance of channels were measured. In this experiment, we used the 4 needle electrode configuration illustlated in Fig.6 Needle electrodes were separated by 140mm each. Parameters of this experiments were ① gap distance : 1mm and 5mm, ② feeder length 50mm. 100 shots at each conditions were performed.

(c) Parameter:Pressure , gap distance

Relation between appearance of arc channels and pressure was measured. Parameters of this experiment were pressure and gap distance. The range of pressure 0.01～0.4MPa for gap distance 1～3mm and 0.01～0.1MPa for gap distance 4 and 5mm. Other conditions were polarity:+,− and atomosphere:air. Total 96 conditions were performed.

(d) Changing the gas kind

Appearance of arc channels were measured by changing the gas kind. Paraneters in this experiments were ① gap distance :1～5mm, ② pressure:0.1MPa, ③ pulse polarity:+,−. total 20 conditions were performed.

III Experimental Results

(a) Parameter:Gap distance , Feeder length

Results are shown in Fig.5(a)Needle electrode:positive,(b)Needle electrode :Negative. Fig.5 shows the relation between average of appeared arc channel number and gap distance for different feeder length. From result appearance of arc channels were increasing with incleasing feeder length. And for long distance of the gap, appearance of channels were decreased. Result of both polarity are almost similar. But channel appearance number of applying positive is little higher than the applying negative.

(b) Influcence of feeding point

Result is illustrated in Fig.7. Because of the polarity effects on result was not recognized, only positive data is illustrated. Fig.7 shows the times of channel appearance in 100 shots. As increasing the feeder length,the times of channel appearance decreased for gap distance 1mm. For gap distance 5mm, feeder length unrelated to the times of channel appearance.

(c) Parameter:Pressure , gap distance

Results are shown in Fig.8(a) Needle electrode:Positive and (b)Needle electrode:Negative. They shows the average of appeared arc channel number at each pressure. Distribution of the channel appearance had peak close to 0.05MPa, beyond the polarity.Numbers of appearance decreased pressure range of over 0.05MPa and under 0.05MPa.

(d) Changing the gas kind

Result is shown in Fig.9. That shows the relation between average of appeared arc channel number and gap distance at each gas. For comparision, data at the air was inserted. For the air and He, appearance of channel were decreased, as increasing gap distance. For Ar, despite of the increasing gap distance, number of appearance was constant.

Ⅳ Conclusion

A spark gap, made of 12 needle electrodes to a rod electrode of 160mm has been tested. Basic data of arc channel appearance have been obtained during 4 experiments.

Ⅴ References

1) G.R.Neil and R.S.Post, "Multichannel high-energy railgap switch." Rev. Sci. Instrum., 49 (3),1978

2) R.L.Standstrom, H.Shields and J.I.Levatter, "Performance characteristics of a high repetition rate, multichannel rail-gap switch." Rev. Sci. Instrum., 58 (4),1987

3) N.Seddon and P.H.Dickinson, "Rail-gap switches triggered by semiconductor edge discharges." Rev.Sci.Instrum.,58 (5),1987

4) D.B.Cohn, W.H.Long, Jr., E.A.Stappaerts, M.J.Plummer and J.B.West, "Multichannel switch triggered by low-voltage auxiliary discharge." Rev.Sci.Instrum.,53 (2),1982

5) R.S.Taylor and K.E.Leopold, "UV radiation triggered rail-gap switches." Rev.Sci.Instrum.,55 (1),1984

6) F.Kawasaki, S.Takano and J.Irisawa, "Studies of coaxial line containing ferrite beads and its applications." J.I.E.E.,112-A (5),1992

7) S.Takano,Y.Hasegawa,T.Muso and J.Irisawa "Characteristics of multichannel gap" NIFS-PROC-26,p.115-122, ,1996

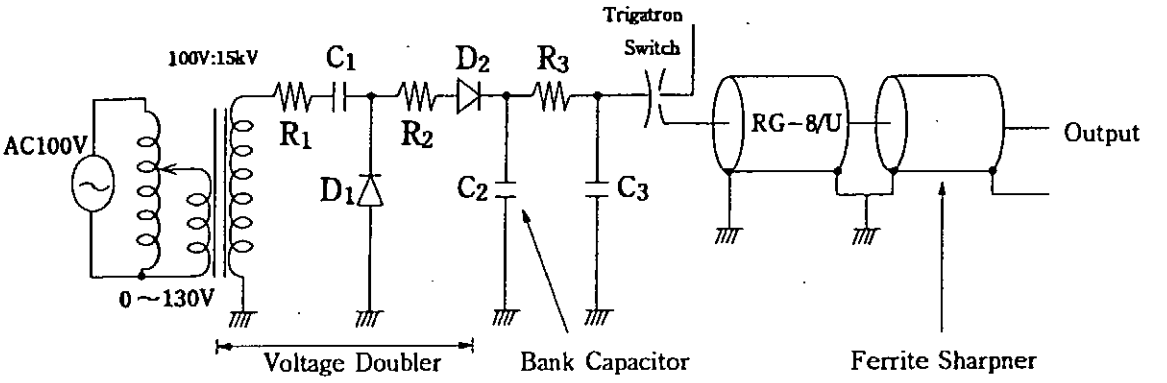

Fig. 1 Pulse Generator with Ferrite Sharpner

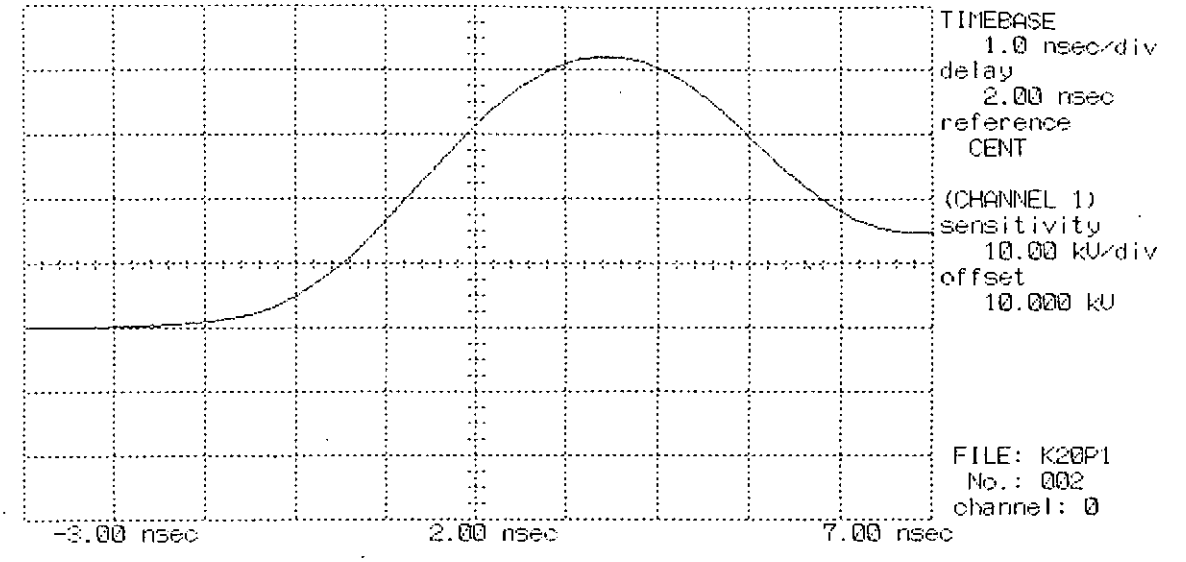

Fig. 2 Output Voltage Waveform ; Open end

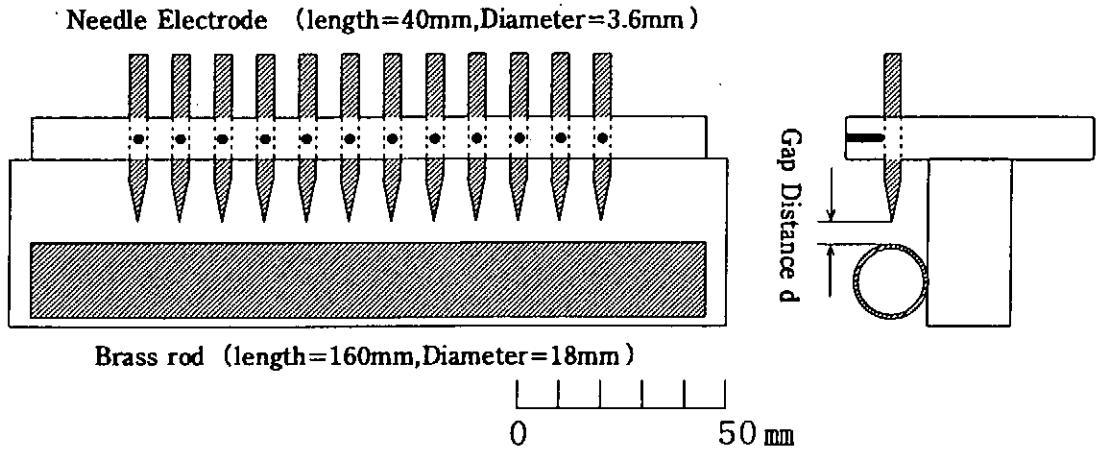

Fig. 3 Geometory of the gap

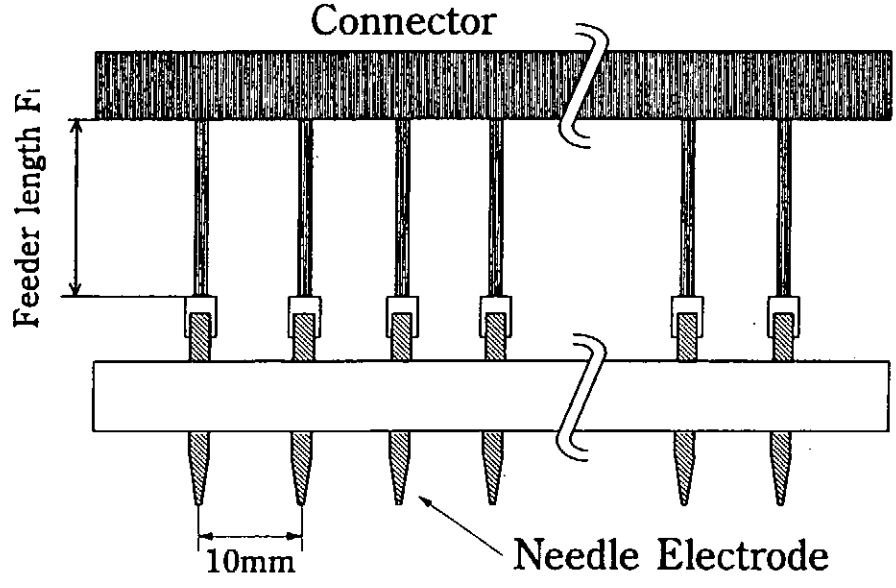

Fig. 4 Connector of needle electrodes

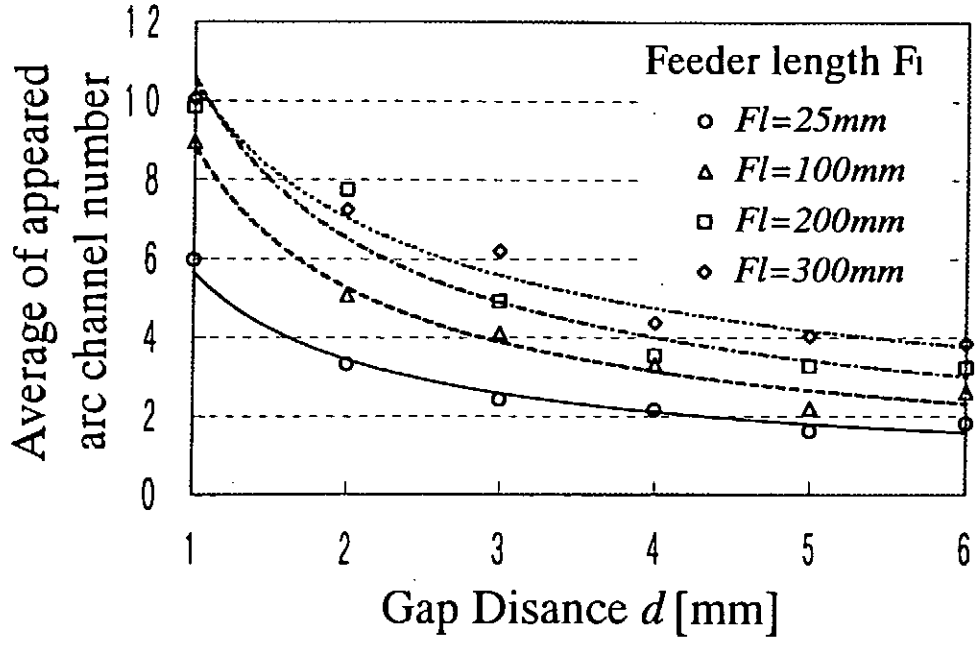

(a) Needle electrode : Positive

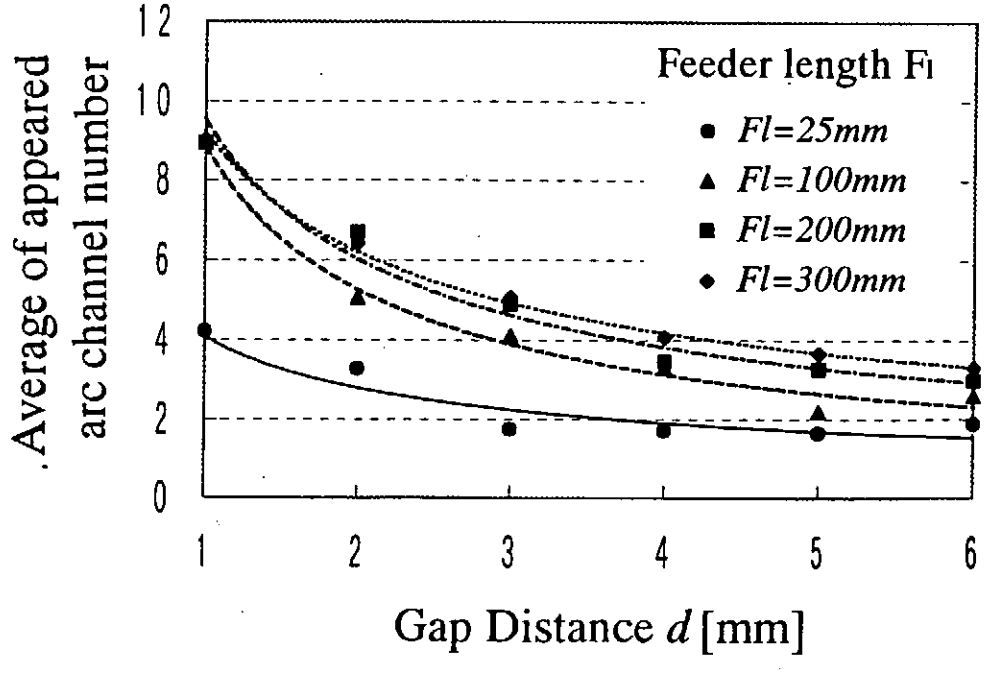

(b) Needle electrode : Negative

Fig. 5 Appearance of channels vs. feeder length / gap distance

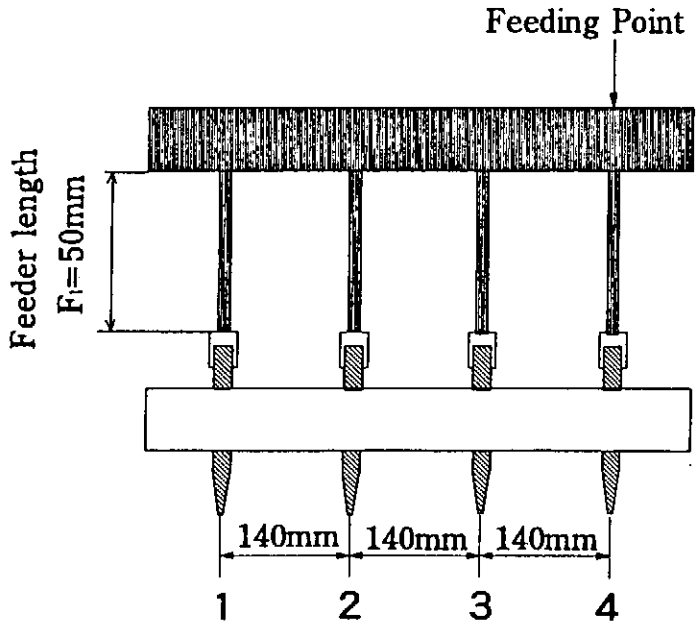

Fig. 6 Configuration of 4 Needle Electorodes

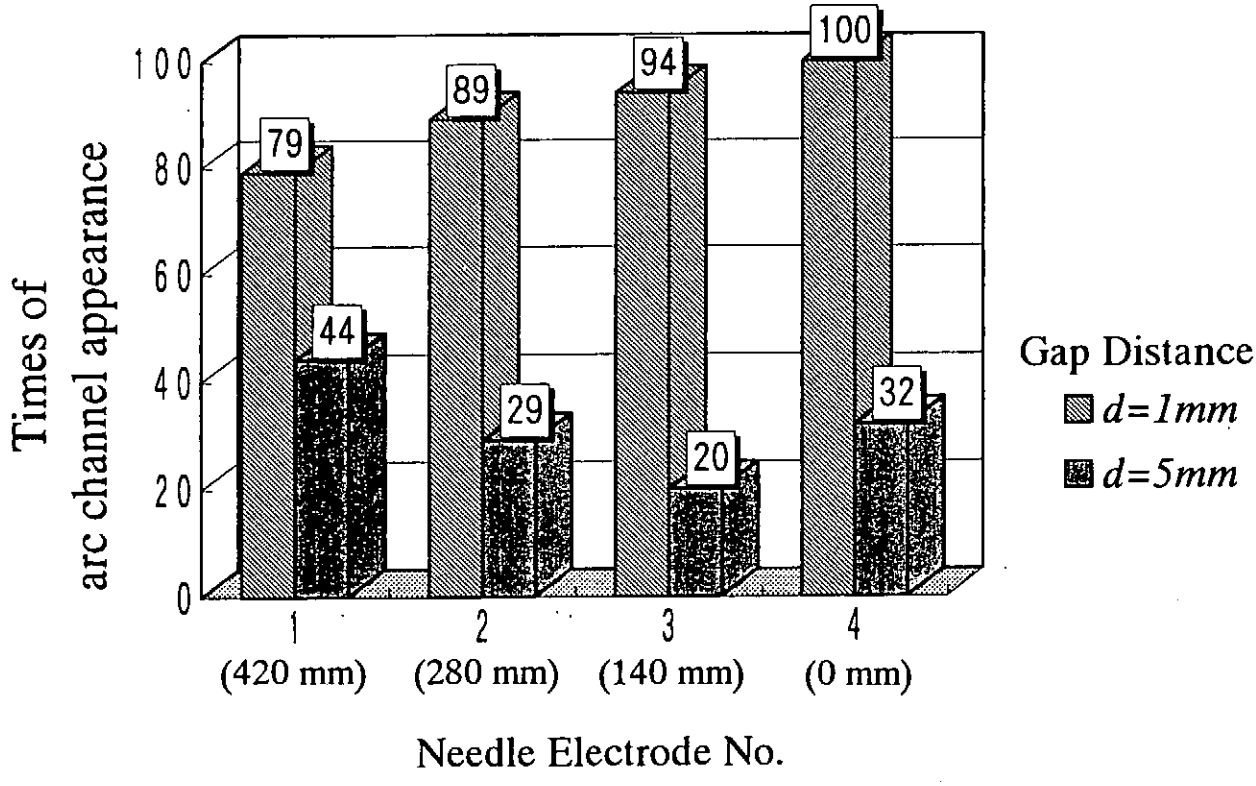

Fig. 7 Relation between feeding point and appearance of channels

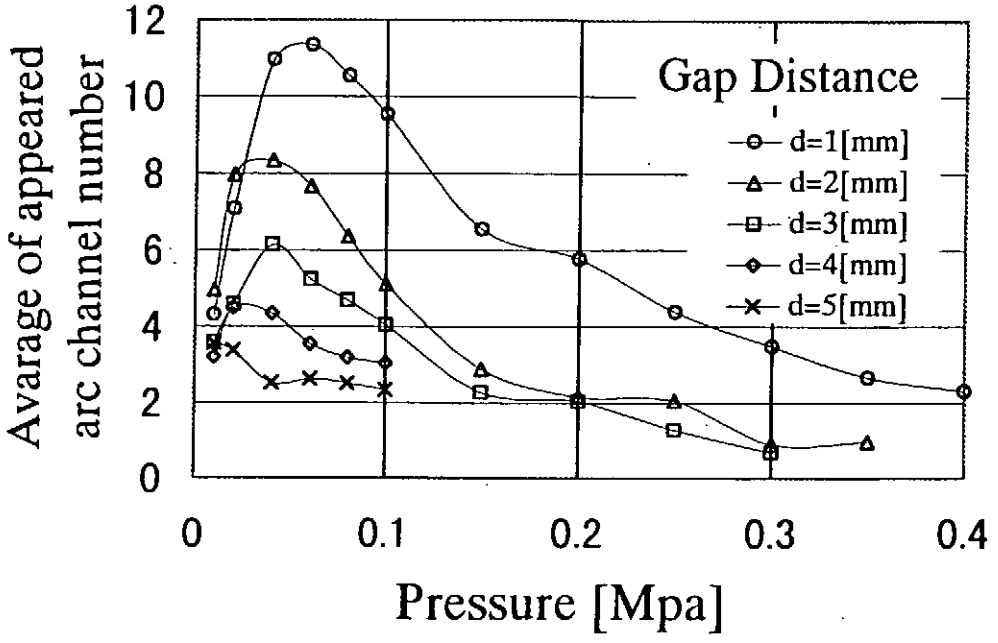

(a) Needle electorde : Positive

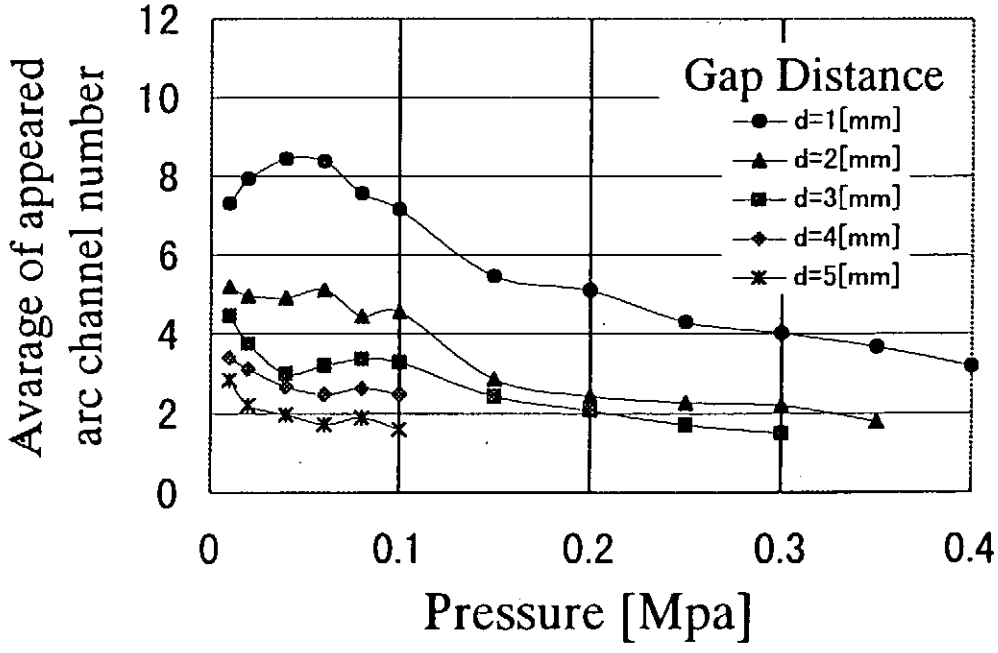

(b) Needle electorde : Negative

Fig. 8 Appearnce of channels vs. gap length / pressure.

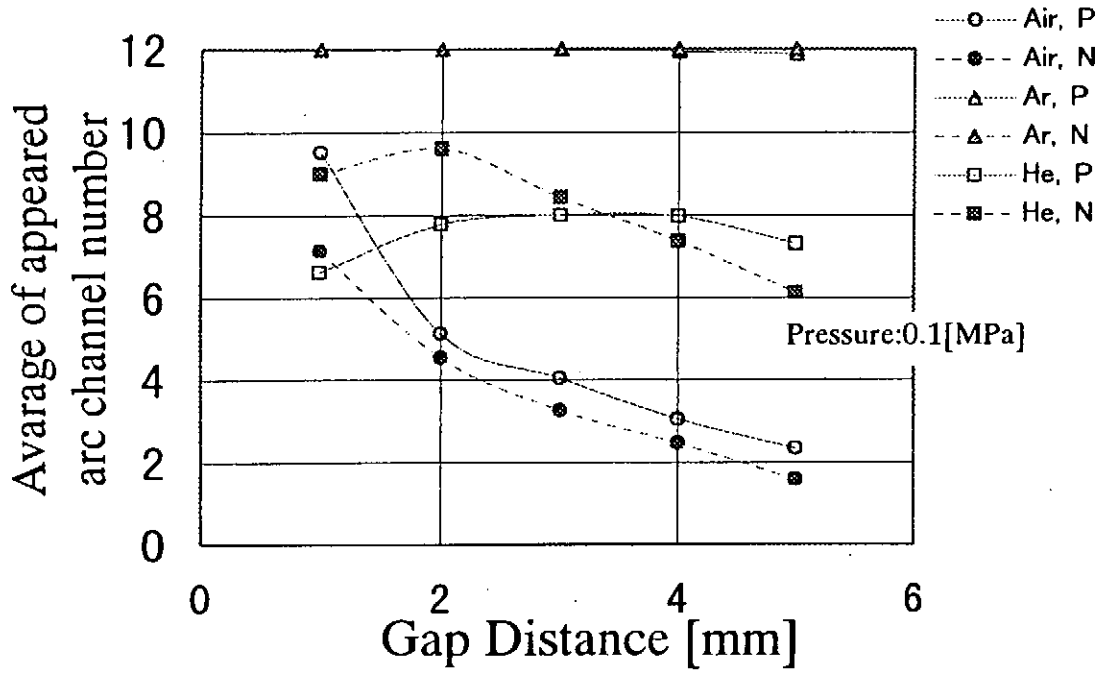

Fig. 9 Appearance of channels vs. gas /gap length

High Density Plasmoid Acceleration by Phased Implosion of Capillary Z-pinch

Kazuhiko HORIOKA, Hiroshi ISHIKAWA*,
Mitsuo NAKAJIMA and Tomonao HOSOKAI
Department of Energy Sciences, Tokyo Institute of Technology,
Nagatsuta 4259, Midori-ku, Yokohama 226, Japan
***Faculty of Engineering, Musasi Institute of Technology,**
Oyamadai, Setagaya-ku, Tokyo, Japan

Tatsuhiko AIZAWA and Minoru TSUCHIDA
Faculty of Engineering, University of Tokyo,
Hongo, Bunkyo-ku, Tokyo 113, Japan

ABSTRACT

A new concept for accelerating a high density plasma to high kinetic energy is proposed. A high density Z-discharge plasma in a tapered capillary tube was electro-magnetically accelerated by a phased implosion of a capillary z-pinch. The implosion was just about timed to the plasmoid drift by the shaped capillary wall. The feasibility of high energy acceleration was experimentally demonstrated using a 100mm long thin capillary and a fast pulse power generator. For filling gas of 100Pa of Ar, the axial drift velocity of the plasma was 7×10^7cm/sec, which correnspond to 70kev argon atoms.

1 INTRODUCTION

We have developed a new concept for high density plasma acceleration principally in connection with a formation of very intense shock waves, material processings and a hyper-velocity acceleration of small projectiles. Implosions driven by chemically explosive materials were conventionally used to make extremely strong shock waves[1,2] or hiper-velocity projectiles,[3,4]. However there was theoretical velocity limit; it was inherently limited to an order of acoustic speed of the hot drive gas. Conventional plasma guns[5,6] can accelerate the plasma up to order of 10^7cm/s, however, they have density limit. The plasma density is order of 10^{16}cm^{-3} at most. In order to overcome these density and velocity limits, we have proposed electro-magnetic acceleration in a tapered

capillary discharge for high density plasmoid acceleration.

The blast wave accelerator employs a phased implosion concept to accelerate a projectile.[4] On the other hands, we have found that capillary z-discharges driven in pre-ionized gas can compress the plasma up-to $10^{19}cm^{-3}$ plasma density with good reproducibility.[7] Based on these principles, we have utilized scheduled pinching of high current pulsed discharges in a long capillary tube to accelerate high density plasma.

The axially phased implosion of current sheet acts as a virtual piston to compress the plasma and drive a high energy directional plasma flow. In other words, we have intended to make controlled zippering along the total length of the narrow discharge channel at very high current level. It has no intrinsic speed limit, and can continuously create impulse on the plasma along the total length of the tube.

If we can assume snow plow approximation, the pinch time τ_p of coaxial discharge is expressed as,[8]

$$\tau_p = \left(\frac{\pi r_0^2}{I_0}\right)\left(\frac{Nimi}{\mu_0}\right) \sim \frac{r_0^2}{I_0}$$

where, Ni is number density of initial filling gas, μ_0 is the peameability of vacuum, I_0 is the discharge current, and r_0 is the initial radius. For rapid contraction, we should drive a plasma of small radius with high current level. As shown above equation, the pinch time strongly depend on the initial radius of the Z-discharge plasma. So, the pinch time can be controlled by slight shaping of the discharge wall.

The basic operational principle of the plasmoid acceleration by scheduled pinching is shown schematically in Fig.1. The high current fast z-discharge of 10^5A current level makes azimuthal magnetic field B_θ which accelerate the plasma radially inward. As it accumulate and compress the plasma upto GPa level via the snow plow effect, a high density plasmoid is formed at the discharge axis. At a suitable time delay for arrival of the plasmoid, the pinching occurs along the discharge axis. The plasma was radially compressed by the self B_θ field and axially driven by the B-gradient made by the phased pinching. Therefore, if the plasma implosion time is exactly phase matched to the plasmoid transit time, we can expect that significant part of the input energy goes into the directional energy of the plasma.

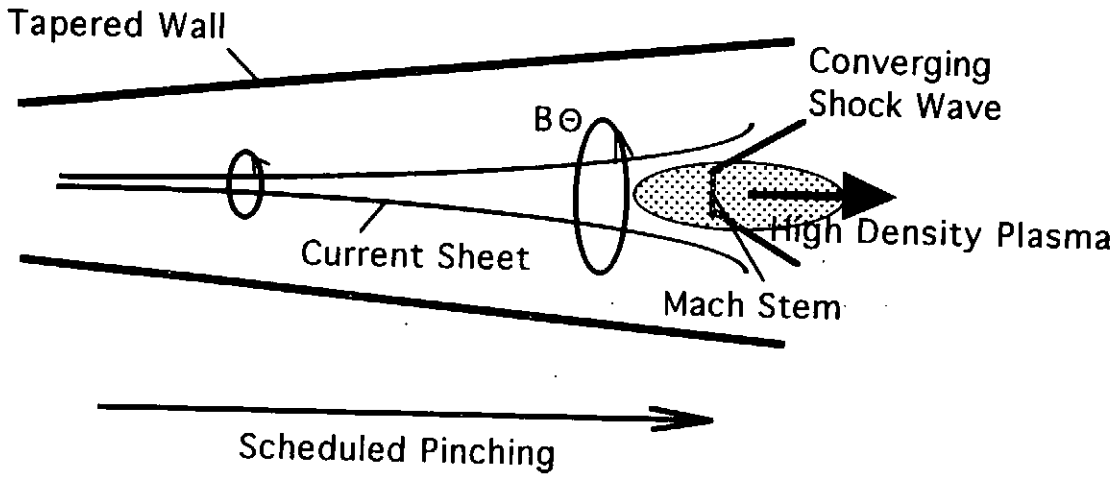

Fig.1 Schematic Diagram of Phased Z-pinch Implosion and Internal Structure of the Plasma

As has been pointed out, the capillary plasma has internal structure; the current sheet drives a converging cylindrical shock wave ahead of itself.[7] The current sheet acquires a strong axial shock wave in the plasma column, if it grow the Mach stem.[4]

2 EXPERIMENTAL SETUP

A schematic diagram of experimental set-up is shown in Fig.2. The capillary of 100mm length has a thin conical wall, whose inlet and exit diameter were 4mm and 8mm respectively. It was slightly tapered so as to implode sequentially and contract the exit plasma within the pulse width (70nsec) of the discharge of 10^5A level. Here, the effect of plasma accumulation along the axis was not taken into account. Because we thought that the plasma should move axially in a leaky-stream-tube mode to avoid discharge instability.

The basic configuration of the experiment was quite similar to the previous capillary Z-pinch experiment[7] except the capillary shape. A fast pulse power generator LIMAY-I is used to drive the capillary discharge. A high voltage pulse was switched on the electrode after weak pre-ionization discharge. Typically it drives load cuurent of 80kA, with rise time of 20ns from the 3ohm-70nsec pulse forming line through a pre-pulse suppression SF_6 switches.

Experimental Set-up for Z-Pinch Acceleration

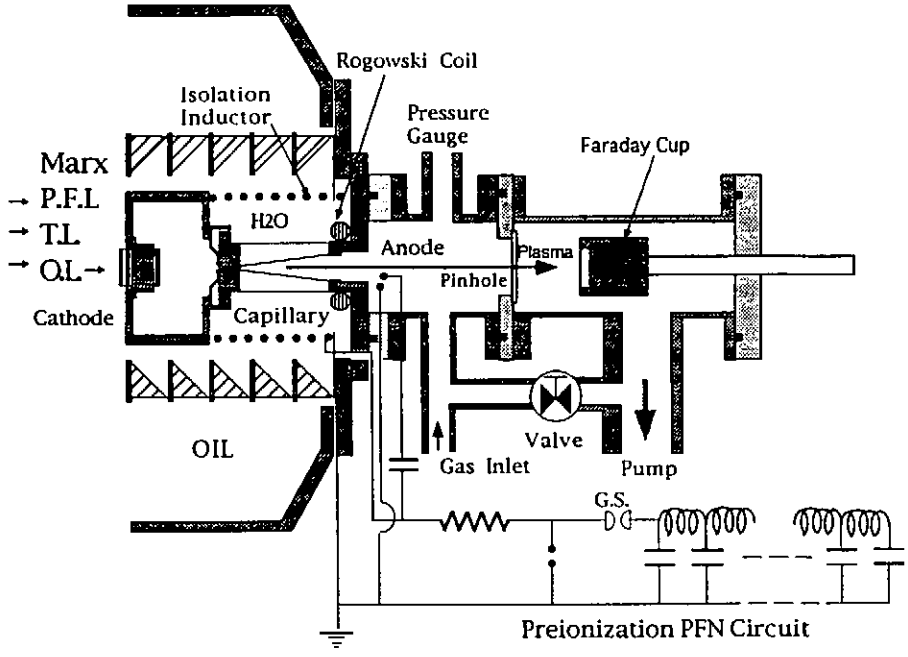

(a)

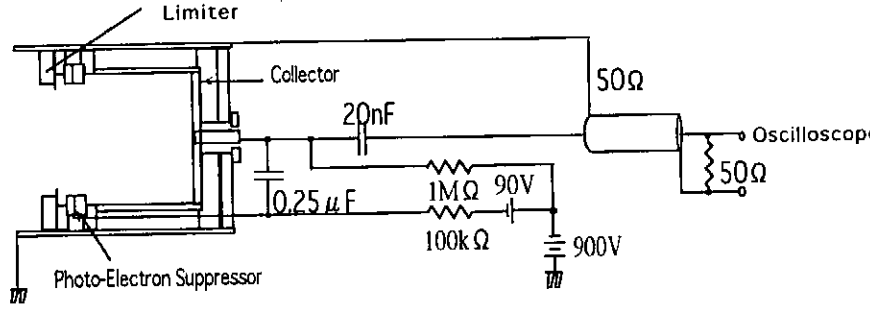

(b)

Fig.2 Experimental Arrangement for Proof-of-Principle Experiments

(a) Experimental Set-up

(b) Faraday Cup for Plasma Flux Measurements

The load current was monitored by a Rogowskii coil of self-integral type. For differential pumping, the discharge section and the diagnostic chamber was separated by a pinhole of ~0.2mm diameter. To avoid the damage by the plasma, the pinhole was located 30mm from the exit of the capillary tube. The initial static densities of the gas was order of $10^{17}cm^{-3}$ and the background pressure of the time-of-flight (TOF) chamber was kept below 10^{-3}mmHg by the differential pumping.

3 EXPERIMENTAL RESULTS

We have measured the wave-forms of the plasma flux through the pinhole by a Faraday cup. The Faraday cup consists of a negatively biased collector plate and a photo-electron suppresser electrode. The collector plate of the Faraday cup is biased to -800V. In order to suppress the photo-electron signal, the second electrode is biased to -980V.

The typical TOF wave-forms of the plasma flux are shown in Fig.3 with the load current signal. The peak of the plasma signal was shifted as function of distance and quantity of gas loading. As it indicates, when the initial filling pressure was 100Pa of Ar, the drift velocity of the plasma was $\sim 7 \times 10^7$cm/s. Then, we find that Ar atoms traveling at this velocity has an energy of about 70keV. The cuurent density of the plasma flux was more than $200A/cm^2$ at the pinhole. Note that the plasma expands rapidly from the exit of the capillary and the pinhole was placed 30mm from the exit of the capillary tube.

An experiment was made to check whether the high energy plasma might not be produced by the instability of z-discharge. To check this effect, the polarity of the pulse power generator was inverted. Typical results are shown in Fig.4. In spite of the polarity inversion, as shown in the figure, the plasma signal had almost the same shape. This means that the high energy plasmoid was purely electro-magnetically accelerated not by anomalous electric field.

A preliminary experiment on flyer acceleration was performed. The experimental arrangement is shown schematically in Fig.5. A thin Cu metal plate of 0.1mm thickness and 5mm diameter was placed at the exit of the capillary tube. When the charging energy of the pulse power generator was 1.1kJ, the flyer was accelerated up to 2.5km/s. That means almost 5% of stored electric energy (~50J) was converted to the kinetic energy of the small projectile.

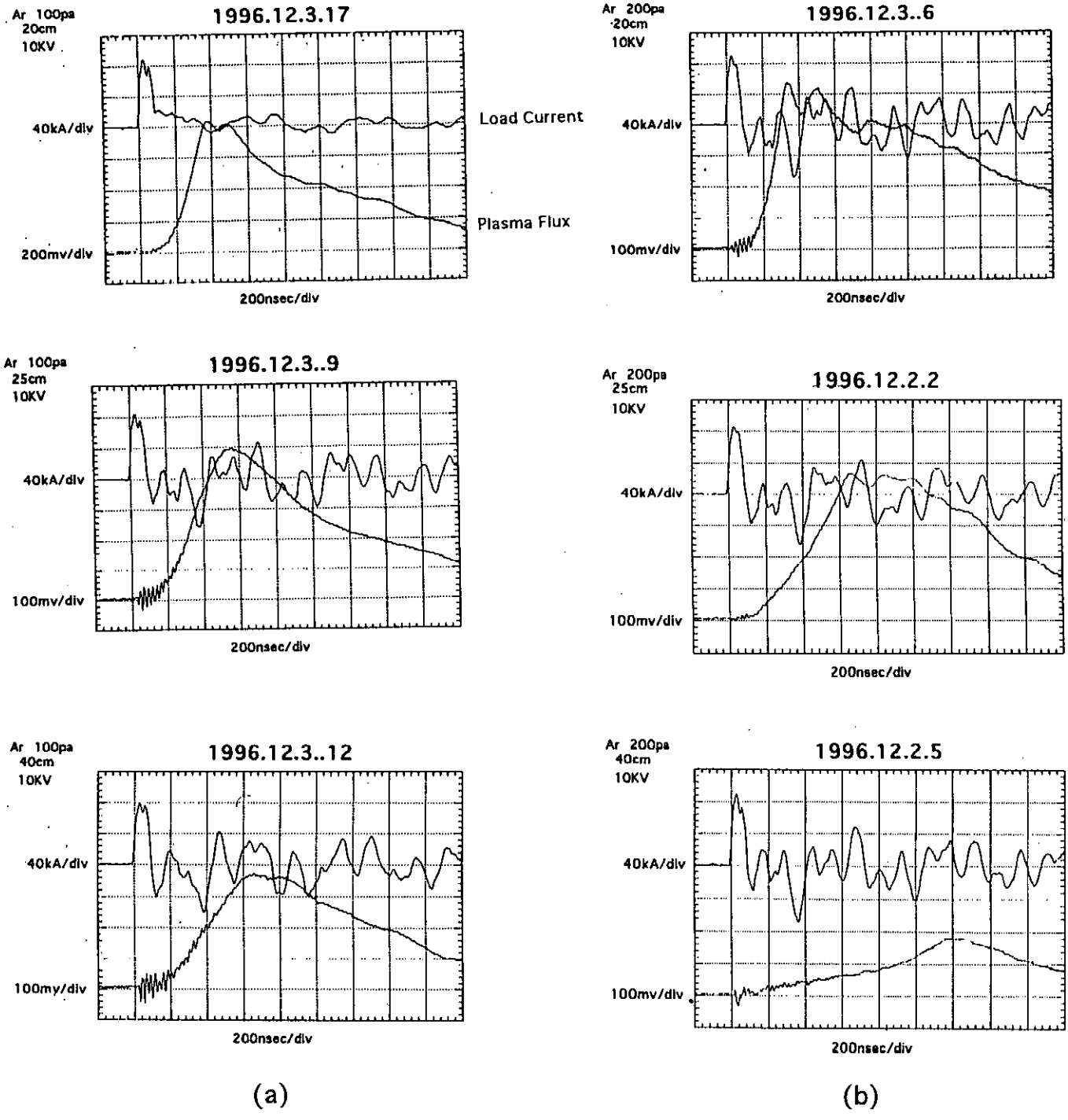

Fig.3 Typical Wave-forms of load current and Plasma Flux as a Function of Axial Distance, at initial filling pressure of 100Pa (a) and 200Pa (b) of Ar

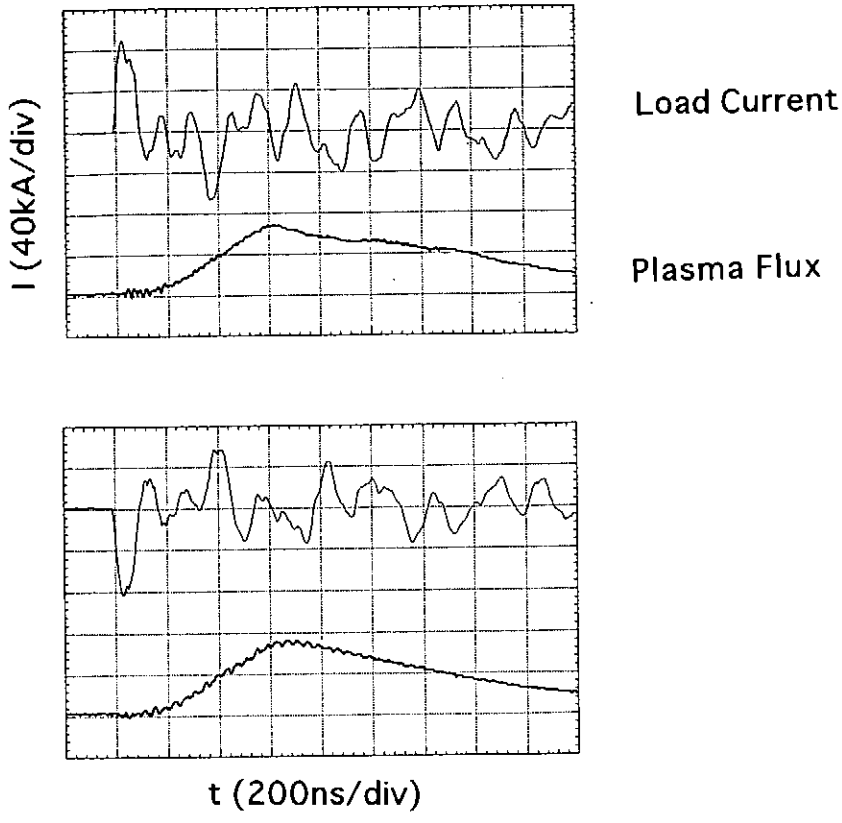

Fig.4 Polarity Effect on the Ion Flux Signal

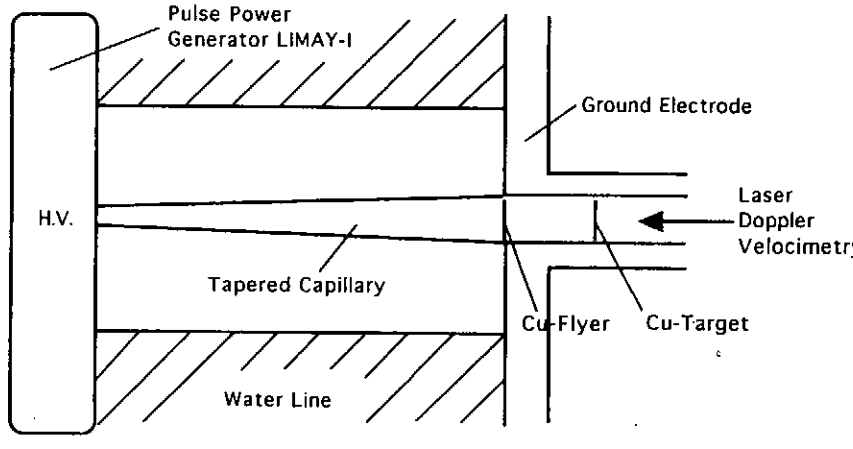

Fig.5 Schematic Diagram of Preliminary Experiments for Flyer Acceleration

4 CONCLUDING REMARKS

In conclusion, a high density plasma was electro-magnetically accelerated in a tapered capillary discharge. The drift velocity of high energy plasma was measured to be $7x10^7$m/s, which corresponds to 70keV Ar. The proof-of-principle experiment shows that high energy plasma flow was driven by the scheduled pinching.

The basic scheme may be related to pinch engine[9] or particle acceleration by zippering of plasma focus discharges[10,11], but we can expect controlled plasma compression and acceleration by the tapered capillary discharge. The plasma acceleration should closely connected to the sweep speed of the pinching. Parameters influencing implosion stability, initial background gas pressure, wall shape, are expected to play an important role to develop optimum acceleration. Although, the implosion should be exactly synchronized to the plasmoid drift by a properly shaped wall including the effect of plasma accumulation along the axis, this scheme appears capable of accelerating plasma of density to 10^{19}cm^{-3}, upto velocities of well above 10^8cm/s. If the implode configuration is made so as to strengthen the Mach stem, it can drive axial plane shock wave.

REFERENCES

(1) I.I.Glass, S.K.Chan and H.L.Brode; AIAA J. Vol.12, No.3, p.367 (1974)

(2) E. Menikoff, K.S.Lackner, N.L.Johnson, S.A.Colgate and J.M.Hyman; Phys. Fluid A3 , (1) p.201 (1991)

(3) D. Wilson, Z.Tan and P.L.Varghese; AIAA J. Vol.34, No.7, p.1341 (1996)

(4) D. A.Tidman and S.A.Goldstein; J. Appl. Phys., Vol.51, No4, p.1975 (1980)

(5) S.Humphries, jr., R.J.M.Anderson, J.R.Freeman and J.B.Greenly; Rev. Sci. Insrum. 52(2), 162 (1981)

(6) C.W.Mendel ; IEEE Conf. Record, 79CH-1310-DNPS, p.76 (1979)

(7) T.Hosokai, M.Nakajima, T.Aoki, M.Ogawa and K.Horioka; Jap. J. Appl. Phys.,No.4 (1997) (in Press)

(8) A.M.Panin, SPIE Proc. Vol.2520, 222 (1995)

(9) P.J.Hart; J. Appl. Phys., 436 (1960)

(10) T. W.Hussey, M.K.Matzen, and N.F.Roderick; J.Appl. Phys., 59(8), 2677 (1986)

(11) K.Hirano and T.Yamamoto, J Phys. Soc. Japan, 56(2), 4361 (1987)

Study of Plasma Parameters in Long Conduction Time Plasma Opening Switch

I.V.Lisitsyn, S.Kohno, T.Kawauchi and H.Akiyama

Department of Electrical and Computer Engineering,
Kumamoto University
Kurokami 2-39-1, Kumamoto 860, Japan

Abstract

The plasma opening switch operation was studied by optical diagnostics such as laser interferometry and spectroscopy. The characterization of plasma source (cable plasma gun) allowed to determine initial plasma conditions for the switch. The process of vacuum gap formation in a microsecond plasma opening switch was also investigated. Time- and spatially resolved density measurements are performed in the plasma opening switch, showing the density drop during switch opening almost in the whole interelectrode gap. The density diagrams are compared to major switch characteristics such as conduction time and load current dI/dt. The study of spectral line intensities from cable gun plasma showed that CII line intensity correspond in time with plasma density measured by interferometer. The intensities of carbon spectral lines tend to drop during switch opening, that substantiates interferometry measurements.

1. INTRODUCTION

Inductive energy storage pulsed power generators require a fast opening switch to transfer energy from a store to a load. The most attractive approach is to use a plasma opening switch (POS) to conduct current during about 1 μs in order to transfer energy from relatively fast capacitor bank or Marx generator to an inductor [1,2]. After this conduction time, the POS opens allowing the current to flow through a load. Since the inductive energy storage is much more compact compared to capacitive one, this approach can sufficiently reduce both size and cost of multimegajoule pulsed power generators, used in ICF experiments [3].

The POS operation can be divided to two distinct phases of conduction and opening. During the conduction phase the POS exhibits extremely low resistance due to existence of a plasma, which is a perfect conductor, between POS electrodes. Then, after some time, the electric or/and magnetic force acting to plasma creates the vacuum gap somewhere in the plasma bridge. The insulation of the current conducting electrons in such a vacuum gap results in opening of the switch. The formation of vacuum gap was proven experimentally [4]. Its appearance in the microsecond POS is explained mostly by magnetohydrodynamic (MHD) plasma displacement [5].

The main goal of this paper is to characterize the behavior of POS plasmas by spectroscopy and interferometry in an electrode system very close to one dimensional that sufficiently reduces the problems with the interpretation of experimental results.

2. EXPERIMENTAL SETUP

Experiments have been performed to improve understanding of the physics of POS operation in the conduction time range of 1-1.5 μs at the current level of 25 kA. The current pulse was generated in the electrode system by a discharge of the capacitor bank (1.2 μF, 16 kV) through a triggered sparkgap. The electrode geometry and magnetic field amplitude were chosen to be similar to the existing mega ampere current generators [6,7]. Two parallel copper rods 8 mm in diameter and 120 mm in length separated by 10 mm served for POS electrodes. The plasma was injected into the center of electrode system by a cable gun powered from an additional generator (0.22 μF, 16 kV). The diagram of experimental setup with laser lines of sight is shown in Fig. 1.

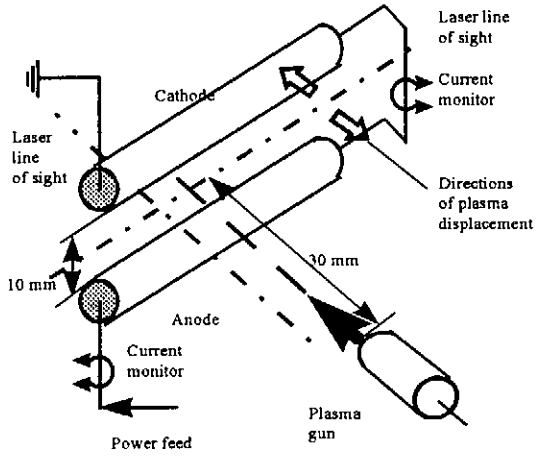

Fig. 1 The diagram of experimental setup. Black arrow shows the direction of plasma injection. White arrows show the most probable directions of plasma

The diagram of the interferometer is presented in Fig. 2. Generally, this is classic, well known, Michelson interferometer scheme with one beam splitter dividing the He-Ne laser beam (5 mW, 0.8 mm in diameter) into reference and scene beams, where the latter passes two times through the experimental plasma. Both beams recombine at the same beam splitter and are focused at the input of optical fiber with a lens. A narrow bandpass (0.1 nm) filter is used to avoid false signals due to the plasma luminosity. Output end of the optical fiber was placed into a shield room allowing to obtain noise free signals at the beam registration scheme based on the standard photodiode with sensitivity equal to 0.4 A/W for He-Ne laser wavelength. A Hamamatsu S5973 Si pin photodiode with extremely low terminal capacitance (1.5 pF) was used to achieve the highest possible temporal resolution in the high load resistance (1 kOhm) scheme used for the beam registration. The signal from the photodiode was recorded with an HP 54512B digital oscilloscope.

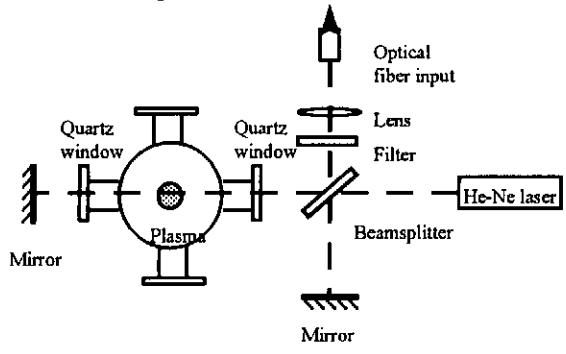

Fig. 2 The diagram of the interferometer setup.

The signal recorded could be analyzed by the linear approximation of the dependence of signal amplitude on the phase shift, which is valid for low density plasma measurements. The linear approximation of the phase shift when the initial phase is close to zero gives the following formula for density evaluation:

$$\int N_e dL = 5.56 \times 10^{16} \frac{\Delta A}{A} \qquad (1)$$

where ΔA is signal amplitude over the zero phase photodiode signal level and A is the amplitude of photodiode signal oscillations due to unavoidable vibration of optical elements with magnitude more than laser beam wavelength. The correction was necessary if the initial phase was sufficiently different from zero. The correction method can be found in [8].

Spectroscopic measurements were performed by using an optical multichannel analyzer (OMA) Macs 320 by Atago Bussan Co. Ltd. It allows to measure spectral line profiles with the resolution of 0.05 nm and with the time resolution better than 100 ns. The optical arrangement allowed to achieve the spatial resolution close to one of the interferometer in the switch region. The average diameter of light emission area in the POS plasma registered by OMA is estimated as 3 mm.

3. EXPERIMENTAL RESULTS AND DISCUSSIONS

The characterization of the cable gun plasma was done in order to determine its parameters and to understand the initial plasma conditions taking place before switch operation. The plasma gun produces several plasma bunches due to current oscillation near the plasma gun nozzle where the bunches are separated from each other (Fig. 3). Such a plasma

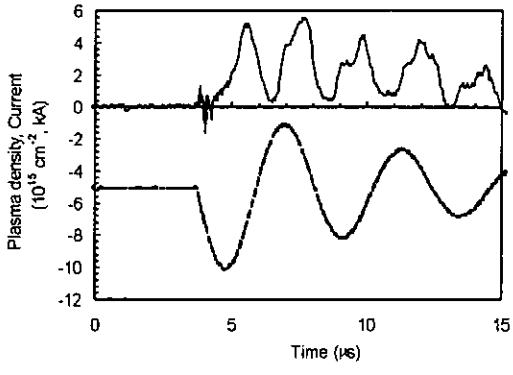

Fig. 3 Line - integrated plasma density at 10 mm away from cable plasma gun nozzle (top, solid) and gun discharge current (bottom, dashed).

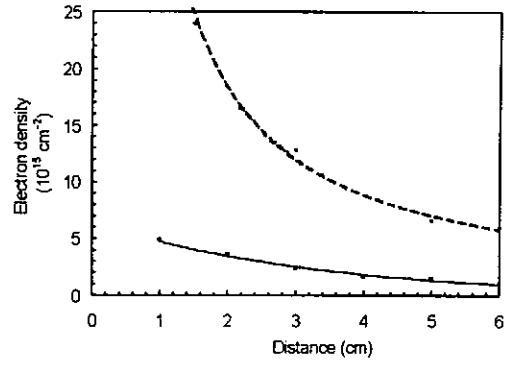

Fig. 4 Line integrated plasma density for cable gun vs distance from the nozzle. Cable gun is fed from 0.22 μF capacitor (solid curve) and 1.2 μF capacitor (dashed curve).

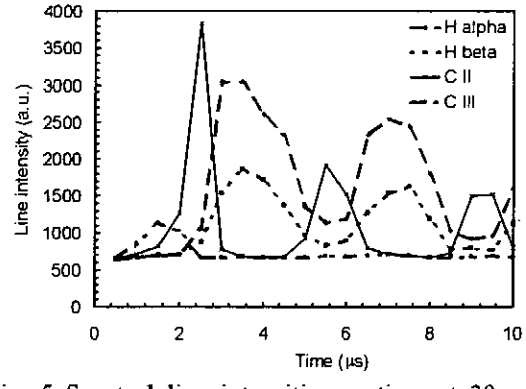

Fig. 5 Spectral line intensities vs time at 30 mm from cable gun nozzle

density oscillation takes place in all locations, but the amplitude of oscillation decreases with distance from the plasma gun due to the plasma velocity dispersion. The line integrated plasma density drops with the distance (Fig. 4). The line- integrated plasma density is higher in presence of POS electrodes compared to one measured at the same location without electrodes in the vacuum chamber. This difference by factor of 1.5 can be explained as the density increase due to the plasma reflection from the electrode surfaces as well as the secondary plasma production.

The measurements of spectral line intensities by OMA showed that the intensity of all lines also oscillates with the frequency corresponding to the oscillation of plasma gun current. The positions of their maximum in time are different for different lines at the distance long enough from the plasma gun nozzle due to non equal velocities, masses and charges of ion species. The intensities of Hα, Hβ, CII and CIII lines are given in time in Fig. 5. It was found that the time dependence of intensity of CII line corresponds well to the plasma density

measured by an interferometer. This fact allows to suggest that our plasma consists mostly of singly ionized carbon ions. The plasma density calculated from spectral line profiles (Stark broadening of Hβ line) gives the value of $2 \cdot 10^{15}$ cm^{-3}, which is quite similar to the result of interferometer measurements at the same distance from the plasma gun nozzle.

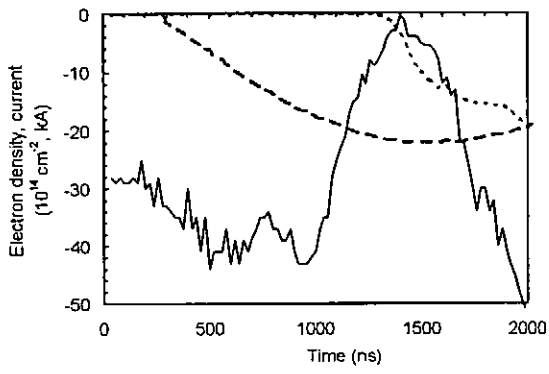

Fig. 6 Waveforms of generator current (dashed), load current (dotted) and line-integrated plasma electron density (solid curve) at 5.3 mm from the POS cathode.

Most measurements of plasma density in the POS were made with laser beam directed along POS electrodes. The measurements without the firing of the main POS current source (plasma gun only) showed that in the time moment corresponding to the main current start, the line - integrated plasma density is similar at all positions between electrodes. Measurements during the POS operation showed that the line-integrated plasma density between the POS electrodes has a minimum, when opening occurs, at almost all measured positions except the ones closest to the electrodes. The waveforms of generator and load currents and the line-integrated plasma density at 5.3 mm from the cathode are shown in Fig. 6. In this shot, the density drop to the zero level is seen indicating vacuum gap appearance in the mentioned location. Nevertheless, such a density drop does not occur in all the measurements for any positions.

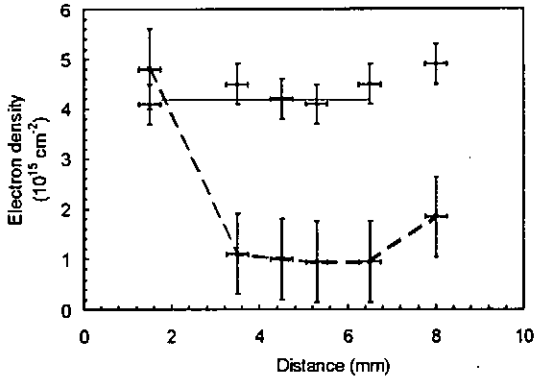

Fig. 7 Averaged line-integrated plasma electron densities before a shot (solid) and during POS opening (dashed curve) vs distance from the cathode.

The plasma densities averaged from ten shots in each location are given in Fig. 7 before the generator current begins to flow (upper curve, solid) and during the POS opening (lower curve, dashed). The predominant gap location corresponding to the lowest average plasma density during the POS opening was observed in the center of the interelectrode gap. The vertical error bars show the average deviation of the density. The highest probability of zero density signal corresponds exactly to the center of interelectrode gap. The probability analysis shows that the vacuum gap spacing is wider than the spatial measurement step giving the value of approximately 2 mm.

The measurements with the laser beam directed across POS electrode axes showed no density drop in any location. Such data allow to propose the model of switch operation where the plasma is displaced from the central part of the electrode system to the directions showed by arrows in Fig. 1. In the electrode system used, the region of highest magnetic field strength is located between POS electrodes making this suggestion reasonable. Plasma, which initially contains no magnetic field, moves from the region of higher magnetic field.

It is known, that changing the time delay between plasma gun shot and main POS current start it is possible to vary the conduction time of the POS. This is due to the change of the plasma density dependent on time. Since our plasma source produces the oscillating plasma density in time, the dependence of the conduction time on the delay time is not monotonous, but oscillating. This dependence is given in Fig. 8. Note, that the period of oscillations on the

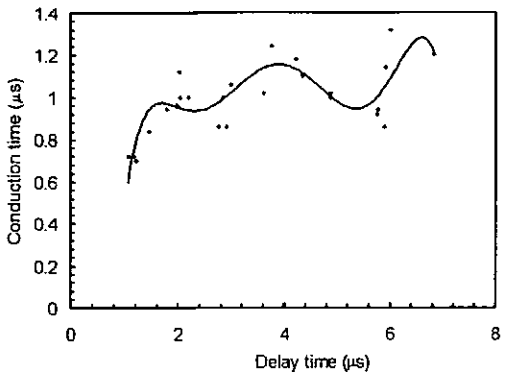

Fig. 8 POS conduction time vs time delay between start of plasma generation and ignition of main POS current source.

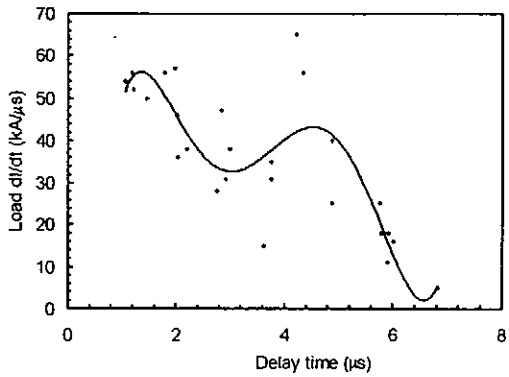

Fig. 9 POS load current dI/dt vs time delay between start of plasma generation and ignition of main POS current source.

curve is similar to the period of oscillations of plasma gun current. The dependence of the load current derivative dI/dt, which is one of major POS parameters, on the delay time shows several maximums corresponding to density peaks (Fig. 9).

Spectral measurements of line intensities during the switch operation was made with an OMA time gate of 100 ns. Varying the triggering time of the analyzer we measured the time dependence of the line intensities. The optical scheme was adjusted to measure plasma emission in the center of the interelectrode gap along the line of sight parallel to the electrodes. This location is characterized by the maximum plasma density drop measured by an interferometer. The time dependent line intensities for Hβ and CIII lines are given in Fig. 10. It is seen that the decrease in the intensity corresponds to the opening time of the POS. The spectroscopic observation of secondary plasma generated after a switch opening showed the absence of copper ions in the gap. This plasma is well seen at interferometer traces as fast density increase after opening drop. The absence of copper ions (copper is material of the POS electrodes) indicates that there are other reasons for the plasma production in the gap except the emission from electrodes. One of such reasons can be ionization of neutrals due to electron impact when fast electrons are accelerated during the switch opening.

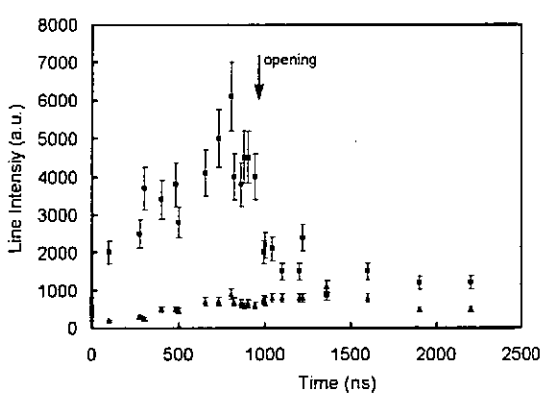

Fig. 10 Hβ (triangles) and CIII (squares) line intensities vs time. Zero time corresponds to ignition of main POS current source. Average time of POS opening is shown with arrow.

Noteworthy, that the line intensity is not proportional (but only dependent) to the plasma density. Generally speaking, the collisional - radiative codes have to be applied to the interpretation of such spectroscopy results for not LTD plasmas. In our case we just suggest that one of major reasons for the decrease of spectral line intensities (especially for highly ionized states) can be fast decrease of plasma density in the POS gap.

References

[1] B.M.Koval'chuk and G.A.Mesyats, Sov. Phys. Docl. **30**, 879 (1985).

[2] B.V.Weber et.al. Proceedings of the 9th International Conference on High Power Particle Beams, Prague, 1992, pp. 375-384.

[3] J.P.Quintenz et.al. Proceedings of the 11th International Conference on High Power Particle Beams, Prague, 1996, pp. 1-6.

[4] R.J.Commisso, P.J.Goodrich, J.M.Grossmann, D.D.Hinshelwood, P.F.Ottinger, and B.V.Weber, Phys. Fluids B **4**, 2368 (1992).

[5] J.M.Grossmann, S.B.Swanekamp, P.F.Ottinger, R.J.Commisso, D.D.Hinshelwood, and B.V.Weber, Proceedings of the 10th International Conference on High Power Particle Beams, San Diego, 1994, pp. 303-306.

[6] A.A.Sinebryukhov, A.A.Kim, V.A.Kokshenev, B.M.Koval'chuk, I.V.Lisitsyn and V.A.Sinebryukhov, Proceedings of the 11th International Conference on High Power Particle Beams, Prague, 1996, pp. 127-130.

[7] B.V. Weber et.al. Proceedings of the 11th International Conference on High Power Particle Beams, Prague, 1996, pp. 121-126.

[8] A.S.Chuvatin, B.Etlicher, N.S.Edison, and C.Rouille, Rev. Sci. Instrum. **64**, 2267 (1993).

Analysis of heat load at bore surfaces in plasma armature railguns

Sunao Katsuki, Tsuyoshi Sueda and Hidenori Akiyama
Department of Electrical and Computer Engineering
Kumamoto University, 2-39-1 Kurokami, Kumamoto 860

Abstract

Erosion of bore surfaces, which is caused by the energy flux from the plasma, is the most serious problem for repetitive operation in plasma armature railguns. Both polycarbonate and ceramic insulating rail spacers were tested to investigate how the heat-resistant materials work on the railgun performance. Also heat load at the bore was analyzed by using 0-D time-dependent plasma simulation, which includes the thermal conduction inside the bore materials. When the ceramic spacers were used, the plasma armature did not broaden so much during acceleration. The erosion on the copper rails, however, were more than that in case of polycarbonate spacers. According to the simulation, plasma temperature became higher in case of ceramic spacers, since the number of particle ablated from the bore was much less.

1. INTRODUCTION

Repetitive operation of railgun launchers [1] must be achieved to apply for the several kinds of applications, for instance, the acceleration of frozen hydrogen pellets for the refueling of magnetically confined fusion plasmas [2]. Ablation of bore materials due to an energy flux from a plasma armature [3][4] is the most serious problem that must be solved in order to increase the projectile velocity and to achieve repetitive operations of plasma armature railguns. The vapor ablated from the bore often becomes a cause of spurious currents and degrades the performance of plasma armature railguns. Also the ablation causes the damage on the bore surfaces, and prevents railguns from being operated repetitively.

There are several ways to reduce the ablation of bore materials [4]. Use of heat-resistant materials for the bore is considered as one of promising ways to decrease the ablation. Here, ceramic insulating rail spacers were examined in order to investigate how the heat-resistant materials work on the railgun performance. Plasma behaviors and heat load at the rail surface in both cases were investigated by analyzing B-dot probe's signals and observing post-shot rail surfaces, respectively.

Also heat load at the bore is analyzed by using non-dimensional time-dependent plasma simulation [5], which includes the thermal conduction into the bore materials. The temperature distribution in the bore materials in both rails and insulators are calculated by solving the one-dimensional thermal conduction equation [6], and the number of particles ablated from the bore surface is determined by both the state of bore surface and the energy flux from the plasma armature.

2. EXPERIMENTAL APPARATUS

A 50 cm small bore railgun, whose magnetic field is augmented by a permanent magnet, are used

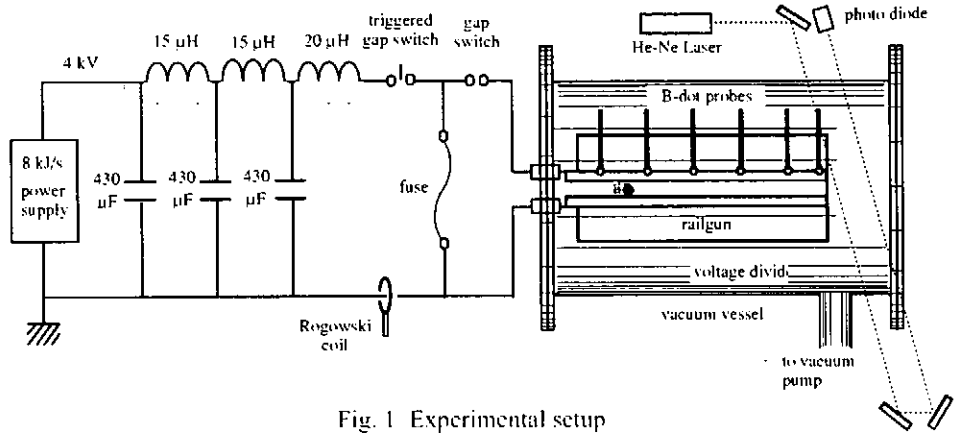

Fig. 1 Experimental setup

[7]. The railgun is composed of copper rails and insulating rail spacers. Two kinds of materials, which are ceramics and polycarbonate (PC), were used for the insulating rail spacers. Ceramics used in this experiment is a composite of SiO_2(45%), MgO(17%), Al_2O_3(16%) and so on. Copper was used as a rail material in both cases. Thermal characteristics of bore materials are listed in Table 1. The values in Table 1 are used in the simulation described in Section 4 and 5. A "C" type magnetic circuit was assembled to supply a constant magnetic flux density of 0.53 T to the gap between the rails. The permanent magnet (NEOMAX-40, Sumitomo Special Metals Co., Ltd.) is composed of Nd, Fe and B. The railgun has a total length of 50 cm and a bore of 5 mm square section. Projectiles are initially placed 5 cm from the breech so that the length for acceleration is reduced to 45 cm. The railguns are set in a vacuum chamber which is evacuated to less than 1.4 Pa.

A pulse forming network (PFN), which consists of three 430 μF capacitors and three 15 μH inductors, was used to produce a current pulse with a duration of 500 μs. The maximum driving currents is controlled to be about 20 kA. In that case, the primary stored energy of the capacitor bank was 9.3 kJ. A resin coated wood block is used to simulate the low mass of a hydrogen ice pellet. The projectile's mass and length are 25 mg and 2.5 mm, respectively. Plasma is formed by an exploding copper wire with a diameter of 0.04 mm. The current is measured by a Rogowski coil, and the plasma behavior is observed by five B-dot probes placed along the rails. Deconvolution of the B-dot signal was performed to determine the edge of the plasma armature [8]. Also post-shot rail surface was analyzed to estimate the heat load at the bore surface. A scanning electron microscopy (SEM) was used to observe rail surfaces.

Table. 1 Thermal characteristics of materials used for railgun experiment [9].

	melting point (K)	heat of transfer (10^5 J/kg)	boiling point (K)	heat of transfer (10^6 J/kg)	heat conduction (W/mK)	specific heat (J/kgK)	mass density (10^3 kg/m^3)
copper	1356	2.1	2868	4.9	415	419	8.92
PC	~500*	0.5	~1000*	0.8	1.7	1200	1.23
ceramics	>1300	1.5	3000	1.5	1.68	756	2.52

3. EXPERIMENTAL RESULTS

Figures 2 and 3 show typical waveforms of the current and signals from six B-dot probes, placed at $z = 0, 5, 10, 15, 20, 25$ cm along the rails, for railguns using polycarbonate (PC) and ceramic insulating rail spacers, respectively. Positive spikes on B-dot signals indicate the passage of the plasma armature at respective B-dot probe position. Plasma was accelerated without its separation in both cases. Mostly the separation of the plasma armature dose not appear up to $z = 25$ cm in our railgun experiment. However, the current distribution in the plasma armature seems complicated. B-dot signal at $z = 0$ also have a spike.

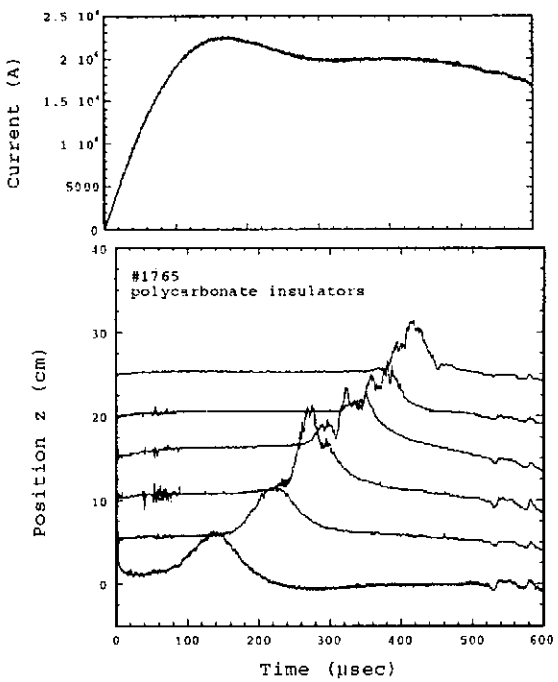

Fig. 2 Driving current and plasma behavior in case of use of PC insulators.

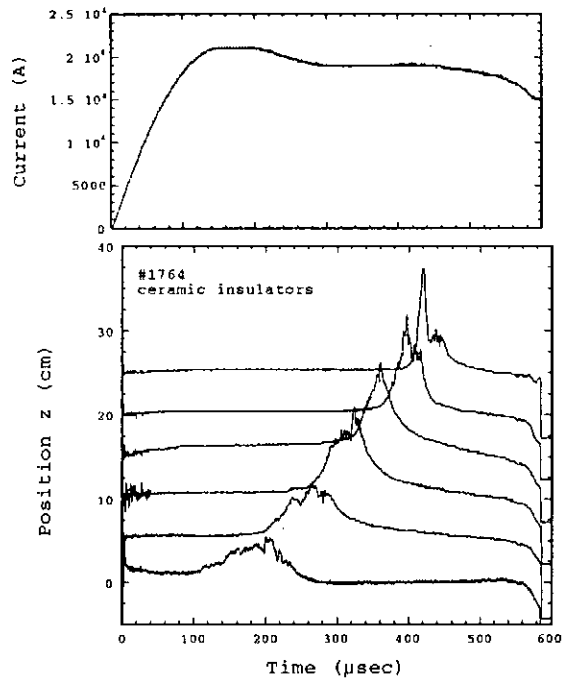

Fig. 3 Driving current and plasma behavior in case of use of ceramic insulators.

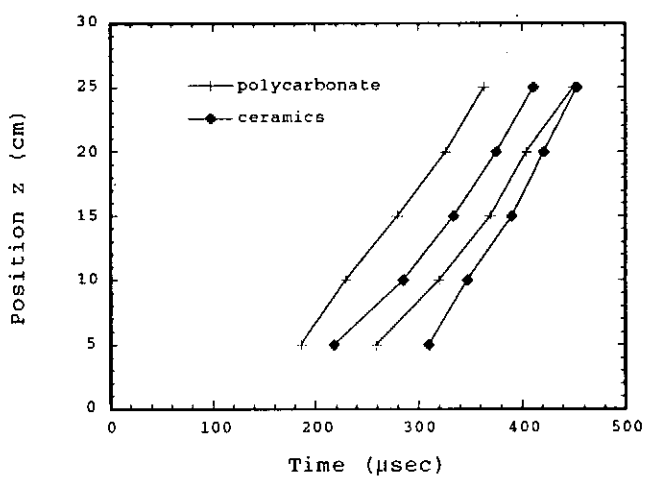

Fig. 4 Trajectories of leading and trailing edges of plasma armature.

Fig. 5 Post-shot rail surface around $x = 0$ in case of use of PC insulating spacers.

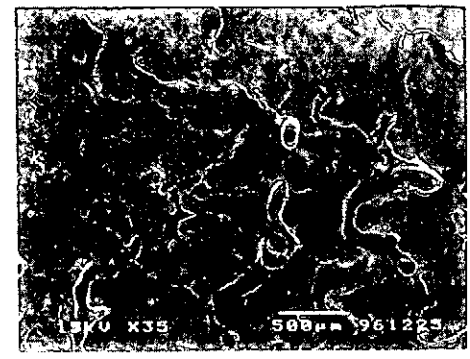

Fig. 6 Post-shot rail surface around $x = 0$ in case of use of ceramic insulating spacers.

This fact makes possible to deduce that the plasma, which is produced by explosion of thin copper wire, initially expands backward and is accelerated forward by the magnetic pressure behind it.

Figure 4 shows a trajectories of plasma armature, which is obtained from B-dot signals on #1764 and #1765. Plasma length in case of ceramics is initially longer, however it does not increase so much during acceleration, in comparison with that in case of PC. The plasma lengths, when the leading edge of the plasma arrived at $z = 25$ cm, were 7 cm and 11 cm, respectively. Slower movement in the early time in case of ceramic insulators was mainly caused by less acceleration due to 5% less current.

Figures 5 and 6 show post-shot rail surface around $z = 0$ in both cases. Projectile moves toward the right in Figs. 5 and 6. Rail material erodes off and flow out toward the right in both cases. However, state of surface are quite different from each other. There are lots of small ripples in case of PC insulation. On the other hand, ripple size is much larger and lots of holes are observed anywhere in case that ceramic spacers were used (Fig. 6). Since this holes might be caused by vaporization in the middle of rail, it can be deduced that heat load at the rail surface in case of ceramics spacers was much more than that in case of PC insulation. The reason why the status of the rail surface varies by insulator materials is discussed in Section 4 and 5.

4. SIMULATION MODEL

4-1. Plasma and projectile motions

In order to simulate the global dynamics of railgun plasma armature, a model as shown in Fig. 7 were used. A light rigid plate was used to express the electromagnetic force. Plasma exists between the plate and the projectile. Motion equations for the projectile and the rigid plate are expressed as

$$(m_p + m_a)\frac{d^2 z_p}{dt^2} = pd^2 - \frac{dz_p}{dt}\frac{dm_a}{dt} \tag{1}$$

$$m_0 \frac{d^2 z_t}{dt^2} = F_{arg} - pd^2 \tag{2}$$

respectively. Where m_p, m_a, and m_0 represent mass of projectile, plasma, and the rigid plate, respectively. z_p and z_t represent respective position of leading and trailing edge along the railgun. p is a plasma pressure and d is a bore size in square bore. F_{arg} shows a electromagnetic force caused by the current I in a

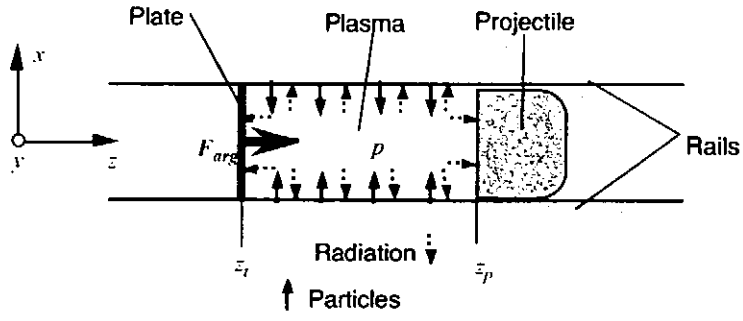

Fig. 7 Plasma model in simulation

augmented railgun with a external magnetic field B_e, such as

$$F_{arg} = \frac{1}{2} L' I^2 + I B_e d \tag{3}$$

where L' is the rail inductance per unit length.

4-2. Plasma characteristics

Two cases, which polycarbonate and ceramic insulator are used, are considered. Since kinds of particles included in the plasma in both cases are different from each other, the reacting processes have to be considered independently. Here, the plasma process in case of polycarbonate insulating spacers is described.

Plasma originally consists of Cu and CH_2. Some part of CH_2 is divided into H and C by degree of dissociation α_{CH2}. Then, the energy conservation can be expressed as

$$\frac{3}{2} N_t k dT = RI^2 dt - S\sigma_s T^4 dt - \frac{3}{2} k(T - T_{Cu}) dN_{Cu} - \frac{3}{2} k(T - T_p) dN_{CH2}$$

$$-2eV_{CH} dN_{CH2} - eV_H dN_H - eV_C dN_C - eV_{Cu} dN_{Cu} - pdV \tag{4}$$

where N_t is the total number of particles, shown as

$$N_t = (1 + \alpha_H) N_H + (1 + \alpha_C) N_C + (1 + \alpha_{Cu}) N_{Cu} + (1 - \alpha_{CH2}) N_{CH2} \tag{5}$$

where

$$N_H = 2\alpha_{CH2} N_{CH2} \tag{6}$$

$$N_C = \alpha_{CH2} N_{CH2} \tag{7}$$

α_H, α_C, α_{Cu} represent degree of ionization for H, C and Cu, respectively, and defined by Saha s equation,

$$\frac{\alpha^2_{H,C,Cu,CH2}}{1 - \alpha^2_{H,C,Cu,CH2}} = \frac{(kT)^{5/2}}{p} \left(\frac{2\pi m_e}{h^2} \right)^{3/2} \exp\left(\frac{-eV_{H,C,Cu,CH2}}{kT} \right) \tag{8}$$

where m_e and h represent electron mass and Plank s constant, respectively. $V_{H,C,Cu,CH2}$ is energy needed for ionization or dissociation in respective particle. S and V in Eq. (4) are surface and volume of plasma armature, respectively. Respective terms from the left in the right arm of Eq. (4) represent dissipation energy, radiation, heating for Cu and CH_2, dissociation for CH_2, ionization for H, C and Cu, and mechani-

cal energy at pressure p.

Plasma resistance is defined by Spitzer's resistivity. Since railgun plasmas are generally high density but low temperature, an effect of collision between electron and neutral can not be negligible, therefore,

$$R = \frac{1}{(z_p - z_r)} \frac{m_e}{n_e e^2} (\upsilon_{ei} + \upsilon_{enH} + \upsilon_{enC} + \upsilon_{enCu} + \upsilon_{enCH2}) \tag{9}$$

where

$$\upsilon_{ei} = 3.62 \times 10^{-6} n_e T^{-3/2} \ln \Lambda$$

$$\upsilon_{en(H,C,Cu,CH2)} = 2.60 \times 10^{-4} \delta^2_{(H,C,Cu,CH2)} n_{(H,C,Cu,CH2)} T^{1/2}$$

$$\ln \Lambda = 1.24 \times 10^{-7} T^{3/2} n_e^{-1/2}$$

When we assume that all the radiative flux from the plasma is absorbed by the walls, input power per unit area into the wall is

$$dq_{(R,I)} = \sigma_s (T^4 - T^4_{(R,I)}) \tag{10}$$

where characters with subscription (R,I) represent the value for rail and insulator surface, respectively. If temperature of wall surface reaches its boiling point, the number of particles ablated from copper rails and PC insulator walls are

$$dN_{Cu} = dq \frac{E_{ht}}{m_{Cu}} 2d(z_p - z_r) dt \tag{11}$$

$$dN_{CH2} = \frac{dq}{E_{cc}} 2d(z_p - z_r) dt \tag{12}$$

respectively. Where E_{htCu} and E_{CC} are the heat of transfer at the boiling point for copper and dissociation energy for C-C bond, respectively. The increment of plasma mass is shown as

$$dm_a = (2m_H + m_C) dN_{CH2} + m_{Cu} dN_{Cu} \tag{13}$$

And theincrement of the number of electron becomes

$$dN_{e(H,C,Cu)} = N_{(H,C,Cu)} d\alpha_{(H,C,Cu)} + \alpha_{(H,C,Cu)} dN_{(H,C,Cu)} \tag{14}$$

Finally, plasma pressure is given as

$$p = \frac{N_t}{V} kT \tag{15}$$

4-3. Thermal conduction

In order to determine the status of both the rail and insulator surfaces, temperature distributions in the middle of both of them were calculated by way of solving one dimensional thermal conduction equations shown as

$$\rho_R c_R \frac{dT_R}{dt} = \frac{J^2}{\sigma_R} + \lambda_R \frac{\partial^2 T_R}{\partial x^2} \tag{16}$$

$$\rho_I c_I \frac{dT_I}{dt} = \lambda_I \frac{\partial^2 T_I}{\partial x^2} \tag{17}$$

respectively. Where ρ, c, σ and λ are mass density, specific heat, electrical and thermal conductivity, respectively. Subscriptions R and I mean the values in rail and insulator materials, respectively. Energy dissipation due to the rail current occurs only inside the rail. The boundary conditions on rail and insulator surface are given as

$$dq_R = -\lambda_R \left(\frac{\partial T_R}{\partial x} \right)_{x=0} \tag{18}$$

$$dq_I = -\lambda_I \left(\frac{\partial T_I}{\partial x} \right)_{x=0} \tag{19}$$

These diffusion equations were solved by the implicit time-integration method.

5. SIMULATION RESULTS

Figure 8 shows a railgun plasma armature dynamics in both cases with polycarbonate and ceramic insulating rail spacers. The same current waveform is used in both cases. A spike, which is shown in pressure waveform in the early time, indicates the explosion of a thin copper wire as a plasma source. After that, the plasma pressure goes up gradually together with the current. There is no difference between two cases on the pressure waveforms since the plasma pressure always balances with the electromagnetic force caused by the current.

Waveforms in both cases behave in almost the same manner until 25 μs in all waveforms. After 25 μs, the plasma temperature in case of ceramic insulation becomes higher than that in case of PC insulation. In the time evolution of the plasma mass, PC insulator has started vaporizing at 25 μs, which corresponds to the time when the temperature saturates. The plasma is cooled down by the particles ablated from both the rail and insulator surface. On the other hand, copper has started vaporizing at 40 μs when ceramic is used for a insulation, since the copper needs less energy to ablate than the ceramic. The temperature increase saturates also at 40 μs. The increasing rate of the plasma mass is much different between two cases. This difference is caused by the thermal characteristics of the bore materials. Since the number of the particles ablated from the ceramic surface is much less, the plasma temperature becomes higher.

Also the increase in the plasma mass lessens the acceleration. The projectile velocity in case of PC insulation is slightly lower. There are two curves in respective case on the time evolution of the plasma position. The upper and lower indicate the leading and trailing edges of the plasma armature, respectively. The difference between two curves is the plasma length along the railgun. The increase in the plasma mass also results the plasma broadening.

Figure 9 shows the radiation power from the plasma. Maximum radiation power, when the ce-

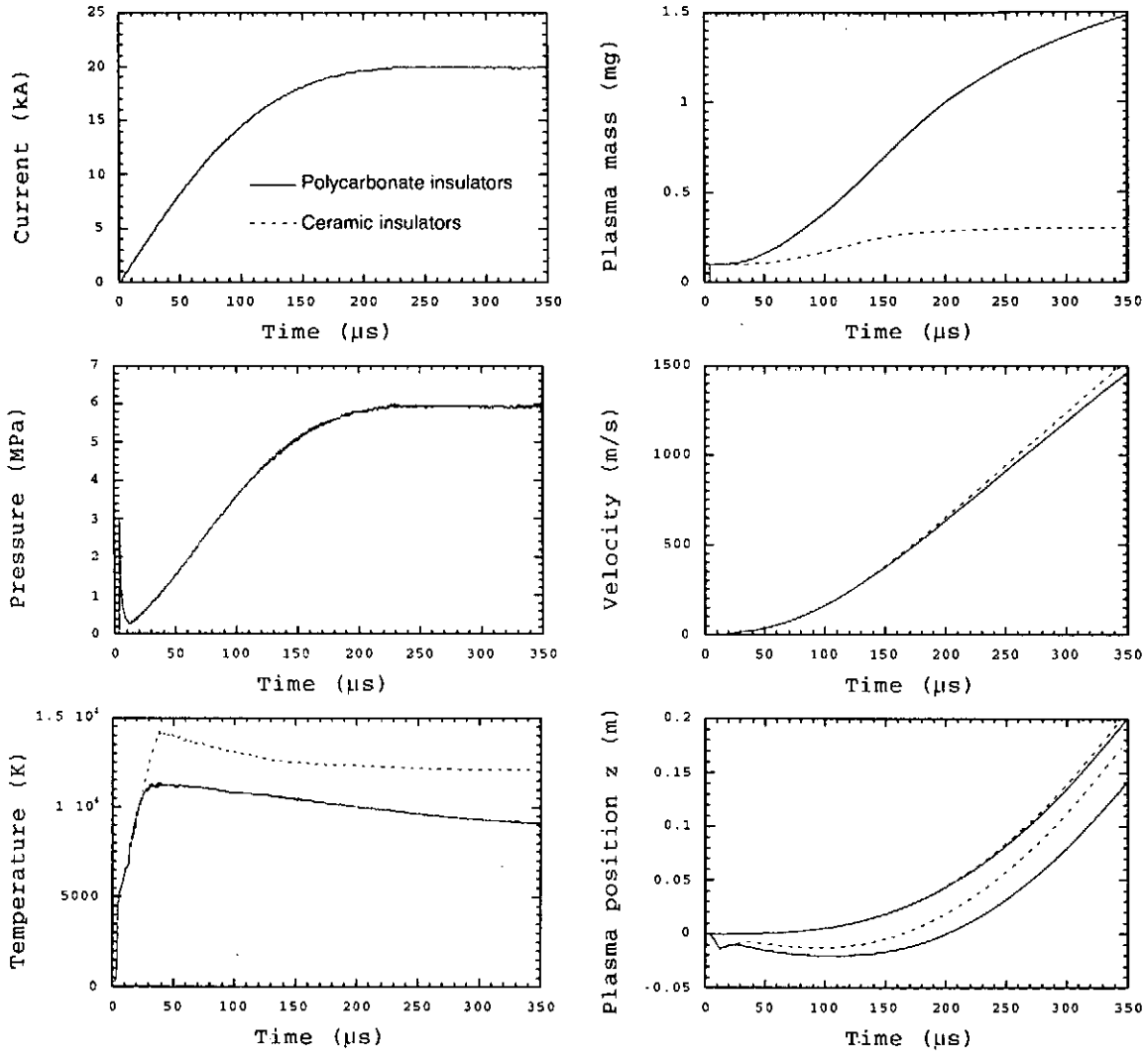

Fig. 8 Simulated railgun plasma dynamics

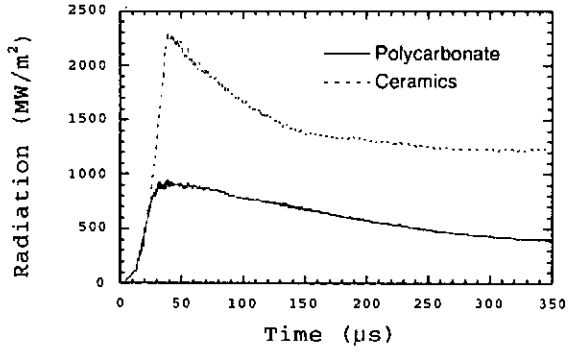

Fig. 9 Radiation power.

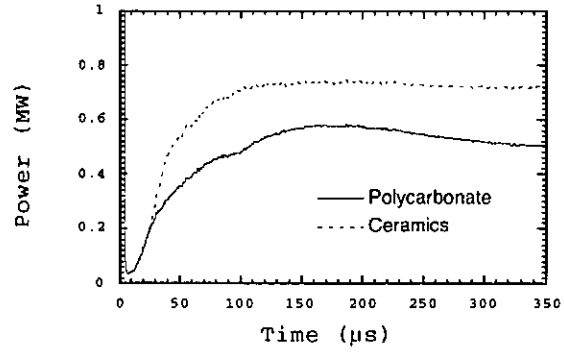

Fig. 10 Electrical power input into the plasma.

ramic insulators are used, is 2.5 times as that in case of PC insulation. This makes the erosion on the rail surface more severe. Electrical power input in both cases are shown in Figure 10. Since the radiation power in case of ceramic insulators is much larger, the electrical power is provided to heat the plasma up.

Figure 11 shows the temperature distributions in both the insulator (a) and the rail (b). The vertical axis shows the position along the rail in mm, and the horizontal axis shows the depth from the surface in

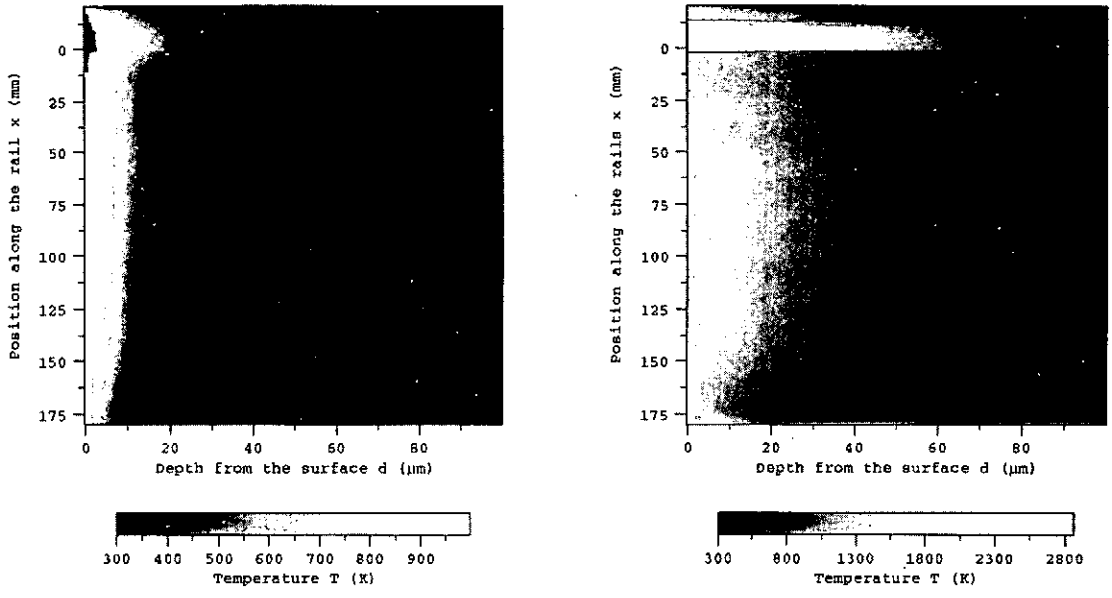

(a) Polycarbonate rail spacer (b) Copper rail

Fig. 11 Temperature distribution inside the bore materials in case of combination of polycarbonate insulator and copper rail

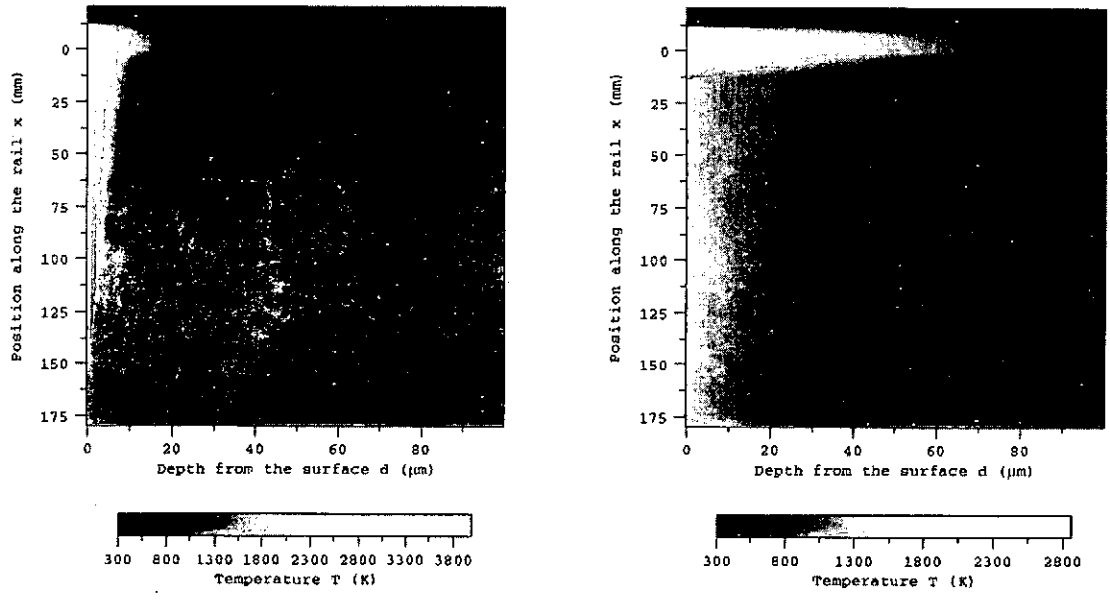

(a) Ceramic rail spacer (b) Copper rail

Fig. 12 Temperature distribution inside the bore materials in case of combination of ceramic insulator and copper rail

μm. The maximum value of the temperature scale is set to its boiling point. It is found that the insulator materials erodes off around the position where the projectile is set initially. Since the thermal conductivity of copper is much larger, heat injected from the surface penetrates deeply. In the insulator, however, the heat is stacked at the surface, therefore the temperature at the surface reaches the boiling point immediately.

Figure 12 shows a temperature distributions in both the ceramic insulator (a) and copper rail (b). No erosion is observed on the ceramic surface. However, the heat load at the copper rail around the initial position of the projectile is obviously larger than that in case of the PC insulation.

6. CONCLUSION

In order to reduce the ablation on the bore surface, ceramics, which is one of the typical heat-resistant materials, were tested as insulating rail spacers. When the ceramic insulators are used, plasma does not broaden so much. However, the erosion on the copper rails seems more severe only around the initial position of the projectile. This is caused by the high plasma temperature due to the less ablation on the ceramic insulator surfaces. In this case, the larger electrical power is provided since the radiative power also increases. The more effective heat-resistant material is used, the more radiative power will be put into the bore.

7. REFERENCES

[1] S. C. Rashleigh, and R. A. Marshall, "Electromagnetic acceleration of macro-particles to high velocities," J. Appl. Phys. vol. 49, no. 4, pp. 2540-2542, 1978.

[2] S. K. Combs, "Pellet Injection Technology," Rev. Sci. Technol., vol. 64, no. 7, pp. 1679-1698, 1993.

[3] J. V. Parker, W. M. Parsons, C. E. Cummings, and W. E. Fox, "Performance loss due to wall ablation in plasma armature railguns," AIAA 18th Fluid Dynamics and Plasmadynamics and Lasers Conf., Cincinnati Ohio, 1985, pp. 1-10.

[4] J. V. Parker, "Why plasma armature railguns don t work (and what can be done about it)," IEEE Trans. Magnetics, vol. 25, no. 1, pp. 418-424, 1989.

[5] P. K. Ray, "Rail gun performance and plasma characteristics due to wall ablations," IEEE Trans. Magn., vol. 22, no. 6, pp. 1699-1705, 1986.

[6] J. D. Powell, "Thermal-energy transfer from arc to rails in an arc-driven rail gun," IEEE Trans. Magn., vol. 20, no. 2, pp. 395-398, 1984.

[7] S. Katsuki, H. Akiyama, et al., "Augmented railgun using a permanent magnet," Rev. Sci. Instrum., vol. 66, no. 8, pp. 4227-4232, 1995.

[8] S. Katsuki, H. Akiyama, at al., "Behaviors of plasma armature in the augmented railgun using permanent magnet," IEEE Trans. Magn., vol. 31, no. 1, pp. 183-188, 1995.

Characteristics of High-Current Pulsed Discharge

K. Masugata, T. Suzuki, N. Nakayama, K. Takao, and K. Yatsui
Nagaoka University of Technology,
Nagaoka, Niigata 940-21 Japan

Abstract

Characteristics of high-current arc discharge in H_2, N_2, CO_2, O_2 and SF_6 were investigated to develop a long life, high-repetition pulse power switch. The discharge gap of gap length 2.5-3.5 mm is pulse discharged with breakdown voltage 10-30 kV, current 6-16 kA, and duration around 400 ns. Damage radius and roughness in the damaged area were evaluated as a function of discharge gas, material of the electrode and the discharge voltage. From the experiment the radius and the roughness were found to be reduced by using H_2. Stability of breakdown voltage on the multi-shot operation was evaluated and found that V_b increases as the shots when using SF_6 or CO_2, whereas it decreases when using N_2, O_2, H_2. The scattering of the breakdown voltages was extremely increased when using SF_6.

1. Introduction

Pulsed power technology[1,2] has a wide area of application such as the generation of high-power particle beams, and X-ray or gas laser excitation. In these applications, it is very important to develop a highly repetitive system to obtain a higher average power. In the pulsed power technology, a number of pressurized discharge gap switches with SF_6 or air have been utilized.[1,2] However, since such the switches take a long time for the recovery of breakdown voltage and the energy loss in the switching is relatively

large, it has been considered to be difficult to achieve a highly repetitive operation.[3] In the previous works dependence of the characteristics of the switches on the filling gas were studied and found that the recovery speed and the efficiency are enhanced by using H_2.[3,4] However, the stability and the life time of the H_2 gas switch were not evaluated, which is also very important to develop highly repetitive pulse power switches.

In the paper damage characteristics and the stability of breakdown voltages are evaluated as parameter of filling gas, electrode material and the discharge voltage. From the study we have found that by using H_2 gas, it is possible to reduce the damage and enhance the stability.

2. Experiment

2 .1 Observation of the damage of electrodes

Figure 1 shows the experimental circuit and the cross-sectional view of the discharge gap switch used in the experiment. A C-R discharge circuit is utilized in the experiment to damp the ringing current and to obtain a single polarity discharge current flow. In the gap switch, a flat electrode is utilized with a hemispherical brass electrode of diameter 25 mm, which are installed inside the acrylic vessel. A copper and an aluminum board of thickness 0.5 mm were used to sample the damage data. The

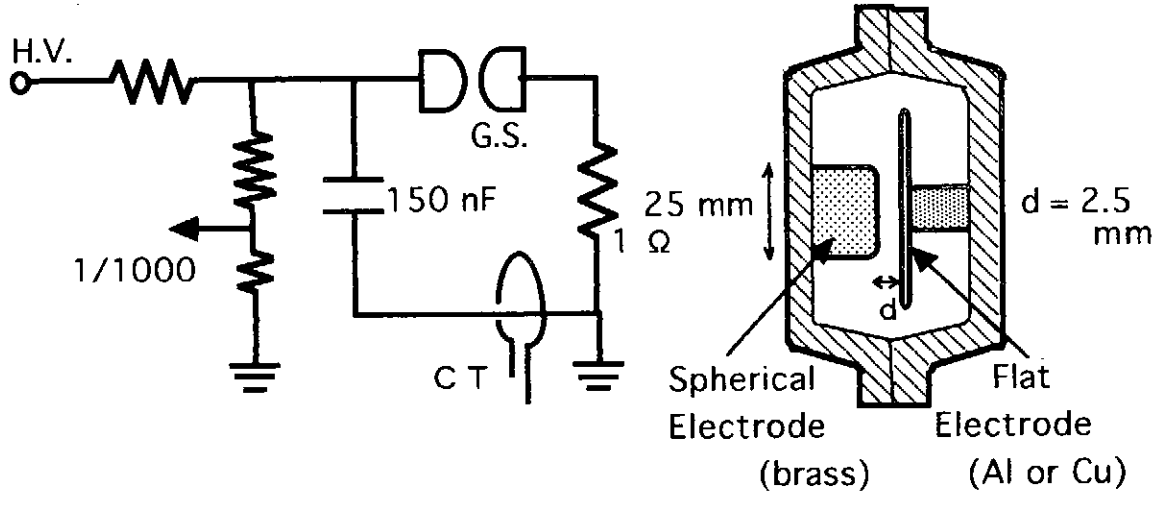

Figure 1 a) Experimental circuit to evaluate the damage of the electrode. b) Cross-sectional view of the discharge gap switch.

surface of the electrode was mirror polished before the discharge. The gap length (d) was adjusted to 2.5 mm and, SF_6 and H_2 were utilized as a filling gas. The switch was operated in a self breakdown mode and the breakdown voltage (V_b) was adjusted by the filling gas pressure (p). For example, for V_b = 30 kV, the switch was filled with 1.2 atm of SF_6 or 6 atm of H_2. Charging voltage of the capacitor was slowly increased until the switch was self broken. The capacitor was charged negatively and positively to obtain a cathode and anode damage on the flat electrode.

For the measurement of V_b and the discharge current (I), a resistive voltage divider and a current transformer were utilized as shown in Fig. 1 and the waveforms were recorded by a digitizing oscilloscope. To evaluate the damage, surface of the flat electrode was observed by an optical microscope or a scanning electron microscope (SEM). The surface profile of the damaged area was measured by a surface roughness meter.

Figure 2 shows the typical waveform of the discharge current when V_b = 23.5 kV. Peak current of 11 kA is observed with pulse duration 400 ns (Full Width at Half Maximum, FWHM). The waveform was almost similar for all conditions in the experiment.

Figure 3 shows the photographs of damage taken with an optical microscope when the switch was filled with 0.6 atm of SF_6. As seen in the figure, circular damage area of radius 0.7 mm is produced on the Al anode whereas 0.5 mm for Cu anode.

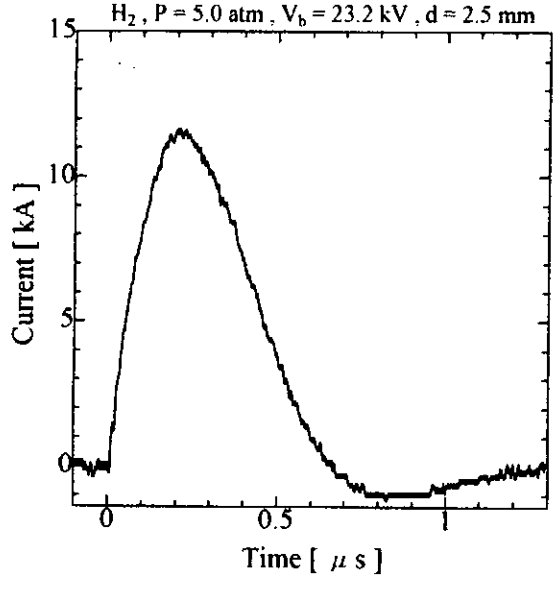

Figure 2 Typical waveform of discharge current.

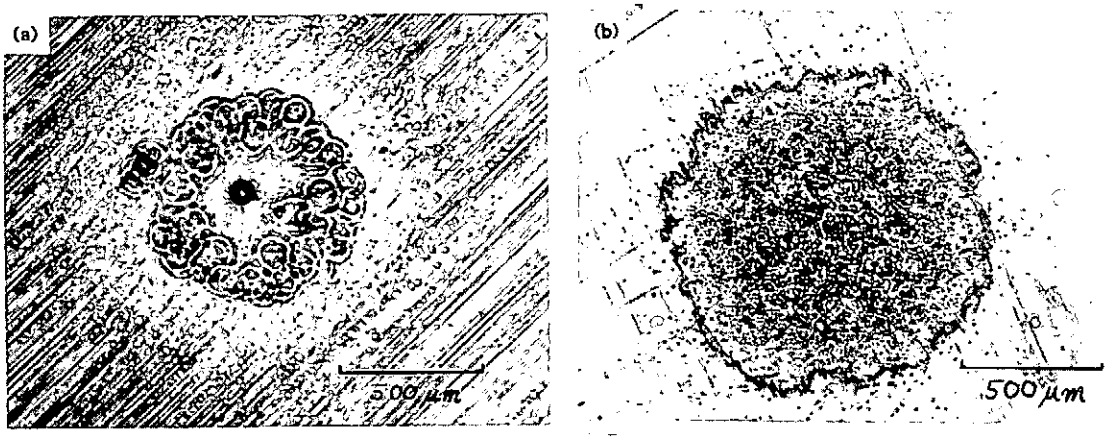

Figure 3 Photographs of the damage on the electrode. a) Al anode, b) Cu anode.

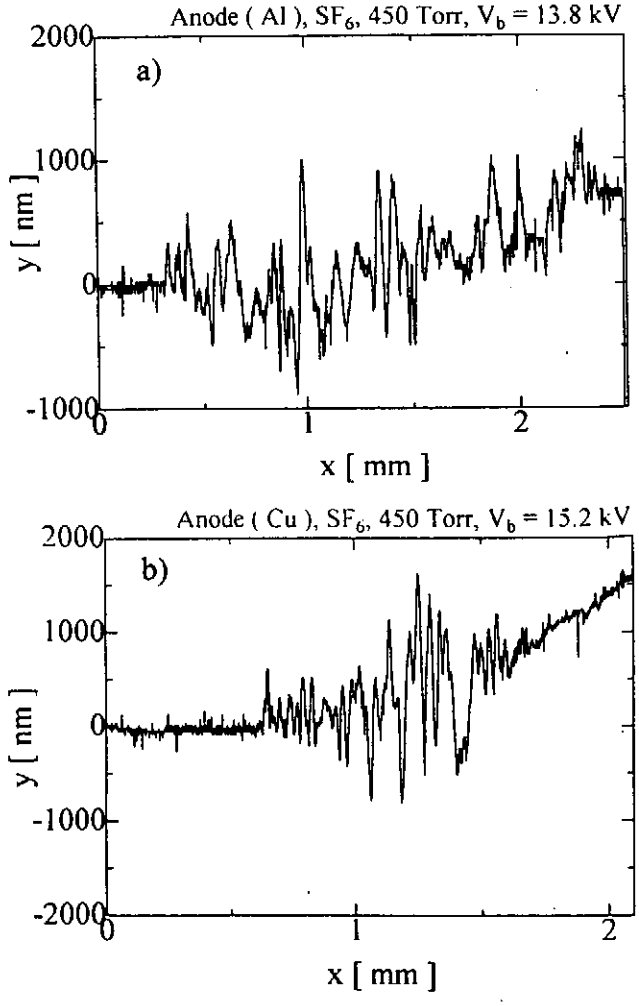

Figure 4 Profiles of the surfaces of damaged area. a) Al anode, b) Cu anode.

Figure 4 shows the profile of the surfaces of damaged area shown in Fig. 3. As seen in the figure, maximum peak to valley height around 2 μm is observed in both case. In addition, the surface was concavely curved.

Figure 5 shows the example of SEM photograph. In the figure, concentric circular wrinkles are observed in the outer area of the damaged area as if the surface is strongly pushed outside whereas relatively flat area is observed inside.

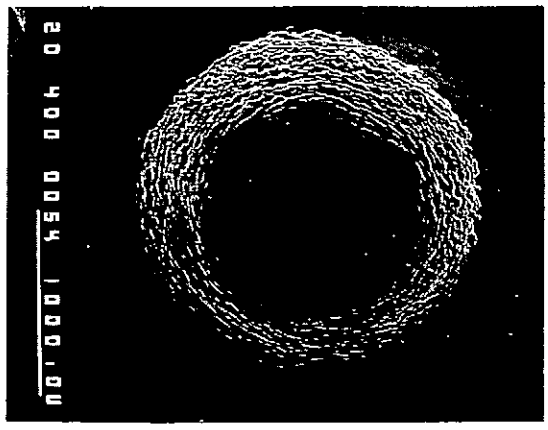

Figure 5 photograph of cathode surface taken with SEM .

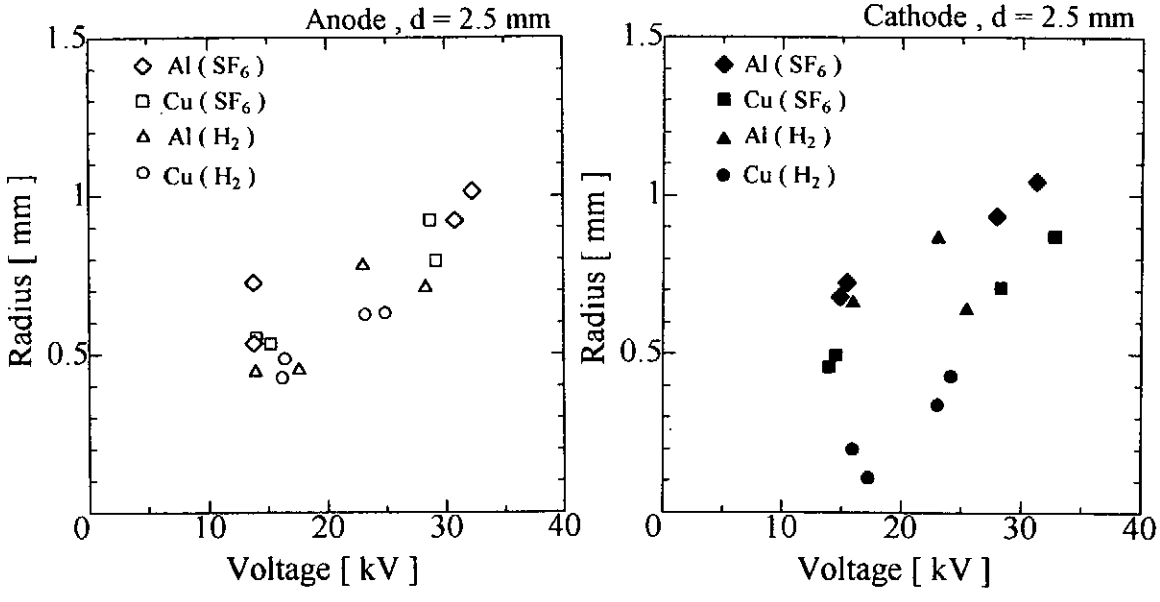

Figure 6 Dependence of the radius of damaged area plotted against V_d

Figure 6 shows the dependence of the radius of damaged area plotted against V_d. As seen in the figure, the radius increases with increasing V_d. The radius tends to increase when using Al electrode or when using filling gas of SF_6.

2.2 Stability of discharge voltage

To evaluate the stability of the discharge voltage when the switch is operated repetitively, the circuit shown in Fig. 1 was again utilized. As the gap switch, a pair of hemispherical electrodes (brass, 25 mm diameter) was utilized with gap length (d) 3.5 mm. The gap switch was continuously discharged at a repetition rate around 3 Hz and V_b was sampled every one minuet. The discharge was repeated for 10000 shot (it

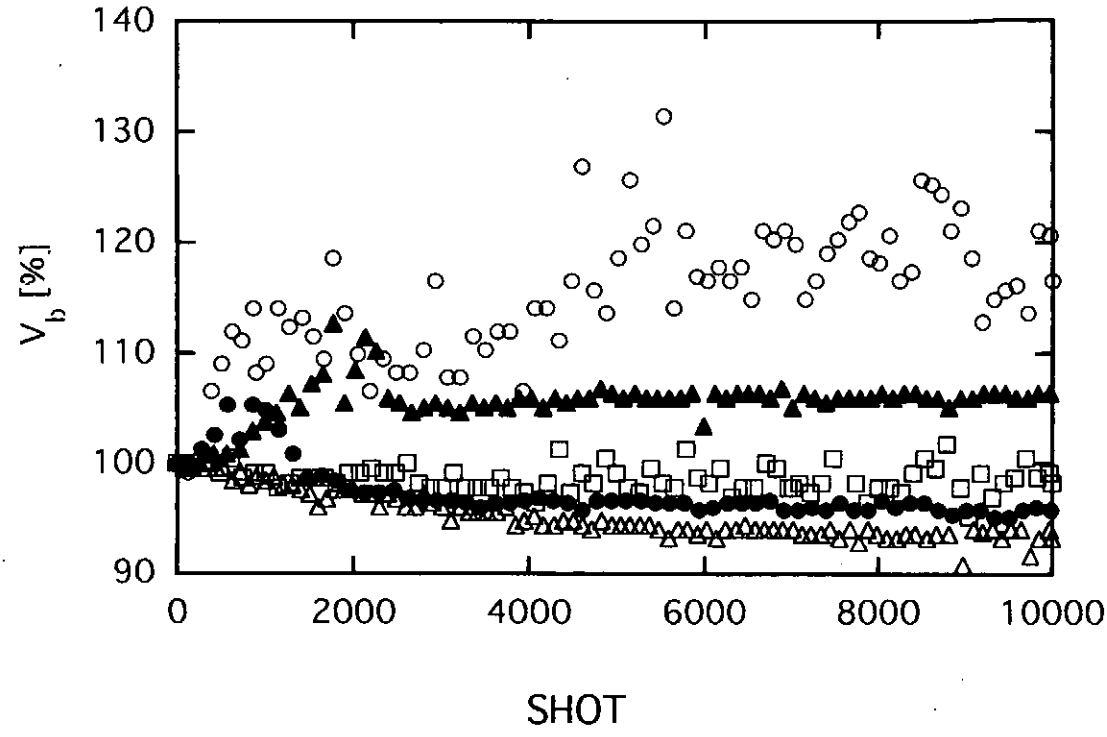

Figure 7 Dependence of V_b on the shot number. ○ SF_6, p = 0.57 atm, V_{b0}=21.6 kV, ▲ CO_2, p =2.40 atm, V_{b0}=22.4 kV, ● N_2, p = 2.00 atm, V_{b0}=21.8 kV, □ O_2, p = 2.10 atm, V_{b0}=21.9 kV, △ H_2, p = 3.38 atm, V_{b0}=20.6 kV.

takes about one hour) continuously without changing the filling gas. Filling gas of SF_6, CO_2, N_2, O_2 and H_2 were utilized, which are filled to the pressure corresponding to the breakdown voltage around 21 kV.

Figure 7 shows the dependence of V_b on the shot number. Here V_b were normalized by the initial breakdown voltages (V_{b0}) for each gas. Filing pressures (P) and V_{b0} are listed in the figure. As seen in the figure V_b increases with increasing the number of shot when using SF_6 or CO_2, whereas it decreases with the shot number when using N_2, O_2 and H_2.gas. Especially for the case of using SF_6, 20 % of enhancement of V_b is observed.

The increase of breakdown voltage is considered to be due to the deposition of fluorine composite or surfer on the surface of the electrode.[5] In addition, Scattering of V_b increases in the case. In contrast, when the switch was filling with N_2, O_2 or H_2, V_b decreases as the shot. The decrees of V_b seems to be due to the heat up of the electrode, which decreases the density of the gas near the electrode. In addition, when using CO_2, and O_2, V_b becomes unstable during shot No. 1000-2000.

Table I Summary of the experiment shown in Fig. 7.

Filling gas	SF_6	CO_2	N_2	O_2	H_2
P [atm]	0.57	2.40	2.00	2.10	3.38
V_{b0} [kV]	21.6	22.4	21.8	21.9	20.6
V_{av} [kV]	25.8	23.7	21.5	21.1	19.3
V_{av}/V_{b0}	1.19	1.06	0.98	0.96	0.94
σ [%]	1.76	0.23	0.57	0.14	0.33

Table I summarize the results of the experiment. Here, averaged breakdown voltage (V_{av}) and the standard deviation (σ) is evaluated from the data from shot number 4000 to 9000. As seen in the table large scattering of σ =1.74 % is observed when using SF_6 whereas it is less than 0.5 % for CO_2, O_2, and H_2. After the operation the surface of the electrode was covered with a white powder when using SF_6.

The surface of the aluminum electrode was analyzed by an x-ray micro analyzer (XMA) after 10000 shots of discharge in H_2 and in SF_6. Metallic atoms of Cu, and Zn were detected in both case, which seems to be produced by the spattering of the brass electrode. In the case of using SF_6, sulfur and fluoride were also detected which seem to be produced by the dissociation of SF_6.

4. Conclusion

Characteristics of high-current arc discharge in H_2, N_2, CO_2, O_2 and SF_6 were investigated to develop a long life, high-repetition pulse power switch. The discharge gap of gap length 2.5-3.5 mm is pulse discharged with breakdown voltage 10-30 kV, current 12-16 kA, and duration around 600 ns. Damage diameter and roughness in the damage area was evaluated as a function of discharge gas and the material of the electrode and found that the area and the roughness were reduced by using H_2 as compared to the case of using SF_6. Stability of breakdown voltage in the multi-shot operation was evaluated and found that V_b increases with increasing the shot number when using SF_6 or CO_2, whereas it decreases as the shots when using N_2,O_2, H_2. Scattering of the breakdown voltages extremely increased when using SF_6, which seem to be due to the deposition of materials produced by the desiccation of SF_6.

References

1) A. Nation: Particle accelerators **10** (1979) 1.

2) C. Martin: Proc. IEEE **80** (1992) 934.

3) L. Moran and L. W. Hardesty: IEEE Trans. Electron Devices **38** (1991) 726 .

4) K. Masugata, H. Maekawa, M. Yoshida, T. Ishii, T. Suzuki, K. Yatsui: Jpn. J. of Appl. Phys. 35(10) (1996) 5487.

5) M. Yumoto, H. Iida, and T. Sakai: "Formation Process of SF_6 gas Decomposition Product and its Effects on Breakdown Voltage", The trans. of IEE of Japan A105(8) (1996) 437. (in Japanese)

Electron density measurements in capillary plasmas

T. Sueda, S. Katsuki, H. Akiyama
Department of Electrical and Computer Engineering, Kumamoto University,
2-39-1 Kurokami, Kumamoto 860, JAPAN

Abstract

Operation of an electrothermal gun is strongly related to capillary discharges. The electrothermal gun has been assembled and studied at Kumamoto University for investigation of the physical phenomena in an initial state of the capillary discharge. The operation of the electrothermal gun with a small capillary diameter is superior to one with a large diameter in the vacuum. In order to understand these experimental results clearly, the plasma parameters of electron density and temperature, which are strongly related to the operation characteristics of the electrothermal gun, were measured for different capillary diameters by a spectroscopic technique. The electron density and temperature of the capillary plasma increase with decreasing the capillary diameter. The early operation of the electrothermal gun with a small capillary diameter is superior to that with a large capillary diameter because of the increase of the capillary plasma pressure. The electron density in the capillary with different diameter was measured by an interferometry technique in order to validate the density estimated by the spectroscopic measurement. The electron densities, 10^{17} - 10^{19} cm^{-3}, estimated by the interferometer measurements agree with those from the spectroscopic measurement. Results from a zero-dimensional time-dependent model are compared with experimental results. The tendency, which the electron density of the capillary plasma increases with decreasing capillary diameter, coincides with the experimental results.

1. Introduction

Electromagnetic launch devices used for acceleration of projectiles to hypervelocity include railguns, coilguns and electrothermal guns. An electrothermal gun facility was assembled and studied at Kumamoto University for investigation of the physical phenomena in an initial state of the capillary discharge. [1] [2] High-density and high-temperature plasmas are produced by high power pulse discharges in the capillary, and projectiles located at the end of capillary are accelerated by the resulting plasma pressure. Since the plasma pressure is strongly dependent on the electrical energy delivered to the capillary discharge, it is necessary to increase the energy absorbed in the capillary by the discharge in order to increase the projectile velocity.

It has been reported that reduction of the capillary diameter leads an increase in the kinetic energy of the projectile in the vacuum because the plasma resistance increases with decreasing capillary diameter and hence, results in an increase in the input energy into the capillary plasma. [3] [4] In order to understand these experimental results clearly, the plasma parameters of electron density and temperature, which are strongly related to the operation characteristics of the electrothermal gun, were measured for different capillary diameters by a spectroscopic technique. [3][4] The electron density and temperature of the capillary plasma increase with de-

creasing the capillary diameter. The early operation of the electrothermal gun with a small capillary diameter is superior to that with a large capillary diameter because of the increase of the capillary plasma pressure. [5]

In this paper, the electron density and temperature of the capillary plasma with different inner capillary diameters are measured by an interferometer in order to validate the density estimated by the spectroscopic measurement. The density estimated by the interferometer measurement are compared with those by the spectroscopic measurement, and results for a zero-dimensional (0-D) time-dependent model [5] are compared with these experimental results. We discussed the physical phenomena in an initial state of the capillary discharge with a view toward achieving the best operating conditions for the electrothermal gun.

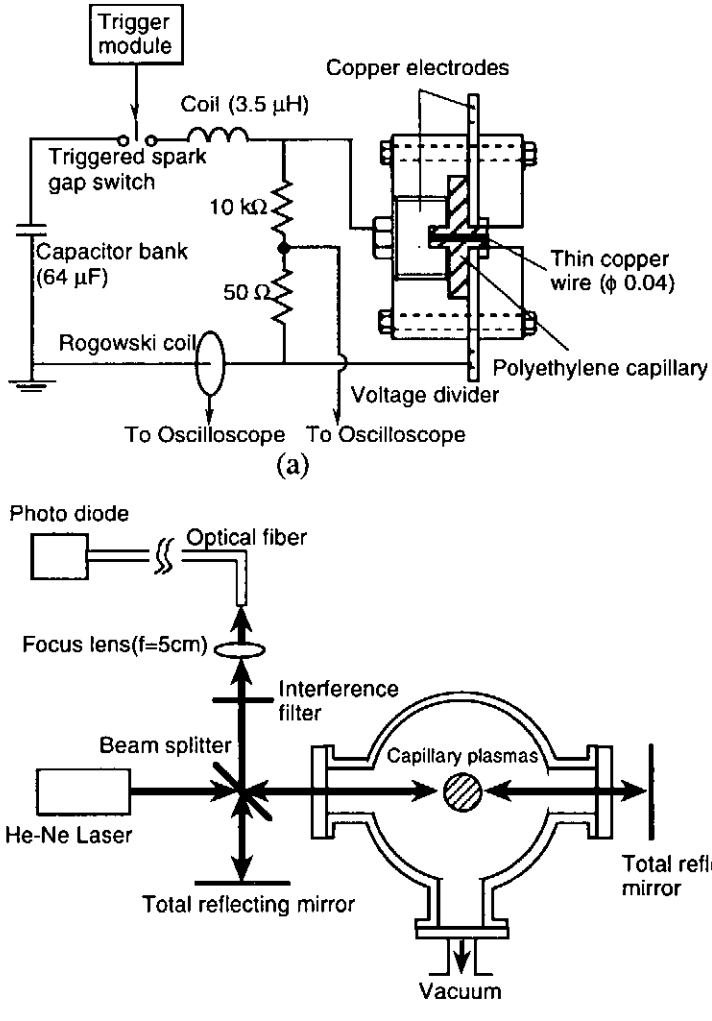

Fig. 1. Experimental set up for an electrothemal gun (a) and Michelson interferometer (b).

2. Experimental apparatus and procedures

Figure 1 (a) shows the experimental setups for measurements of the capillary discharges and the voltage across the capillary. The power supply consists of a capacitor bank with a maximum stored energy of 80 kJ and a capacitance of 64 μF, a coil with an inductance of 3.5 μH and a triggered spark gap switch. An electrothermal gun usually consists of copper electrodes, a polyethylene capillary and a steel barrel, although the barrel is removed from the electrothermal gun during this experiment for observation of the radiation from the capillary plasma. The inner diameter of the cylindrical capillary is varied from 2 to 6 mm, and the length is constant at 30 mm. A thin copper wire with a diameter of 0.04 mm is placed in the capillary, and connected to both electrodes. The discharge current through the capillary is measured using a Rogowski coil, and the voltage across the capillary is measured using a voltage divider with a 1/200 voltage ratio.

Figure 1 (b) shows the experimental setups for the laser interferometer of Michelson scheme. The He-Ne laser beam with the maximum power of 5 mW and the diameter of 0.8 mm is divided into reference and probe beams by a beam splitter. Both beams recombine at the same beam splitter again and are focused at the input of a quartz optical fiber using a focus lens (f = 5 cm) through the interference filter. This filter is used to avoid the plasma luminosity. Interferometry signals are detected using Si PIN photodiode with sensitivity equal to 0.4 A/W for He-Ne laser wavelength (Hamamatsu, S5973).

The electron density of the capillary plasma is estimated by analyzing the interferometry signal. [6] The plasma has an index of refraction, N_p,

$$N_p = \left(1 - \frac{{\omega_{pe}}^2}{{\omega_0}^2}\right)^{\frac{1}{2}} = \left(1 - \frac{n_e}{n_c}\right)^{\frac{1}{2}}, \tag{1}$$

where n_e is the electron density of the plasma and n_c is the critical electron density where the probe laser frequency, ω_0, equals the electron plasma frequency, $\omega_{pe}=(4\pi n_e e^2/m_e)^{1/2}$. The critical density is calculated from $n_c=(1.12 \times 10^{27})\lambda_L^{-2}$ cm^{-3}, where λ_L is the incident laser wavelength in nanometer. The critical density in the case of He-Ne laser is 2.8×10^{21} cm^{-3}. Since the electron density of the capillary plasma estimated using the spectroscopic measurements is less than 1×10^{19} cm^{-3}, the density can be measured using the He-Ne laser interferometer. The plasma produces a phase shift, $\Delta\phi$, relative to the reference beam which is given by

$$\Delta\phi = \left(\frac{2\pi}{\lambda_L}\right)\int_0^L N_p dl = \left(\frac{2\pi}{\lambda_L}\right)\int_0^L \left(1 - \frac{n_e}{n_c}\right)^{\frac{1}{2}} dl, \tag{2}$$

where L is the path length of the probe beam through the plasma. For $n_e << n_c$, eq. (2) is approxi-

mated by

$$\Delta\phi \approx \left(\frac{\pi}{\lambda_L n_c}\right)\int_0^L n_e dl. \tag{3}$$

For the He-Ne laser wavelength of 632.8 nm, the line integrated plasma density is given by

$$\int_0^L n_e dl = 5.61 \times 10^{16} \Delta\phi, \tag{4}$$

in units of cm^{-2}. Figures 2 (a) and 2 (b) show the fringe pattern before a shot and during a shot in different time scale, respectively. Oscillations as shown in fig. 2 (a) are mechanical vibrations coming from a rotary pump, mainly. The characteristic period of mechanical vibrations (more than several ms) is much longer than that of the measurement time for the capillary plasma (less than 10 μs). Therefore, the mechanical vibration does not influence the phase shift due to the refraction of the capillary plasma. Each minimum and maximum in Fig. 2(b) shows the phase shift equal to π, that is, the line integrated plasma density is 1.76 x 10^{17} cm^{-2}. The attenuation of the interferometry signal is due to the decrease of the transmissivity of He-Ne laser through the capillary plasma because of high plasma density.

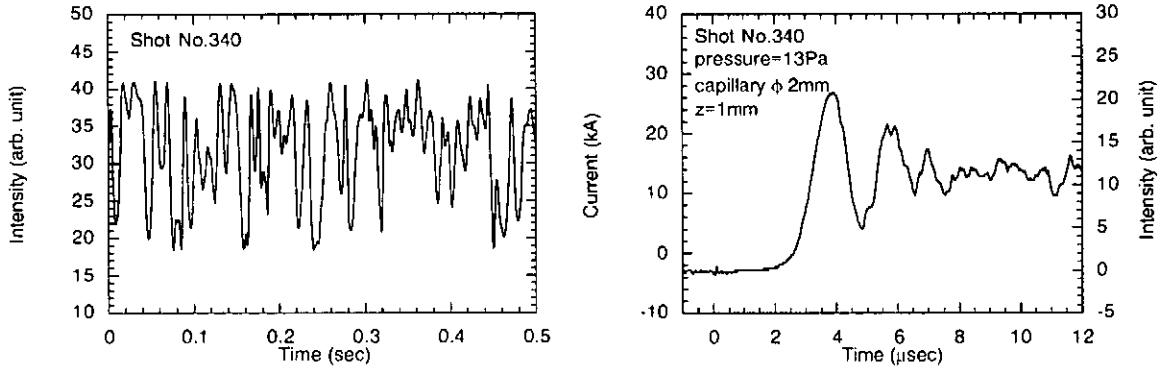

(a) (b)

Fig. 2. Fringe pattern before a shot (a) and during a shot (b).

3. Results and Discussion

Figure 3 shows typical waveforms of the discharge current (a) and the voltage across the capillary (b) for capillary diameters of 2, 4 and 6 mm. After the pulsed voltage is produced by the melting and vaporization of the thin copper wire, the voltage increases for about 6 μs, and then becomes constant. The voltage increases with reduction of the capillary diameter. The current does not change much since it is determined by the circuit capacitance and inductance. Thus, the capillary plasma resistance increases with decreasing capillary diameters. The absorbed energy into the capillary also increases with the reduction of the capillary diameter.

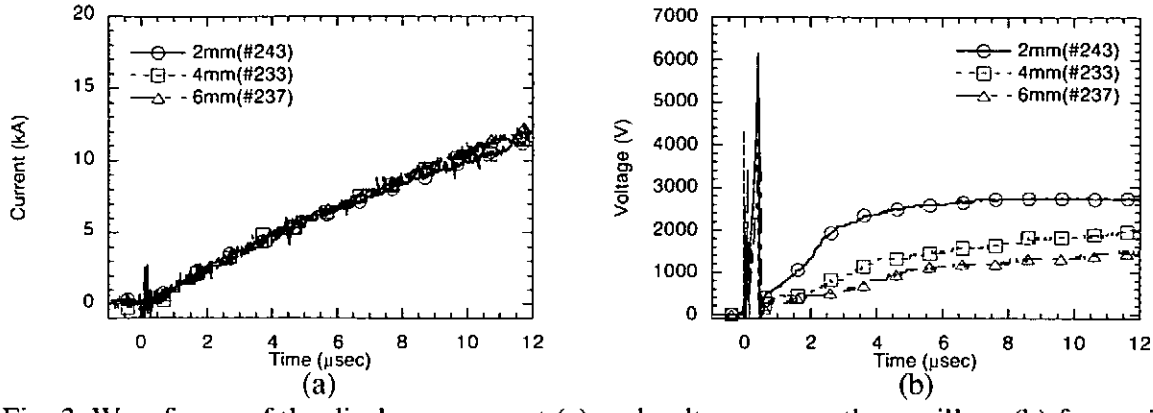

Fig. 3. Waveforms of the discharge current (a) and voltage across the capillary (b) for capillary diameters of 2, 4, 6 mm.

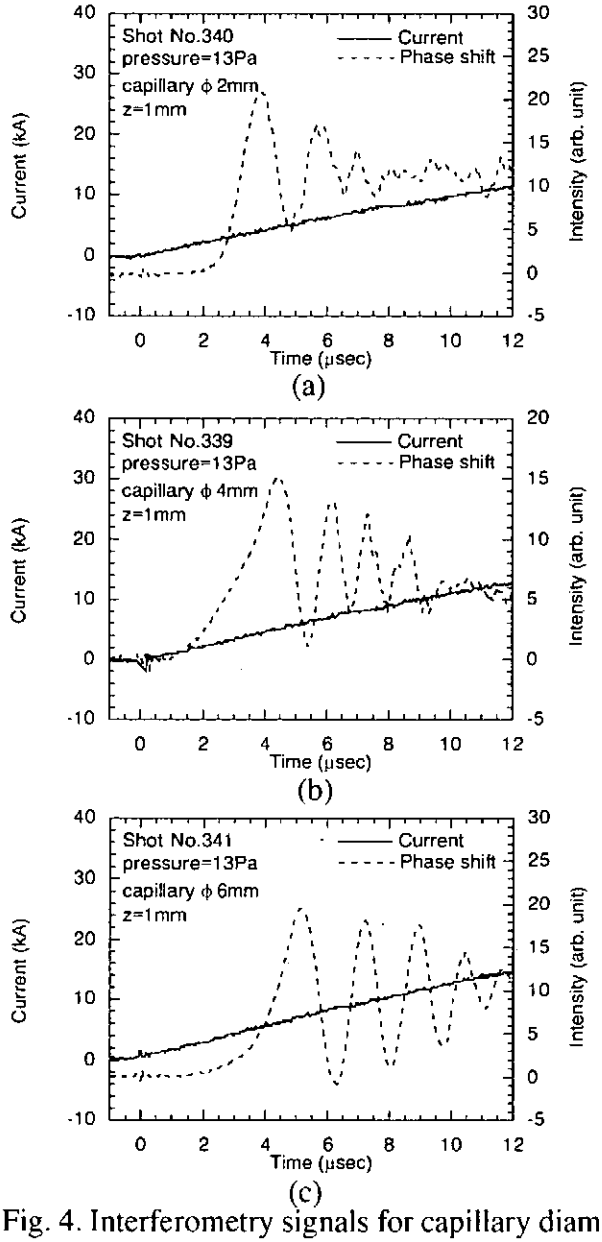

Fig. 4. Interferometry signals for capillary diameters of 2 (a), 4 (b), 6 mm (c).

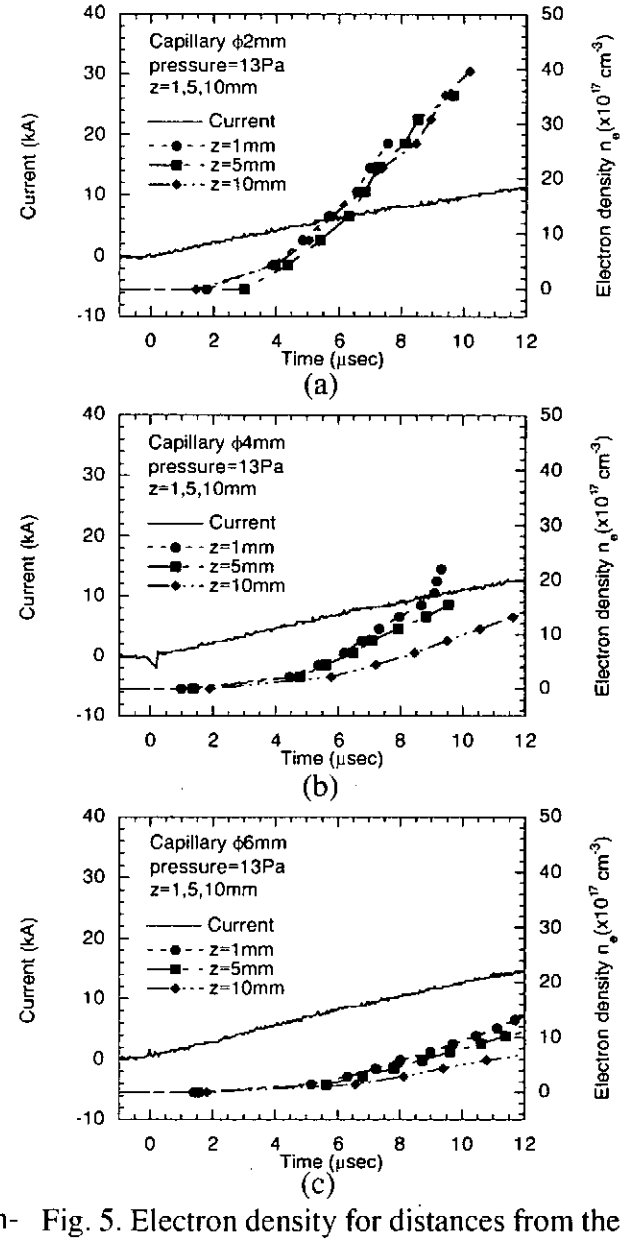

Fig. 5. Electron density for distances from the capillary muzzle of 1, 5, 10 mm in capillary diameters of 2 (a), 4 (b), 6 mm (c)..

Figure 4 shows the typical waveforms of the discharge current and the interferometry signal for capillary diameters of 2 (a), 4 (b) and 6 mm (c). The attenuation of the interferometry signal becomes small as the capillary diameter is large, since the transmissivity of the laser beam through the capillary plasma does not decrease due to the low density of the capillary plasma.

The electron density for the different distances from the capillary muzzle estimated by the phase shift as shown in Fig. 4 are shown in Fig. 5. In all cases, the density slightly decreases with increasing the distance from the capillary muzzle.

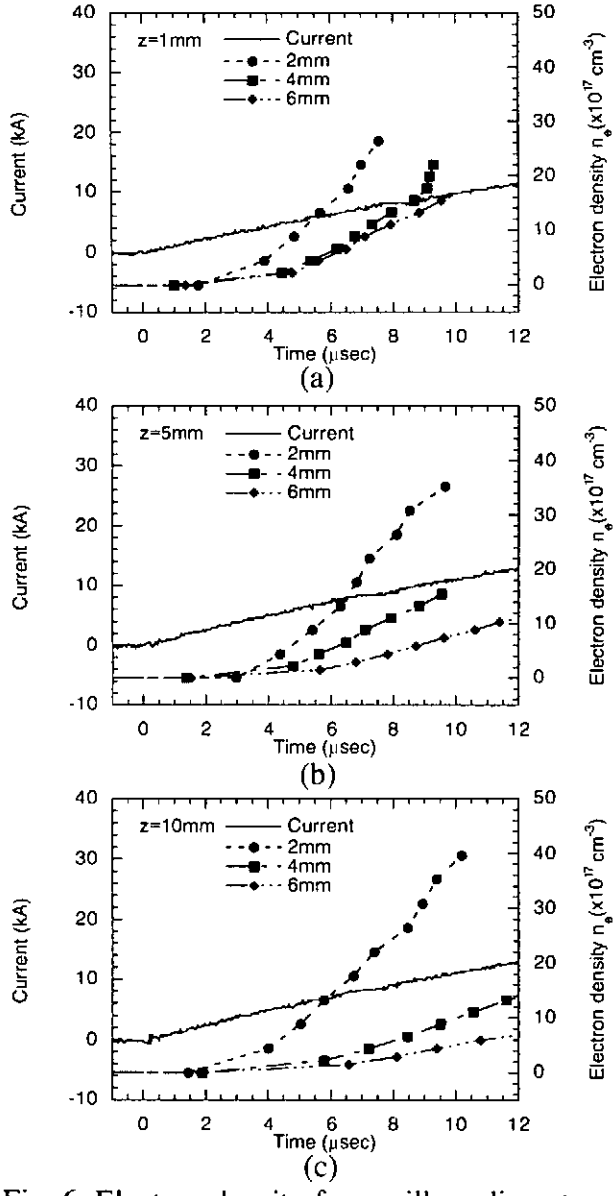

Fig. 6. Electron density for capillary diameters of 2, 4, 6 mm in distances from the capillary muzzle of 1 (a), 5 (b), 10 mm (c).

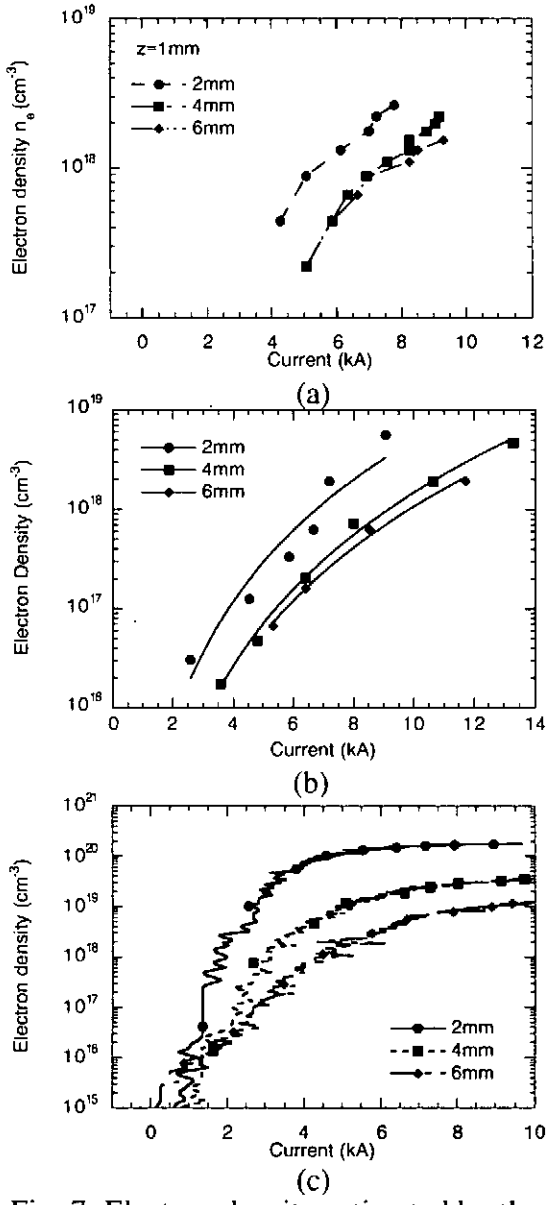

Fig. 7. Electron density estimated by the interferometer (a), the spectroscopic measurement (b) and the simulation (c).

Fig. 6 shows the electron density for different capillary diameters of 2 (a), 4 (b) and 6 mm (c). The density increases with reduction of the capillary diameter. Therefore, it is demonstrated experimentally that the rate of wall ablation increases markedly because of the increase of the absorbed energy into the capillary as the capillary diameter decreases.

Fig. 7 shows the electron density estimated from the interferometer measurement (a), the spectroscopic measurement (b), and the simulation (c). The electron densities, 10^{17} - 10^{19} cm^{-3}, estimated from the interferometer agree with those from the spectroscopic measurement. The density calculated with the simulation also increases with decreasing the capillary diameter. The tendency coincides with the experimental result. However, the absolute values of the density, especially at 2 mm, are larger than those estimated from both measurements. Further modification of the simulation model is necessary for coincidence of not only the trend, but also the absolute values of density.

4. Conclusion

The electron densities of the capillary plasmas for different capillary diameters were measured using an interferometer and a spectroscopic techniques, and compared with simulation results obtained using a 0-D time-dependent model in order to investigate the physical phenomena in an initial state of the capillary discharges and understand the operation of an electrothermal gun. The electron densities, 10^{17} - 10^{19} cm^{-3}, estimated by the interferometer measurement agree with those from the spectroscopic measurement. It was found experimentally and theoretically that the electron density tends to increase with decreasing the capillary diameter. Consequently, the early operation characteristics of an electrothermal gun with a small capillary diameter are superior to those of with a large capillary diameter because of the increase in the capillary plasma pressure.

References

[1] T. Sueda, S. Katsuki and H. Akiyama, "Early phenomena of capillary discharges for an electrothermal gun", Appl. Phys. Lett., Vol. 68, No. 13, pp. 1766-1768 (1996).
[2] T. Sueda, S. Katsuki and H. Akiyama, "Early phenomena of capillary discharges in different ambient pressures", IEEE Trans. on Magnetics, Vol. 33, No. 1, pp. 334-339 (1997).
[3] M. Rott, "The LRT/TUM Small Caliber Electrothermal Accelerator", IEEE Trans. on Magnetics, Vol. 29, No. 1, pp. 597-602 (1993).
[4] M. Shahinpoor, J. R. Asay et. al., "Use of a Two-Stage Light-Gas Gun as an Injector for Electromagnetic Railguns", IEEE Trans. on Magnetics, Vol. 25, No. 1, pp. 514-518 (1989).
[5] T. Sueda, S. Katsuki and H. Akiyama, "Behavior of capillary plasmas with different diameters", Jpn. J. Appl. Phys., Vol. 36, No. 4, Part 1 (1997).
[6] N. Edison, P. E. Young, N. Holmes and R. W. Lee et. al., "Characterization of a capillary-discharge plasma", Phys. Rev. E, Vol. 47, No. 2, pp. 1305-1312 (1993).

A high-speed image converting system for impulsive soft x-ray image observation

Takeshi Yanagidaira, Toshikazu Yamamoto, Morihiko Sato,
Katsuji Shimoda and Katsumi Hirano
Department of Electronic Engineering, Gunma University,
Kiryu, Gunma 376, Japan

Abstract

A high-speed soft x-ray imaging system is described. Time-resolved images of impulsive sources are restructured from data obtained with a multi-channel soft x-ray detector and a soft x-ray pinhole camera by the inversion technique. The system can display images both in framing- and streak mode at the same time. The temporal resolution is 3 ns. This system is used to study the time evolution of soft x-ray generation in plasma focus discharges with puffed Ar.

1. Introduction

The plasma focus and the gas puff z-pinch are impulsive soft x-ray sources of intense line- and continuous emission when the discharges are carried out using high Z gases. In studying the mechanism of soft x-ray generation, imaging techniques which provide time-resolved measurements are indispensable.

The streak and the framing mode measurements are equally useful for observing the time variation of source intensity.[1,2] For observation of the pulsed x-ray source, a pinhole camera with a gated microchannel plate (MCP) and/or a soft x-ray streak camera in which an image converter tube is installed has often been used. Streak mode is a method which enables continuous observation. However, it is carried out through a slit, hence the viewing field is limited to a very narrow region. On the other hand, the framing mode enables the recording of a complete view of the object although it is only a discrete observation in time.

We have developed a soft x-ray imaging system with time resolution without employing image tubes or gated MCP's. This system can be composed of commercially available components. We employed a soft x-ray pinhole camera and a multi-channel

soft x-ray detector consisting of a scintillator-photomultiplier tube combination.[3] With this system, it is possible to record time varying phenomena and to display both in streak and framing mode.

2. Description of the system

2. 1. Streak- and framing mode imaging of soft x-ray sources

The proposed soft x-ray imaging system in framing- and streak mode makes use of two complementary parts which are an arrayed scintillator-photomultiplier detector and a soft x-ray pinhole camera. The schematic diagram of the arrayed detector is shown in Fig. 1. The arrayed detector includes a soft x-ray sensitive scintillator plate, slits, bundled fiber optics and photomultiplier tubes. The image of the soft x-ray source is formed on the plastic scintillator plate, NE142 of $t = 0.2\,\mathrm{mm}$ in thickness through a Be foil filter of $25\,\mu\mathrm{m}$ in thickness and a pinhole of $d = 0.1\,\mathrm{mm}$ in diameter. The thickness of the scintillator and the Be filter is determined so that photon energy around 3 keV can be selectively detected. The visible image on the scintillator generated by exposure of the soft x-rays is divided into 12 segments by the 12 slits which are attached on the rear side of the scintillator. The optical signals from each channel are led to the photomultipliers (Hamamatsu Photonics, H5783 photo sensor module) through the bundled fiber optics and recorded in storage oscilloscopes (Hewlett-Packard 54542A). The signal from each channel is spatially integrated along the slit. The pinhole camera is used for determining the position of the x-ray source and its time-integrated intensity. The pinhole image of the soft x-ray source is formed on a MCP (Hamamatsu Photonics F2223-11P) through a pinhole $25\,\mu\mathrm{m}$ in diameter and Be-Ag combination foil filter ($25\,\mu\mathrm{m}$ and $1\mu\mathrm{m}$ in thickness, respectively). The filters and the MCP give a passband between 1.8 keV and 3.4 keV, which accepts Ar K-lines.[4] Electrons from the MCP are accelerated onto a phosphor screen to produce a visible image. The visible image is then recorded by a charge-coupled device (CCD) camera and processed with a PC in which an image memory board is installed. The CCD camera was operated in a mode in which the response of the CCD is proportional to the luminosity of the image.

The temporally- and spatially varying x-ray source can be restructured with the

source image distributed over detector channels and the pinhole image by the inversion technique. At the inversion, the viewing field is divided into pixels. For processing of the x-ray sources, we adopted a one-dimensional grid of 20 pixels, 1 mm $\times$ 8 mm rectangles, which are numbered by J along z. The time axis was divided into 25 fragments of 3.0 ns. The source intensity to be determined is then expressed as $i(J,T)$, where T is the time.

Let the quantities measured experimentally in the analog signals of the m-th channel and the pinhole image be $V_m^{(\mathrm{m})}(T)$ and $I^{(\mathrm{m})}(J)$, respectively. Determination of $i(J,T)$'s is made possible by using the least-squares method. We tentatively assume an initial value for the presumed intensity. Corresponding to the presumed intensity $i(J,T)$, the analog signals and pinhole image are calculated as

$$V_m^{(\mathrm{c})}(T) = \sum_J S_m(J) i(J,T) \tag{1}$$

and

$$I^{(\mathrm{c})}(J) = \sum_T i(J,T), \tag{2}$$

where $S_m(J)$ is the sensitivity of the m-th channel at the pixel J. We compare the calculated $V_m(T)$ and $I(J)$ with their measured values by taking the summation of the square of the residual, R. Therefore,

$$R = w_1 \sum_m \sum_T [V_m^{(\mathrm{c})}(T) - V_m^{(\mathrm{m})}(T)]^2 + w_2 \sum_J [I^{(\mathrm{c})}(J) - I^{(\mathrm{m})}(J)]^2, \tag{3}$$

where w_1 and w_2 are the coefficients for adjusting the weight of each term. The optimum $i(J,T)$ is obtained by iteration to make R minimum. We used the genetic algorithm to find a solution for the intensity $i(J,T)$.

Each frame in the framing mode display is obtained by multiplying the luminosity of each pixel in the pinhole image by coefficients calculated from the corresponding $i(J,T)$. Namely, the luminosity of the framing images is given as

$$i_{\mathrm{f}}(\boldsymbol{x},T) = i_{\mathrm{p}}(\boldsymbol{x}) i[J(\boldsymbol{x}),T] / \sum_T i[J(\boldsymbol{x}),T], \tag{4}$$

where $\boldsymbol{x}$ is an arbitrary location in the images and $i_{\mathrm{p}}(\boldsymbol{x})$ is the luminosity of the pinhole image at $\boldsymbol{x}$. And, $J(\boldsymbol{x})$ is the pixel in which the position $\boldsymbol{x}$ is included.

On the other hand, the streak mode display is obtained by sweeping a region

specified arbitrarily by introducing a 'virtual slit' after the acquisition of the data. The luminosity of the streak image is given as

$$i_s(L,T) = \sum_w i_f(\boldsymbol{r} + L\boldsymbol{e}_1 + w\boldsymbol{e}_2, T), \tag{5}$$

where $\boldsymbol{e}_1$ and $\boldsymbol{e}_2$ are unit vectors parallel and perpendicular to the virtual slit, and $\boldsymbol{r}$ is the location of the virtual slit in the pinhole image. L is the position in the virtual slit, and w is the width of the virtual slit.

2. 2. Temporal and spatial resolution

There are several factors which limit the temporal resolution of the system. They include the decay time of the scintillator (2.5 ns), the rise time of the photomultiplier (0.65 ns) and the frequency response of the oscilloscope (0-500 MHz). The impulse response of the system, which was estimated to be 3.0 ns full width at half-maximum (FWHM), was nearly consistent with a measured value using a transversely excited atmospheric (TEA) N_2 laser pulse (<1 ns in FWHM, 337.1 nm).

As shown in Fig. 1, the sampling of the source image is made by the 12 channels separated by $pL_1/L_2 = 1.5$ mm while each channel has a viewing field of 1.3 mm in FWHM, and so any two points separated by $pL_1/L_2 = 1.5$ mm can be resolved both spatially and temporally by the arrayed detector. The spatial resolution, by minimizing Eq. (3), is limited to 1 mm by the number of divisions of the grid, which is restricted by the available array size of the software.

2. 3. Plasma focus device as a soft x-ray source

Performance of the system was examined using a soft x-ray source generated with a Mather-type plasma focus device. The inner and outer diameters of the coaxial electrodes are 50 mm and 100 mm. The lengths of the inner and outer electrodes are 280 mm and 230 mm, respectively. The anode (inner electrode) is hollow. The condenser bank consists of $28 \times 1.56\,\mu$F capacitors. The device was operated at a bank voltage of 45 kV and an embedded H_2 gas pressure of 5.5 Torr. Additional Ar gas was puffed with a fast acting valve through the anode hole immediately before each discharge.

3. Experimental results

Despite the same operational condition of the plasma focus device, various differing features of the soft x-ray sources were observed from shot to shot. Examples of the time integrated, streak- and framing mode display of the soft x-ray source generated with the plasma focus device are shown in Figs. 2 (a)-A $\sim$ 2 (b)-C. In the first example, three filamentary sources were observed as shown in Fig. 2 (a)-A. The filaments appear successively from the location which is near the electrode face as shown in Fig. 2 (a)-B. This fact is confirmed by the framing mode observation as shown in Fig. 2 (a)-C. In the second example, many spots which were scattered along the electrode axis were observed as shown in Fig. 2 (b)-A. The spots were of various lengths along the axis ranging from 0.2 to 1 mm. It is recognized that the spot with the shorter length tends to have a shorter lifetime. The x-ray emitting part in the pinched plasma initially appears several mm (2.5 mm in this example) distant from the anode and moves with a velocity of about 10^6 m/s from a point, demonstrating the zippering effect. The overall duration of emission by the scattered spots was extended up to about 30 ns.

Bayley, et al. used an x-ray streak camera with which a conventional image tube and an image intensifier are installed. They also observed the zippering effect.[2] They did not use a slit. When the objects fluctuate around the electrode axis, the time sequence of their appearance cannot be determined from their locations on the streak photograph. On the other hand, determination of the time of appearance in our system is not affected by the source location.

The advantages of our system is that both the streak- and the framing mode images with quantitativity are obtained simultaneously for each shot. The source location is determined with reasonable accuracy by this system.

In summary, the system which we developed has been successfully used to observe the time evolution of soft x-ray sources generated with a plasma focus device. The temporal resolution was sufficient to determine the time sequence of the appearance of x-ray sources. The spatial and the temporal resolution can be improved by using a finer mesh representing $i(J,T)$ in the inversion.

References

1) P. Röwekamp, G. Decker, W. Kies, F. Schmitz, G. Ziethen, J. M. Bayley, K. N. Koshelev. Y. V. Sidelnikov, F. B. Rosmej, A. Schulz and D. M. Simanovskii, *Dense Z-Pinches, Third International Conference*, edited by M. Haines and A. Knight (AIP Press, New York, 1994), p. 332.

2) J. M. Bayley, G. Decker, W. Kies, M. Mälzig, F. Müller, P. Röwekamp, J. Westheide and Y. V. Sidelnikov, J. Appl. Phys. **69**, (1991) 613.

3) T. Yanagidaira, M. Sato and K. Hirano, Jpn. J. Appl. Phys. **35**, (1996) 5862.

4) Y. Takahama, J. Du, T. Yanagidaira and K. Hirano, Rev. Sci. Instrum. **65**, (1994) 2505.

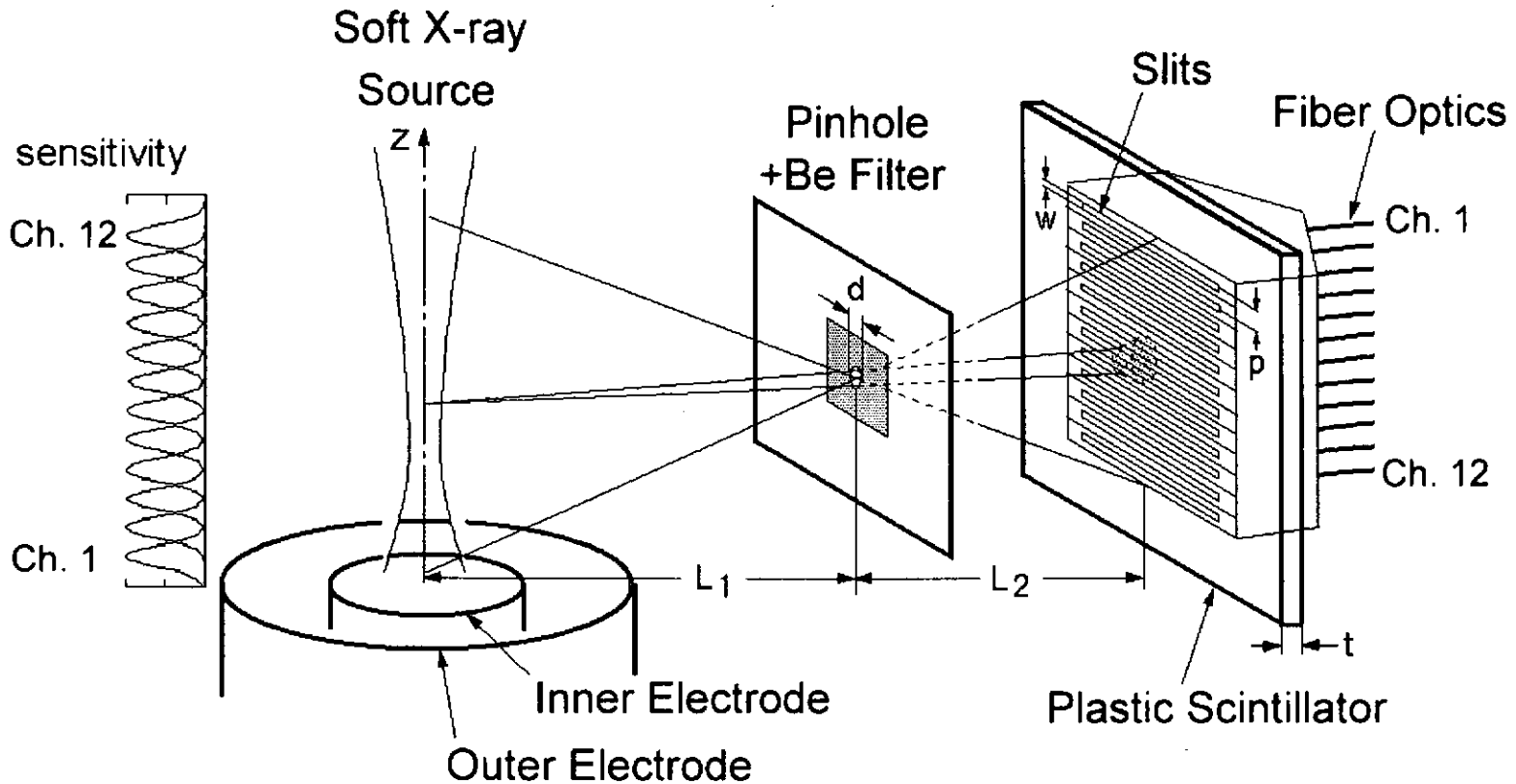

Fig. 1. Arrayed scintillator-photomultiplier detector. L_1 = 441 mm, L_2 = 147 mm, diameter of pinhole d = 0.1 mm. Thickness of the Be filter is 25 μ m. Thickness of the plastic scintillator t = 0.2 mm, slit width w = 0.1 mm. Center to center distance of the slits is p = 0.5 mm. The inset shows the viewing field of each channel.

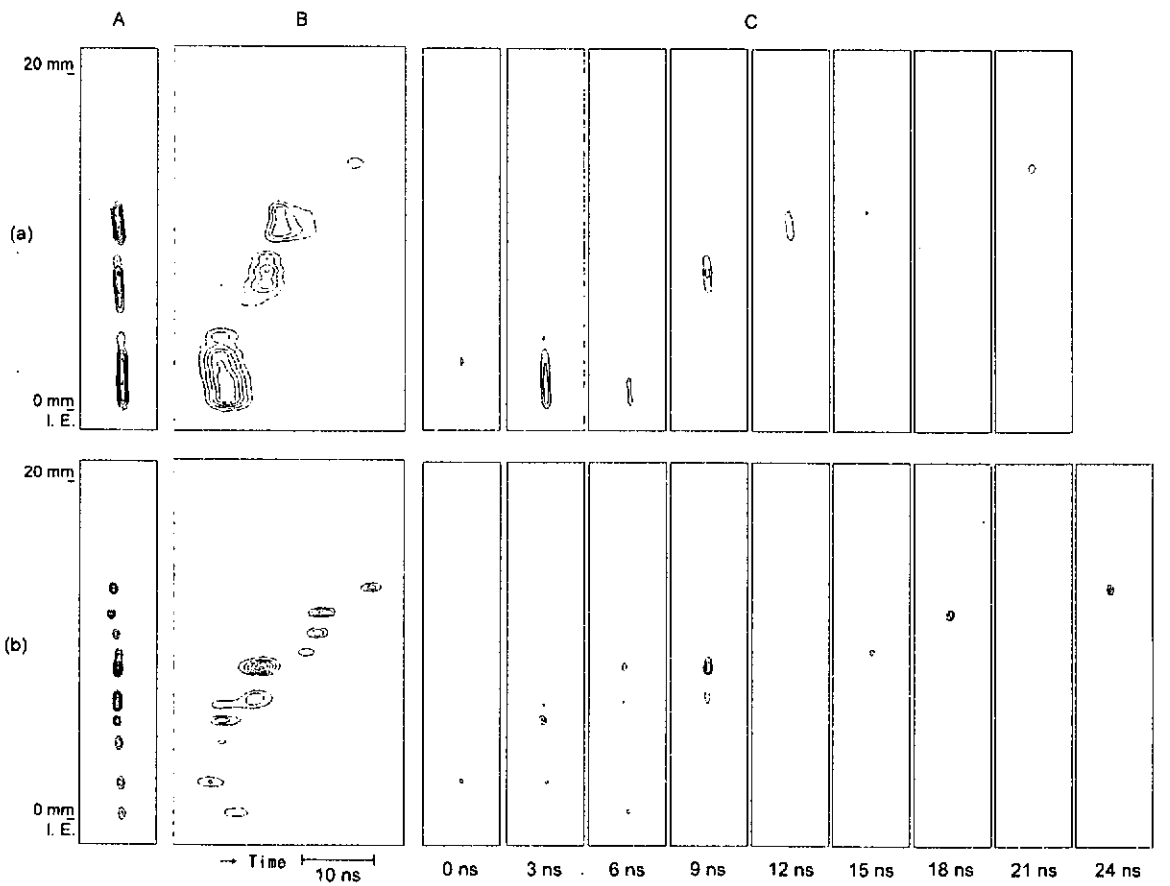

Fig. 2. Examples of the pinhole image, the streak- and framing mode images for (a) filamentary sources and (b) spot-like sources. The pinhole images are time integrated. The streak images are different from the images to be taken with the conventional image tubes in that the position of the slit is determined in the course of data processing. The 'virtual slit' 8 mm in width was set parallel to the electrode axis. The exposure time and the interframe time of the framing images are 3 ns.

FUSION CRITERIONS ON Z-PINCH PLASMAS

T. Miyamoto

Atomic Energy Research Institute, Nihon University

1. INTRODUCTION

Classical z-pinches were studied intensively in the early phase of the nuclear fusion research, but were once given up as a fusion approach since the end of 1950's. J. Hammel and his collaborators in the middle of 1970' s carried out the pioneer work, which gave a new aspect to the z-pinch/1/. Their proposal consisted of keeping a dense z-pinch plasma column with the density near solid state and several 10 μm in diameter in a quasi-steady state for the order of μs. The fusion approach based on this dense z-pinch is quite simple and clear except the assumption that the dense plasma has to be sustained during the required period. Laser initiated gas embedded z-pinches and frozen deuterium fiber z-pinches carried out under this guiding principle/2,3/. In the frozen deuterium fiber z-pinch, large neutron yield was observed /3/, but the observed neutrons mainly resulted from instabilities as well as in the classical z-pinch. A lot of investigations carried out on the fiber z-pinch have not yet given a clear insight to the fusion on the basis of the fiber z-pinch. Recently, it was reported in the polyethrene fiber z-pinch that the instabilities lead turbulently the plasma column to expand, and as a result it may give an lower limit to the attainable plasma radius/4 /. The similar results were given in numerical simulation/5/. These results show that the fusion approach based on z-pinches needs a new guiding principle/6/.

In this paper, fusion conditions based on two types of z-pinches -- fiber and sheet z-pinches -- are summarized and compared.

2. CYLINDRICAL Z-PINCH

The pressure balance in the cylindrical Z-pinch such as a fiber z-pinch is given the Bennett condition

$$\mu_0\left(I^{(f)}\right)^2 = 16\pi N^{(f)} kT^{(f)} \tag{1}$$

where I, N and T are the total current, the line density, and the temperature respectively, and the suffix (f) denotes the quantities relating with the fiber z-pinch. The steady state is established in z-pinches only when the energy balance holds. When thermal conduction is fast enough, the energy balance for an isolated plasma column with so high temperature that the energy loss occurs only by the bremsstrahlung radiation is given by

$$\int\left[P_J - P_B\right]dV \equiv \int\left[\overline{\eta}T^{-3/2}i^2 - \overline{P}_B n^2 T^{1/2}\right]dV = 0$$

where the Joule heating P_J and Bremsstrahlung radiation loss P_B per unit time and unit volume are expressed as

$$\begin{aligned} P_J &= \eta i^2 = \overline{\eta}T^{-3/2}i^2 \quad , \quad \overline{\eta} = 6.5\times 10 \ln\Lambda \ (\Omega/\mathrm{m}) \\ P_B &= \overline{P}_B n^2 T^{1/2} \quad , \quad \overline{P}_B = 1.4\times 10^{-40} \ (\mathrm{W/m}) \end{aligned} \tag{2}$$

where we assume $Z = 1$. Carrying out the integration, we obtain the relation

$$I = \left(\frac{4}{3}\right)^{1/2}\left(\frac{\overline{P}_B}{\overline{\eta}}\right)^{1/2} NT \ , \tag{3}$$

between I and NT. From eqs.(1) and (3), the total current is nealy constant in the steady state, so called Pease-Braginskii current which is given by

$$I_{PB}^{(f)} = \left(\frac{8\pi k}{\mu_0}\right)\left(\frac{3\overline{\eta}}{\overline{P}_B}\right)^{1/2} = 3.26\times 10^5\sqrt{\ln\Lambda} \ \ (\mathrm{A}) \ , \tag{4}$$

The line plasma and magnetic energies are give as

$$W_P^{(f)} = \left(3N^{(f)}kT^{(f)}\right)_{PB} = \frac{36\pi k^2\overline{\eta}}{\mu_0\overline{P}_B} \approx 7.96\times 10^3 \ \ (\mathrm{J/m}) \tag{5}$$

$$W_M^{(f)} = \frac{\mu_0 (I^{(f)})^2}{4\pi}\left(\ln\left[\frac{d}{a}\right] + \frac{1}{4}\right) = \frac{4W_P^{(f)}}{3}\left(\ln\left[\frac{d}{a}\right] + \frac{1}{4}\right) \qquad (6)$$

where a and d are the radius of the plasma and the return current, respectively.

3. SHEET Z-PINCH

The fiber Z-pinch is extremely unstable, as well known. The stability problem in cylindrical plasma columns is removed in a sheet plasma. For simplicity, let us consider a current carrying plasma sheet enclosed by two yz plane at $x = \pm a$. Hence, the sheet is $2a$ in thickness and infinite in the y and z directions. The current flows along the z-axis. We assume that thermal conduction is fast enough as well as in conventional z-pinches, and that the relaxation between ions and electrons is also fast enough. Then, the plasma temperatures are assumed to be constant in space, i.e. $T_i = T_e \equiv T$. As the electric potential is assumed to be constant in an arbitrary xy plane without generality, the current density i is also constant in space. As a result, the magnetic field has only the y component $B_y = B = \mu_0 ix$, and the plane $x = const.$ is an isobaric surface. The plasma density at a pressure equilibrium state is given by

$$\frac{dn}{dx} = -\frac{\mu_0 i^2}{2kT} x \ .$$

Under the boundary conditions $n = 0$ at $x = \pm a$, This equation gives the density distribution and the pressure balance relation

$$n = n_0\left(1 - \frac{x^2}{a^2}\right) \qquad (7)$$

$$\mu_0 i^2 a^2 = 4 n_0 kT \ . \qquad (8)$$

where $n = n_0$ is the density at $x = 0$. The current density per unit length of y direction I^* and the density per unit length of y and z direction N^* (which we call the plane current and the plane plasma density,

respectively) are expressed as

$$I^* = 2ia \qquad \text{and} \qquad N^* = \frac{4}{3} n_0 a \ , \tag{9}$$

respectively. The pressure balance (8) is rewritten using I^* and N^* as

$$\mu_0 \left(I^*\right)^2 = \frac{12}{a} N^* kT \tag{10}$$

This is so called Bennett condition in case of the sheet pinch. Carrying out the integration, we obtain the relation

$$I^* = \left(\frac{6}{5}\right)^{1/2} \left(\frac{\overline{P}_B}{\overline{\eta}^*}\right)^{1/2} N^* T \tag{11}$$

between I^* and N^*T. From eqs.(10) and (11), the plane current and the plane plasma energy density (that is, the energy per unit length and width) in the quasi-steady state of the sheet z-pinch are given by

$$I^* = \left(\frac{120\overline{\eta}}{\overline{P}_B}\right)^{1/2} \frac{k}{\mu_0 a} \equiv I^*_{PB} = 8.18 \times 10^4 \frac{\sqrt{\ln \Lambda}}{a} \quad (\mathrm{A/m}) \tag{12}$$

$$W_P^* = 3N^* kT = \frac{30\overline{\eta} k^2}{\overline{P}_B \mu_0 a} \equiv \left(N^* kT\right)_{PB} = 2.11 \times 10^3 \frac{\ln \Lambda}{a} \quad (\mathrm{J/m^2}). \tag{13}$$

The plane magnetic energy per unit length and width is given by

$$W_M^* = \frac{3}{a} N^* kT \left(d - \frac{2}{3} a\right) = W_P^* \left(\frac{d}{a} - \frac{2}{3}\right) \tag{14}$$

where we put the position of return current as $x = \pm d$. The current I^*_{PB} corresponds to the so called Pease-Braginskii current in the cylindrical z-pinch, which is roughly constant. However, the current I^*_{PB} (and the plasma energy density W_p^*) is no longer constant in the sheet z-pinch, but is inversely proportional to the thickness $2a$, and can increases indefinitely.

Ratios of the quantities in the sheet z-pinch with the width y to those in the fiber z-pinch are

$$\frac{I_{PB}{}^* y}{I_{PB}{}^{(f)}} = \sqrt{\frac{5}{8}} \frac{y}{\pi a} \tag{15}$$

$$\frac{(N^{*}kT)_{PB}\,y}{(N^{(f)}kT^{(f)})_{PB}}=\frac{5}{6\pi}\frac{y}{a}\quad\text{or}\quad\frac{(n_0kT)_{PB}}{(n_0^{(f)}kT^{(f)})_{PB}}=\frac{5}{16}\left(\frac{a^{(f)}}{a}\right)^2 \tag{16}$$

When $y>>a$, the current or the line energy density in the steady state of the sheet z-pinch is much higher than the Pease-Braginskii current in the fiber z-pinch or the corresponding line energy density. However, the current is almost same in both cases for the same line plasma energy, that is, $y/a=6\pi/5$.

4 CONDITIONS FOR FUSION

4.1 Criterion for Fiber Z-Pinch

In order to examine the possibility of fusion by means of the steady state of the sheet z-pinch, let us simplify the Lawson condition as follows

$nt\geq[nt]_L=10^{20}$ ($m^{-3}\cdot s$) and $T=T_L=5\times10^8$ (K) for DT reactions (17)

$nt\geq[nt]_L=10^{22}$ ($m^{-3}\cdot s$) and $T=T_L=10^9$ (K) for DD reactions (18)

The line density is

$$N=\frac{12\pi k}{\mu_0 T}\frac{\overline{\eta}}{\overline{P}_B}=1.92\times10^{26}\frac{\ln\Lambda}{T}\ (m^{-1})$$

from eq.(5). So the corresponding density is given by

$$n_0=\frac{2N}{\pi a^2}=1.22\times10^{26}\frac{\ln\Lambda}{Ta^2}\ (m^{-3}) \tag{19}$$

This density leads to requirement for the sustaining time and the radius

$$t\geq[nt]_L/n_0=8.18\times10^{-27}[nt]_L Ta^2/\ln\Lambda\ (s) \tag{20}$$

$$2a=2.21\times10^{13}\sqrt{\frac{\ln\Lambda}{n_0T}}=0.0989\sqrt{\frac{n_s}{n_0}}\sqrt{\frac{\ln\Lambda}{T}}\ (m) \tag{21}$$

where solid density is given by $n_s=5\times10^{23}\ (m^{-3})$. Thus, when $n_0=n_s$ and $\ln\Lambda=14$, the Lawson conditions (17) and (18) reduce to

$2a=1.65\times10^{-5}$ (m), $t\geq1.99\times10^{-9}$ (s) and $N=5.38\times10^{18}\ (m^{-1})$ (22)

$2a=1.17\times10^{-5}$ (m), $t\geq2.00\times10^{-7}$ (s) and $N=2.69\times10^{18}\ (m^{-1})$, (23)

respectively. Both conditions show that the plasma column must be very

slender. It results from choosing solid density for plasma. The radius is fat for lower plasma density and, on the other hand, the sustaining time must be prolonged. The radius a and the line density N required for the DD reaction hardly differ from those for the DT reaction except only small factor. The main difference between the DT and DD conditions appears in their sustaining time, which leads to another condition on the length of the plasma column.

The sustaining time required for fusion results in two conditions. The first condition relates with the energy loss along the direction of length, and given in Sec.5. The second one relates with growth rate of instabilities.

4.2 Criterions for Sheet Z-Pinch

The necessary surface density is

$$N^* = \frac{3.52\times10^2 \ln\Lambda}{kTa} \approx 2.55\times10^{25}\frac{\ln\Lambda}{Ta} = 3.57\times10^{26}\frac{1}{Ta} \quad (\mathrm{m}^{-2}) \tag{24}$$

from eq.(13), so the corresponding plasma density at the central plane is

$$n_0 = \frac{3N^*}{4a} = 1.91\times10^{25}\frac{\ln\Lambda}{Ta^2} \quad (\mathrm{m}^{-3}) \tag{25}$$

from eq.(9). Therefore, the sustaining time and thickness are given from eq.(25) as

$$t \geq [nt]_L/n_0 = 5.23\times10^{-26}[nt]_L Ta^2/\ln\Lambda \quad (\mathrm{s}) \tag{26}$$

$$2a = 8.74\times10^{12}\sqrt{\frac{\ln\Lambda}{n_0 T}} = 0.039\sqrt{\frac{\ln\Lambda}{T}}\sqrt{\frac{n_s}{n_0}} \quad (\mathrm{m}) \tag{27}$$

When $\ln\Lambda = 14$, conditions (17) or (18) reduce to

$$2a = 6.53\times10^{-6}\ (\mathrm{m}),\quad t \geq 1.98\times10^{-9}\ (\mathrm{s}) \text{ and } N^* = 2.19\times10^{23}\ (\mathrm{m}^{-2}) \tag{28}$$

$$2a = 4.62\times10^{-6}\ (\mathrm{m}),\quad t \geq 2.00\times10^{-7}\ (\mathrm{s}) \text{ and } N^* = 1.55\times10^{23}\ (\mathrm{m}^{-2}) \tag{29}$$

respectively. The conditions are similar with those of the cylindrical z-pinch, if we replace the thickness by the diameter and the surface density by the line density. Both conditions show that the plasma sheet must be

very thin.

5. AXIAL ENERGY LOSS

In real z-pinches with finite length, axial energy loss is important. It is consisted of thermal conduction and energy brought away with loss particles. The energy loss occurs mainly in the weak field region characterized by $\omega_L \tau_c \le 1$, where ω_L and $\tau_c = \bar{\tau}_c T^{3/2}/n$ are Larmor radius and collision time, and is brought away mainly by electrons there/7/. For the fiber z pinch, the weak field region is given by

$$\left|\frac{r}{a}\right| \le \frac{r_t}{a} \equiv -\alpha + \sqrt{\alpha^2 + 1} \ , \tag{30}$$

where

$$\alpha = \frac{8e\mu_0 \bar{\tau}_c}{m}\left(\frac{\pi k}{\mu_0}\right)^{5/2}\left(\frac{3\bar{\eta}}{\bar{P}_B}\right)^2 \frac{a}{N^{5/2}} \tag{31}$$

$$= 6.62\times10^{54}\frac{\ln\Lambda}{Z^5}\frac{a}{N^{5/2}} = 3.83\times10^{-18}\frac{\ln\Lambda}{Z^5}\frac{1}{a^4}\left(\frac{n_z}{n_0}\right)^{5/2}$$

where $\bar{\tau}_c = \bar{\tau}_e = 2.76\times10^5/(Z\ln\Lambda)$ for electrons. When $\alpha >> 1$, i.e., $n_0^{5/2}a << 1.24\times10^{18}(\bar{\tau}_c/m)(\ln\Lambda)^2/Z^4$, thermal conduction loss occurs only within the radius $r_t < a/2\alpha$. However, we suppose that $\alpha << 1$, that is, that the thermal conduction occurs in the almost whole cross section. The ratio of the thermal conduction loss to the Joule heating is

$$\frac{\int \nabla\cdot(\kappa\nabla T)dV}{\int \eta i^2 dV} = \frac{\int \kappa\nabla T\cdot dS}{\int \eta i^2 dV} \approx \frac{2(\kappa T/z)\pi r_t^2}{\eta i^2 \pi a^2\cdot 2z} \approx \frac{\bar{\kappa}}{\bar{\eta}}\frac{T^5(\pi a^2)^2}{I^2 z^2}\frac{r_t^2}{a^2}$$

where $\kappa = \gamma_0(nk^2T\tau_c/m) = \bar{\kappa}T^{5/2}$ and $\bar{\kappa} = \gamma_0 k^2\bar{\tau}_c/m$ and $\gamma_0 = 3.16$. The condition for negligible thermal conduction is to satisfy

$$z^2 >> \frac{\bar{\kappa}T^5}{\bar{\eta}i^2}\left(\frac{r_t}{a}\right)^2 = 6^4\frac{\bar{\kappa}}{\bar{\eta}}\left(\frac{\pi k}{\mu_0}\right)^3\left(\frac{\bar{\eta}}{\bar{P}_B}\right)^4\frac{(\pi a^2)^2}{N^5}\left(\frac{r_t}{a}\right)^2 = \frac{\gamma_0}{4}\alpha^2 a^2\left(\frac{r_t}{a}\right)^2$$

Considering eq.(30), we have the condition for the plasma length

$$\frac{z}{a} >> \frac{z_c}{a} \equiv \frac{\gamma_0^{1/2}}{2}\alpha\frac{r_t}{a} = 0.89\alpha\left(-\alpha + \sqrt{\alpha^2+1}\right) \tag{32}$$

When $\alpha \ll 1$, eq.(32) shows that the critical plasma length z_c increases linearly with α, and approaches to constant value 0.89/2 for $\alpha \gg 1$. We obtain $N = 2.13 \times 10^{22} a^{2/5}$ for $\alpha \approx 1$. Conditions (32) shows that the length needed for hot plasma production depends strongly with the density and radius. The necessary length is short enough for the extremely dense plasma. However, the lower limit seems to exist for the length, because of avoiding the effects of electrodes such as impurity flow. The result is similar for the sheet z-pinch except a numerical factor.

References

1. J.Hammel, D.W.Scudder and J.S.Schlchter, Nucl.Instrum. Methods **207**, 161(1983); J.Hammel, LANL Report No.LA-6203-MS(1976).
2. J.D.Sethian, A.E.Robson, K.A.Gerber and A.W.DeSilva, Phys. Rev. Lett. **59**, 892, 1790(E)(1987).
3. P.Sheehey, J.E.Hammel, I.R.Lindemuth, D.W.Scudder, S.Shlachter et.al., Phys.Fluids **B4**,3698 (1992).
4. R.Relay, D.Scudder, J.Schlachter and R.Lovberg, Phys. Plasmas **3**,1314-1323 (1996).
5. P.Sheehey and I. Lindemuth, Phys. Plasma, **4**, 146-152 (1997).
6. T.Miyamoto, NIFS-PROC-26, p.71-80 (Physics, Diagnostics and Application of Pulsed High Energy Density Plasma as an Extreme State, ed. by S.Ishii, 1996).

Characteristics of laser ablation plume for deposition of YBCO thin films

X. Wang, A. Marcu, T.Yukawa, W. Jiang,
T. Masugata and K. Yatsui

Laboratory of Beam Technology
Nagaoka University of Technology
Nagaoka, Niigata 940-21

Abstract

The behavior of laser ablated plume in ambient gas has been studied by using high-speed framing camera and spectrometer. Comparing the photographic results with ideal blast wave models, we found that the one dimension spherical blast wave model agrees with the experimental data very well at higher gas pressure. The optical emission spectroscopy results showed that the distribution of particles was strongly affected by the ambient gas pressure .

1. Introduction

Laser ablation has been recognized as a powerful technique for deposition of high-T_c superconducting thin films with high quality. Usually, the films are deposited in ambient gas conditions. The collision and reaction of ablated particles with ambient oxygen gas will form oxides, this may aid oxygen incorporation in the growing films[1,2]. It is believed that the interactions between ablated particles and ambient oxygen gas greatly affect the quality of the deposited film. Since the behavior of the ablation plume is very complex for different gas pressure, the characteristics of the plume are still not very clear.

In this paper, the expansion characteristics of the plume have been studied by high-speed framing camera, which will be analyzed by ideal blast wave models. Furthermore the distribution of the ablated particles is studied by optical emission spectroscopy.

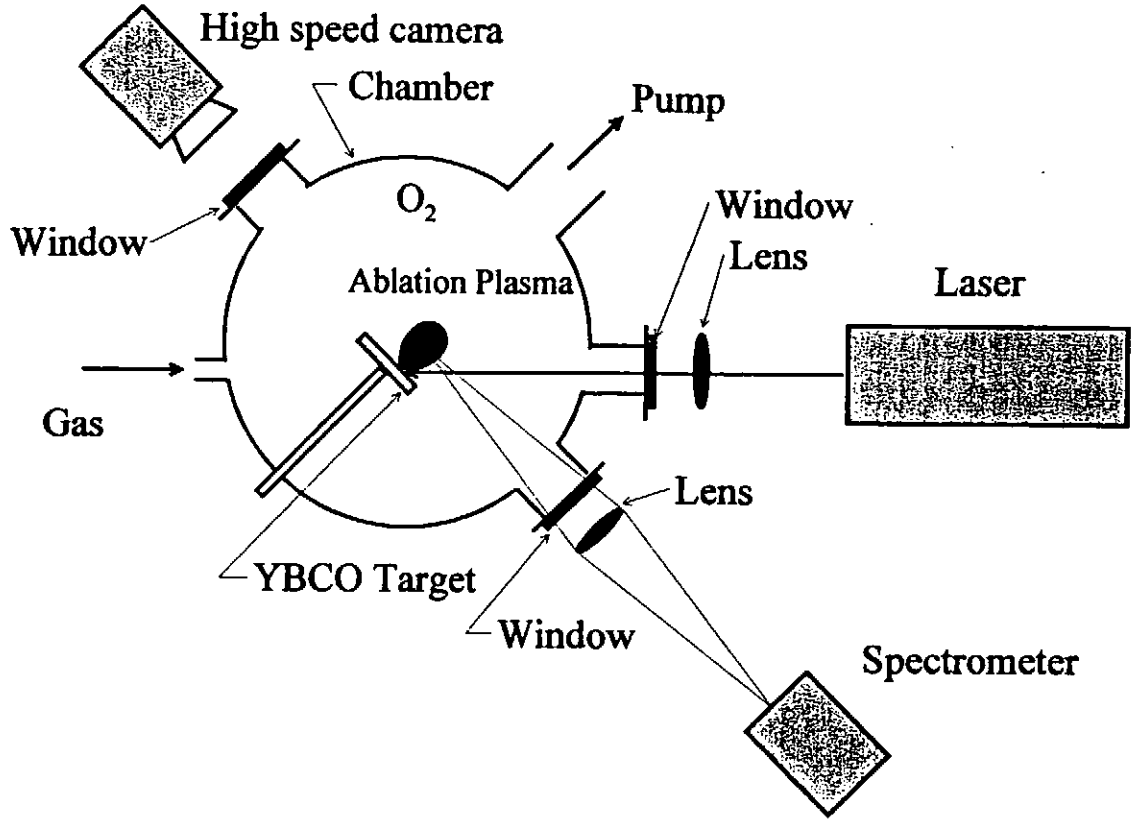

Fig.1 Experimental setup

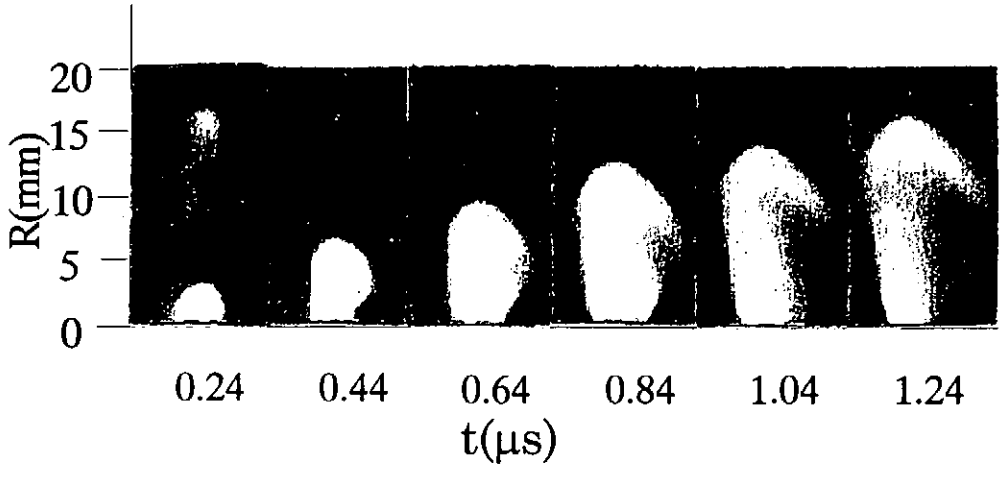

Fig.2 High-speed framing photographs of YBCO plume ablated by KrF laser(~1J/cm²) in 25Pa of oxygen.

2. Experimental setup

Figure 1 shows the experimental setup. Two types of experiments were carried out to investigate the behavior of ablated plume. One is the high-speed photographic experiment, where the expansion process of KrF laser (248nm, 0.8~1J/cm^2) ablated YBCO plume was monitored by a high speed framing camera. The other is spectroscopic experiment, where a gated (50ns) image intensified optical multichannel analyzer (OMA) and a monochromator system were used to study the distributions of the ablated particles. YBCO target was irradiated by Nd:YAG laser (1064nm, ~3J/cm^2).

3. Results and discussions

3.1 Photographic results

Figure 2 shows the expansion of the plume in ~25Pa background gas pressure. A bright luminous front appeared on the leading edge of the plume. We noticed that the appearance of this luminous front is related with ambient gas pressure. The higher the pressure, the brighter the luminous front. At lower pressure (for example, $p \leq 8$Pa) this kind of the luminous front appears far away from the target. This can be explained by using a blast wave model since the expansion of the laser ablated plume in the ambient gas will produce the blast wave[3-5]. A lot of the ablated particles are accumulated behind the shock front and formed a high density region (as seen from the photographs). This will be discussed in detail in the next section.

To analyze the propagation characteristics of the plume, the following two kinds of blast waves were compared with the experimental data.

1) Spherical blast wave (1-D)[3] :

$$R = 1.27\left[\frac{2(\gamma^2-1)}{(\gamma^2+4\gamma-1)}\right]^{0.2}\left(\frac{E_0}{\rho_0}\right)^{0.2} t^{0.4}, \qquad (1)$$

where γ is the specific heat ratio, E_0 the laser energy and ρ_0 the ambient gas density, respectively.

2) Cylindrical blast wave (1-D)[6]:

$$\tau = \frac{1}{2}\left[\sqrt{1+4\lambda^2}-1\right], \qquad (2)$$

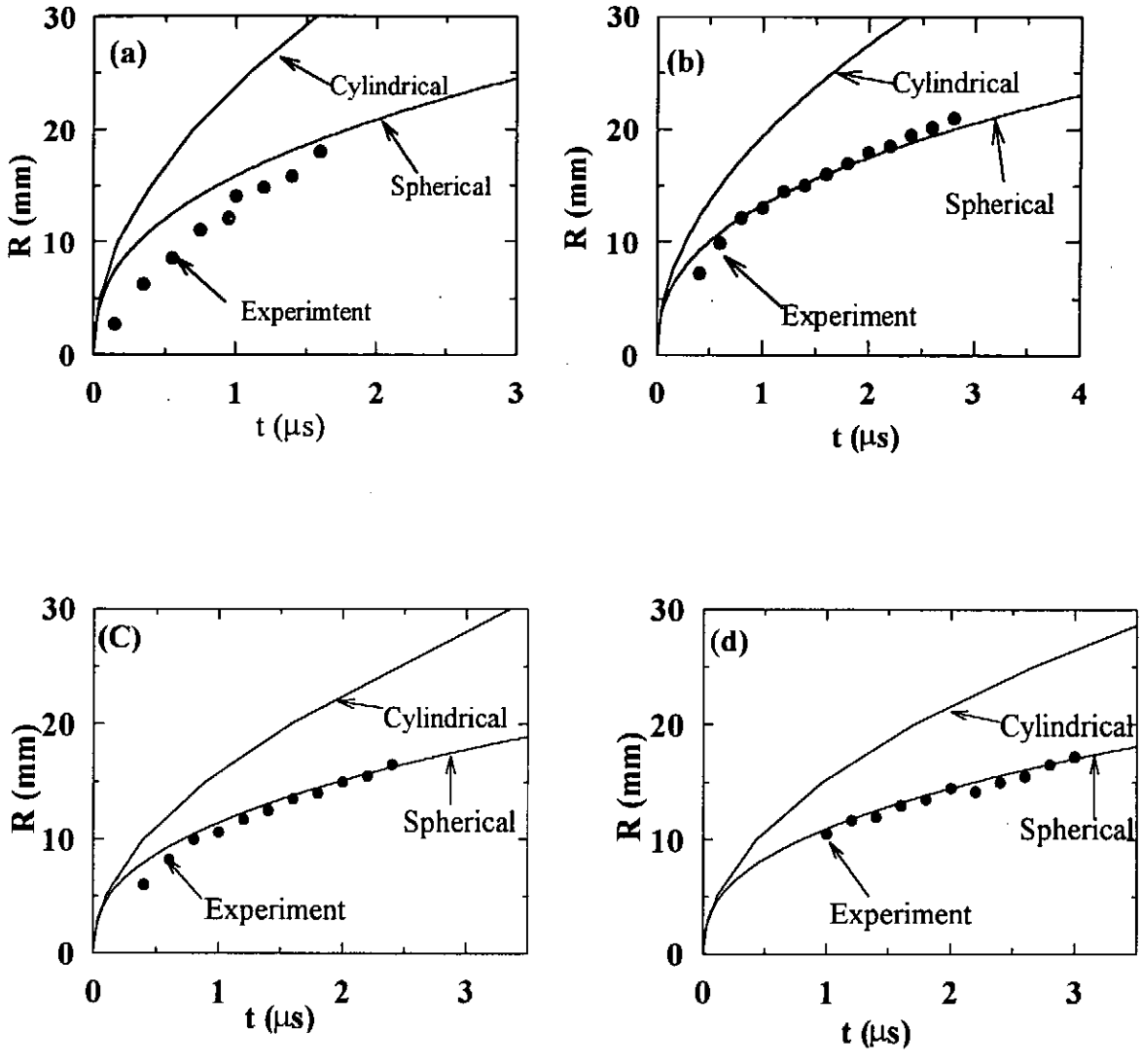

Fig.3 Time evolution of luminous fronts of YBCO plume produced in background oxygen pressure of (a) 8Pa, 0.8J/cm²; (b) 25Pa, 1J/cm²; (c) 40Pa, 0.8J/cm²; (d) 65Pa, 1J/cm², respectively. The solid lines were fitted using Eqs. (1) and (2).

where $\tau = Ct / R_0$, $\lambda = R / R_0$, C the sound velocity of undisturbed fluid, R_0 (characteristic radius) = $(E_0 / B\gamma p_0)^{1/2}$, and B=2.205 .

The expansion distance of the plume versus time is shown in Fig. 3. The ideal spherical blast wave model agrees with the experimental data very well at higher pressure. At lower pressure (for example, p = 8Pa), however, the experimental data deviate from the blast wave model. From the photographic pictures we also see that at lower gas pressure, the bright luminous front will not be produced.

3.2 Spectrometric results

The schematic diagram of the spectrometer system is shown in Fig.4. The Spectral multichannel analyzer (SMA) detector is gated by the pulse of duration of ~ 50ns. Delay time was adjusted by pulse generator. The Ba^+ ion line (455.4nm) was measured to study the distribution characteristics of the plume. This line was chosen because it is the strongest emission line from the YBCO plume.

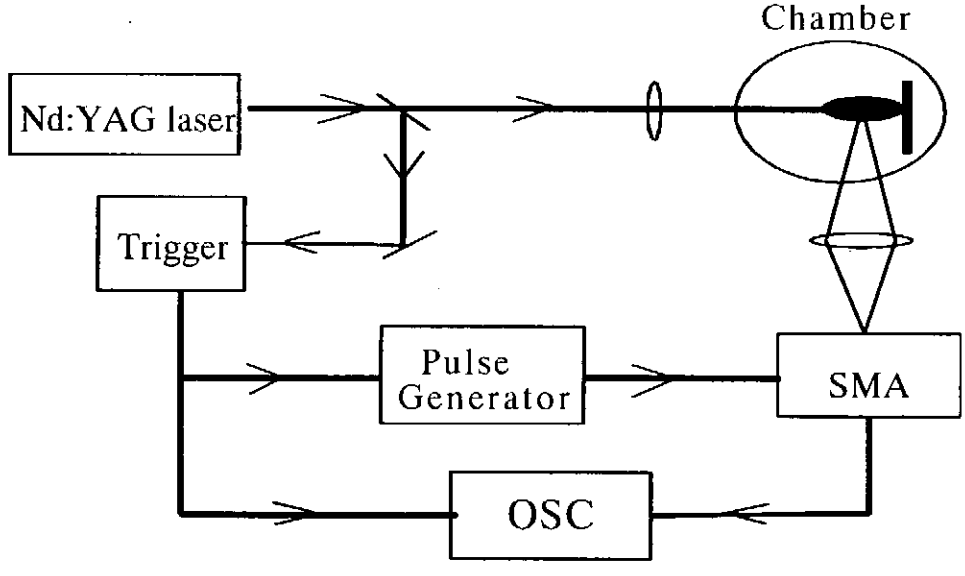

Fig.4 Schematic diagram of spectrometer system

Figure 5 shows the time evolution of Ba^+ intensity distributions of ablation plume for different ambient gas pressures. From Fig. 5 we see that the plasma emission intensity increases with increasing gas pressure, and the

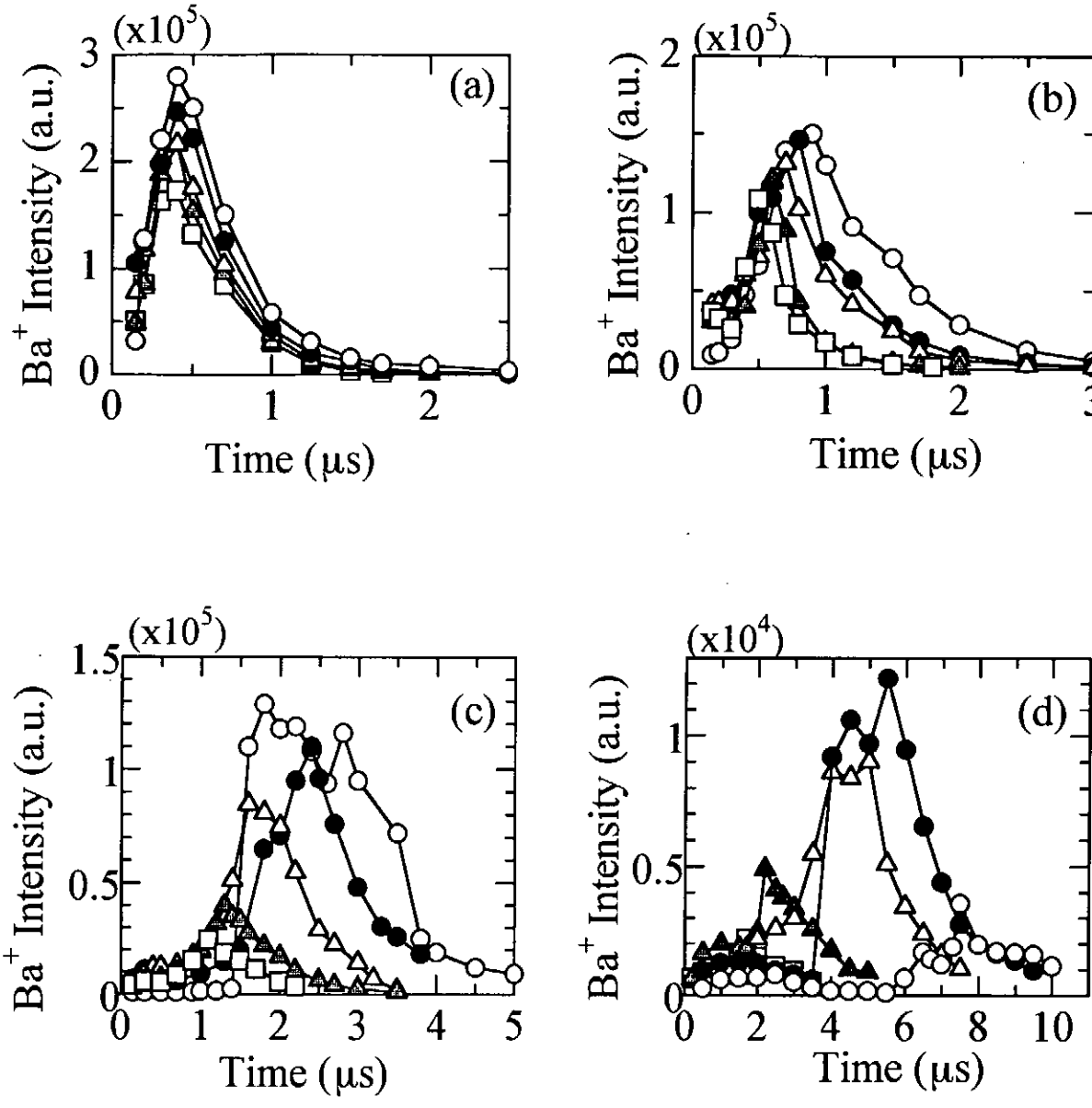

Fig. 5 Time evolution of Ba^+ intensity of ablation plume at different distance from target ((a) 5mm, (b) 10mm,(c) 20mm, (d) 30mm), and different oxygen gas pressure ((○) 65pa, (●) 40pa, (Δ) 25pa, (▲) 13pa, (□)7pa).

distribution of the ablation plume varies with the ambient gas pressure at higher pressure ($p \geq 13$Pa), the distribution front becomes steep at a certain distance.

The variation of the distributions with the gas pressure may be correlated with the effect of the collision between the ablated particles and the background gas, which will be discussed below.

The mean free path of the ablated particles in oxygen gas can be given by[7]

$$\lambda = \frac{1}{\pi d^2 n_0 \sqrt{1 + m/m_0}} \quad , \tag{3}$$

where n_0 is the oxygen gas density, m_0 the oxygen molecular mass, m the ablated particle mass, and d the collision radius of two species, respectively. The mean free path of Ba particles in the experimental conditions are shown in Table Ⅰ.

Table Ⅰ. Mean free path of particles

Gas pressure, p_0 (Pa)	7	13	25	40	65
Mean free path, λ(mm)	0.65	0.33	0.17	0.11	0.07

As seen from Table Ⅰ, the mean free path of the ablated particles becomes shorter as the pressure is increased. Therefore, most of the collision between the plume particles and ambient gas appear only at the boundary of the plume. The expansion of the ablated particles push and compress the ambient gas just like a piston which forms a gas layer in front of the plume. Because of the high collision rate and compression by the plume, a large amount of the excited and ionized particles are concentrated near the boundary of the compressed oxygen gas layer. This phenomenon has been observed in the last section from the photographic pictures that at the boundary of the plume appeared a bright luminous front. Some researchers considered this behavior as the formation of the blast wave[3-5]. We also found that the propagation characteristics of the plume can be explained very well by an ideal spherical blast wave model.

The thickness of the gas layer increases as the plume expands. It is approximately given by[3]

$$\Delta h = R(\gamma-1)/3(\gamma+1) \, , \tag{4}$$

where R is the boundary radius of the plume, and γ is the ratio of

specific heats of the oxygen gas ($\gamma \approx 1.4$). At R=20mm, Δh=1.1mm. Comparing Δh with the mean free path, we obtain that the thickness of the gas layer is much larger than the mean free path at high gas pressure. Few particles can pass through the gas layer, and therefore large amount of ablated particles are accumulated just behind the gas layer which formed a high density region. At low pressure (for example, $p \leq 7$Pa), the mean free path λ can be comparable with the gas layer (Δh). Otherwise, because of the large mean free path, the gas layer will not be formed. Hence, the distribution of the ablated particles varies with the gas pressure.

4. Conclusions

High speed framing camera and spectrometer have been used to investigate the behavior of the laser ablated YBCO plume in an ambient oxygen gas. Both results showed the formation of the blast wave at higher gas pressure. The expansion radius of the plume can be explained well by an ideal spherical blast wave model. Because of the formation of the blast wave, the distribution of the particles is strongly affected by the ambient gas pressure.

References

[1] C. E. Otis et al.: Appl. Phys. Lett., 62, 102 (1993).

[2] A. Gupta : J. Appl. Phys., 73, 7877 (1993).

[3] J. L. Bobin et al.: J. Appl. Phys., 39, 4184 (1968).

[4] R. B. Hall: J. Appl. Phys., 40, 1941 (1968).

[5] P. E. Dyer et al.: Appl. Phys. Lett., 57, 186 (1990).

[6] Q. Zhu et al.: AIAA. J., 33, 2422 (1995).

[7] W.G.Vincenti et al.: Introduction to Physical Gas Dynamics, (Robert E. Krieger Publishing Company, Malabar,Florida,1975), p. 54.

Production of Nanosize Powders of AℓN by Pulsed Laser Ablation and Related Plasma Diagnostics

K. Nishiura, T. Yukawa, W. Jiang, K. Masugata, C. Grigoriu and K. Yatsui

Laboratory of Beam Technology Nagaoka University of Technology
Nagaoka, Niigata 940-21

Abstract

Nanosize powders of AℓN was successfully synthesized by aluminum target with the ambient gas of nitrogen using pulsed laser ablation. Diameter of the powders was typically 2.5 ~ 25 nm. In addition, we have diagnosed the plasma parameters by SMA under the same condition as the powder production. The ablation plasma obtained by Aℓ target in oxygen consists of Aℓ atoms, $A\ell^{+}$ ions, $A\ell^{++}$ ions, O atoms and O^{+} ions.

1. Introduction

Nanosize powders of many materials have specific magnetic, optical, chemical and sintering properties[1]. These properties have made the nanosize powders very interesting in the applications of magnetic media, catalysts, gas sensors, and other industrial fields.

Nanosize powders can be produced by using chemical method.[2] With this method, the nanosize powders have been produced of large amount, but the purity is a little bit poor. It has been realized that the purity of nanosize powders by this method are hardly improved due to its reliance on chemical reactions. In recent years, physical methods, such as pulsed laser ablation method [3, 4] and pulsed ion beam evaporation method [5-10], are developed for production of high purity nanosize powders.

In this paper, our recent results will be reported on nanosize powder production by using pulsed laser ablation and related plasma diagnostics carried out under the same condition as the powder production. The characteristics of AℓN powders analyzed by XRD (x-ray diffraction) and TEM (transmittion electronic microscope) in § 3.1, and the diagnostic results obtained using high-speed camera, spectrometer and SMA (Spectrum Multichannel Analyzer) will be presented in § 3.2.

2. Experimental Setup

Figure 1 shows the basic principle of synthesizing nanosize powders by using the pulsed laser ablation method. When the high power laser beam is irradiated on the target, the target

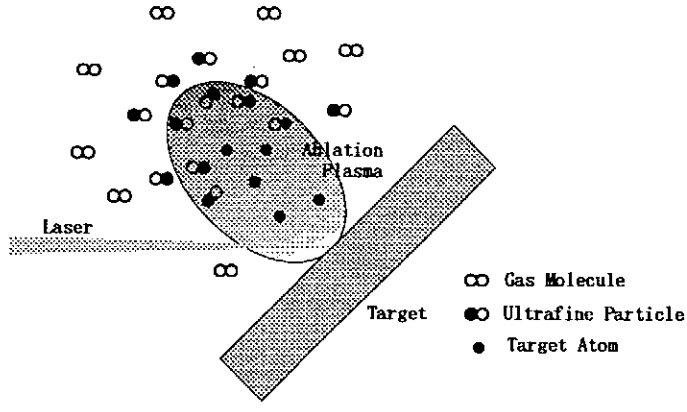

Fig. 1 Principle of nanosize powder production.

surface is heated to high temperature due to very high energy deposition of the laser beam. It is vaporized, partially ionized and expands into the surrounding space. If the surrounding space is filled with gas, the ablated materials will be cooled by the interaction with the gas molecules. The uniform solidification of the materials results in the synthesizing nanosize powders.

Figure 2 shows the schematic of experimental setup. A Q-switched Nd:YAG laser (1.064 μm, 7 ns) was used to ablate the aluminum target with an angle of 45 degree to the target surface. Throughout the experiments, the ambient gas was flowing with the speed of 1Nℓ/min (2.0 kg/cm^2) and the target was being rotated to avoid the concentrated damage. At the outlet of the gas flow, a membrane filter is located to collect the powder produced.

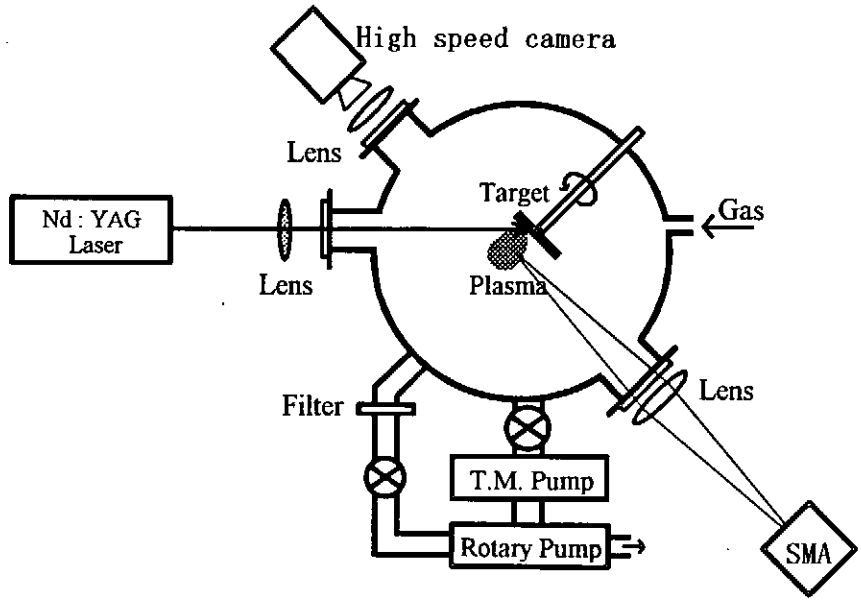

Fig. 2 Experimental setup.

3. Experimental results

3.1 Production of AℓN nanosize powders

Nanosize powders was produced by pulsed laser ablation method. The target was aluminum (99.5 % in purity) and the ambient gas was nitrogen (99.9999 % in purity). The pressure of the ambient gas was varied from 10 to 500 Torr.

Figure 3 shows SEM (scanning electron microscope) photographs of the powders. Figures 3(a) and 3(b) show the samples obtained at nitrogen pressure of 60 and 200 Torr, respectively. It is seen from these photographs that the produced particles are smaller than 1 μm.

Figure 4 shows the typical result of XRD. In Fig. 4, the diffraction peaks of SUS (stainless steel) originate from the steel mesh that was used as the supporter of the particles in the XRD analysis. We see from Fig. 4 that, at nitrogen pressure lower than 60 Torr, the particles are aluminum or mixture of aluminum and aluminum nitride. When the pressure is higher than 200 Torr, however, the particles are pure aluminum nitride.

Figure 5 shows the TEM photograph of the particles obtained at nitrogen pressure of 200 Torr. The particle sizes are seen to be ~ 10 nm. Futhermore, some particles are seen to be hexagonal, which is consistent with the hexagonal structure of the AℓN crystal.

Figure 6 shows the particle size distribution obtained from Fig. 5. All particles are smaller than 25 nm, and the average particle size is ~ 11 nm.

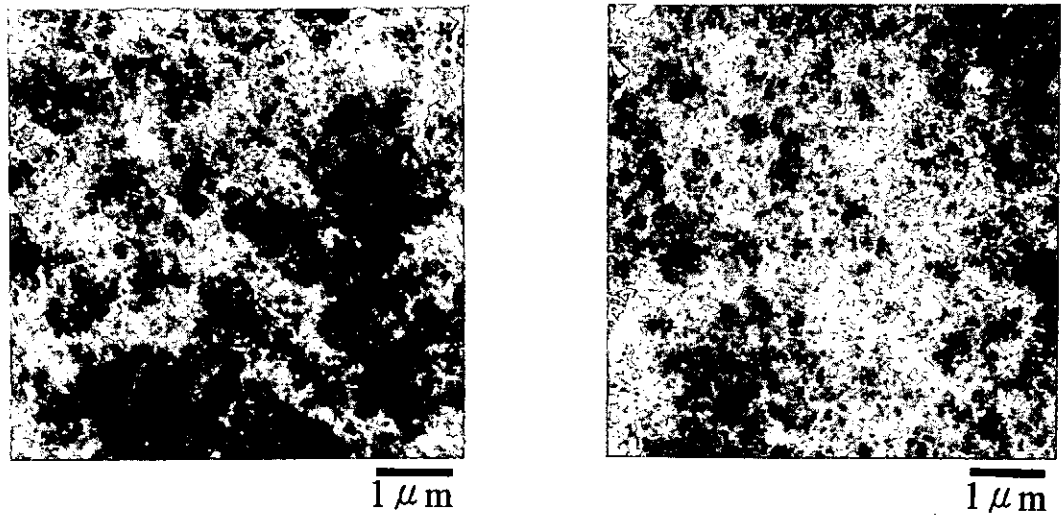

(a) N_2, 60 Torr (b) N_2, 200 Torr

Fig. 3 SEM photographs of powders.

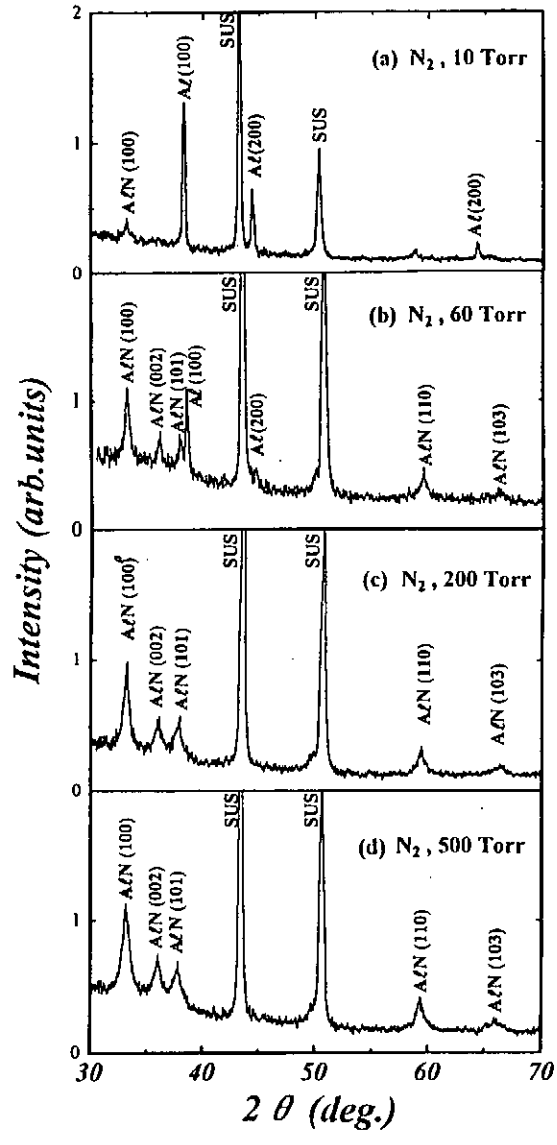

Fig. 4 XRD data of powders.

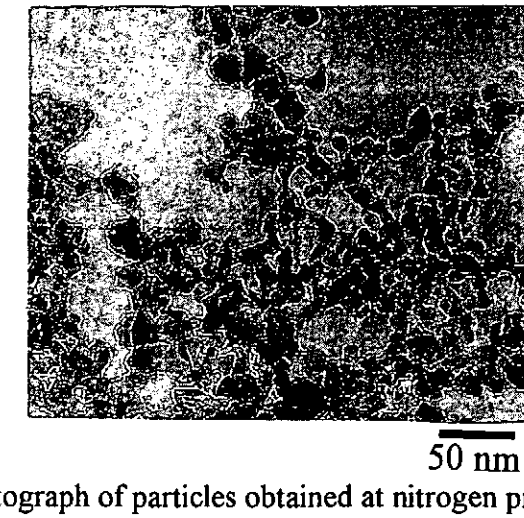

Fig.5 TEM photograph of particles obtained at nitrogen pressure of 200 Torr.

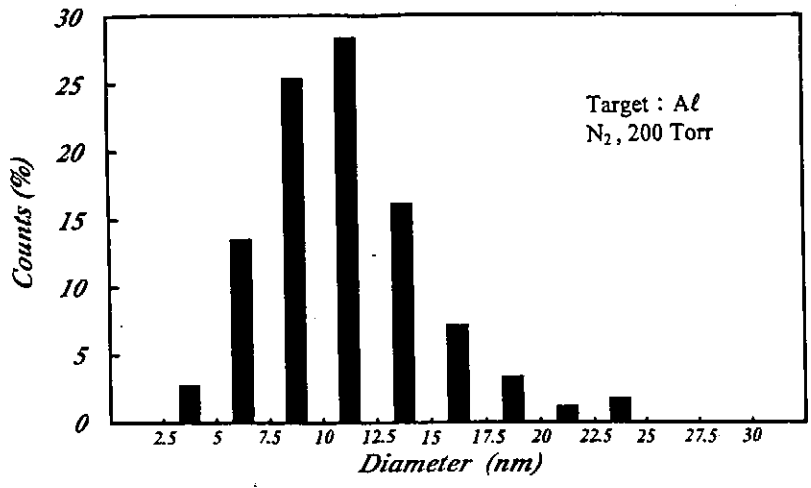

Fig.6 Size distribution obtained from Fig. 5.

3.2 Diagnostics of Ablation Plasma

3.2.1 High-Speed Photography

The expansion process of the ablated plasma was observed by a high speed camera. Figure 7 shows the framing photographs obtained with laser energy density of 16 J/cm^2 and oxygen pressure of 200 Torr. The time of exposure and the interframe were 40 ns and 200 ns, respectively. In Fig. 7, the number indicates the sequence of the photographs, where the first photograph was taken 200 ns after the laser pulse. The vertical line in each photograph shows the position of the target surface, and the luminant on the left hand side corresponds to the ablated plasma and that on the opposite side the reflection by the target surface. It is seen from Fig. 7 that the shape of the ablated plasma is initially spherical, and later changes to a mushroom with decreasing luminosity.

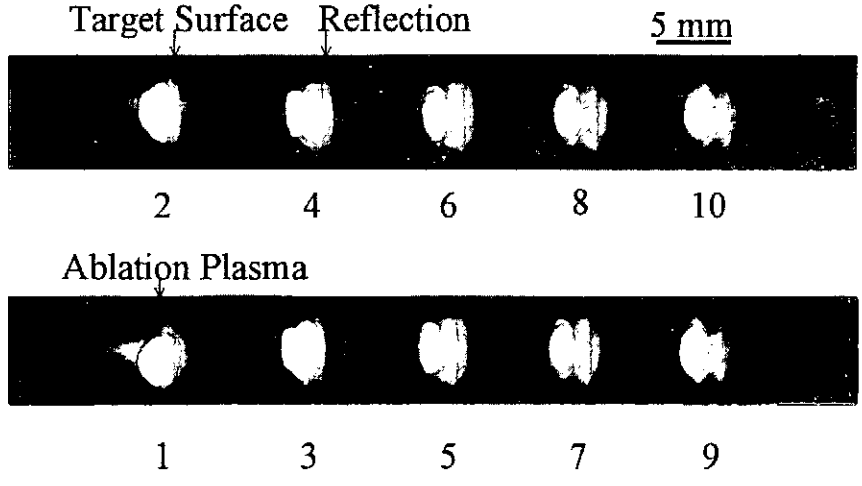

Fig.7 Framing photographs of ablated plasma at $F \approx 16$ J/cm^2, $P_{oxygen} = 200$ Torr.

3.2.2 Spectral Photography

The light emission from the ablated plasma was studied by using spectrometer. Figure 8 shows the time-integrated spectroscopy photographs obtained with laser energy density of 10 J/cm^2 and oxygen pressure of 200 Torr. Figures 8(a) and 8(b) show the experimental configrations where the slit of the spectrometer is placed in the direction parallel and

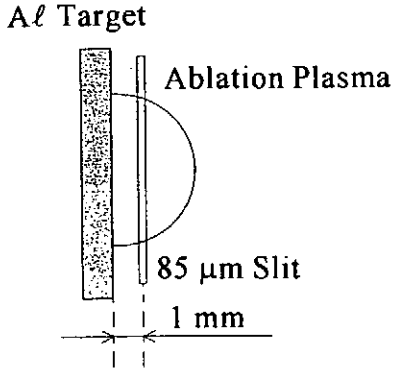

(a) Survey of spectrometry parallel to target surface.

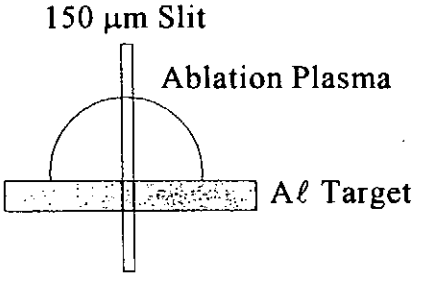

(b) Survey of spectrometry perpendicular to target surface.

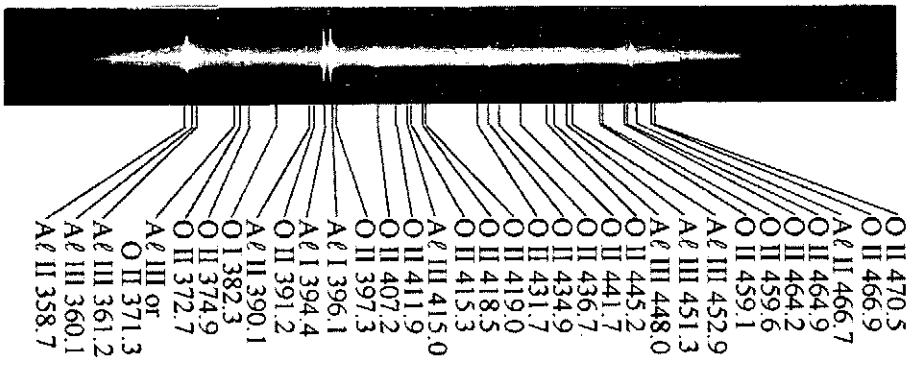

(c) Ablation plasma emission spectra parallel to target surface.

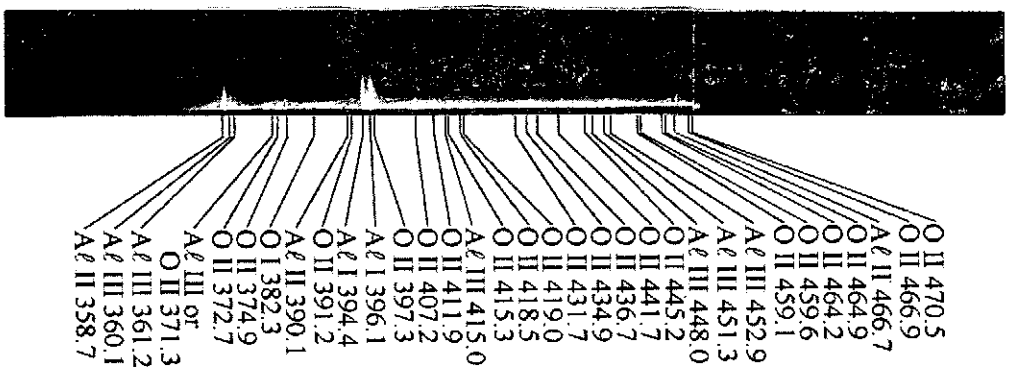

(d) Ablation plasma emission spectra parpendicular to target surface.

Fig. 8 Spectrographs of the ablated plasma at $F \approx 10$ J/cm^2, $P_{oxygen} = 200$ Torr.

perpendicular to the target surface, respectively. The photographs obtained by the configurations of Figs. 8(a) and 8(b) are shown in Figs. 8(c) and 8(d), respectively. The spectra to be mesured are limited above 300 nm due to ultraviolet absorption of the lens. From Figs. 8(c) and 8(d), we see the spectral lines of aluminum atoms, $A\ell^{+}$ ions, $A\ell^{++}$ ions, oxygen atoms, and O^{+} ions. The strong lines are observed for $A\ell$ II at 358.7 nm and $A\ell$ I at 394.4 nm and 396.6 nm. Furthermore, the spectral width is larger than other lines, indicating larger emission volume. Besides the above lines, a continuous spectrum is also seen in Figs. 8(c) and 8(d), which is probably driven by recombinations and bremsstrahlungs.

3.2.3 SMA Measurement

The spectra of the ablated plasma have also been studied by SMA in both time-integrated mode and time-resolved mode. Figure 9 shows the time-integrated spectra obtained by the SMA with different oxygen pressure, where the laser energy density was 10 J/cm^2. The slit of the spectrometer was placed in parallel to the target surface and the position of the observation was 0.5 mm from the target surface. From Fig. 9, it is seen that both the line spectra and the continuous spectra increase when the oxygen pressure is increased. It may be due to the fact that, at higher pressures, the expansion of the ablated plasma is suppressed by the ambient gas, resulting in high density and high temperature plasma that sustains for longer time.

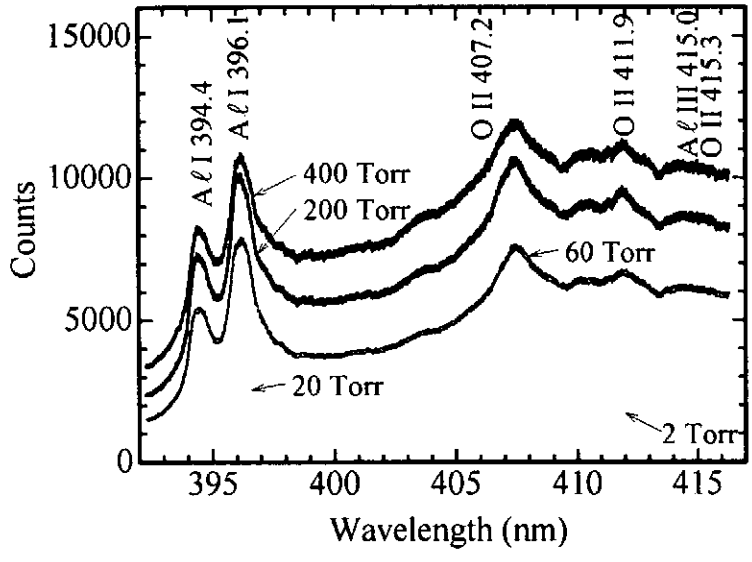

Fig. 9 Time integrated spectra of ablated plasma at $F \approx 10$ J/cm^2.

Figure 10 shows the time-resolved spectra obtained by SMA with different delay times from 100 ns to 2,050 ns. The laser energy density and oxygen pressure were 10 J/cm^2 and 200 Torr, respectively. The slit of the spectrometer was parallel to the target surface and the position of the observation was 1 mm from the target surface. The gate pulse was 100 ns. It is seen from Fig. 10 that the initial light emission consists of a continuous spectrum and oxygen lines. At 250 ns after the laser pulse, the continuous spectrum and oxygen lines reach the peak and the aluminum lines appear. The oxygen lines disappear at about 450 ns and the aluminum lines last for a few microseconds.

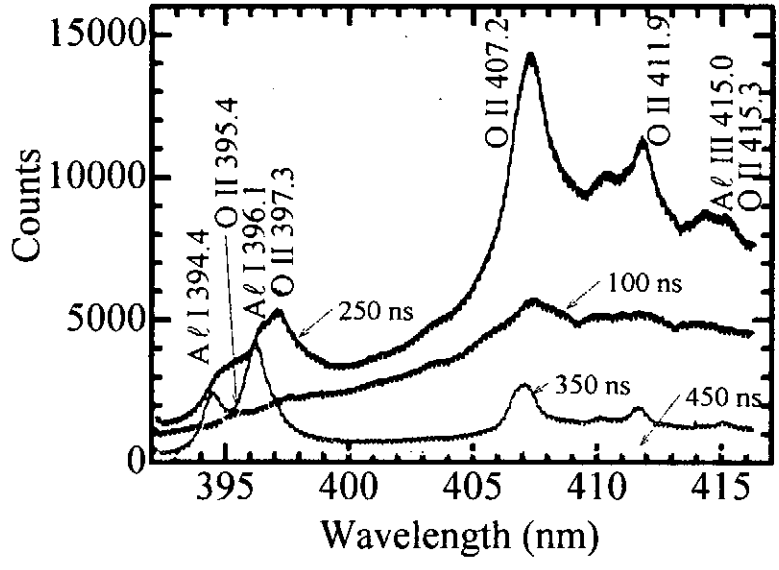

(a) 100 - 450 ns delay

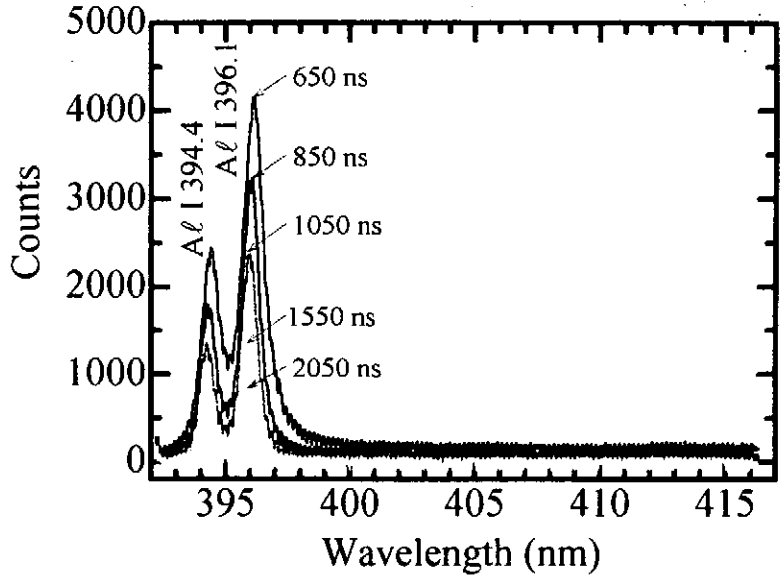

(b) 650 - 2050 ns delay

Fig. 10 Time-resolved spectra of ablation plasma at $F \approx 10$ J/cm^2, $P_{oxygen} = 200$ Torr.

4. Conclusions

From the results of XRD and TEM analysis of the aluminum nitride powders, we have obtained the following conclusions:

1) When the nitrogen pressure is lower than 60 Torr, the produced powders are Aℓ or mixture of Aℓ and AℓN. When the nitrogen pressure is higher than 200 Torr, the produced powders are pure AℓN.
2) At nitrogen pressure of 200 Torr, the particle sizes are less than 25 nm with the average diameter of ~ 11 nm.

From the results of plasma diagnostics experiments under the same condition as the nanosize powder production by laser ablation, we have obtained the following conclusions:

1) The ablation plasma expands in a spherical shape.
2) The ablation plasma consists of aluminum atoms, $A\ell^{+}$ ions, $A\ell^{++}$ ions, oxygen atoms, and O^{+} ions.
3) The strong light emissions are seen due to Aℓ II at 358.7 nm and Aℓ I at 394.4 nm and 396.6 nm.
4) The intensity of the light emission increases when the ambient gas pressure is increased.
5) The light emission starts with continuous spectrum and oxygen lines, and last for about 450 ns. The aluminum lines start at about 250 ns and last for a few microseconds.

References

[1] A. Kato and H. Arai : "Nanosize powder" Asakura Syoten (1993) Ch.1 [in Japanese].

[2] T. Yoshino : "Nanosize powder and materials", Nippon Zairyou Kagaku Kai (1993) Ch.1 [in Japanese].

[3] A. Matsunawa and S. Katayama : Transaction of JWRI, **19**, 137 (1990).

[4] G. P. Johnston, R. E. Muenchausen, D. M. Smith, and S. R. Foltyn : J. Am. Ceram. Soc., **75**, 3465 (1992).

[5] Y. Simotori, M. Yokoyama, S. Harada, H. Isobe, K. Masugata and K. Yatsui : J Appl. Phys., **63**, 968 (1988).

[6] Y. Shimotori, M. Yokoyama, S. Harada, K. Masugata and K. Yatsui : Jpn. J. Appl. Phys., **28,** 468 (1989).

[7] K. Yatsui : Laser & Particle Beams, 7, 733 (1989).

[8] K. Yatsui, X. Kang, T. Sonegawa, T. Matsuoka, K. Masugata, Y. Shimotori, T. Satoh, S. Furuuchi, Y. Ohuchi, T. Takesita and H.Yamamoto : Phys. Plasmas, **1**, 1730 (1994).

[9] K. Yatsui, C. Grigoriu, H. Kubo, K. Masugata and Y. Shimotori : Appl. Phys. Lett., **67**, 1214 (1995).

[10] C. Grigoriu, Y. Nakagawa, E. P. A. Chamdani, T. Sonegawa, K. Nishiura, K. S. Nathan, K. Masugata and K. Yatsui : Physics, Diagnostics, and Application of Pulsed High Energy Density Plasma as an Extreme State, p.25, (1996).

Ozone Formation and Diffusion after a Wire-to-Plate Streamer Discharge

F. Hegeler and H. Akiyama

Kumamoto University
Department of Electrical and Computer Engineering
Kurokami 2-39-1, Kumamoto 860, Japan

Abstract

A UV absorption technique is used to investigate the spatial and temporal distributions of ozone after a positive streamer discharge in air at atmospheric pressure. The discharge apparatus consists of a 45 cm long wire-to-plate configuration with an electrode gap distance of 2.5 cm. Results show an average ozone density of about $5 \cdot 10^{15}$ cm^{-3} in an area of 2 mm^2 just below the positive electrode after application of a voltage pulse with an amplitude of 65 kV and a duration of 80 ns. Towards the cathode, the ozone density decreases rapidly. The ozone diffusion coefficient ranges from below 0.3 cm^2/s to about 0.6 cm^2/s, indicating a spatial and temporal distribution of the gas temperature throughout the discharge gap as well.

1. Introduction

Ozone is increasingly used for the treatment of drinking and waste water (e.g., deodorization, decolorization, and disinfection) and for the decomposition of aqueous hazardous organic wastes. The advantage of the ozone treatment lies in extremely powerful oxidation without disinfectant residues which makes it, unlike chlorine, an environmental friendly agent. Current work on ozone production emphasizes the design and construction of more efficient systems in order to reduce costs. Recently, positive streamer discharge systems have been investigated as an alternative to silent discharge ozone generators since they do not require a dielectric barrier between electrodes [1-3]. Although ozone generation has been measured under the influence of various parameters such as the electric field strength, pulse duration, electrode diameter, electrode gap distance, and gas flow rate [4], the spatial distribution of ozone after a streamer discharge in air has not been fully understood. The ozone distribution has been simulated only for a pure oxygen environment [5-9] since the nitrogen in air adds significantly to the complexity of the reaction system. This paper describes experimental measurements of ozone by UV absorption after a positive streamer discharge and calculates the ozone diffusion coefficient.

2. Experimental Setup

The basic experimental apparatus is shown in Figure 1. Two setups have been used. Setup (I): The dc output of a Hamamatsu 30 W deuterium lamp L1626 is focused by a fused silica plano convex lens. The resulting UV beam with a spectrum of 190 to 400 nm passes through a pinhole, the discharge gap, and again through a pinhole. A Hamamatsu photomultiplier R955 detects photons with a wavelength of 254 nm ± 0.3 nm which have been filtered out by a Minuteman 302-VM monochromator with an exit slit width of 150 μm, a slit height of 2 cm, and a dispersion of 4 nm/mm. Setup (II): Instead of irradiating the discharge gap with a wide spectrum UV beam, this setup produces a photon beam with a wavelength of 254 nm ± 0.1 nm. The aperture of the UV beam source has been reduced from 1 mm in setup (I) to 50 μm (the monochromator exit slit width) in setup (II) without large losses in photon flux at 254 nm. Due to the smaller aperture, the UV beam collimation is significantly improved in setup (II) when the beam is focused by a plano convex lens. A Hamamatsu PMT R166, which is sensitive only between 160 and 320 nm, observes the UV beam. In addition to the ozone measuring photon beam, the PMT detects streamer generated UV light as well.

The 45 cm long discharge gap consists of a 1 mm tungsten wire which is placed 25 mm above a copper plate with a width of 6 cm. The discharge configuration does not include walls, except for the ground plate and three 2 cm wide wire supporting dielectric frames. Thus, the generated ozone diffuses freely into the background volume (i.e., air at atmospheric pressure).

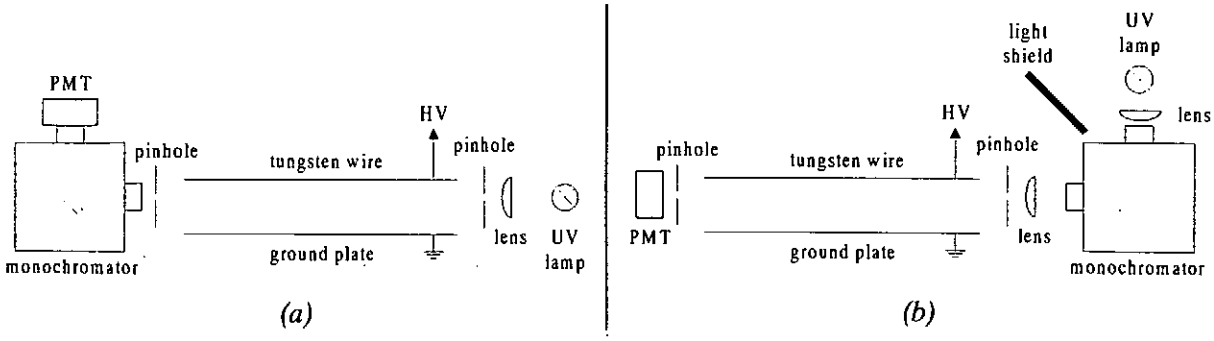

Fig. 1. Basic experimental apparatus. (a) side view of setup (I) and (b) setup (II).

UV absorption of ozone has been measured with two pinhole sizes, 1.6 and 3 mm in diameter. The right half of the discharge gap was investigated with the 3 mm UV beam. This area was divided into sections with a grid width of 3 mm, proceeding in the horizontal direction from the centerline (x = 0) to 15 mm and in the vertical direction from y = 2 to 23 mm (see Fig. 2a). The ground plate is located at y = 0, and all positions are measured from the UV beam center. The pinhole positions were calibrated by a He-Ne laser beam which passed through the pinholes prior to the UV absorption measurements. The accuracy of the pinhole positions is within 0.3 mm. The 1.6 mm UV beam has been used to investigate the ozone density near the wire electrode (see Fig. 2b). Positions of this smaller UV beam are 0, ±1.5, and ±3 mm in horizontal direction and 20, 21.5, 23, and 24.2 mm in vertical direction.

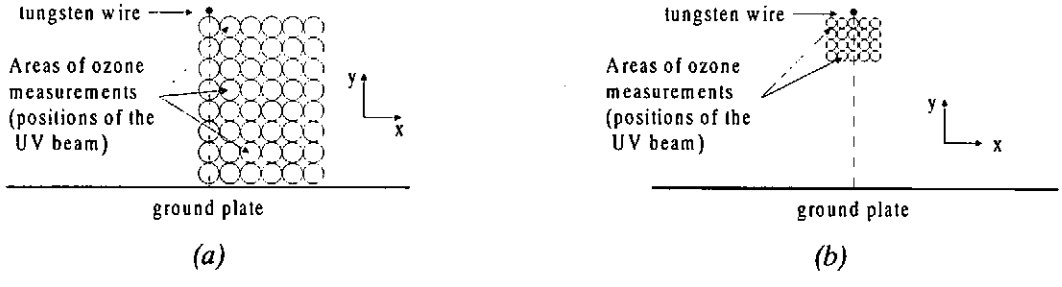

Fig. 2. Cross section of the discharge gap. Areas of ozone absorption measurements are identified by the unfilled circles. (a) with a 3 mm pinhole configuration and (b) with 1.6 mm pinholes.

An inductive energy storage generator, shown in Figure 3a, provides a single voltage and current pulse to the discharge gap as shown in Figure 3b. The 20 nF capacitor is charged to 20 kV, and an output pulse, with amplitudes of 65 kV and 120 A and a duration of 80 ns, is generated after the copper fuse, with a length of 10 cm and a diameter of 30 μm, opens. The pulse amplitude and duration are highly reproducible. The voltage and current waveforms are measured by a standard capacitive voltage divider and a Pearson Rogowski coil, respectively. A Hewlett Packard digital oscilloscope, HP 54542A, with a maximum bandwidth of 500 MHz and a maximum sample rate of 2 GSa/s, records the signals. The photocurrent is detected via the potential drop across a 167 kΩ resistor at the scope (i.e., 200 kΩ in parallel with the 1 MΩ scope input impedance). The temporal resolution of the PMT signal is a few 100 μs (i.e., the 6 m long coaxial signal line with a line capacitance of 600 pF and the 167 kΩ resistor create a low pass filter with an RC time constant of 100 μs).

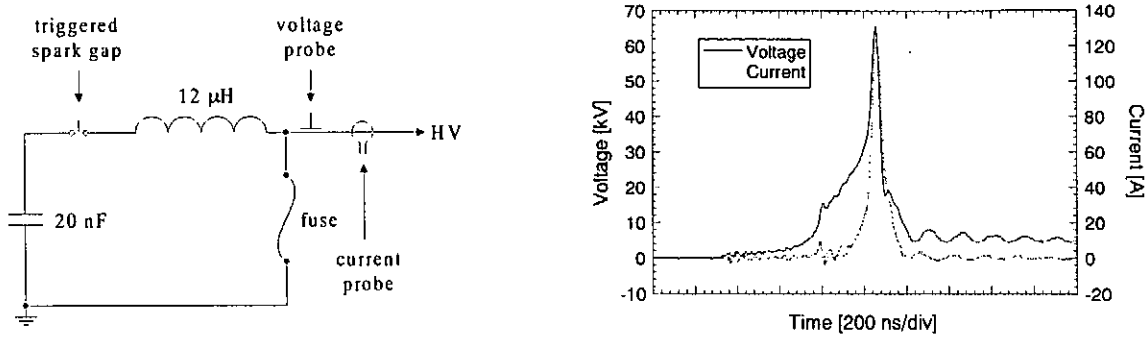

(a) *(b)*

Fig. 3. (a) inductive pulse generator and (b) voltage and current waveforms during a streamer discharge.

3. Results and Discussion

3.1. Streamer Measurements

The spatial distribution of the streamer channels in the discharge gap has been investigated with an open-shutter camera since ozone generation, which requires the dissociation of O_2 molecules by electrons, originates only in the near vicinity of the streamers. The camera pictures show a homogeneous streamer channel distribution along the wire in the z-direction, with about 8 streamer channels per centimeter. Figure 4 shows the streamer cross section distribution in the discharge gap. The highest streamer light intensity is seen just underneath the wire electrode. Above the wire electrode, the streamer development is ineffective due to the weak electric field strength.

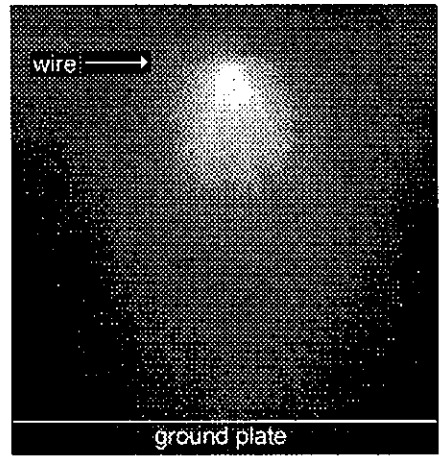

Fig. 4. Cross section of the streamer distribution at an electrode gap distance of 25 mm.

3.2. Ozone Absorption Measurements with a 3 mm UV beam

Ozone absorption measurements were taken for three time windows: 8 ms at a scope sample rate of 1 MSa/s, 160 ms at 50 kSa/s, and 3.2 s at 2.5 kSa/s. The UV beam was blocked and the discharge gap was vented with air for 10 minutes until 30 s prior to each streamer discharge. Since the ozone concentration varied slightly from one streamer discharge to another, the arithmetic average of 3 measurements for each time window and position was taken. The dissociation of O_2 molecules by electrons and other important reactions leading to ozone formation are described in reference [2]. The ozone density, N, is calculated by

$$N = -\frac{\ln(I / I_0)}{\sigma z} \qquad (1)$$

where I and I_0 are the collected and incident photon intensities, σ is the absorption cross section, and z is the length of the discharge gap. This calculation assumes that the ozone density is constant throughout the UV beam cross section. Ozone has its maximum absorption cross section of $1.15 \cdot 10^{-17}$ cm^2 at a photon wavelength of 254 nm [10]. The PMT operates in the linear region; thus, the photon intensity ratio corresponds to the photocurrent ratio. In all figures, the ozone density has been expressed as a concentration in ppm for clarity, where 1 ppm equals to a density of $2.5 \cdot 10^{13}$ cm^{-3}. Figure 5 shows the average ozone concentration underneath the wire electrode and just above the ground plate. The collective results of about 500 ozone absorption measurements are given in Figure 6. The results include a high frequency noise signal which relates to the PMT photoelectron emission instability (e.g., a constant photon flux produces only a constant time-averaged output current).

The highest ozone concentration of about 50 ppm is found underneath the wire electrode at t = 500 μs (i.e., t = 0 corresponds to the time of the streamer discharge). Near the ground plate, the streamers generate an ozone concentration of about 3 ppm. A similar ozone density can be assumed for the left hand side of the centerline, since the discharge gap is symmetric. The high ozone density at the wire diffuses into the background volume in tens of milliseconds. At t = 200 ms, the ozone concentration in the discharge gap ranges from 0 to 6 ppm, which decreases further to less than 3 ppm at 500 ms and below 1 ppm at 2 s.

Several positions have been evaluated at different wavelengths of 210, 230, and 280 nm. The measured signals corresponded to the ozone absorption cross section at these wavelengths, verifying the above ozone measurements. Likewise, the cross sectional distribution of the streamers channels (see Fig. 4) matches the initial ozone distribution shown in Figure 6a.

The ozone absorption results with setup (I) are identical to the ones with setup (II) which indicates that the UV beam does not influence the streamer development in the discharge gap. The decrease of ozone is mainly caused by diffusion (see Fig. 6). Thermal decomposition [11] or photolysis of ozone [11-14] can be neglected for the time of interest due to the low intensity of the UV beam (i.e., although both decomposition methods occur during the measurements, only a small portion of the generated ozone is decomposed within 500 ms). The ozone concentration integrated over the cross-sectional area decreases in time (see Fig. 6), because ozone diffuses into areas outside the discharge gap (e.g., mainly into regions above the wire electrode). The results in Figure 6a show that the ozone density, throughout the gap, is roughly constant within the cross section of the 3 mm UV beam except for the area near the positive wire electrode.

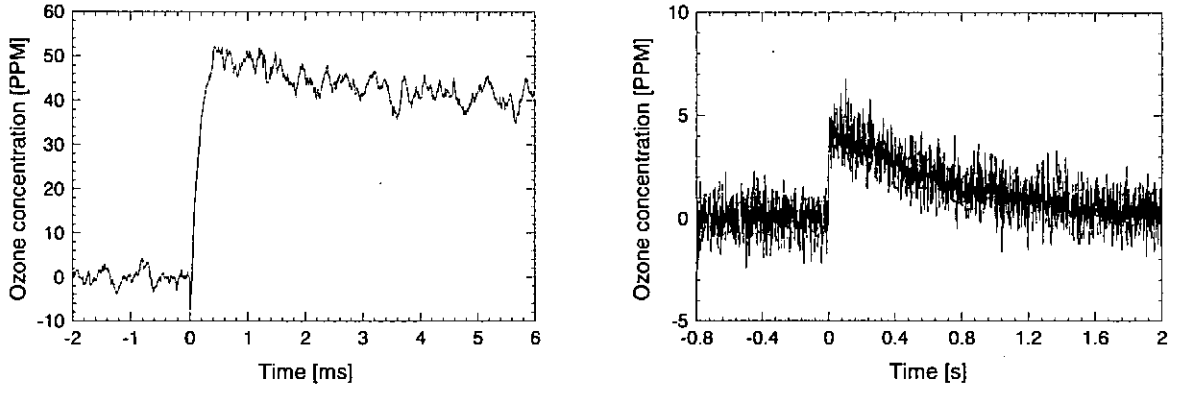

Fig. 5. Average ozone concentration after a streamer discharge, measured with a 3 mm UV beam. (a) near the wire electrode at (x = 0 mm, y = 23 mm) and (b) near the ground plate at (3 mm, 2 mm).

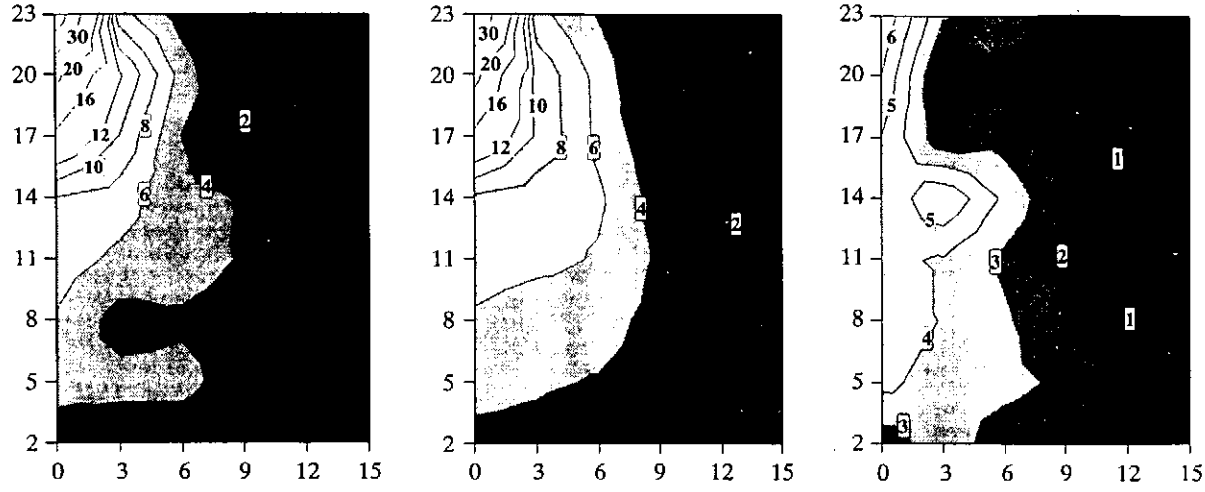

Fig. 6. Average ozone concentration in ppm at (a) 0.5 ms, (b) 10 ms, and (c) 200 ms after the streamer discharge, and detected with a UV beam with a diameter of 3 mm. Axis labels represent distance in millimeters from the ground plate in the vertical direction and distance in millimeters from the centerline of the discharge gap in the horizontal direction. The wire electrode is located between y = 25 mm and 26 mm.

3.3. Ozone Absorption Measurements with a 1.6 mm UV beam

The spatial resolution of the ozone absorption measurements around the wire is improved with a smaller diameter UV beam. At (x = 0 mm, y = 24.2 mm), an average ozone concentration of about 200 ppm is found in an area of 2 mm^2 (see Fig. 7). In this case, the UV beam with a diameter of 1.6 mm is located just underneath the wire electrode. At t = 0, the PMT detects the streamer generated UV light as well, which is shown by the "negative" ozone concentration.

The summation of the 1.6 mm UV beam absorption measurements is given in Figure 8. As expected, the ozone distribution is roughly symmetric along the gap center, within the accuracy of the UV beam positioning. The standard deviation of the ozone density measurements is about 5% in most areas except for streamer boundary regions, such as at (±1.5 mm, 24.2 mm) and (±3 mm, 21.5 mm). In these locations, the initial ozone density deviates as much as 25% due to the unstable streamer formation.

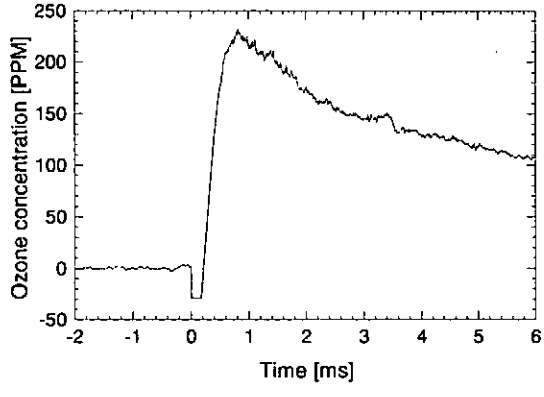

Fig. 7. Average ozone concentration after a streamer discharge, measured with a 1.6 mm UV beam at (0 mm, 24.2 mm).

Near the wire electrode, the 1.6 mm UV beam measures a higher initial ozone concentration than the 3 mm beam because of the ozone density gradient within the cross section of the 3 mm beam at t = 1 ms. At position (0 mm, 20 mm), 5 mm below the wire, ozone is generated more homogeneously over larger areas, since no difference in the ozone absorption measurements is found at this position with the 1.6 mm and 3 mm UV beams for the first tens of milliseconds. This result corresponds well with the cross sectional streamer channel distribution shown in Figure 4.

The measurements in Figure 8 show a shift of the ozone density maximum by about 3 mm at t = 200 ms (e.g., the maximum shifts from just underneath the wire electrode to position (0 mm, 21.5 mm)). A similar shift of roughly 10 mm has been also seen with the 3 mm UV beam setup at t = 500 ms.

Integrating the initial ozone density over the gap cross section shows that about 30% of the ozone is generated in an area within a radius of 5 mm around the positive electrode. Although the highest ozone density exists in proximity to the wire, the ozone near the ground plate can not be neglected. One third of the total ozone is produced in the lower half of the gap.

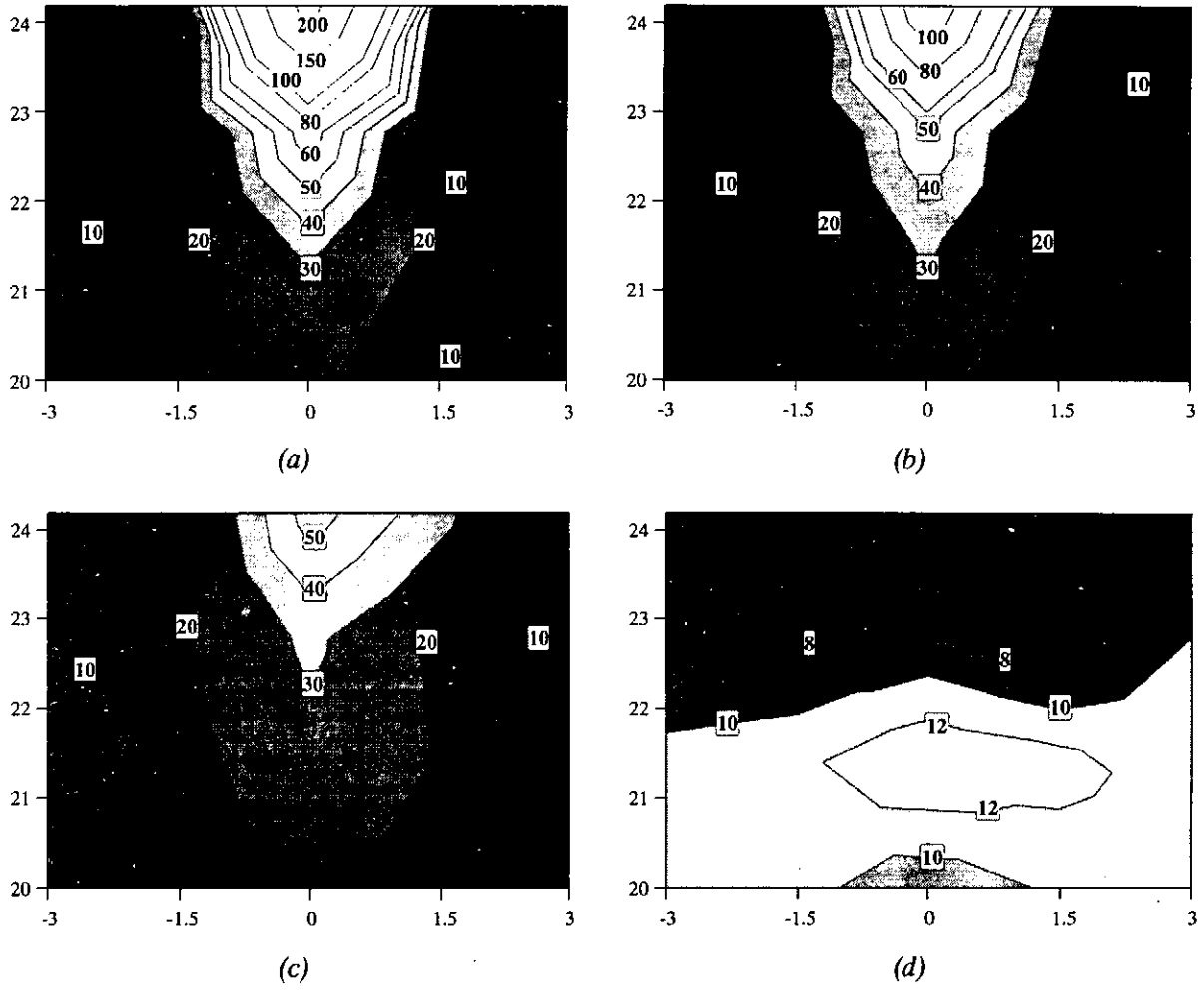

Fig. 8. Average ozone concentration in ppm at (a) 1 ms, (b) 5 ms, (c) 20 ms, and (d) 200 ms after the streamer discharge, as detected by a UV beam with a diameter of 1.6 mm. Axis labels represent distance in millimeters from the ground plate in the vertical direction and distance in millimeters from the centerline of the discharge gap in the horizontal direction.

3.4. Ozone Formation Time

The ozone formation time had been simulated by solving the rate equations [2, 15-17], but few supporting experimental results exists. In pure oxygen, an ozone formation time constant of about 3 μs was estimated which led to a generation of about 10% of the total ozone at t = 1 μs and 60% at t = 10 μs [2]. In air, ozone formation is delayed due the existence of additional processes involving nitrogen. Simulations for air [16] showed about 10% of the ozone at t = 15 μs and 60% at t = 90 μs.

The ozone formation time in air has been measured by the 3 mm UV beam at position (0 mm, 21 mm) where the streamer formation is homogeneous within the cross section of the beam. The length of the PMT signal cable was reduced from 6 m to 1.5 m, which decreased the RC time constant to 25 μs (i.e., with a 167 kΩ resistor at the scope), and the result is shown in Figure 9a. The maximum ozone concentration at this position is approximately 35 ppm, which corresponds to an ozone density of $8.8 \cdot 10^{14}$ cm^{-3}. The signal to noise ratio decreases slightly compared to previous measurements since the RC low pass filter allows higher frequencies to pass (e.g., the high frequency noise signal from the PMT photoelectron emission instability). Figure 9b shows the ozone signal with a further reduction of the RC time constant to less than 1 μs by decreasing the resistor at the scope to 5 kΩ with shortened cable. Although the signal to noise ratio decreases significantly compared to the case in Figure 9a, the ozone formation time is clearly seen. The ozone increase is roughly linear with time for most parts, from 10 μs (10 ppm) to about 30 μs (30 ppm). The linear increase in ozone agrees with the simulations in air [16]. Around 60% of the total ozone is formed after 20 μs.

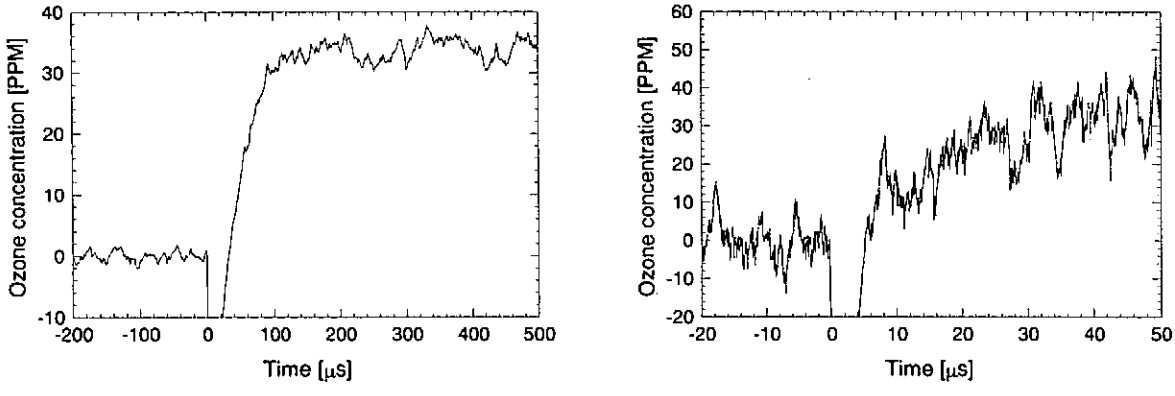

Fig. 9. Average ozone concentration in ppm at (0 mm, 21 mm), 4 mm below the wire electrode. (a) measured with an RC time constant of 25 μs and (b) with RC < 1 μs.

3.5. Ozone Diffusion Results

Figures 6 and 8 have shown the ozone diffusion in the discharge gap. In addition, ozone diffusion at a single position has been clearly seen with the 1.6 mm UV absorption setup near the wire electrode, as shown in Figure 10. The ozone, which is generated near the wire, drifts into the position of the UV beam and causes maximum ozone absorption at 11 ms after the streamer discharge at position (1.5 mm, 24.2 mm) as shown in Figure 10a. At (3 mm, 24.2 mm), the maximum absorption signal is further delayed (see Fig. 10b).

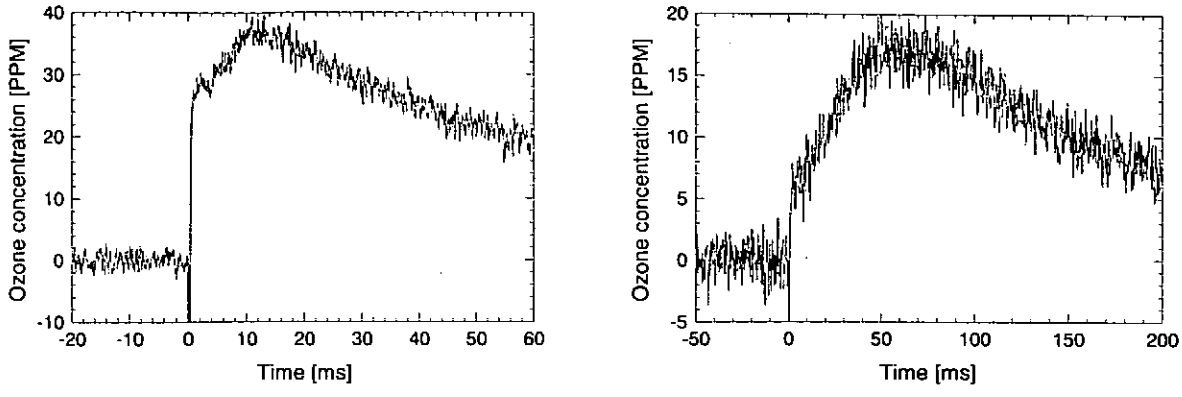

(a) *(b)*

Fig. 10. Temporal distribution of ozone in an area near the positive wire electrode, measured with a UV beam 1.6 mm in diameter. (a) at (1.5 mm, 24.2 mm) and (b) at (3 mm, 24.2 mm).

3.6. Calculation of the Ozone Diffusion Coefficient

The simple diffusion of ozone into the background volume is expressed by

$$\frac{\partial n}{\partial t} = \frac{\partial}{\partial x}\left(D\frac{\partial n}{\partial x}\right) + \frac{\partial}{\partial y}\left(D\frac{\partial n}{\partial y}\right) + \frac{\partial}{\partial z}\left(D\frac{\partial n}{\partial z}\right) \tag{2}$$

where n is the ozone density and D is the diffusion coefficient.

The diffusion coefficient can be estimated by modeling the gas molecules as rigid elastic spheres [18],

$$D_{12} = \frac{3}{8(n_1 + n_2)(r_1 + r_2)^2}\sqrt{\frac{kT(m_1 + m_2)}{2\pi m_1 m_2}} \tag{3a}$$

with the effective molecular collision radius, r, the mass of the molecule, m, Boltzmann's constant, k, and the absolute temperature, T. The subscripts denoting the different gas components.

Since the ozone density is very small compared to the background density and $D_{12} = D_{21} = D$,

$$D \cong \frac{3}{8(n_2)(r_1 + r_2)^2}\sqrt{\frac{kT(m_1 + m_2)}{2\pi m_1 m_2}} \tag{3b}$$

$$D \cong \frac{3}{8(p_2)(r_1 + r_2)^2}\sqrt{\frac{(kT)^3(m_1 + m_2)}{2\pi m_1 m_2}} \tag{3c}$$

where n_2 and p_2 are the density and pressure of the background gas component, respectively. Empirically, the diffusion coefficient varies with temperature and pressure by [18]

$$D \cong D_o\left(\frac{T}{T_o}\right)^{1.75}\left(\frac{p_o}{p}\right). \tag{3d}$$

The temperature dependence is slightly higher than the power of $^3/_2$ since the effective molecular collision radius decreases with higher temperatures [19].

Estimates of the ozone diffusion coefficient for pure oxygen range from about 0.2 cm^2/s [2] to 0.27 cm^2/s [17] at 760 torr and 300 K. Since the mass and effective molecular collision radius of nitrogen are similar to those of oxygen [19], the ozone diffusion coefficient in oxygen and air should be comparable.

The ozone diffusion coefficient in air has been calculated from equation (2). It has been assumed that $dn/dz = 0$, corresponding to a homogeneous ozone generation along the wire. A grid size of 0.2 mm has been used in the x- and y-directions, with a time step of 50 μs, in order to solve the two dimensional discrete diffusion equation. The measured ozone density at t = 1 ms is utilized as the initial ozone concentration, and the spatial and temporal ozone density profiles are calculated for a constant diffusion coefficient.

Figure 11 shows the calculated diffusion of ozone at several beam positions near the wire electrode. Note that the ozone concentration is normalized, with 1 ppm corresponding to a density of $2.5 \cdot 10^{13}$ cm^{-3} as in all previous figures. At position (0 mm, 24.2 mm), the initial diffusion coefficient is roughly 3 times larger than the estimated one at T = 300 K (see Fig. 11a). The ozone measurements are closely simulated with D ranging from 0.6 to 0.8 cm^2/s for the first few milliseconds. At (1.5 mm, 24.2 mm), an average diffusion coefficient of 0.4 cm^2/s best fits the measured ozone concentration (see Figs. 10a and 11b), compared to 0.3 cm^2/s at (3 mm, 24.2 mm) as shown in Figures 10b and 11c. The calculated ozone density in the simulations is slightly higher than the measured value since the ozone diffusion in the z-direction, and therefore, the ozone diffusion in the vertical and horizontal directions outside the discharge gap has been neglected.

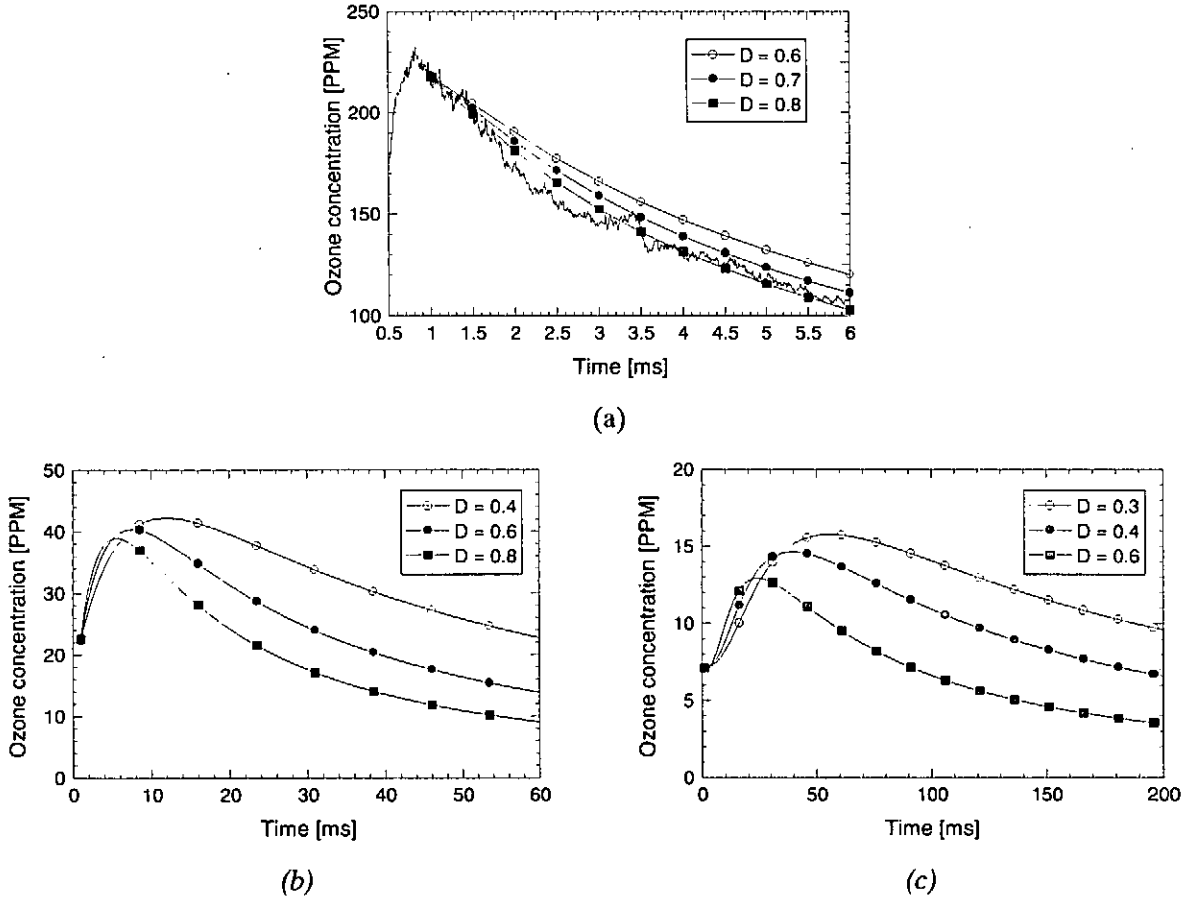

Fig. 11. Simulation of the ozone diffusion coefficient, D, at several positions. (a) at (0 mm, 24.2 mm), (b) at (1.5 mm, 24.2 mm), and (c) at (3 mm, 24.2 mm). Values of D are given in [cm^2/s].

The high diffusion coefficient of 0.6 to 0.8 cm^2/s underneath the wire electrode can be explained by an increase of the gas temperature due to a high streamer channel density (see Fig. 4). In other areas of the discharge gap, the diffusion coefficient is lower since the temperature of the gas molecules is near room temperature.

Figure 12 gives the simulated spatial ozone concentration in the gap at t = 200 ms. For these calculations, a diffusion coefficient of D = 0.3 cm^2/s has been used for all areas. It shows a distinct shift of the density maximum along the centerline towards the ground plate, which corresponds well with the measurements in Figure 8d. The shift is due to the discharge configuration which generates only minor ozone concentrations above the wire. Therefore, the high ozone density in proximity to the positive electrode diffuses faster into an area above the wire than towards the ground plate. In a coaxial discharge geometry, for example, the maximum ozone density should be always near the wire electrode for simulations with a constant diffusion coefficient.

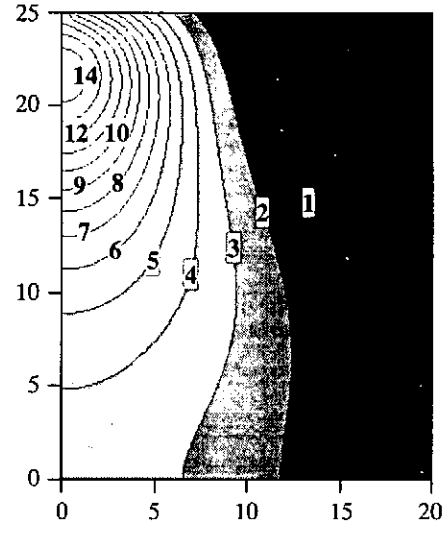

Fig. 12. Simulation of the ozone diffusion in the discharge gap with D = 0.3 cm^2/s at t = 200 ms.

4. Conclusion

As expected, a positive streamer discharge generates the highest ozone density near the wire electrode. The results show an ozone diffusion into the background volume in tens of milliseconds. With this wire-to-plate configuration, about 30% of the total ozone is generated in an area within a radius of 5 mm around the positive electrode, and $^1/_3$ of the ozone is produced in the lower half of the gap. Simulation of the ozone diffusion distinguished different diffusion coefficients ranging from below 0.3 to about 0.6 cm^2/s in the discharge gap because of the initial temperature distribution in the gap.

Acknowledgment

Frank Hegeler has been supported by Kyushu Electric Power Company through the Advanced Technology for Electrical Energy program of the Department of Electrical and Computer Engineering at Kumamoto University.

References

[1] B. Held "Coronas and their Applications," *The 11th International Conference on Gas Discharges and their Applications, Tokyo, Japan, Sept. 11-15, 1995*, vol. 2, pp. 514-525.

[2] B. Eliasson, M. Hirth, and U. Kogelschatz, "Ozone Synthesis from Oxygen in Dielectric Barrier Discharges," *Journal of Physics D, Applied Physics*, vol. 20, 1987, pp. 1421-1437.

[3] S. Masuda et al., "A Ceramic-Based Ozonizer Using High-Frequency Discharge," *IEEE Transactions on Industry Applications*, vol. 24, no. 2, 1988, pp. 223-231.

[4] I. Chalmers, et al., "Ozone Synthesis in Oxygen in a Dielectric Barrier Free Configuration," *10th IEEE International Pulsed Power Conference, Albuquerque, July. 3-6, 1995*, pp. 1249-1254.

[5] P. Pignolet, S. Hadj-Ziane, and B. Held, "Ozone Generation by Point to Plane Corona Discharge," *Journal of Physics D, Applied Physics*, vol. 23, 1990, pp. 1069-1072.
[6] S. Hadj-Ziane, B. Held, and P. Pignolet, "Ozone Production in an Oxygen-Fed Wire to Cylinder Ozonizer," *Journal of Physics D, Applied Physics*, vol. 23, 1990, pp. 1390-1395.
[7] A. R. Bestman, "Analytical Solutions for Ozone Generation by Point-to-Plane Corona Discharge," *Journal of Physics D, Applied Physics*, vol. 25, 1992, pp. 195-197.
[8] S. Hadj-Ziane et al., "Ozone Generation in an Oxygen-Fed Wire to Cylinder Ozonizer at Atmospheric Pressure," *Journal of Physics D, Applied Physics*, vol. 25, 1992, pp. 677-685.
[9] J. Loiseau, F. Lacassie, and C. Monge, "Numerical Simulation of Ozone Axial and Radial Distribution in a Cylindrical Oxygen-Fed Ozonizer," *Journal of Physics D, Applied Physics*, vol. 27, 1994, pp. 63-73.
[10] K. Yoshino et al., "Measurements of Absolute Absorption Cross Section of Ozone in the 185 to 254 nm Wavelength Region and the Temperature Dependence," *Journal of Geophysical Research*, vol. 98, March 1993, pp. 5205-5211.
[11] J. Wen and M. Thiemens, "Experimental and Theoretical Study of Isotope Effects on Ozone Decomposition," *Journal of Geophysical Research*, vol. 96, no. D6, 1991, pp. 10911-10921.
[12] D. J. Giachardi and R. P. Wayne, "The Photolysis of Ozone by Ultraviolet Radiation," *Proc. R. Soc. Lond. A.*, vol. 330, 1972, pp. 131-146.
[13] P. W. Fairchild and E. Lee, "Relative Quantum Yields of $O(^1D)$ in Ozone Photolysis in the Region between 250 and 300 nm," *Chemical Physics Letters*, vol. 60, Dec. 1978, pp. 36-39.
[14] I. Arnold and F. J. Comes, "Photolysis of Ozone in the Ultraviolet Region," *Chemical Physics*, vol. 47, 1980, pp. 125-130.
[15] R. Peyrous, P. Pignolet, and B. Held, "Kinetic Simulation of Gaseous Species Created by an Electrical Discharge in Dry or Humid Oxygen," *Journal of Physics D, Applied Physics*, vol. 22, 1989, pp. 1658-1667.
[16] B. Eliasson and U. Kogelschatz, "Modeling and Applications of Silent Discharge Plasmas," *IEEE Transactions on Plasma Science*, vol. 19, no. 2, 1991, pp. 309-323.
[17] C. Gutierrez-Tapia et al., "Perturbative Method for Ozone Synthesis From Oxygen in a Single Discharge," *IEEE Transactions on Plasma Science*, vol. 22, no. 5, 1994, pp. 979-985.
[18] R. C. Roberts, American Institute of Physics Handbook, New York, McGraw-Hill, 1963, Molecular Diffusion of Gases.
[19] J. H. Jeans, The Dynamical Theory of Gases, London, Cambridge University Press, 1904, Chapter XI, Free Path Phenomena.

Energy Deposition Profiles and Unsteady Flowfields in Discharge-Pumped XeCl Laser

Qifeng Zhu[1], Go Imada[1], Wataru Masuda[2], and Kiyoshi Yatsui[1]

[1]*Laboratory of Beam Technology, Nagaoka University of Technology*

Nagaoka, Niigata 940-21, Japan

[2]*Department of Mechanical Engineering, Nagaoka University of Technology*

Nagaoka, Niigata 940-21, Japan

A nonuniform distribution of gas temperature in a discharge-pumped excimer laser is produced by inhomogeneous energy deposition. Shock waves and nonuniform flowfields due to the relaxation of the heated gas can induce discharge instability and limit the repetition rate of the laser. Gas dynamic simulations require to know the initial gas temperature profile which is calculated in this work using a discharge model. The numerical results show that the temperature profile tends to be steeper at a higher xenon concentration and when the nonuniformity in electric field becomes stronger. Furthermore, the shock waves and unsteady flowfields are studied using two-dimensional compressible gas dynamic equations and total variation diminishing (TVD) numerical scheme.

KEYWORDS: excimer laser, electric discharge, gas temperature profile, shock wave, unsteady flowfield, computational fluid dynamics.

1. Introduction

In the discharge-pumped excimer lasers, a large fraction of the input energy rapidly heats the gas. Shock waves and density disturbances cause a deterioration of discharge uniformity, which can induce discharge instability and limit the repetition rate of excimer lasers.

Experimentally, we have observed three kinds of shock waves:[1, 2] the wave #1 moving upstream and downstream, the wave #2 moving between the electrodes, and the wave #3 originating from preionization pin arrays.

An inhomogeneous energy deposition results in a nonuniform distribution of gas temperature. The gas temperature profile, which is necessary for the numerical study of the shock waves and flowfields in the laser cavity, is rarely reported for a discharge-pumped XeCl excimer laser. This work is in an effort to calculate the temperature profile using a discharge model. Furthermore, the shock waves and unsteady flowfields in the laser cavity will be

studied numerically using computational fluid dynamics (CFD).

2. Description of Discharge Model

The discharge model consists of (1) reaction kinetics, (2) Boltzmann equation, (3) circuit equations, and (4) optical resonator equations.[3, 4] The reaction kinetics has been simplified to save the CPU time and memory space by neglecting Xe_2^+, Xe_2^*, Ne_2^+, Ne_2^*, HCl*(A), HCl*(B, C), HCl^+, H^-, Cl*, Cl^+, Cl_2, Cl_2^*, NeCl*, and Xe_2Cl^*. The electron-impact rate coefficients are obtained by solving the Boltzmann equation. In the Boltzmann equation, we take into account elastic collisions, excitations, superelastic collisions, ionizations, and dissociative attachments as shown in Table 1. The optical model and discharge circuit are the same as those in refs. 3 and 4. The nonuniformity in electric field is taken into account in this work, whereas it was not considered in refs. 3 and 4.

Table 1. Electron-heavy particle collisions in the Boltzmann equation.

Processes	Processes
Elastic collisions	$He^* + e \rightarrow He + e$
$Ne + e \rightarrow Ne + e$	$HCl(1) + e \rightarrow HCl(0) + e$
$He + e \rightarrow He + e$	$HCl(2) + e \rightarrow HCl(0) + e$
$Xe + e \rightarrow Xe + e$	$HCl(2) + e \rightarrow HCl(1) + e$
$HCl + e \rightarrow HCl + e$	
	Ionizations:
Excitations:	$Xe + e \rightarrow Xe^+ + 2\,e$
$Xe + e \rightarrow Xe^* + e$	$Xe^* + e \rightarrow Xe^+ + 2\,e$
$Ne + e \rightarrow Ne^* + e$	$Ne + e \rightarrow Ne^+ + 2\,e$
$He + e \rightarrow He^* + e$	$Ne^* + e \rightarrow Ne^+ + 2\,e$
$HCl(0) + e \rightarrow HCl(1) + e$	$He + e \rightarrow He^+ + 2\,e$
$HCl(0) + e \rightarrow HCl(2) + e$	
$HCl(1) + e \rightarrow HCl(2) + e$	Dissociative attachments:
	$HCl(0) + e \rightarrow H + Cl^-$
Superelastic collisions:	$HCl(1) + e \rightarrow H + Cl^-$
$Xe^* + e \rightarrow Xe + e$	$HCl(2) + e \rightarrow H + Cl^-$
$Ne^* + e \rightarrow Ne + e$	

We use a parallel resistor model[5] as shown in Fig. 1. The discharge region is divided into 30 channels with a common voltage drop V_d. The parameters in each channel are assumed to be homogenous. Diffusions of heavy particles and electrons are negligible. The electric field and current density in the channel i are given by $E_i = V_d/d_i$ and $j_i = (e_0 n_e v_d)_i$, respectively, and subscript i represents the parameters in the channel i. Here, d_i is the effective gap distance of the electrodes for the channel i, e_0, n_e, and v_d are the electron charge, electron density, and drift velocity, respectively. The drift velocity v_d is calculated from the Boltzmann equation. The effective gap distances are chosen to reproduce the electric field distribution at the midplane of the discharge for Chang-type electrodes.[6] If A_i is the cross-sectional area of the channel i, the plasma resistance R_d can be given by $R_d = V_d / \sum_i j_i A_i$.

Since the duration of the discharge pulse is much shorter than the thermal relaxation time of gas, there is no depopulation and no formation of shock waves during the discharge. The gas temperature T_i in the channel i can be calculated using the following formula:

$$\partial (\rho C_v T_i)/\partial t = E_i j_i, \tag{1}$$

where ρ and C_v are the gas density and the specific heat at constant volume, respectively.

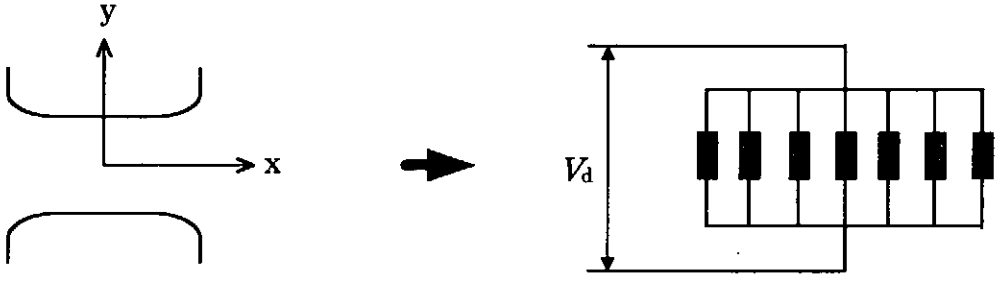

Fig. 1. Schematics showing parallel resistor analogy for gas discharges. Optical axis is perpendicular to the x-y plane.

3. Description of Fluid Model

Two-dimensional compressible gas dynamic equations have been used, which can be written in conservation-law form as

$$\frac{\partial U}{\partial t} + \frac{\partial F}{\partial x} + \frac{\partial G}{\partial y} = 0, \tag{2}$$

where

$$\boldsymbol{U}=\begin{pmatrix}\rho\\ \rho u\\ \rho v\\ E_s\end{pmatrix},\qquad \boldsymbol{F}=\begin{pmatrix}\rho u\\ \rho u^2+p\\ \rho uv\\ (E_s+p)u\end{pmatrix},\qquad \boldsymbol{G}=\begin{pmatrix}\rho v\\ \rho uv\\ \rho v^2+p\\ (E_s+p)v\end{pmatrix},\qquad E_s=\frac{p}{\gamma-1}+\rho\left(u^2+v^2\right)/2.$$

Here, ρ, u, v, E_s, p, and t are the mass density, x-direction velocity, y-direction velocity, total energy, static pressure, and time, respectively.

Equation (2) can be transformed into the generalized coordinates ξ and η as:

$$\frac{\partial \hat{\boldsymbol{U}}}{\partial t}+\frac{\partial \hat{\boldsymbol{F}}}{\partial \xi}+\frac{\partial \hat{\boldsymbol{G}}}{\partial \eta}=0, \tag{3}$$

where

$$\hat{\boldsymbol{U}}=J^{-1}\boldsymbol{U},\quad \hat{\boldsymbol{F}}=J^{-1}(\xi_x\boldsymbol{F}+\xi_y\boldsymbol{G}),\quad \hat{\boldsymbol{G}}=J^{-1}(\eta_x\boldsymbol{F}+\eta_y\boldsymbol{G}),$$

$$J=\xi_x\eta_y-\xi_y\eta_x,\quad \xi_x=Jy_\eta,\quad \eta_x=-Jy_\xi,\quad \xi_y=-Jx_\eta,\quad \eta_y=Jx_\xi.$$

Equation (3) has been solved using the Harten-Yee TVD (Total Variation Diminishing) scheme.[7] The initial temperature profile is determined from the discharge model. The initial velocities are zero in the present study. The initial density ρ is the same as that before the discharge. In order to describe the wave #2, we should know the ratio of the energy density in the sheath to that in the plasma. Different values of this ratio have been used for numerical calculations.

4. Results and Discussions

The gas temperature profile for the Chang-type electrodes has been obtained using the discharge model and taking into account the nonuniformity in electric field. The dependence of the temperature profile on the electric field distribution and gas mixture has been investigated. The shock waves and flowfields have been calculated using CFD method and the temperature profile obtained from the discharge model.

4.1. Gas temperature profiles

Figure 2 shows the gas temperature profiles at 80 ns, 90 ns, 100 ns, 115 ns, and 200 ns, respectively. The gas mixture is He/Ne/Xe/HCl = 31.9% / 66.9% / 1.0% / 0.2% at a total pressure of 294.2 kPa. Chang parameter k[6] is 0.10. There is little change in the temperature profiles after 115 ns.

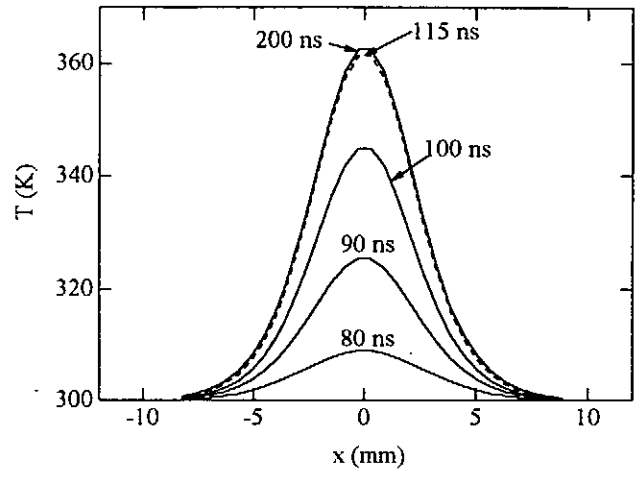

Fig. 2. Gas temperature profiles at different time. Gas mixture is He/Ne/Xe/HCl = 31.9% / 66.9% / 1.0% / 0.2% at total pressure of 294.2 kPa. k (Chang parameter[6]) = 0.10.

Figure 3 shows the effects of electric field distribution on the temperature profile. The electric field distribution is characterized by the Chang parameter k. The larger the parameter k, the stronger the nonuniformity in the electric field. The total deposition energies in both cases are approximately the same, whereas the temperature profiles are quite different. As the parameter k increases, the peak temperature increases and the discharge width decreases.

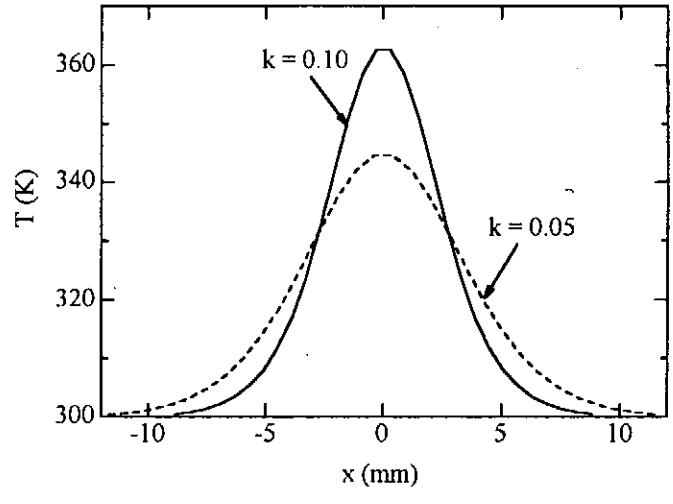

Fig. 3. Gas temperature profiles at 200 ns for different electrodes. Gas mixture is the same as that in Fig. 2. k = 0.10 and 0.05 for solid and dashed curves, respectively.

From Eq. (1), we see that the rate of change in the gas temperature depends on the electric power density which is proportional to the electron density. With the definition of the normalized electric field as $f(x) = E(x) / E(0)$, the profile of the normalized electron density $n_e(x) / n_e(0)$ could be expressed as $f^{\alpha}(x)$ with $\alpha >> 1$.[8] Therefore, the gas temperature profile is sensitive to the nonuniformity in the electric field.

Figure 4 shows the effects of xenon on the temperature profile. As the fraction of xenon increases from 1% to 5%, the total deposition energy increases by 7%. The peak temperature rise increases by 43% and the discharge width decreases. In other words, the temperature profile tends to be steeper at a higher xenon concentration. Furthermore, as the fraction of xenon increases from 1% to 5%, the maximum value of the electron density increases by 66%. Since the peak electron density depends on the ratio of Xe to HCl,[9] the increase in Xe leads to the increase in the electron density.

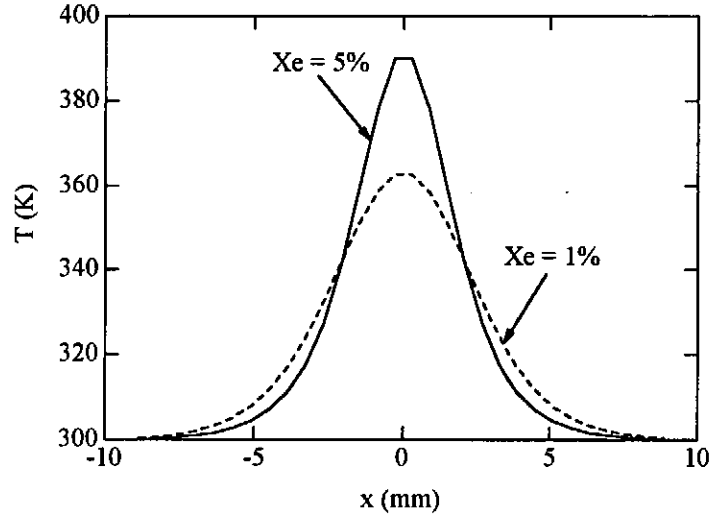

Fig. 4. Gas temperature profiles at 200 ns for different xenon concentrations. Gas mixture for dashed curve is the same as that in Fig. 2. Gas mixture for solid curve is He/Ne/Xe/HCl = 30.6% / 64.2% / 5.0% / 0.2% at total pressure of 294.2 kPa. $k = 0.10$.

4.2. Shock waves and unsteady flowfields

The shock waves and flowfields in the main discharge region have been calculated using the fluid model as described in Sec. 3. Different gas temperature profiles have been used as the initial conditions. The numerical results presented below correspond to the temperature

profile in Fig. 4 for the fraction of xenon of 5%. The ratio of the energy density in the sheath to that in the plasma is assumed to be 3. The sheath thickness is assumed to be 0.1 mm. The discharge region is transformed into a rectangular computational domain which is divided by 404 × 204 uniform grids. Because of symmetry, only quarter of the discharge region is calculated.

Figures 5(a)-5(b) show the pressure contours at 15 μs and 25 μs, respectively. The dense contours show the waves #1 and #2 which move in the x and y directions, respectively. The propagation and interaction of these waves are readily identified.

Figure 6 shows the three-dimensional plot of the pressure at 15 μs. It is seen that the pressure increases across the shock fronts and is highest at the intersection points of the waves #1 and #2.

Figure 7 shows the three-dimensional plot of the density at 15 μs, which is low near the electrode surfaces and in the central discharge region due to the expansion of the heated gas.

5. Conclusions

The gas temperature profile in a discharge-pumped XeCl excimer laser has been calculated using a self-consistent discharge model. The temperature profile tends to be steeper at a higher xenon concentration and when the nonuniformity in electric field becomes stronger. Furthermore, the shock waves and unsteady flowfields in the main discharge region have been numerically studied using two-dimensional compressible gas dynamic equations and TVD scheme. The initial temperature profile for the gas dynamic simulations is obtained from the discharge model. The numerical results clearly show the propagation and interaction of the waves #1 and 2. The gas density is low in the central discharge region and near the electrode surfaces, which in turn causes a deterioration of discharge homogeneity and induces arc transitions in high-repetition-rate excimer lasers.

Acknowledgment

We would like to thank Dr. M. Hishida in Department of Mechanical Engineering at Nagaoka University of Technology for providing the TVD program.

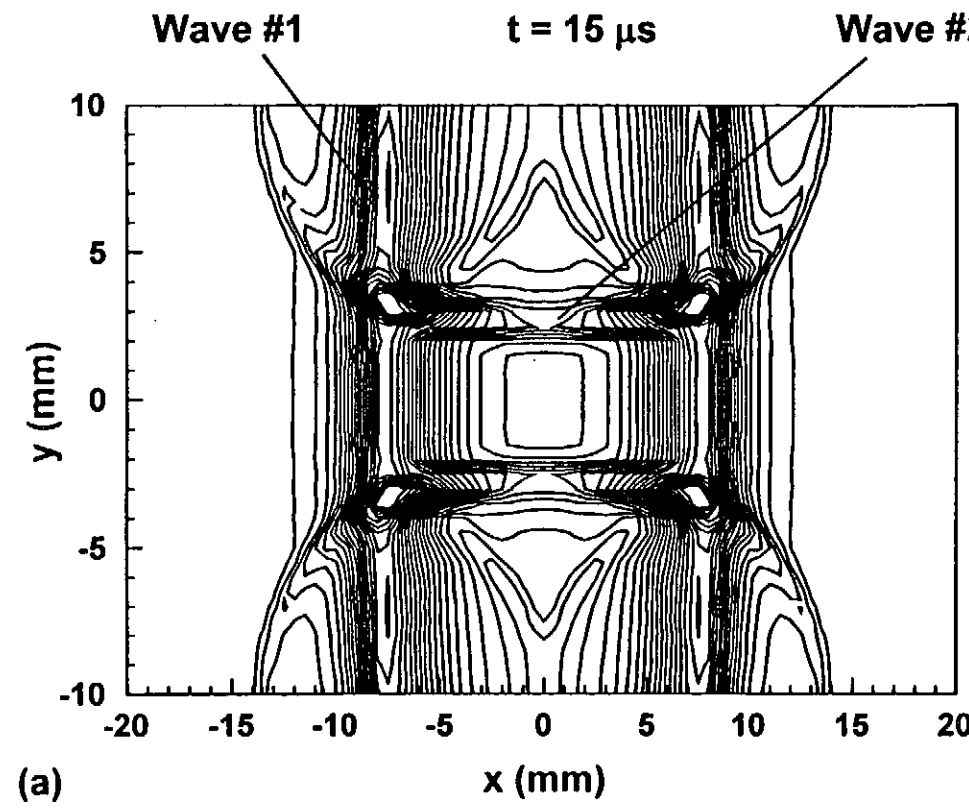

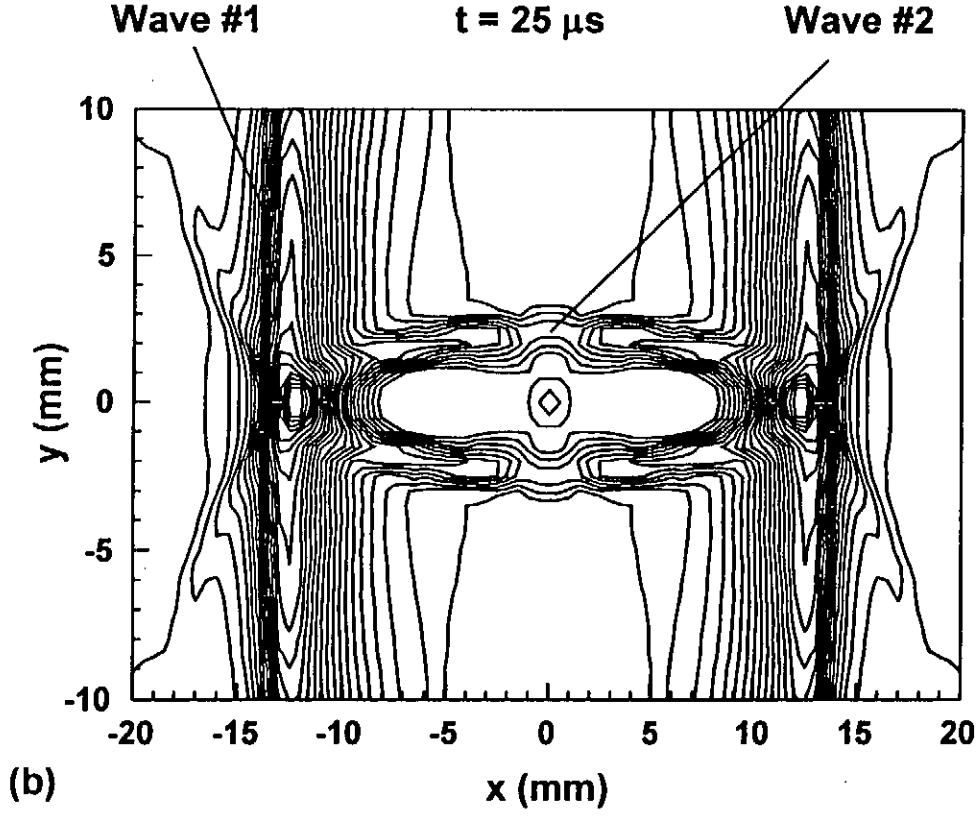

Fig. 5. Pressure contours at (a) 15 μs and (b) 25 μs. Initial gas temperature profile is the same as that in Fig. 4 for the fraction of Xe of 5%.

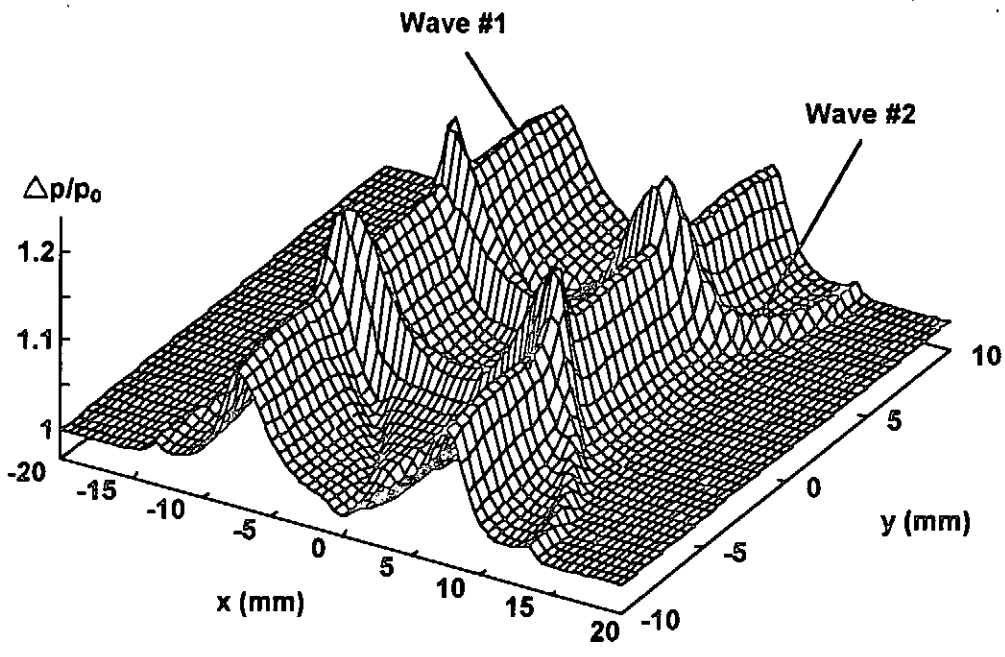

Fig. 6. Three-dimensional plot of pressure at 15 μs. Same condition as that in Fig. 5.

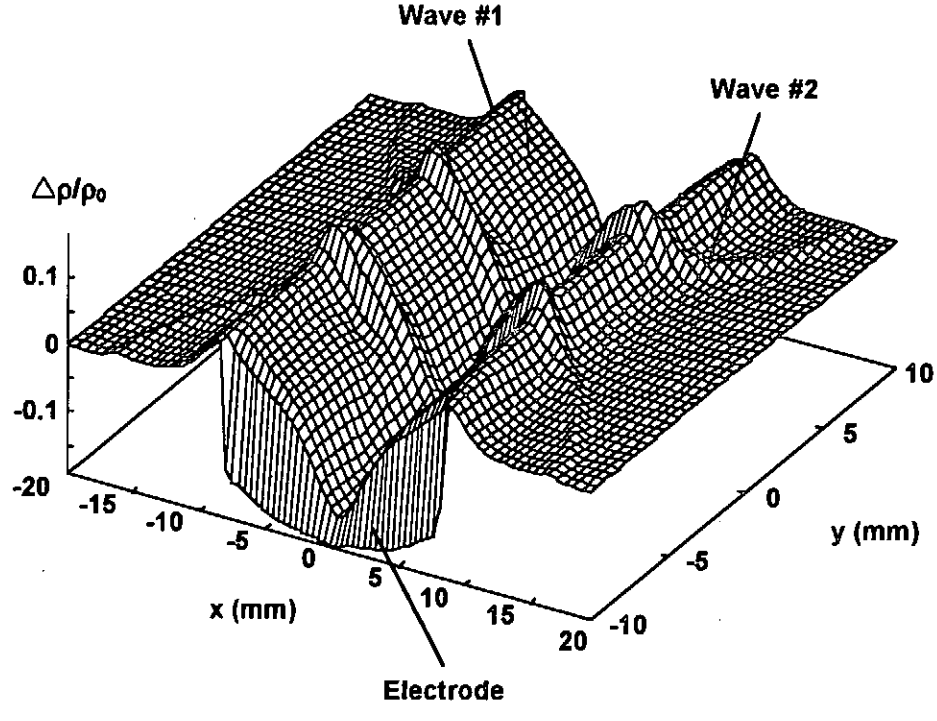

Fig. 7. Three-dimensional plot of density at 15 μs. Same condition as that in Fig. 5.

References

1) K. Yatsui, Y. Joudai, G. Imada, K. Masugata and W. Masuda: Proc. SPIE **2502** (1994) 134.

2) G. Imada: Dr. Thesis, Nagaoka University of Technology (1994) (in Japanese).

3) Q. Zhu, G. Imada, W. Masuda and K. Yatsui: Phys. Plasmas **3** (1996) 2813.

4) Q. Zhu, G. Imada, W. Masuda and K. Yatsui: Phys. Plasmas **3** (1996) 4225.

5) M. J. Kushner, A. L. Pindroh, C. H. Fisher, T. A. Znotins and J. J. Ewing: J. Appl. Phys. **57** (1985) 2406.

6) T. Y. Chang: Rev. Sci. Instrum. **44** (1973) 405.

7) H. Yee: J. Comp. Phys. **68** (1987) 151.

8) A. B. Treshchalov and V. E. Peet: IEEE J. Quantum Electron. **QE-24** (1988) 169.

9) M. Ohwa and M. Obara: J. Appl. Phys. **59** (1986) 32.

Angular Distribution of Soft X-Ray Radiation by a Plasma Focus with High Z Gas Puff

Hiroyuki Kitaoka, Toshikazu Yamamoto, Morihiko Sato,
Katsuji Shimoda and Katsumi Hirano
Department of Electronic Engineering
Gunma University

Abstract

To develop an intense soft x-ray source for the microlithography and x-ray microscope, a puffed high Z gas is imploded by a pinched plasma produced with a plasma focus device. A photographic film, Tri-X is tried as recording medium for the soft x-ray and successfully used. Depending on the delay time between the puffing of the high Z gas and main discharge, the generated soft x-ray source is divided into two categories, namely filamentary and scattered spot sources. The soft x-ray intensity of the filamentary source is much higher than that of the scattered spot sources. It is observed that the delay time should be adjusted to generate the filamentary x-ray source in the pinched plasma and outputted from the axial direction for the microlithography and the x-ray microscope in spite of absorption by the x-ray emitting plasma.

1. Introduction

Soft x-ray sources with high brightness are required for many purposes such as x-ray spectroscopy, high density lithography for the manufacture of electronic devices, x-ray microscopy and x-ray laser pumping. Suitable soft x-ray source can be provided in the high energy density plasma by the Z-pinch and the plasma focus.

In the pinch plasma experiment, the soft x-ray emission comes from very small regions known as the hot spots or micropinches when high Z materials are added to hydrogen or deuterium which are normally employed in the Z-pinch gas filled mode.[1-4]

The strong collapse occurs in a narrow region of the ratio of added gas to the initial pressure of the admixture. In the gas-filled mode moreover, the soft x-ray sources generated in the pinched plasma are typically divided into three categories by their shapes.[5] They are filamentary, scattered spot and mixture both of spots and filaments, in spite of the identical experiment condition. In the previous paper, a high Z gas to generate the soft x-rays was injected with a fast acting valve through the inner electrode to the pinch region immediately before each discharge. This makes possible to decouple the initial phase, that is, the current sheath formation and the final phase for pinch formation. The soft x-ray intensity by the plasma focus device with high Z gas puffing is more than one

order higher than that of the gas embedded mode with additional high Z gas.[6]

However, it is found that there is much difference in soft x-ray intensity and the shape of the source depending on the delay time which is interval between the opening of the fast acting valve and high current discharge for the plasma focus.

For the microlithography and x-ray microscopy it is desired that the x-ray source of small size is generated at a fixed location from shot to shot. It is expected that the intensity of the soft x-ray in the axial direction was higher than that in the radial direction when absorption of the soft x-ray in the pinched plasma is negligible. However, the plasma may be optically thick in the axial direction for pinch formation phase.

In this paper, the opacity of the plasma and angular distribution of the soft x-ray emission is examined in the axial and radial direction. A photographic film Kodak Tri-X is examined as a recording medium for the soft x-ray. The angular distribution of the soft x-ray emission was observed by the soft x-ray pinhole cameras with an MCP and a photographic film, Kodak Tri-X. The pinhole cameras enabled to make a quantitative measurement of the soft x-ray intensity.

2. Apparatus

2.1 Plasma focus device

A Mather type plasma focus device with a squirrel cage outer electrode was employed to produce a high energy density plasma. A cross sectional view of plasma focus device is shown in Fig. 1. The diameters of coaxial electrodes are 50 and 100 mm, respectively. The length of the outer- and the inner electrode were 230 and 280 mm, respectively. The condenser bank consisted of 28 $\times$ 1.56 μF, 80 kV capacitors. The device was operated at the bank voltage of 45 kV in this experiment.

Argon was puffed with a fast acting valve through the inner electrode immediate before each discharge. The hydrogen base pressure of 5.5 Torr and the argon plenum pressure of 3 atm were employed.

2.2 Diagnostic Tools

The alignment of the diagnostic tools is shown in Fig. 1. A soft x-ray pinhole camera with a quantitative image acquisition system has been developed for soft x-ray image observation with time resolution. A pinhole image of the x-ray source is made on the MCP through a pinhole and Be-Ag combination foil filter (25 μm and 1 μm in thickness, respectively) which prevent the visible light also emitted from the source. The spectral

response of the MCP system is described in the previous paper.[7] The combination of the filters and MCP gives a pass band between 3.7 and 7 Å, which accepts Ar K-lines (~4Å). Using the system we can evaluate a number of photons which pass through the pinhole after taking absorption by the metal foil into account. In this experiment the system is fixed in the radial direction.

The soft x-ray images were also recorded with two pinhole cameras, in which a photographic film, Kodak Tri-X, with a set of filters (25 μm Be and 1 μm Ag) were employed in the axial and the radial direction. Arrangement of the pinhole camera are also shown in Fig. 1. The Tri-X film is sensitive to the soft x-rays and used in He 1atm to avoid absorption of the soft x-rays. The blackening on the Tri-X by exposure of the soft x-ray can be restructured using an image which is simultaneously taken with a sensor of linear sensitivity like the MCP. In order to calibrate intensity of the soft x-ray on the Tri-X film, the image was quantitatively compared with that of the soft x-ray pinhole camera system in which the MCP is installed. Relationship between the emitted photon number and the blackening of Tri-X is shown in Fig. 2. The soft x-ray images on the film were registered in a computer memory in 8 bits by a scanner.

The soft x-rays were monitored with a x-ray PIN diode, which also coupled with a set of filters (25 μm Be and 1 μm Ag), in the radial direction.

3. Experimental results

It was found that the soft x-ray source generated in the plasma focus discharge typically divided into two categories which are filamentary- and spotted sources depending mainly on the delay time between gas puffing and main discharge. When the delay time was shorter than 6 ms, neither the filaments nor spots were observed in the pinched plasma. When the delay time was between 6 and 7 ms, the soft x-ray sources were mostly filamentary. For delay time longer than 7 ms, on the other hand a series of spot-like sources which are aligned roughly along the electrode axis were observed. No soft x-ray sources generated, when the gas was puffed with the valve facing the base of the electrode.

Figure 3(a) shows an example for a filamentary soft x-ray source. We processed Fig. 3(a) using the relationship between x-ray intensity and the blackening of Tri-X shown in Fig. 2. The result is illustrated in Fig. 3(b). This is compared favorably with the image taken with the pinhole camera in which the MCP is installed. It is therefore concluded that Tri-X film can be used as a recording medium of the soft x-rays. Discrepancy in details of between the images come considered occuring from the difference of their spectral response.

Typical examples of the spatial distribution of the soft x-ray sources are shown in Fig. 4. Those are taken by Tri-X film and processed by the method mentioned above and

then displayed in contour plots. In Fig. 4(a)A, three filamentary sources are seen. Figure 4(b)A shows the example that there are more than ten scattered spots appear along the electrode axis. The monitor signals obtained by the filtered x-ray diode show that the emission duration are different between the filamentary- and the spot-like sources. It is obvious that overall emission from the filamentary source is much higher than that of spot-like sources as recognized in Figs. 4(a)A and 4(b)A. This agreed with the measurement by the diode. In the end on image of the source blackening of the former is also conspicuous than that of the latter as shown in Figs. 4(a)B and 4(b)B.

We calculated the spatial distribution of the emission intensity in the direction of the electrode axis using the side on image shown in Figs. 4(a)A and 4(b)A. The calculation was carried out on the assumption that the any part in the source emits the soft x-rays and point-symmetrically. Results for the filamentary source is shown in Fig. 5(a)A. On the other hand, the spatial distribution of the emission which is obtained from the end on image is displayed in Fig. 5(a)B. Absorption of the emission which is to be suffered by the plasma and neutral gases between the source and film is shown in Fig. 5.

For the spot-like x-ray sources, distributions between the calculated and the experimental results are obtained as shown in Figs. 5(b)A and 5(b)B. Figures 5(a)B and 5(b)B are quite simulare in their intensity. This fact shows that the absorption occurs not only in the x-ray emitting plasma, but in the puffed Ar and also in the pinched plasma which does not emit the x-rays.

Stormberg et al [8] made a simulation for angular distribution of the soft x-ray emission in a pinched plasma solving the radiation transfer equation. Their results show that the average intensity of the x-rays in radial direction is rather higher than that of the axial direction for the resonance line Ar^{16+} $^1P_1(1s2p)$.

Our experimental results show that absorption is remarkable. This is ascribed to absorption of the resonance line in the axial direction. Ar^{16+} ions are exited by the resonance line, then reemit the soft x-rays of the same wave length isotropically.

This is considered that Ar k-lines are mainly absorbed. It is desirable that the x-ray source has smaller size for the microlithography and x-ray microscope. Therefore, it is concluded that the operation condition of the plasma focus device should be adjusted to generate the filamentary x-ray source in the pinched plasma, and the x-rays should be out-putted from the axial direction of the electrodes inspite of absorption by the x-ray emitting plasma.

References

1) P. S. Antsiferov, F. B. Rosmej, O. N. Rosmej, H. Schmidt, D. Schulz and A. Schulz: J. Appl. Phys. **77** (1995) 4973.

2) K. N. Koshelev, V. I. Krauz, N. G. Reshetniak, R. G. Salukvadze, Yu.V. Sidelnikov and E. Yu. Khautiev: J. Phys. D : Appl. Phys. **21** (1988) 1827.

3) I. V. Volobuev, V. A. Gribkov, D. Denus, N. V. Kalachev, T. A. Kozlova, O. N. Krokhin, S. Sledziński, S. A. Startsev and S. Czekaj: Sov. J. Plasma Phys. **14** (1988) 401.

4) J. M. Baylay, G. Decker, W. Kies, M. Mälzig, F. Müller, P. Röwekamp, J. Westheide and Y. V. Sidelinkov: J. Appl. Phys. **69** (1991) 613.

5) K. Hirano and H. Kitaoka : J. Phys. Soc. Jpn. **65** (1996) 139.

6) H. Kitaoka, A. Sakurai, T. Yamamoto, K. Shimoda and K. Hirano: J. Phys. Soc. Jpn. **64** (1995) 4191.

7) Y. Takahama, J. Du, T. Yanagidaira and K. Hirano: Rev. Sci. Instrum. **65** (1994) 2505.

8) H. P. Stormbeng, S. Murayama and Y. Watanabe: J. Appl. Phys. **62** (1987) 4090.

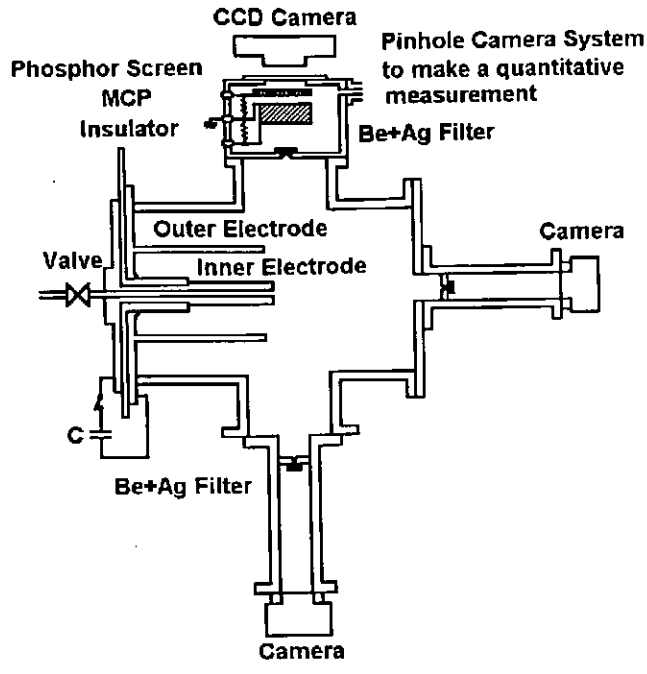

Fig. 1 Plasma focus device and alignment of diagnostic tools.

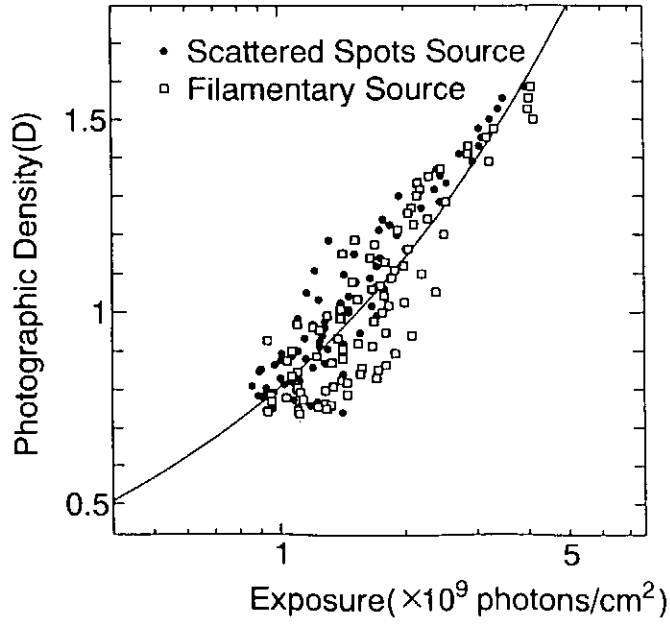

Fig. 2 Relationship between exposure photon number and blackening of Tri-X film.

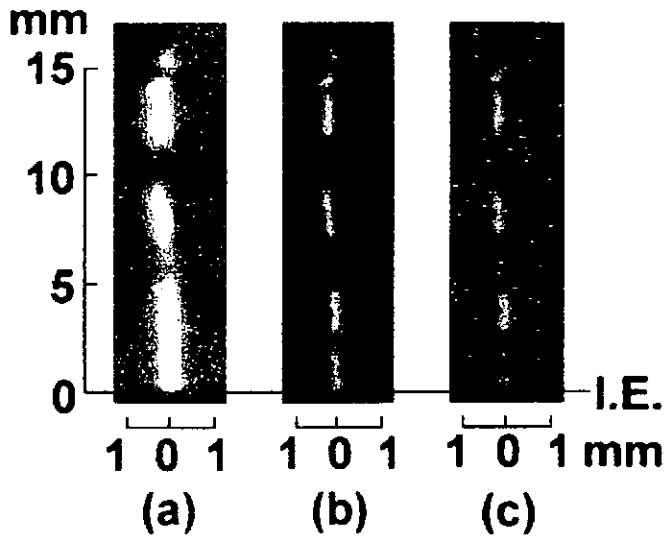

Fig. 3 Examples of the soft x-ray images. Soft x-ray image (a) taken by Tri-X film, (b) restructured using the relationship shown in Fig. 2 and (c) taken by the MCP.

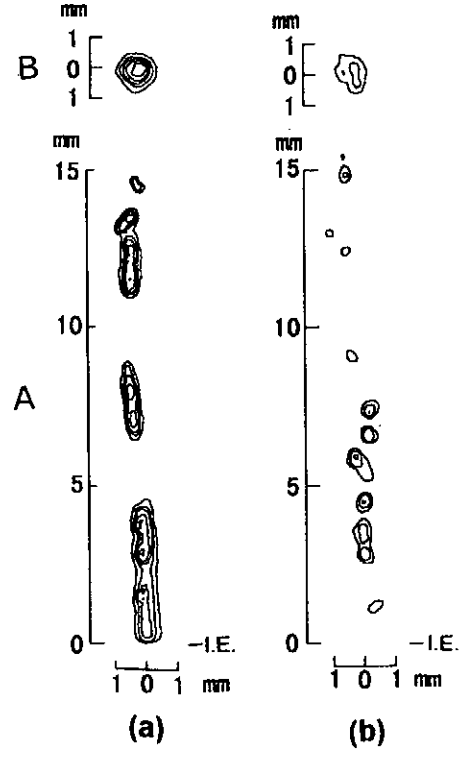

Fig. 4 Contour plots of the soft x-ray intensity corresponding 5.0×10^8 photons/mm^2 · mrad^2 · 1shot per contour line , in the axial (A) and the radial direction(B). (a) and (b) are the filamentary soft x-ray source and the spot-like sources, respectively.

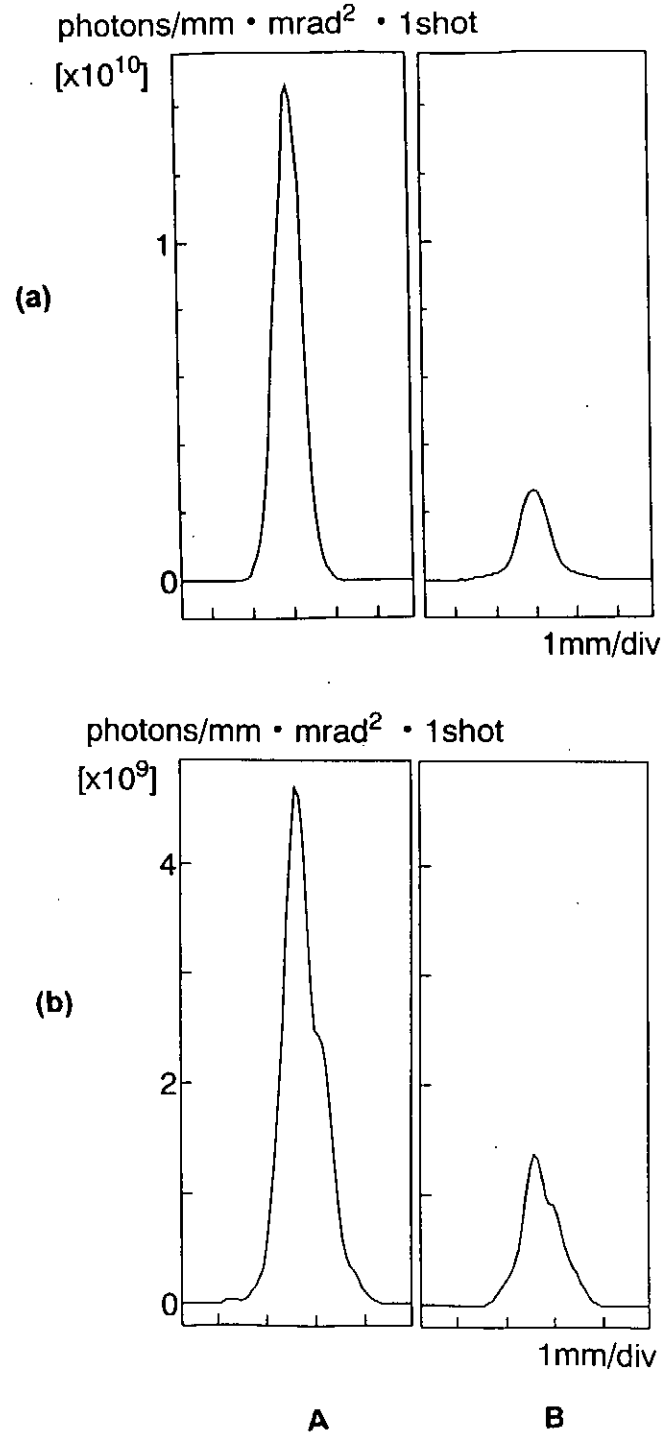

Fig. 5 Spatial distribution of the soft x-ray intensity of the filamentary source (a) and scattered spot sources (b) in the axial direction, (A) calculated from the side on image, (B) measured using the pinhole camera .

Soft X-Ray Microscopy by a Z-Pinch Soft X-Ray Source

Toshikazu Yamamoto, Morihiko Sato, Katsuji Shimoda and Katsumi Hirano
Department of Electronic Engineering, Gunma University

Abstract

A contact type soft X-ray microscope system, in which a plasma focus device with additional gas puff is employed, is developed. The system is examined in a biological sample, a fine whisker grown on the dragonfly's wing. The transcribed pattern on the photoresist is observed with an atomic force microscope (AFM). It is revealed that the spatial resolution of the system is sub-μm when Ar K-lines ($\sim$ 4 Å) as an X-ray source and PMMA are used as the photoresist. A pattern transcription on the photoresist with a single discharge was carried out also by using Ne gas puff.

1 Introduction

Intense sources of soft X-rays have received considerable interest in the field such as microlithography [1,2] and microscopy.[3–6] By use of soft X-rays, it is expected to obtain a higher resolution in these applications.

The Z-pinch plasma generates pulsed soft X-rays of nanosecond duration. It is, therefore, considered that the Z-pinch is useful for the soft X-ray microscope for live and moving specimens without blurring. Several authors have estimated the sensitivity of photoresist for the soft X-rays.[2] The photoresist for the soft X-rays is hardly obtained, and so we inevitably employ photoresist which is prepared for the exposure by the electron beam.

In this paper, we intend to discuss feasibility of Z-pinch soft X-ray source for X-ray microscopy of contact type. First of all, the spatial resolution of the exposure system is studied experimentally and a biological sample is examined in the soft X-ray microscopy.

2 Experimental

To obtain a high resolution for the lithography, quasi-monochromatic soft X-rays which mainly consists of Ar K-lines (3.944 $\sim$ 3.985 Å)[7] are provided in this experiment. In order to get a flash microscope image, soft X-rays emitted from ionized Ne were also used to expose in a single discharge. A Mather-type plasma focus device with a squirrel cage outer electrode was employed. The diameters of the inner and the outer electrodes were

50 and 100 mm. The lengths of the electrodes were 280 and 230 mm, respectively. The condenser bank consisted of 28 $\times$ 1.56 μF, 80 kV capacitors. The device was operated at the bank voltage of 45 kV and an embedded gas pressure of 5 Torr H_2. To obtain intense soft X-ray emission, additional argon or neon was puffed with a fast-acting valve through the inner electrode immediately before each discharge. When the bank was operated at 45 kV, the current in the plasma column was approximately 0.8 MA at its peak.

The schematic diagram of soft X-ray exposure system is shown in Fig. 1. The soft X-ray source in this experiment has a large ratio of the source length to the diameter, and so a longer penumbra of the mask is produced in the parallel direction to the electrode axis than that of the perpendicular direction. To reduce the penumbra, an aperture whose diameter is 2 mm is mounted at 120 mm from the electrode axis. This allows almost the same spatial resolution in the parallel direction to the electrode axis. A Be foil, 25 μm in thickness, and a combination of Myler (4 μm) and Al (1.5 μm) were used as a X-ray extraction windows for Ar K-lines and Ne soft X-rays, respectively. In Fig. 2 transmission curves of these filters are shown. In the experiment with Ne gas puff, taking into account the wavelength of soft X-rays and the transmission of the filter and the air layer, it is considered that a continuum radiation (8 $\sim$ 10.6 Å) may contribute to the exposure of PMMA. If we assumed that the same numbers of photons are emitted in the most intensive lines of Ar K-line and Ne K-line, the amount of photons included in the Ne continuum radiation which are irradiated to the resist are estimated to be approximately 20 times that of Ar K lines. This suggests that sufficient exposure to transcribe the contact image on the resist will be enable with a single discharge with Ne gas puff instead of several tens of discharges with Ar gas puff as shown in experimental results.

A positive type PMMA (polymethylmethacrylate) resist (OEBR-1000, Tokyo Ohka) was employed. This resist was orignally manufactured for the electron beam exposure. The sensitivity of the PMMA is presented as 50 μC/cm^2 for the electron beam. It is, however, known that the resists for the electron beam are also sensitive to the soft X-rays. The sensitivity of the PMMA is estimated to be 1800 mJ/cm^2 for the X-ray.[8] The resist was spin-coated on silicon wafer and prebaked at 170 °C for 20 minutes. The resist was mounted at a distance of 24 cm from the electrode axis. The gap between the resist and photomask is 30 μm. This brings $\sim$ 0.2μm as the spatial resolution. On the other hand, the spatial resolution caused by the diffraction is estimated to be $\sim$ 0.1μm. This means the spatial resolution is less than 0.3 μm in total. To evaluate the spatial resolution of the exposure system, a wedge-shaped photomask was used. The mask consisted of nets of 19 μm meshes and 6 μm in thickness (G1000HS, Oken) which are made of Cu. The wedge was formed to put 2 meshes with an inclined angle of 8.3°. The modulation transfer function (MTF) has been commonly used as a figure of merit for describing the spatial

resolution of optical systems. The $MTF, M(\nu)$ is defined as[9]

$$MTF \approx \frac{I(\nu)}{I(\nu)} \tag{1}$$

where ν is the spatial frequency. In this equation, $O(\nu)$ and $I(\nu)$ stand for the magnitude of Fourier transform of the cross-sectional shape in the mask and the etched resist.

We employed fine whiskers which grows on the dragonfly's wing as biological samples. The whisker is hollow and the end is as thin as the phase contrast microscope can not recognize.

A soft X-ray pinhole camera[10] with a quantitative image acquisition system was used to observe the soft X-ray source generated in the pinched plasma. A pinhole image of the X-ray source is made on the MCP through a pinhole and Be + Ag foil filters (25 μm and 1μm in thickness, respectively) which prevent the visible light also emitted from the source. The spectral response of the MCP system is described in a previous paper. [11] The combination of the filters and the MCP gives a pass band between 3.7 and 7 Å, which accepts Ar K-lines.

The soft X-rays were monitored with an X-ray PIN diode which was coupled with a set of filter (25 μm Be and 1 μm Ag). The view field of the diode was limited only to the plasma produced by the discharge using a collimator. The monitor allows to expose the photoresist up to the required dose by controlling the number of the discharge.

The etched resist was observed with an atomic force microscope (AFM, Nanoscope II, Digital Instruments)

3 Experimental results

The feature of the Ar K-line soft X-ray sources which are recorded with the pinhole camera are shown in Figs. 3 a) which are the soft X-ray images by a single discharge and b) overlapped by 80 discharges, respectively. These show that the position of the soft X-ray source is fairly reproducible from discharge to discharge. The average intensity of the soft X-rays at the photoresist by a single shot is 18 mJ/cm^2.

A mask image observed with the AFM is shown in Fig. 4 a). The picture was taken after development of 14 min. at 25°C. The depth made by etching was also measured with the AFM. A 3-D display of the etched resist (Fig. 4 a)) is shown in Fig. 4 b).

The MTF which is calculated using the etched depths along scanning lines shown in Fig. 4 b) is shown in Fig. 5. If we assume that the 60 % of the MTF is the upper limit of the spatial frequency to form the image, we obtain 735 lp/mm, approximately. This corresponds to the spatial resolution of 0.68 μm. However, it is obvious that the image of the wedge is recognized up to $\sim$ 0.3 μm in its width. According to the definition, the

spatial resolution is the minimum resolvable distance between two points. Therefore, the resolution should be ~ 0.3 μm in this exposure system.

A contact image of the whisker grown on a dragonfly's wing is demonstrated in Fig. 6 a). Soft X-ray dose exposed to form the image was 324 mJ/cm^2 which was achieved by 50 discharges of our plasma focus device. Four whiskers appear in this figure. The thicker images show that whisker are hollow. The cross-sectional view of the whisker which is observed with a optical microscope is shown in Fig. 6 b). On the other hand, it is obviously recognized that the diameter of the pointed end of the thinner whisker is estimated to be less than 0.3 μm. This means that the spatial resolution of the exposure system is ~ 0.3 μm in total.

Figure 7 shows the Cu mesh pattern which is transcribed by a single discharge with Ne gas puff. The MTF calculated from this pattern is shown in Fig. 8. If we assume that 60 % of the MTF is the upper limit of the spatial frequency to form the image, we obtain $\sim$ 3300 lp/mm. This correspond to the spatial resolution 0.15 μm.

In summary, a biological sample (a fine whisker of the dragonfly's wing) was successfully observed with a submicron spatial resolution using a soft X-ray microscope in which the X-ray was generated by a plasma focus device.

References

1) J. S. Pearlman, J. C. Riordan and A. C. Kolb: Radiat. Phys. Chem. **25** (1985) 709.

2) I. Okada, Y. Saitoh, S. Itabashi and H. Yoshihara: J. Vac. Sci. Technol. **B4** (1986) 243.

3) R. Feder, J. S. Pearlman, J. C. Riordan and J. L. Costa: J. Microscopy **135** (1984) 347.

4) R. Feder, V. Banton, D. Sayre, J. Costa, M. Baldini and B. Kim: Science **227** (1985) 63.

5) I. N. Weinberg and A. Fisher: Appl. Phys. Lett. **47** (1985) 1116.

6) I. N. Weinberg and A. Fisher: Nucl. Instrum. Methods **A242** (1986) 535.

7) H. Kitaoka, A. Sakurai, T. Yamamoto, K. Shimoda and K. Hirano: J. Phys. Soc. Jpn. **64** (1995) 4191.

8) J. Lingnau, R. Dammel and J. Theis: Solid State Technology (1989) 105.

9) M. Nakase and Y. Matsumoto: Jpn, J. Appl. Phys. **16** (1977) 2017.

10) Y. Takahama, J. Du, T. Yanagidaira and K. Hirano: Rev. Sci. Instrum. **65** (1994) 2505.

11) W. Parkes, R. Gott and K. A. Pounda: IEEE Trans. Nucl. Sci. **NS-17** (1970) 360.

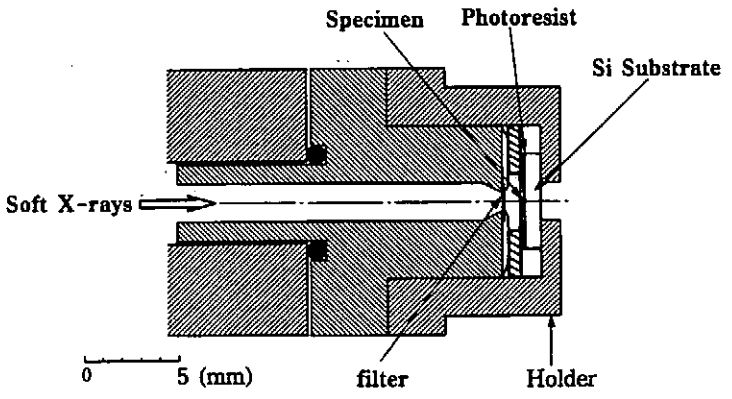

Fig. 1 Alignment of the sample and photoresist of the soft X-ray microscope.

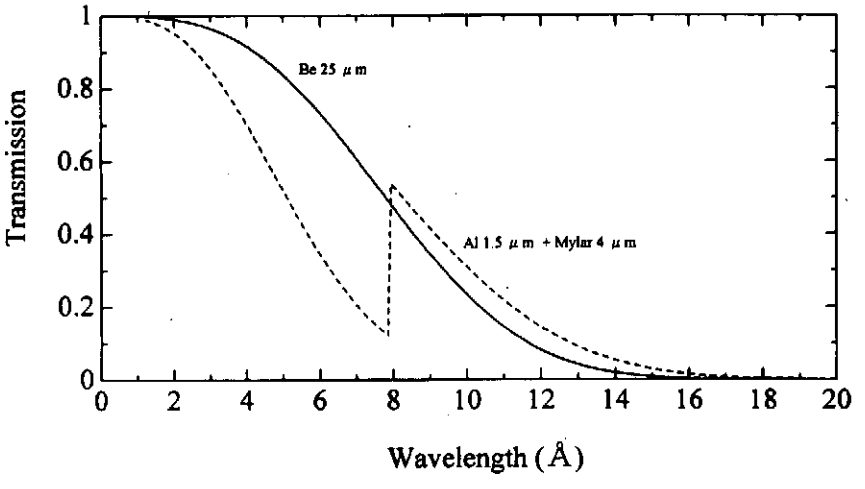

Fig. 2 Transmission curves of X-ray filters.

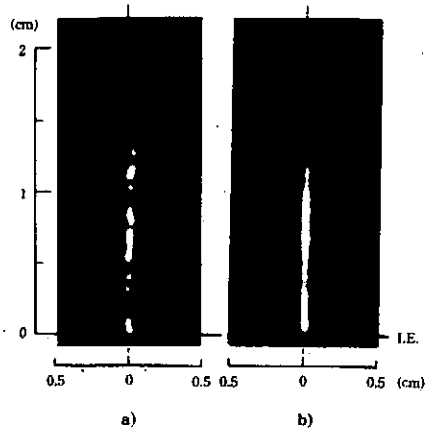

Fig. 3 Soft X-ray source generated in the pinched plasma.
a) a single discharge. b) Superposition of 80 discharges.
I.E. : inner electrode.

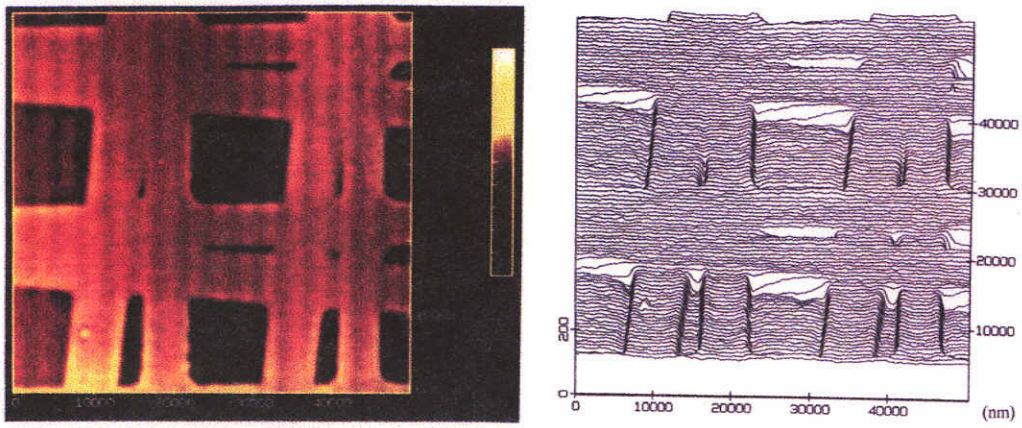

a) b)

Fig. 4 a) Contact image of two meshes inclined 8.3°. b) 3-D display of the the etched resist, Fig. 4 a).

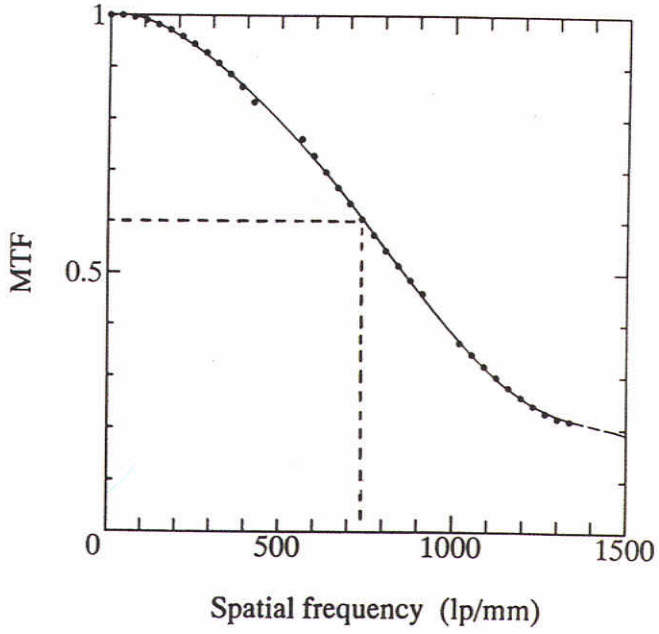

Fig. 5 Modulation transfer function of the soft X-ray microscope system.

a)

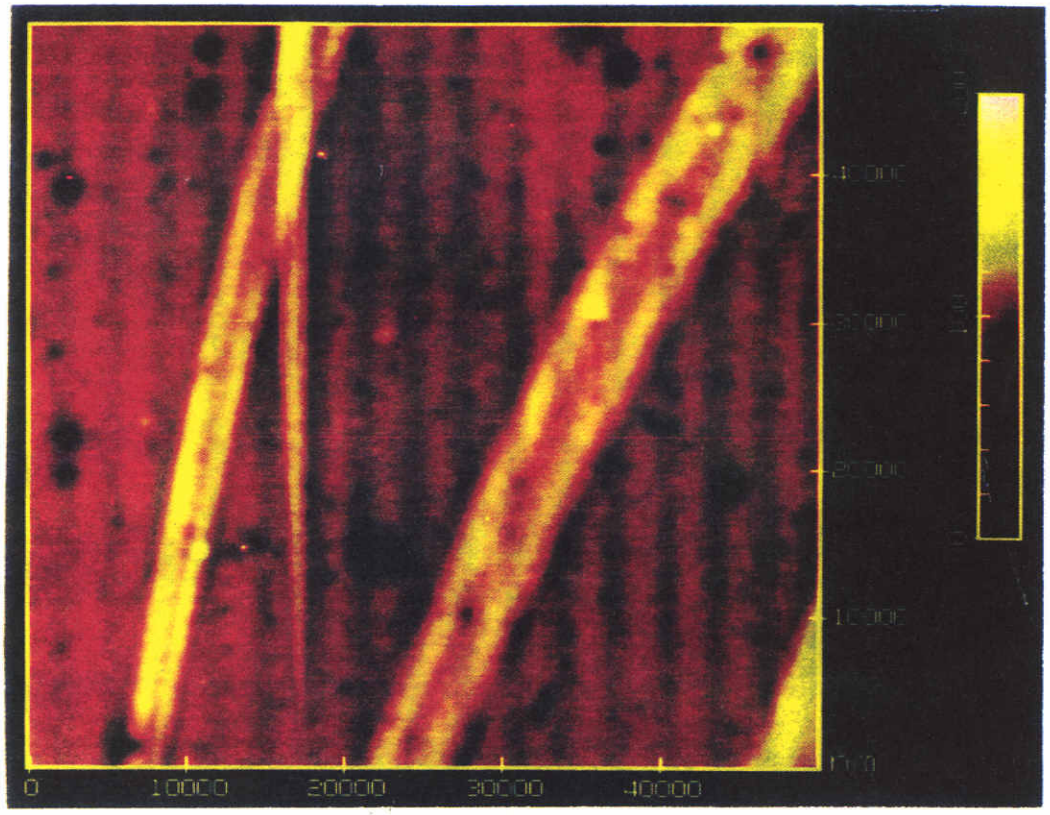

b)

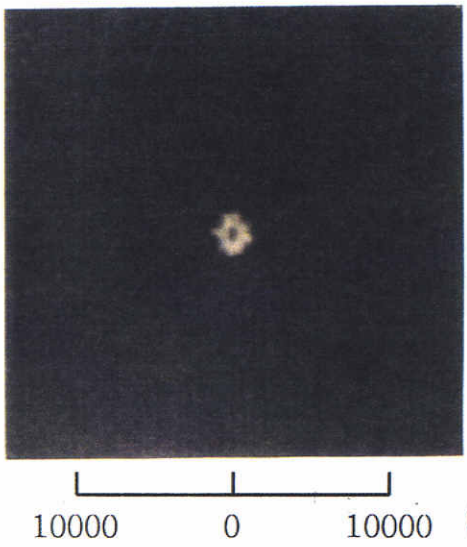

Fig. 6 a) Contact image of the whiskers grown on the dragonfly's wing observed with a soft X-ray microscope.

b) Cross-sectional view of the whisker by an optical microscope.

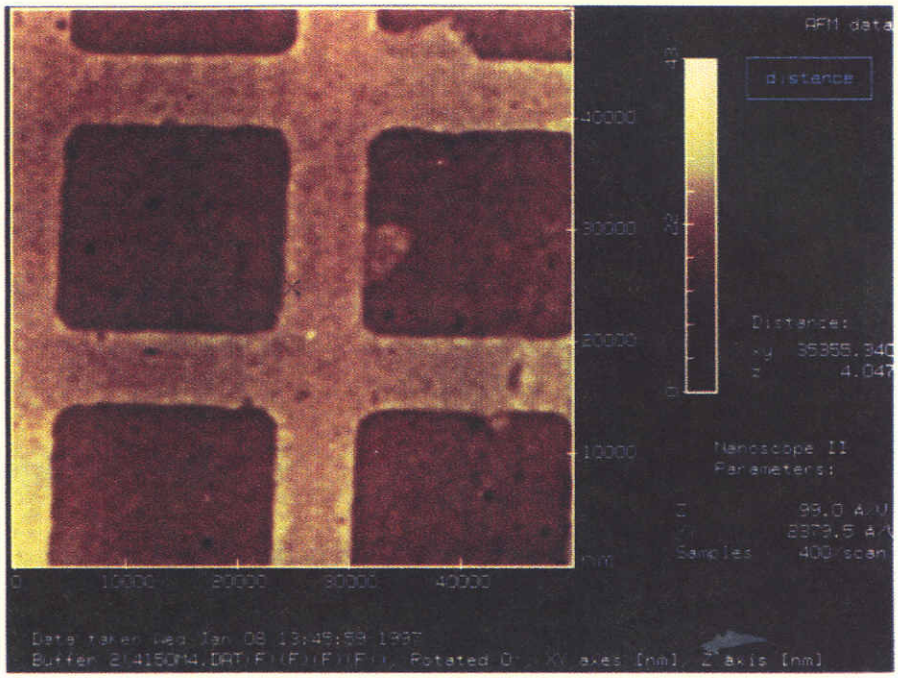

Fig. 7 Contact image of the Cu Mesh which is transcribed by a single discharge with Ne gas puff.

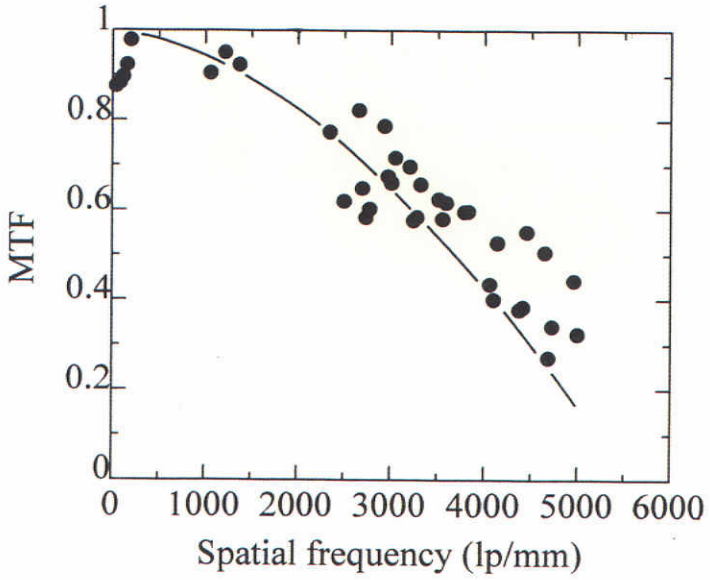

Fig. 8 Modulation transfer function obtained from Fig. 7.

Stabilization of Gas-puff Z-pinch and Control of X-ray Emission by Axial Magnetic Field

Katsuhiro Tatsumi,[+] Keiichi Takasugi,
Takehito Igusa[+] and Tetsu Miyamoto

Atomic Energy Research Institute, Nihon University

[+]*College of Science and Technology, Nihon University*

Abstract

This report describes a new approach to the control of x-ray emission from z-pinch plasma using externally applied axial magnetic field. Hard component of x-ray (due to K-shell radiation of Ar ions) was suppressed and soft x-ray (mostly from L-shell radiation) was intensified by the use of the axial magnetic field. Strong compression due to $m = 0$ mode instability was avoided, and the lifetime of the pinched plasma was extended.

I. Introduction

Hot spots of z-pinch plasmas are produced as the results of $m = 0$ mode instability, which is originated from non-uniform collapse of the z-pinch column.[1] Increasing the uniformity of the z-pinch will not always contribute to strong x-ray generation.[2] However, the uniform and long life x-ray source will expand its range of applications.

The application of axial magnetic field to z-pinch plasma have been examined to stabilize and sustain the plasma for the controled nuclear fusion research in the 1950's. This technique was used for pulsed high magnetic field generation[3] or creating a new magnetic configuration

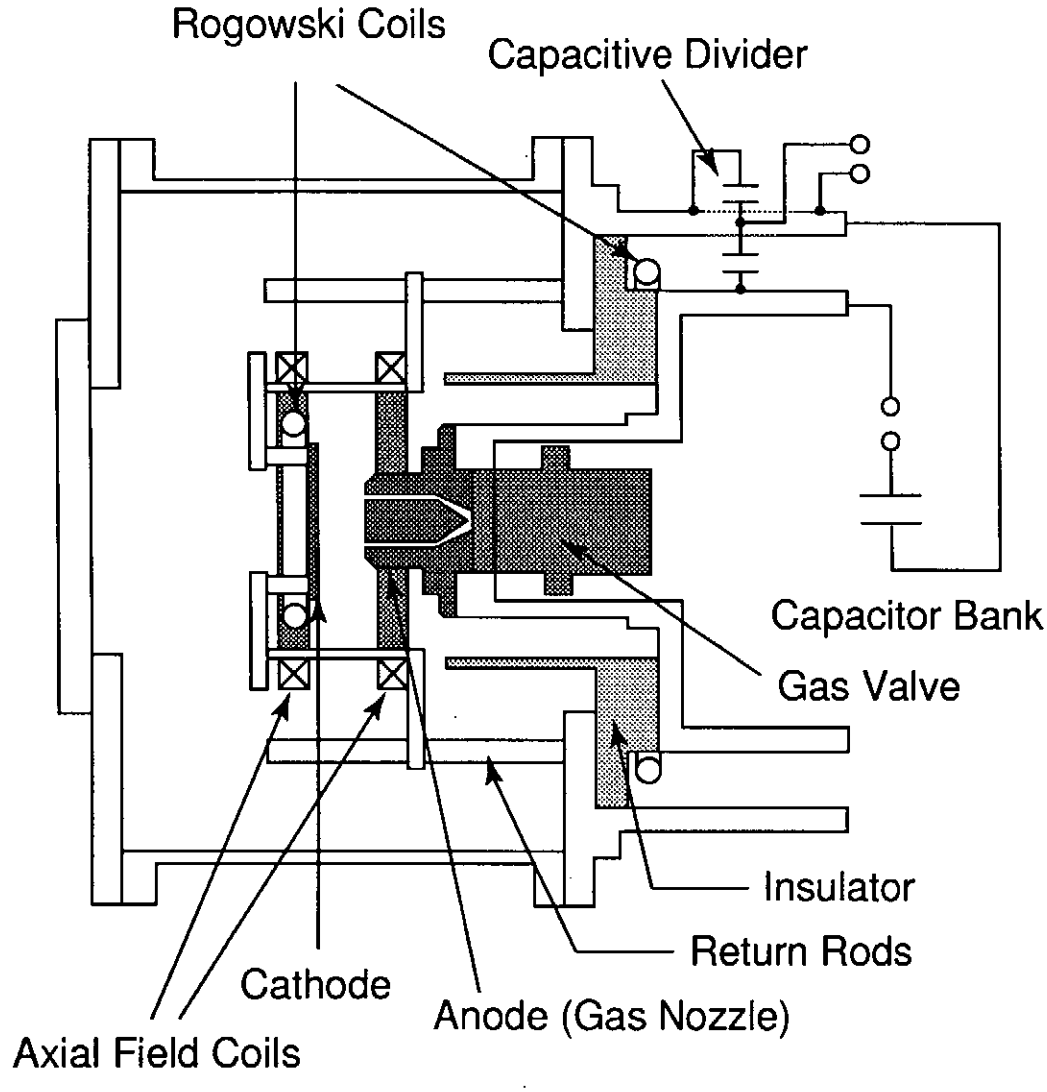

Fig. 1. Schematic view of the "SHOTGUN" z-pinch device.

for plasma confinement.[4] We applied the same technique to control the x-ray radiation from z-pinch plasma.

In Ar z-pinch the x-ray occurrs mostly in K-shell (0.3–0.4 nm) and L-shell (3–4 nm) radiations of ions.[5] The addition of axial magnetic field will control the extent of the maximum pinch, the temperature of the hot spots, hence the wavelength region of x-ray emission. The same technique was examined in a Marx generator machine, and enhancement of x-ray was observed.[6] This experiment is also intended to clarify the role of axial magnetic field on the dynamics of the plasma and the x-ray generation.

II. Experimental Setup

Figure 1 shows the schematic configuration of the gas-puff z-pinch device, "SHOTGUN". The storage capacitance is 24 μF, and the storage energy is 7.5 kJ at the charged voltage of 25 kV. The spacing of electrodes is 40 mm. Annular gas shell with the diameter of 28 mm is formed between the electrodes using a high speed gas valve. Ar gas is used thoughout the experiment.

Discharge current of the plasma is measured by a Rogowskii coil placed near the cathode. Discharge voltage is not directly measured in this experiment. A scintillation probe with Be 10 μm filter is used to detect hard x-ray from the pinched plasma ($\lambda < 1.2$ nm). A vacuum x-ray diode (XRD) with Ni photocathode is used to detect wide range of XUV to soft x-ray ($1.2 < \lambda < 105$ nm).

Axial magnetic field is produced by a pair of parallel coils placed near the electrodes. The radius and the separation of the coils are 8.7 cm and 7.0 cm, respectively, and the coil winding is 100. The magnetic field of 11.5 G is generated at the center of the coil at the coil current of 1 A. Figure 2 shows the radial and the axial distributions of the magnetic field produced by the coils. The field intensities are normalized at the center of the coils. Almost uniform magnetic field distribution is formed within the starting discharge volume ($r < 1.4$ cm and $z < 2.0$ cm).

The storage capacitance for the axial field coils is 1.6 mF, which is chargeable up to 2

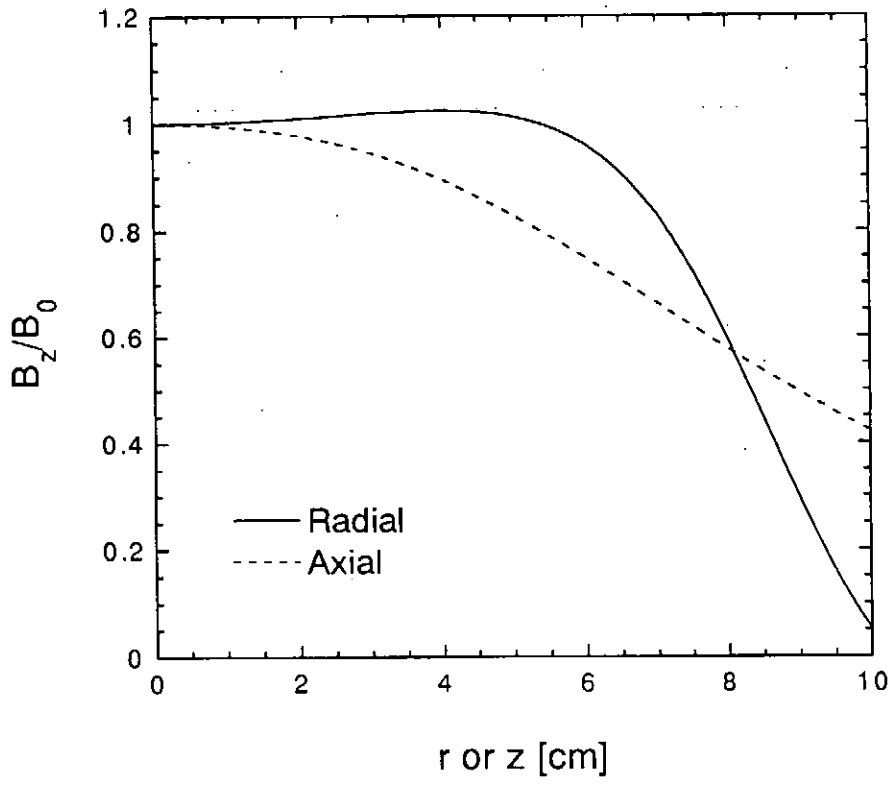

Fig. 2. Radial and axial distributions of the axial magnetic field.

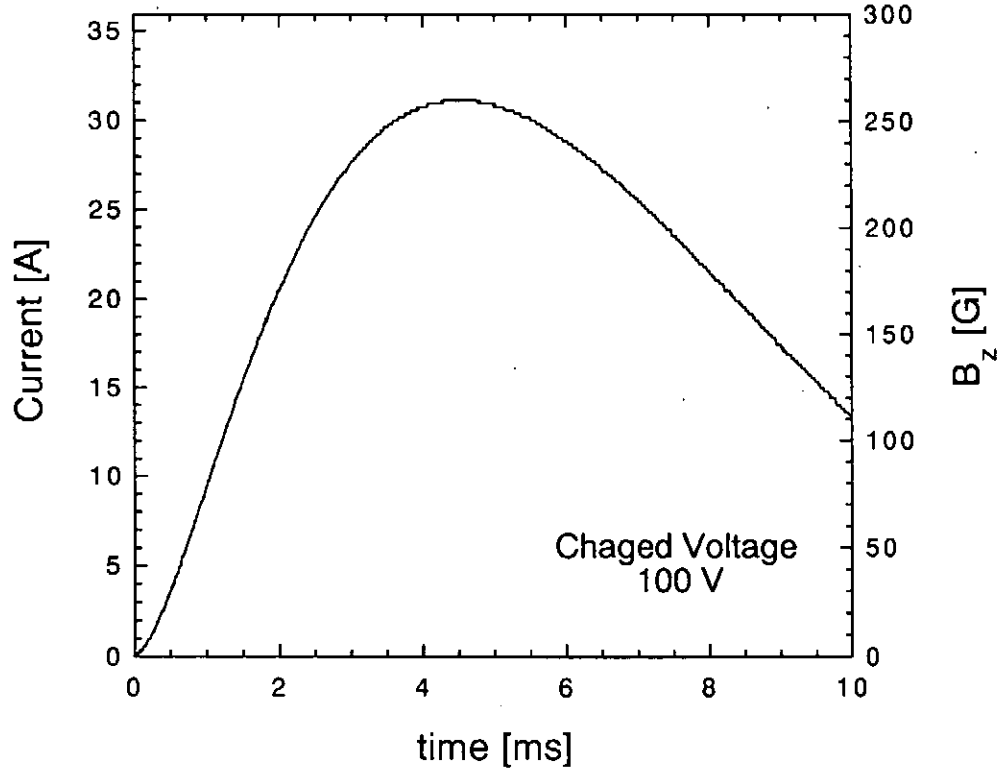

Fig. 3. Current and magnetic field of axial field coil.

kV. The current waveform of the coils is shown in Fig. 3 at the charged voltage of 100 V. The peak current of 31 A (the peak magnetic field of 260 G) is formed at 4.5 ms after the start of the current. The main discharge of the plasma is adjusted to occur at the peak field.

III. Experimental Results

Figure 4(a) shows typical discharge current, x-ray and XUV signals without axial magnetic field. Maximum pinch occurrs at about 1.5 μs after the discharge starting. The plasma current is about 200 kA. A dip is formed on the current signal, which shows a sudden increase of circuit inductance due to the maximum pinch of the plasma. Pulses of x-ray and XUV signals are observed coincident with the current dip.

When the axial magnetic field of 700 G is applied (Fig. 4(b)), the dip of the current becomes shallow and wide. The x-ray signal almost disappears. The XUV signal still exists, and the duration of the signal becomes longer than the case without the axial field.

The dependences of x-ray and XUV on the axial magnetic field intensity was investigated. Figure 5 shows the time-integrated signals of x-ray and XUV plotted as a function of the axial field. The x-ray signal rapidly decreases with the field and almost disappears above the field of 350 G. On the other hand the XUV signal increases almost linearly with the field. As the peak intensity of the XUV do not change much (as shown in Fig. 4), the duration of the XUV signal increases. This increase implies that the life time of the pinched plasma is extended by the axial magnetic field.

IV. Circuit Analysis

The change of circuit inductance can be estimated from the current signal by assuming a simple circuit model.[7] The capacitor voltage $V(t)$ is obtained by integrating the current $I(t)$.

$$V(t) = V_0 - \frac{1}{C}\int I(t)dt, \tag{1}$$

where V_0 is the charged voltage of the capacitor. Except only the onset of discharge the

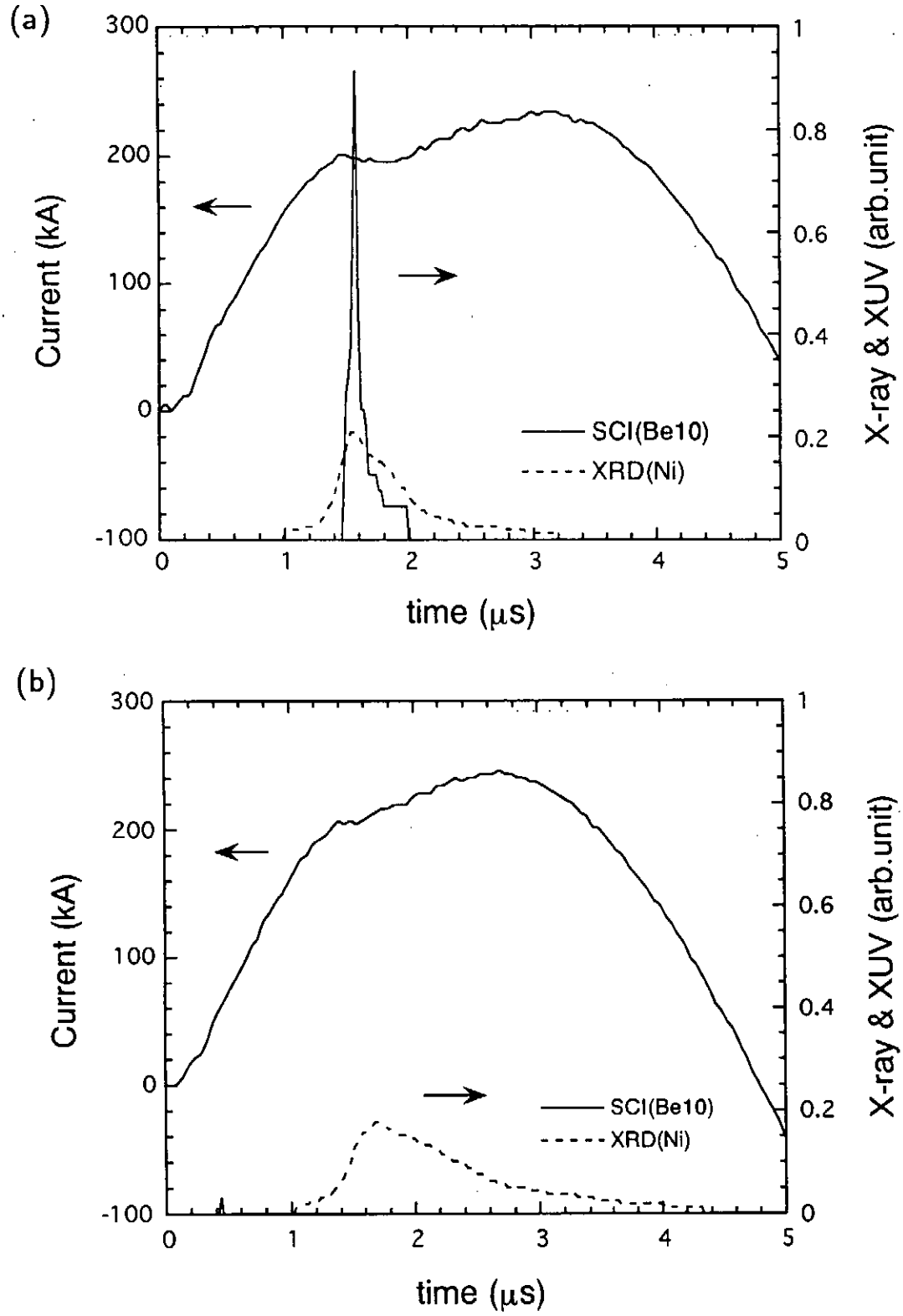

Fig. 4. Discharge current and x-ray radiation intensities (a) without and (b) with axial magnetic field (700 G).

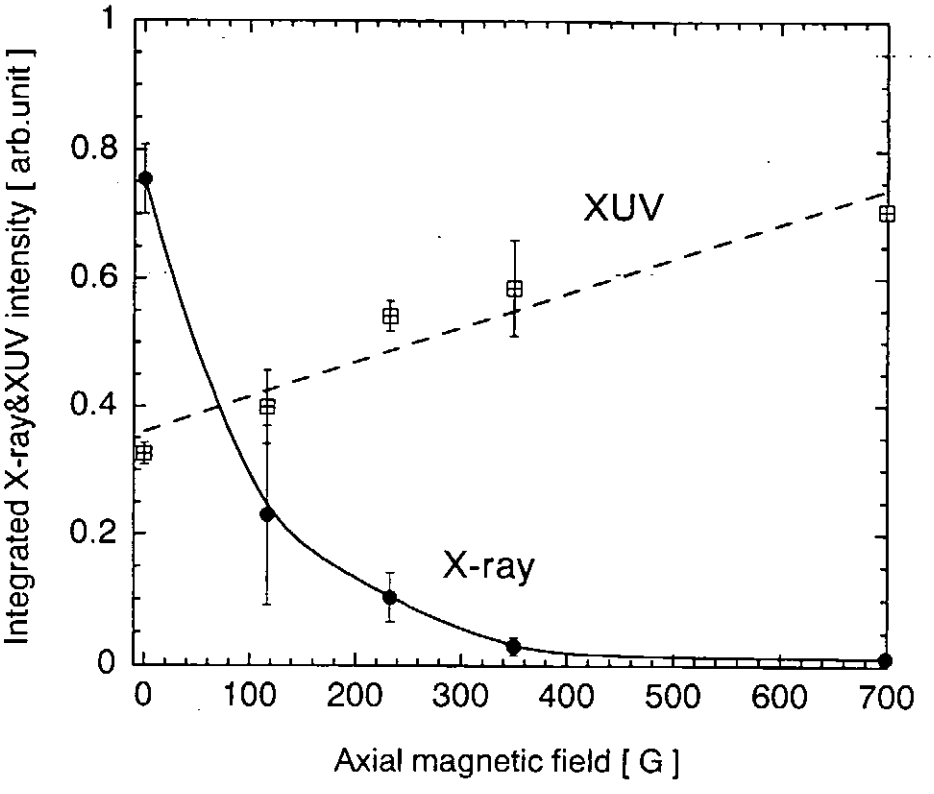

Fig. 5. Dependences of x-ray and XUV intensities on the axial field.

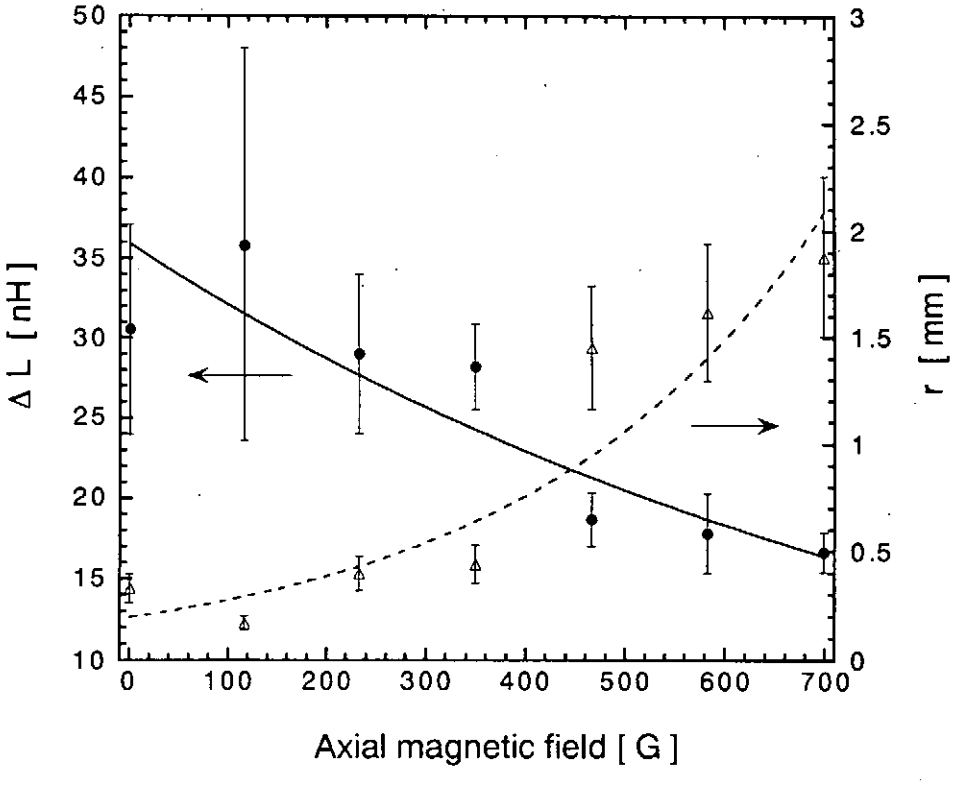

Fig. 6. The calculated inductance and average plasma radius.

plasma resistance is low, and it is neglected. The circuit equation is

$$V(t) = \frac{d}{dt}L(t)I(t) + RI(t), \tag{2}$$

where R is circuit resistance, and $L(t)$ is total inductance. Thus the inductance is

$$L(t) = \frac{1}{I(t)} \int (V(t) - RI(t))dt. \tag{3}$$

The change of inductance $\Delta L = L(t) - L_0$ occurrs only in the plasma. The parameter L_0 is the initial inductance. If the plasma current flows at the surface of cylindrical plasma, the change in the inductance ΔL is related to the characteristic plasma radius r,

$$r = r_0 \exp\left(-\frac{2\pi\Delta L}{\mu_0 l}\right), \tag{4}$$

where l is the length of plasma column.

The change of the inductance ΔL and the radius r are shown in Fig. 5 as a function of the axial magnetic field. The inductance ΔL decreases with the axial field and the radius r increases.

V. Summary

The axial magnetic field was applied to the gas-puff z-pinch plasma for stabilization of the plasma and for control of x-ray emission. The stabilization was not identified directly, however, x-ray (due to K-shell radiation of Ar ions) was suppressed and XUV and soft x-ray signal (mostly from L-shell radiation) was intensified by the axial field. The lifetime of the pinched plasma was extended by the axial magnetic field. Strong compression due to $m = 0$ mode instability was avoided and the average radius of the z-pinch increased with the axial field.

References

[1] K. Takasugi, T. Miyamoto, K. Moriyama and H. Suzuki: AIP Conf. Proc. **299**, 251 (1994).

[2] K. Takasugi, K. Moriyama, T. Shibuya and T. Miyamoto : Proc. 1996 Int. Conf. Plasma Physics Vol. 2, 1098 (1997).

[3] F.J. Wessel, F.S. Felber, N.C. Wild, H.U. Rahman, E. Ruden and A. Fisher: Appl. Phys. Lett. **48**, 1119 (1986).

[4] H.U. Rahman, P. Ney, F.J. Wessel and N. Rostoker: AIP Conf. Proc. **299**, 696 (1994).

[5] V.L. Kantsyrev, K. Takasugi, K. Tatsumi, T. Miyamoto and A.S. Shlyaptseva: Proc. 1996 Int. Conf. Plasma Physics Vol. 2, 1106 (1997).

[6] N.D. Edison, B. Etlicher, S. Attelan and C. Rouille: AIP Conf. Proc. **299**, 199 (1994).

[7] K. Takasugi, H. Suzuki, K. Moriyama and T. Miyamoto : Jpn. J. Appl. Phys. **35**, 4051 (1996).

The influence of absorption of own radiation on the steady state of fully ionized hydrogen Z-pinch.

Alexander Muravich, Tetsu Miyamoto, Keiichi Takasugi

§ 1. Introduction.

Recently, the interest to extremely dense Z-pinch plasma is increases relating with fusion research. So far steady states of Z-pinches have been investigated by many authors[1-5]. The steady state of an isolated Z-pinch, in which Joule heating is balances by bremsstrahlung radiation losses, is established only at the specific current (so called, Pease-Braginskii current)[1,2]. Thermal conduction in Z-pinch surrounding by gas was taken into account[3,4]. In the consideration of high temperatures it is reasonable to assume a radiation losses only as bremsstrahlung. The absorption is negligible for a conventional Z-pinch, however, it is not small in extremely dense Z-pinches. In this paper the steady state of Z-pinch is reexamined taking into consideration the absorption effect. We take the inverse bremsstrahlung as a mechanism of absorption. In § 2 we have considered absorption of own radiation in axially symmetric system, in § 3 we are writing one-fluid MHD equations of pinch equilibrium state and in § 4 we are unite results of § 2 and § 3 in order to obtain stationary state of z-pinch with uniform temperature.

§ 2. Absorption of own radiation in axially symmetric system.

If the matter is in the thermodynamic equilibrium, linear coefficient of absorption $\alpha(T,\nu,n)$ and radiation spectral power of matter $P_R(T,\nu,n)$, according to Plank-Kirhgof low, are related as follows:

$$\alpha(T,\nu,n) \equiv \alpha_\nu = \frac{P_R(T,\nu,n)}{I_P(\nu,T)}$$

where T is temperature, ν is frequency, n is density of matter and $I_P(\nu,T)$ is a Plank distribution function:

$$I_P(\nu,T) = \frac{2h\nu^3}{c^2\left(\exp\left(\frac{h\nu}{k_B T}\right)-1\right)}$$

If one consider a two small volumes $dV_1(\vec{r_1})$ and $dV_2(\vec{r_2})$ of radiating (and accordingly

absorbing) plasmas, intensity of radiation with frequency ν from $dV_1(\vec{r}_1)$ in the point $\vec{r}_2$ will be

$$dI_{\nu 1}(\vec{r}_2)=\frac{P_{R\nu}(T(\vec{r}_1),n(\vec{r}_1))dV_1}{4\pi(\vec{r}_1-\vec{r}_2)^2}\exp\left(-\int_{\vec{r}_1}^{\vec{r}_2}\alpha_\nu(\vec{l})d\vec{l}\right),$$

where $\vec{l}=\vec{r}_1-(\vec{r}_2-\vec{r}_1)t, \quad 0\le t\le 1.$

Thus, radiation of given frequency that absorbed by volume $dV_2(\vec{r}_2)$ from the volume $dV_1(\vec{r}_1)$ is

$$dP_{A1}(\vec{r}_2)dV_2=dI_{\nu 1}(\vec{r}_2)\alpha_\nu(\vec{r}_2)dV_2=$$

$$=\frac{P_{R\nu}(T(\vec{r}_1),n(\vec{r}_1))P_{R\nu}(T(\vec{r}_2),n(\vec{r}_2))dV_1dV_2}{4\pi(\vec{r}_1-\vec{r}_2)^2 I_{P\nu}(\vec{r}_2)}\times\exp\left(-\int_{\vec{r}_1}^{\vec{r}_2}\alpha_\nu(\vec{l})d\vec{l}\right) \qquad (2.1)$$

Let us consider the full power, absorbed by the volume $dV(r_2)$ in the case of cylindrical symmetry. In this case $T=T(r)$, $n=n(r)$, and, $P_R(T,\nu,n)=P_R(r,\nu)$. We will use cylindrical coordinate system (R,ϕ,θ) with the center in the point $dV(r_2)$. This coordinates are connected with usual cylindrical coordinates (r,φ,z) as:

$$r=\sqrt{R^2+r_2^2+2Rr_2\cos\phi},\quad \tan\varphi=\frac{R\sin\phi}{r_2+R\cos\phi},\quad z=R\tan\theta.$$

Rewriting equation (2.1) for the system (R,ϕ,θ) we have $(\vec{r}_1-\vec{r}_2)^2=\frac{R^2}{\cos^2\theta}$ and

$$dP_{A1}(\vec{r}_2)dV_2=\frac{\cos^2\theta}{4\pi R^2}\frac{P_{R\nu}(\vec{r})P_{R\nu}(\vec{r}_2)dV_1dV_2}{I_{P\nu}(\vec{r}_2)}\exp\left(-\frac{1}{\cos\theta}\int_0^R\frac{P_{R\nu}(l)}{I_{P\nu}(l)}dl\right) \qquad (2.1.a)$$

Jacobian in the coordinate system (R,ϕ,θ): $J=\frac{\partial(x,y,z)}{\partial(R,\phi,\theta)}=\frac{R^2}{\cos^2\theta}$

If we are suppose the limit radius of system is b, then, for the given ϕ R will change from 0 to $b_1(r_2,\phi)=\sqrt{b^2-r_2^2\sin^2\phi}-r_2\cos\phi$, ϕ will change from 0 to 2π and θ from $-\frac{\pi}{2}$ to $+\frac{\pi}{2}$.

In order to find full absorbed by $dV(r_2)$ power, we must integrate (2.1.a) by all volume and by all frequency range:

$P_A(\vec{r}_2)=$

$$=\int_0^{\infty}\frac{P_{R\nu}(r_2)}{I_{P\nu}(r_2)}d\nu\int_{-\frac{\pi}{2}}^{\frac{\pi}{2}}d\theta\int_0^{2\pi}d\phi\int_0^{b_1(r_2,\phi)}dR\times J\frac{\cos^2\theta}{4\pi R^2}P_{R\nu}(R,\phi)\exp\left(-\frac{1}{\cos\theta}\int_0^R\frac{P_{R\nu}(l)}{I_{P\nu}(l)}dl\right)=$$

$$=\frac{1}{\pi}\int_0^{\infty}\frac{P_{R\nu}(r_2)}{I_{P\nu}(r_2)}d\nu\int_0^{\frac{\pi}{2}}d\theta\int_0^{\pi}d\phi\int_0^{b_1(r_2,\phi)}dR\times P_{R\nu}(R,\phi)\exp\left(-\frac{1}{\cos\theta}\int_0^R\frac{P_{R\nu}(l)}{I_{P\nu}(l)}dl\right)\qquad(2.2)$$

Equation (2.2) can not be simplified in general case, but it is possible for the case of $T=const$ in all volume. If the only radiation process in plasma is a bremsstrahlung, the spectral power of radiation from the volume unit

$$P_{RB}(\nu)\approx\frac{32\pi e^6n^2}{3(4\pi\varepsilon_0)^3c^3m_e}\left(\frac{2\pi}{3m_ek_BT}\right)^{1/2}\exp\left(-\frac{h\nu}{kT}\right),\ \text{so}$$

$$\frac{P_{RB\nu}(l)}{I_{P\nu}(l)}=\frac{32\pi e^6h^2}{6(4\pi\varepsilon_0)^3cm_e}\left(\frac{2\pi}{3m_e(k_BT)^7}\right)^{1/2}\times\frac{1-e^{-u}}{u^3}\times n^2(l),\qquad\text{where } u=\frac{h\nu}{k_BT}.$$

Therefore

$$\left(\int_0^{b_1(r_2,\phi)}\frac{P_{R\nu}(l)}{I_{P\nu}(l)}dl\right)=\frac{32\pi e^6h^2}{6(4\pi\varepsilon_0)^3cm_e}\left(\frac{2\pi}{3m_e(k_BT)^7}\right)^{1/2}\times\frac{1-e^{-u}}{u^3}\int_0^{b_1(r_2,\phi)}n^2(l)dl\qquad(2.4)$$

As we will show later, in such a case the plasma density distribution expresses by

$$n(r)=n_0(1-r^2/a^2)$$

and for this distribution we can find integral in expression (2.4) analytically

$$\int_0^{b_1(r_2,\phi)}n^2(l)dl=$$

$$=\left(\frac{3}{10}(1-\frac{r_2^2}{a^2})^2+\frac{1}{30}(\sqrt{1-\frac{r_2^2}{a^2}\sin^2\phi}-\frac{r_2}{a}\cos\phi)^2(7-3\frac{r_2^2}{a^2}-4\frac{r_2^2}{a^2}\sin^2\phi)\right)n_0^2a$$

For this reason we can carry out integration by frequency range and by spatial variables independently, and finally we obtain

$$\frac{P_A(T)}{P_R(T)}=\int_0^{\infty}e^{-u}\bar{S}(K\times\frac{1-e^{-u}}{u^3})du=F(K)\qquad(2.5)$$

where $K=\frac{32\pi e^6 h^2}{6(4\pi\varepsilon_0)^3 c m_e}\left(\frac{2\pi}{3m_e k_B^{\,7}}\right)^{1/2}\times\frac{n_0^{\,2}a}{T^{7/2}}\approx 5.13\times10^{-32}(m^5K^{7/2})\times\frac{n_0^{\,2}a}{T^{7/2}}$

Numerical calculation of functions $\bar{S}(k)$ and $F(K)$ shows, that with accuracy better than 0.5% $\bar{S}(k)=\frac{k^2+0.814k}{k^2+2.314k+1.523}$ and for $F(K)$ we have

$K\ll1$ $\quad F(K)\approx 1.6\sqrt{K}$

$F(1)\approx 0.499$, $\quad F(45)\approx 0.90$;

$K>100$ $\quad F(K)\approx 1-\frac{9}{K}$

§ 3.Equations of equilibrium state.

The basic assumptions of the model is cylindrical symmetry, so all quantities are varies only in the radial direction. We neglect viscosity and degeneracy effects. Equal electron and ion temperature are assumed: $T_e = T_i \equiv T$. The temperature and density in the axis of pinch are noted accordingly as T_0 and n_0. The connection between current density, temperature and electric field intensity in the case of fully ionized hydrogen plasma is

$E=j\,T^{-\frac{3}{2}}\,\alpha\,\bar{\eta}\log\Lambda$, so

$j=E\,T^{3/2}(\alpha\,\bar{\eta}\log\Lambda)^{-1}$ (3.1),

where E is the axial electric field, j is current density, $\bar{\eta}=65.3\Omega\times m\times K^{3/2}$ is Spitzer conductivity for the fully ionized hydrogen plasma without magnetic field, and α is a value, depending on electrons Hall parameter

$$\beta_e=\frac{\omega_{ce}}{\langle\nu_{ei}\rangle}\approx\frac{3\varepsilon_0^{\,2}(k_BT)^{3/2}}{4\sqrt{2\pi m_e}e^4 n\log\Lambda}eB$$

Parameter α changes from 1.0 for $\beta_e=0$ to about 1.95 for $\beta_e=\infty$.

So, full current I within radius r is

$$I(r)=2\pi\int_0^r r\,j(r)\,dr=\frac{2\pi ET_0^{3/2}}{\bar{\eta}\log\Lambda}\int_0^r r\,\frac{g^{3/2}}{\alpha}(r)\,dr \qquad (3.2),$$

where $g(r)=T(r)/T_0$, consequently, the dependence of magnetic field on radius

$$B(r)=\frac{\mu_0 ET_0^{3/2}}{\bar{\eta}\log\Lambda}\,\frac{1}{r}\int_0^r r\,\frac{g^{3/2}}{\alpha}(r)\,dr \qquad (3.3)$$

Equation for the pressure balance

$$\nabla p = [j\ B] \Rightarrow 2k_B \frac{d}{dr}(nT) = -\frac{\mu_0 E^2 T_0^{\,3}}{(\bar{\eta}\log\Lambda)^2} \frac{g^{3/2}(r)}{\alpha r} \int_0^r r \frac{g^{3/2}}{\alpha}(r)\,dr .$$

So, noting $f(r) = n(r)/n_0$, we can write

$$f(x) = \frac{1}{g(x)} \left\{ 1 - 4 \int_0^x \frac{g^{3/2}(x_1)}{\alpha x_1} \left(\int_0^{x_1} x_2 \frac{g^{3/2}(x_2)}{\alpha} dx_2 \right) dx_1 \right\} \tag{3.4}$$

noting $r = \alpha x$, a is a characteristic dimension of pinch

$$a = 2\bar{\eta}\log\Lambda \sqrt{\frac{2k_B}{\mu_0}} \frac{n_0^{1/2}}{ET_0} \tag{3.5}$$

Then we can estimate β_e in the main part of the pinch, evaluating $B(a)$:

$$B(a) \approx \frac{\mu_0 ja}{2} \approx \sqrt{2\mu_0 n_0 k_B T_0} \Rightarrow$$

$$\beta_e(a) \approx \frac{3\varepsilon_0{}^2 (k_B T)^{3/2}}{4\sqrt{2\pi m_e} e^3 n \log\Lambda} \sqrt{2\mu_0 k_B T_0 n_0} \approx 0.2 \frac{\left(\frac{T_0}{10^6 K}\right)}{\sqrt{\left(\frac{n_0}{10^{24} m^{-3}}\right)}} \frac{n_0}{n},$$

so for the case of high density in the center (more than $10^{24} \div 10^{25} m^{-3}$) β_e will be not small only in the very narrow boundary layer where density n less than $10^{-1} \div 10^{-2} n_0$. For this reason we can suppose β_e small in all pinch volume, hence. α =1 and transport coefficients are those for the case of weak magnetic field.

There will be four terms in the equation of the energy equilibrium in each point: current heating, radiation, absorption of radiation and thermal conductivity.

For the thermal conductivity we have

$$P_C = \frac{1}{r}\frac{d}{dr}\left(r\chi \frac{dT}{dr}\right), \quad \chi = 2.286 \sqrt{\frac{(k_B T)^5}{m_e}} \frac{k_B}{\log\Lambda} \left(\frac{4\pi\varepsilon_0}{e^2}\right)^2 = \frac{\zeta T^{5/2}}{1+\beta_e{}^2} \Rightarrow$$

$$P_C = \frac{1}{r}\frac{d}{dr}\left(r \frac{\zeta T^{5/2}}{1+\beta_e{}^2} \frac{dT}{dr} \right) = \frac{\zeta T_0^{7/2}}{a^2} \frac{1}{x}\frac{d}{dx}\left(\frac{x g^{5/2}}{1+\beta_e{}^2} \frac{dg}{dx} \right) \tag{3.6.a}$$

For the current heating

$$P_J = E\ j = \frac{E^2 T^{3/2}}{\bar{\eta}\log\Lambda} = \frac{E^2 T_0^{3/2}}{\bar{\eta}\log\Lambda}\, g^{3/2}(x) \qquad (3.6.b)$$

If we suppose the main radiation mechanism in plasma is a bremsstrahlung, for radiation losses we have

$$P_R = \frac{32\pi e^6 n^2}{3(4\pi\varepsilon_0)^3 hc^3 m_e}\left(\frac{2\pi k_B T}{3m_e}\right)^{1/2} = \frac{32\pi e^6}{3(4\pi\varepsilon_0)^3 hc^3 m_e}\left(\frac{2\pi k_B}{3m_e}\right)^{1/2} T_0^{1/2} n_0^{\ 2} g^{1/2}(x) f^{\ 2}(x) =$$

$$= B\, T_0^{1/2} n_0^{\ 2} g^{1/2}(x) f^{\ 2}(x) \qquad (3.6.c),$$

$$B \approx 1.43 \times 10^{-40}\, J \times m^3 \times s^{-1} \times K^{-1/2}$$

Dividing expressions for P_R, P_J, P_C and P_A by factor $BT_0^{1/2} n_0^{\ 2} g^{1/2}$ we can write the equation for the energy equilibrium in each point only in terms of dimensionless variables: coordinate x and function g (x)

$$P_R = P_C + P_J + P_A \Rightarrow$$

$$f^2(x) = L\frac{E^2 T^5}{n_0^{\ 3}}\,\frac{g^{-1/2}(x)}{x}\,\frac{d}{dx}\left(\frac{x g^{5/2}(x)}{1+\beta_e^{\ 2}}\frac{dg(x)}{dx}\right) + M\frac{E^2 T_0}{n_0^{\ 2}} g(x) +$$

$$f^2(x) I\left(K_1, x, g(x), f(x)\right), \qquad (3.7),$$

where

$$L = \frac{15\sqrt{3}}{16\pi^3}\,\frac{\mu_0 k_B^{\ 2} c^{\ 3} h m_e}{\bar{\eta}^2 \log^2\Lambda}\left(\frac{4\pi\varepsilon_0}{e^2}\right)^5 \approx \frac{7.29\times 10^{43}}{\log^3\Lambda}\,(K^{-5}V^{-2}m^{-7})$$

$$M = \frac{1}{B\bar{\eta}\log\Lambda} \approx \frac{1.07\times 10^{38}}{\log\Lambda}\,(K^{-1}V^{-2}m^{-4})$$

$$I\left(K_1, x, g(x), f(x)\right) =$$

$$= \frac{K_1}{g(x)}\,\frac{1}{\pi}\int_0^{\infty}\frac{1-e^{-u/g(x)}}{u^3}du\int_0^{\pi}d\phi\int_0^{b_1(x,\phi)}dX\,\frac{f^2(X,\phi,x)}{g^{1/2}(X,\phi,x)}\exp\left(-\frac{u}{g(X,\phi,x)}\right)\times$$

$$\times\,\Omega\left(-\frac{K_1}{u^3}\int_0^{X}\frac{f^{\ 2}(l_1)}{g^{1/2}(l_1)}\left(1-\exp\left(-\frac{u}{g(l_1)}\right)\right)dl_1\right)$$

Equation (3.7) was solved numerically, and it was shown that in the region of validity of

given theory ($\log\Lambda > 5$. T_0 is some $10^5 K$), temperature distribution is very slightly distinguished from uniform, so it is possible to use simplification of homogenious temperature that means infinite thermal conductivity.

§ 4. Stationary state of z-pinch with infinite thermal conductivity.

For such a case $g(r) \equiv 1$ and it is possible to simplify system of equations (3.1)-(3.5) :

$$j = E\, T_0^{3/2}\, (\bar{\eta}\log\Lambda)^{-1} \qquad (4.1)$$

$$I(r) = \frac{\pi E T_0^{3/2}}{\bar{\eta}\log\Lambda} r^2 \qquad (4.2)$$

$$B(r) = \frac{\mu_0 E T_0^{3/2}}{2\bar{\eta}\log\Lambda} r \qquad (4.3)$$

$$f(x) = 1 - x^2 \qquad (4.4)$$

$$a = 2\bar{\eta}\log\Lambda \sqrt{\frac{2k_B}{\mu_0}}\, \frac{n_0^{1/2}}{E T_0} \qquad (4.5)$$

Full current I_0 can be found from the equations (4.2) and (4.5):

$$I_0 = \frac{\pi E T_0^{3/2}}{\bar{\eta}\log\Lambda} a^2 = \frac{8\pi k_B \bar{\eta}\log\Lambda}{\mu_0}\, \frac{n_0}{T_0^{1/2} E} \qquad (4.2'),$$

Linear density N will be simply

$$N = \frac{\pi}{2} n_0 a^2 = \frac{4\pi k_B (\bar{\eta}\log\Lambda)^2}{\mu_0} \left(\frac{n_0}{E_0 T_0}\right)^2 \qquad (4.6)$$

For the following calculations it is more convenient to take N, I_0 and a as a variables. Expressing the rest quantities in terms of this variables we obtain:

$$n_0 = \frac{2N}{\pi a^2}$$

$$T_0 = \frac{\mu_0 I_0^2}{16\pi k_B N}$$

$$E = \frac{64\sqrt{\pi} k_B^{3/2} \bar{\eta}\log\Lambda}{\mu_0^{3/2}}\, \frac{N^{3/2}}{I_0^2 a^2}$$

In order to obtain energy equation for the pinch unit length equation (3.7) must be integrated by radius. Summarizing there will be only three components: current heating, radiated power and absorbed power. For the current heating we have:

$$P_j = E\ I_0 = \frac{64\sqrt{\pi}k_B^{3/2}\bar{\eta}\log\Lambda}{\mu_0^{3/2}}\frac{N^{3/2}}{I_0 a^2} \qquad (4.7)$$

The full radiated power:

$$P_R = \int_0^a 2\pi r B T_0^{1/2} n^2(r)dr = 2\pi B T_0^{1/2} a^2 n_0^2 \int_0^1 x(1-x^2)^2 dx =$$

$$= \frac{B\mu_0^{1/2}}{3\pi^{3/2}k_B^{1/2}}\frac{I_0 N^{3/2}}{a^2} \qquad (4.8.)$$

where $B = \frac{32\pi e^6}{3(4\pi\varepsilon_0)^3 hc^3 m_e}\left(\frac{2\pi k_B}{3m_e}\right)^{1/2} \approx 1.43\times10^{-40} J\times m^3\times s^{-1}\times K^{-1/2}$.

As was shown before, absorption in such a system is determined by the only one factor

$$K_1 = \frac{32\pi e^6 h^2}{6(4\pi\varepsilon_0)^3 cm_e}\left(\frac{2\pi}{3m_e k_B^{\ 7}}\right)^{1/2}\times\frac{n_0^{\ 2}a}{T^{7/2}} = \frac{2^{10}\pi^3 e^6 h^2}{3(4\pi\varepsilon_0)^3 cm_e}\left(\frac{2}{3m_e\mu_0^{\ 7}}\right)^{1/2}\times\frac{N^{11/2}}{I_0^{\ 7}a^3} =$$

$$= K_2\times\frac{N^{11/2}}{I_0^{\ 7}a^3} \approx 0.823\times\frac{\left(\frac{N}{10^{22}m^{-1}}\right)^{11/2}}{\left(\frac{a}{10^{-2}m}\right)^3\left(\frac{I_0}{10^6 A}\right)^7} \qquad (4.9).$$

and $P_A = P_R\,F(K_1)$, where $F(K_1)$ is expresses by (2.5).

So, instead of the equation (3.7) we have

$$P_R = P_A + P_j \Rightarrow \frac{B\mu_0^{1/2}}{3\pi^{3/2}k_B^{1/2}}\frac{I_0 N^{3/2}}{a^2}(1-F(K_1)) = \frac{64\sqrt{\pi}k_B^{3/2}\bar{\eta}\log\Lambda}{\mu_0^{3/2}}\frac{N^{3/2}}{I_0 a^2} \Rightarrow$$

$$I_0\,(1-F(K_1))^{1/2} = \frac{8\pi k_B}{\mu_0}\sqrt{\frac{3\bar{\eta}\log\Lambda}{B}} = 3.23\times10^5\sqrt{\log\Lambda}(A) \equiv I_{PB} \qquad (4.10)$$

§ 5. Results of calculations and discussion.

Solution of (4.10) is shown in the Figure 1 as a dependence of full current on radius for the different values of line density. As can be seen the absorption effect cause increasing

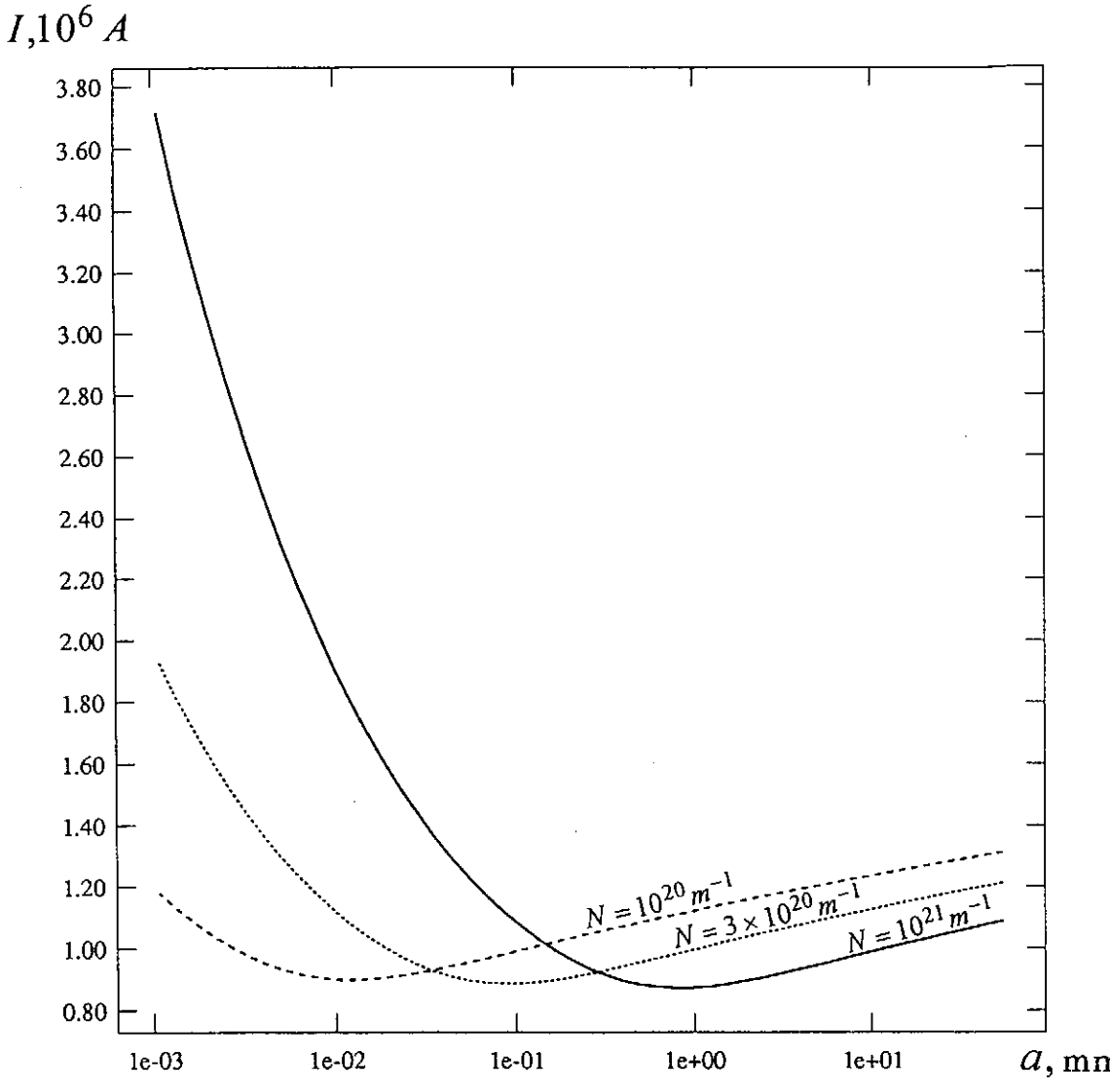

Figure1. Dependence of the pinch full current on radius for the different line densities.

of full current for the state of large compression of pinch. We can assume radius of a current minimum a_{min} as a characteristic dimension for absorption effect negligibility, and for $a=a_{min}$ with a good accuracy the coefficient of absorption $K_1(a_{min}) \approx 1.2 \times 10^{-2}$ for all linear densities N i.e. absorption is significant if $a << a_{min}$. From the calculations $a_{min} \approx 5.65 \times \left(\frac{N}{10^{22}\, m^{-1}}\right)^{1.84} cm$, so it is possible to obtain a significant increasing of limit current for the implosion up to radius $a<100\,\mu$ m for $N=10^{21}$m^{-1}, and up to $a<10\,\mu$ m for $N=3 \cdot 10^{20}$m^{-1}. For the smaller densities it is quite difficult to obtain a homogeneous implosion to reasonable radius.

It was obtain a very small difference between results of solution of equations (3.7) and (4.10) even for the case of small thermal conductivity parameter $L\frac{E^2 T_0^5}{n_0^3}$. It seems to be because radiative heat transport is large in considered temperature and density range.

§ 6. Conclusions.

(1) There was obtained expression for the absorption of own radiation in cylindrical z-pinch (2.2), (2.5). It follows that for the small absorption degree full absorbed and radiated power are related as

$$\frac{P_A(T)}{P_R(T)} \approx 1.6\sqrt{K_1} \approx 1.4 \times \frac{\left(\frac{N}{10^{22}m^{-1}}\right)^{11/4}}{\left(\frac{a}{10^{-2}m}\right)^{3/2}\left(\frac{I_0}{10^6 A}\right)^{7/2}}$$

(2) Total current is not depends simply on Coulomb logarithm (Pease-Braginskii current), but also on radius in accordance with solution of (4.10) (fig.1).

(3) For the case of large internal absorption of radiation thermal conductivity value is not significant because of intensive radiation transport.

REFERENCES

(1) R. S. Pease, Proc. Phys. Soc., B70 (1957) 11.

(2) S. I. Braginskii, Sov. Phys. JETP, 6 (1958) 494.

(3) C. G. Falthammer, Phys. Fluids 4 (1961) 1145.

(4) D. W. Sccuder, Phys. Fluids 26 (1983) 1330.

(5). N. R. Pereira, Phys. Fluids B 2(3) (1990) 677

Broadband millimeter-wave radiation from a beam driven strong turbulence

H. Yoshida, M. Masuzaki, S. Oyama, R. Ando, K. Kamada

Department of Physics, Faculty of Science, Kanazawa University, Kanazawa 920-11, Japan

Abstract

High power broadband millimeter-wave radiation is emitted from an IREB-plasma interaction system in a strong Langmuir turbulence state. In order to investigate the radiation mechanism, radiation spectra were measured by two spectrometers covering 18 - 140 GHz. We applied the collective Compton boosting model proposed by Benford and Weatherall to describe the radiation mechanism in our experiments. However, the observed spectra and the parameter dependencies of the spectra differ from the results calculated by the model quantitatively.

Introduction

A number of investigators [1]-[7] have recently studied the high power broadband electromagnetic wave radiation from an interaction system of an intense relativistic electron beam (IREB) with an unmagnetized or weakly magnetized plasma. These studies show that the radiation has a broadband spectrum above plasma frequency and disappears after the electron beam passes through the plasma. Also the studies indicate that when the broadband radiation is emitted the system is in a strong Langmuir turbulence state in which creation, collapse , and burnout of cavitons are repeated [8, 9]. Benford and Weatherall proposed collective Compton boosting model [10, 11] which based on the interaction between bunched beam electrons and caviton electric fields. Masuzaki *et al.* [7] demonstrated experimentally that the radiation spectra determined by 18 - 90 GHz spectrometer disagreed with the spectra calculated by the collective Compton boosting model. In this paper, first, we explain an improvement of the resolution of high-frequency band by a new spectrometer. Second, we show the spectra measured by 18 - 140 GHz spectrometer and investigate the dependencies of the radiation spectra shapes on three parameters: beam current, observation direction, and plasma density. Last, we compare the obtained spectra with the spectra obtained from the theoretical model.

Apparatus

The setup of the interaction system is sketched in Figure 1. Major components of the system included a modified pulserad 110A electron beam generator, a plasma gun system, and a drift chamber. The 110A consisted of a Marx generator, a Blumelein line, and a diode consisting of a carbon cathode of 36 mm diameter and a titanium foil anode of 20 μm thick. The 110A produced by Physics International could generate diode voltage up to 1.4 MeV and diode current up to 27 KA with a pulse duration of 30 ns. In this experiment, anode-cathode gap distance (A - K) was 20 mm or 30 mm. When A-K was 20 mm long, the beam currents, I_b, was about 17 KA. When A-K = 30 mm, $I_b \sim 10$ KA.

The plasma gun system was composed of a pair of rail-type plasma gun, a capacitor bank, and a trigger set. A plasma was produced by discharging the capacitor energy to the gun when trigger signal was entered. The plasma density became maximum at about 12 μs after the triggering and then decays as shown in Figure 2. The plasma guns were installed opposite to each other at 100 mm downstream from the anode in the stainless steel drift chamber of 600 mm long and 160 mm in diameter. The chamber had two observation ports at 175 mm downstream from the anode. An electromagnetic-wave absorber, which absorbed the power over 24 dB, was installed on the inner wall of the chamber. The chamber was evacuated to less than the pressure 5 $\times 10^{-5}$ torr.

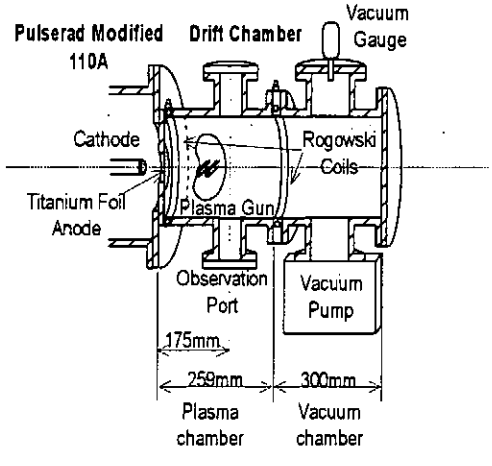

Figure 1: The experimental setup.

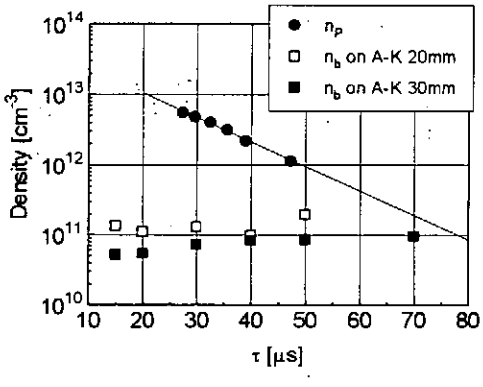

Figure 2: n_p and n_b vs. τ.

Net currents were measured by two Rogowski coils which were set just behind the anode foil and 260 mm downstream from the anode, respectively. To determine the plasma

density, n_p, and the beam density, n_b, at 175 mm, we used a microwave interferometer and a 9-channel Faraday cup array, respectively. Figure 2 shows n_p and n_b versus the delay time, τ, after gun firing. In Figure 2, closed circle indicates n_p and open and closed square indicate n_b corresponding to $I_b \sim 17$ KA and $I_b \sim 10$ KA, respectively.

We measured millimeter-wave radiation spectra by two spectrometers. For K, Ka, and U bands (18 - 60 GHz) a 6-channel filter-bank spectrometer was used. The filter-bank spectrometer consisted of six branches each of which composed of a directional coupler, a variable attenuator, a bandpass filter, and a detector. Each branch had a frequency resolution of about 5 GHz except U band the band width of which was 20 GHz. A detector system for E and F bands (73 - 140 GHz) included a filter block, a variable attenuator, a Schottky detector, and a pulse amplifier as shown in Figure 3. Three filter blocks were prepared to change the observation window for radiation. The block for 73 - 90 GHz consisted of an E band bandpass filter and a F band waveguide. The block for 90 - 140 GHz consisted of a F band bandpass filter and a F band waveguide. The block for 117 - 140 GHz consisted of a F band bandpass filter and a G band waveguide.

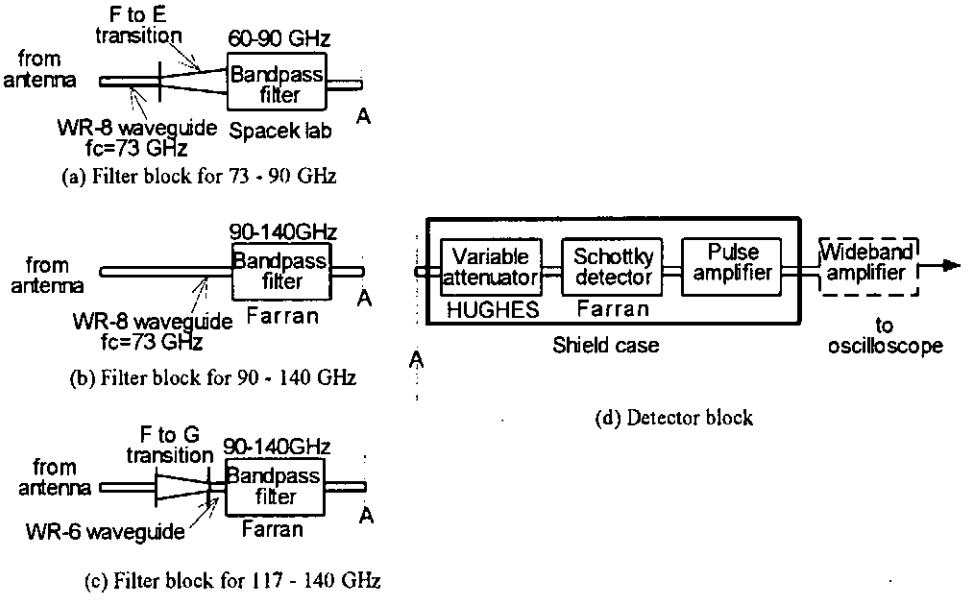

Figure 3: The detector system for 73 - 140 GHz.

In order to measure radiation directivity, two kinds of the setup were prepared. Figures 4 and 5 show experimental setups for the radial observation and for the observation at the end of the chamber, the axial observation, respectively. In the radial observation, a horn

antenna was attached in the observation port. In the axial observation, a horn antenna, which received radiation coming through a Lucite window into the air, was set outside of the chamber. An electromagnetic wave absorbing chamber was prepared to avoid interfering of electromagnetic waves. To avoid damage of the window by the beam electrons, a permanent magnet was installed at 100 mm upstream from the end of the chamber.

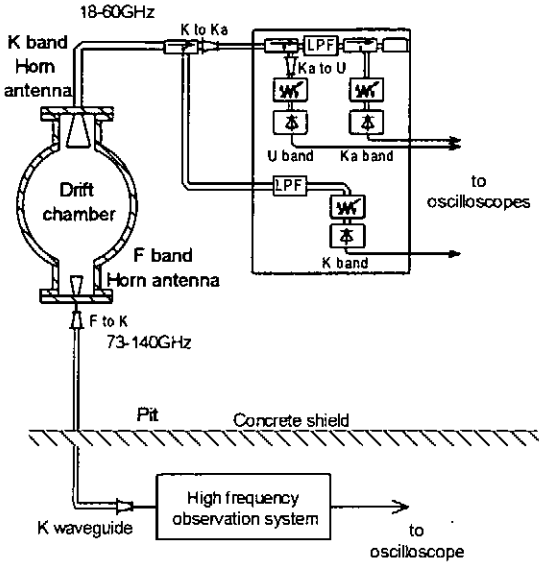

Figure 4: The set up for the radial observation.

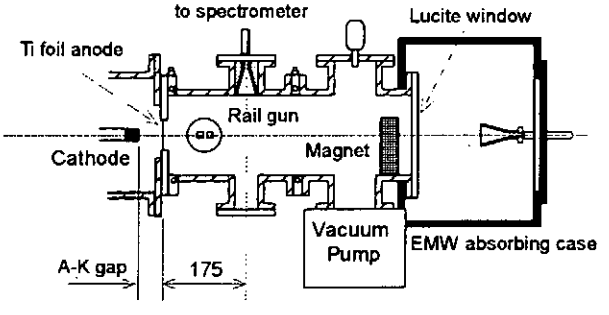

Figure 5: The set up for the axial observation.

Experimental Results

Figure 6 shows (a) the dependence of the ratio of n_b to n_p and (b) the total power density on τ when the beam current was changed. The total power density means the amount of the power obtained at each band for the unit effective area of the antenna.

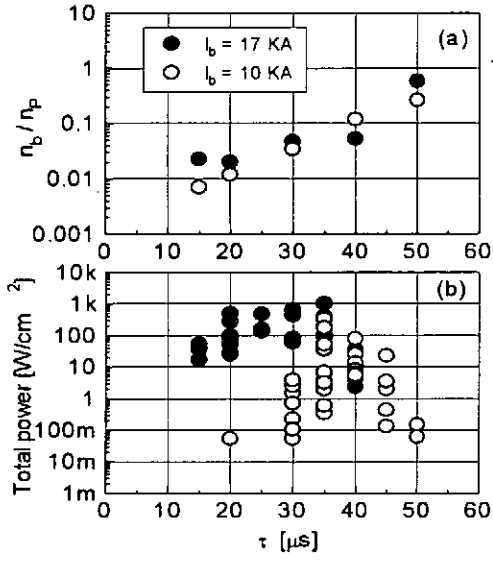

Figure 6: (a) Beam plasma density ratio and (b) total power density vs. τ.

The spectrum measurements were made for each of the three parameters: the beam current, the directivity, and the plasma density.

Beam current Obtained spectra for the cases of $I_b = 10$ KA and $I_b = 17$ KA are shown in Figures 7 (a) and (b), respectively. The observation direction was radial. An optimum τ was opted for each of the beam current since n_b/n_p might affect the radiation power, and it was 30 μs for the case of $I_b = 10$ KA and 20 μs for the case of $I_b = 17$ KA. The horizontal axis is the frequency normalized by the plasma frequency, ω_p. The vertical axis is the radiation power for a unit frequency interval divided by the effective area of the antenna. Each of the plot points shows the power averaged over the bandwidth of each filter. In these spectra the shapes in low frequency region are flat and the powers are high,

while in high frequency region the spectra decay steeply. The power for the case of I_b = 10 KA is lower approximately one order than that for the case of I_b = 17 KA.

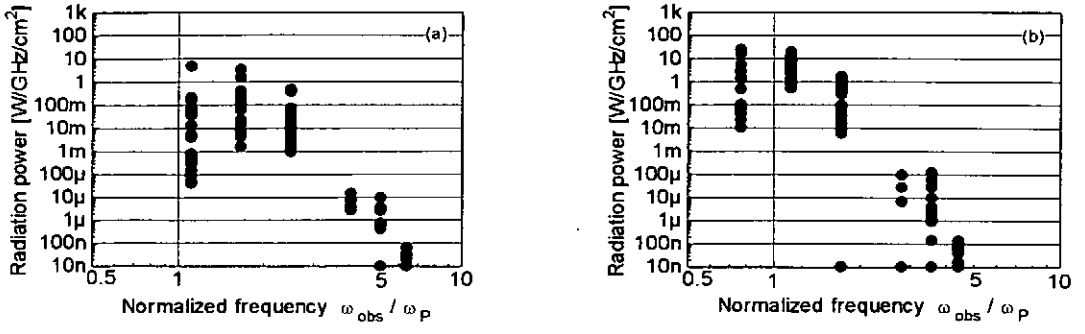

Figure 7: The dependence of the beam current: (a) I_b = 10 KA, (b) I_b = 17 KA.

Directivity For the estimation of the directivity, the power spectra were measured axially and radially. Comparison of the observed power spectra in each direction requires that both radiation sources should be in the same region around z = 175 mm. We measured the total power radially at three points: z = 175 mm, z = 255 mm, and z = 305 mm to know whether the total power depends on z or not, because the plasma was long along the beam propagation axis and had a density gradient. The results indicated that the radiation power at the observation point at 175 mm downstream from the anode was highest compared with the others at τ = 30 μs. The directivity of the radiation under the condition in which the beam current equals 10 KA and τ equals 30 μs is shown in Figure 8. The spectrum observed axially differs slightly from that observed radially in low frequency region. It does not have flat part. The radiation power observed axially is 0 - 10 dB larger than that radially.

Plasma density Figures 9 (a), (b), and (c) are the spectra when the plasma density was changed. In order to change the plasma density, τ was varied in 10 μs increment from 20 μs to 40 μs. At this time, the beam current was 30 KA and the radiation was observed axially. In this experiment, we could not fix the ratio of n_b to n_p because n_b could not be changed at a certain n_p arbitrarily. But the radiation power seems to decrease as the plasma density decreases.

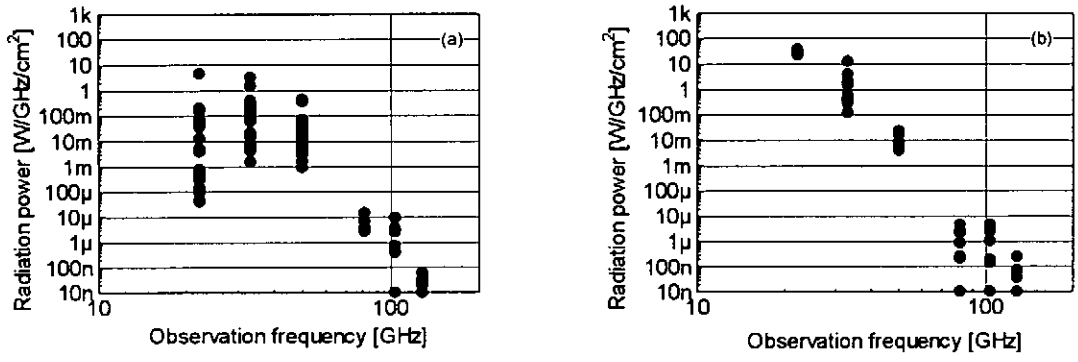

Figure 8: The dependence of the observation direction: (a) radially, (b) axially.

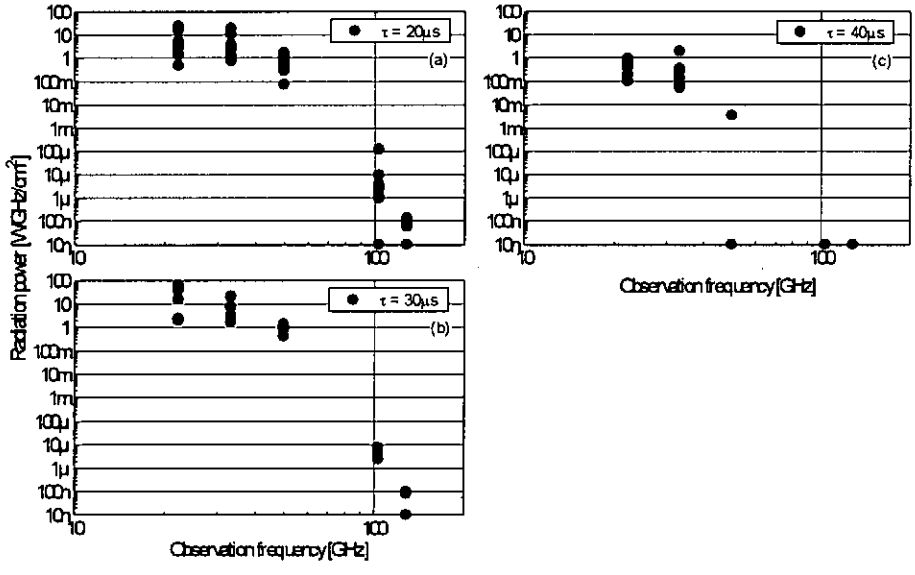

Figure 9: The dependence of the plasma density: (a) $n_p = 10^{13}$, $n_b/n_p = 0.02$ (b) $n_p = 6 \times 10^{12}$, $n_b/n_p = 0.05$, (c) $n_p = 2 \times 10^{12}$, $n_b/n_p = 0.06$.

Discussions

Parameter dependence Let us compare the parameter dependencies of the obtained spectrum with the dependencies of the calculated spectrum using the collective Compton boosting model. The model takes into account the following things:

1. The radiation is originated from acceleration of beam electrons by caviton fields.
2. The electron beam has density fluctuation.
3. The radiation spectrum is collectively affected by this density fluctuation.

In the collective Compton boosting model [10], the equation for total radiated energy per unit frequency per unit solid angle is

$$\frac{\mathrm{d}E(\omega)}{\mathrm{d}\Omega} = \frac{\mathrm{d}I(\omega)}{\mathrm{d}\Omega}(\pi D^2)^2 2\pi L\{v_0 n_b^2 \delta(\omega - \omega_p) + V[(\omega - \omega_p)/v_0]\}, \quad (1)$$

where $\mathrm{d}I(\omega)/\mathrm{d}\Omega$ is the single-particle radiation spectrum. D is the scale length of the caviton and is approximately 20 λ_D. Here λ_d is the Debye length. L is the beam length and v_0 is the beam velocity. The first term in the parenthesis is the plasma line emission. The second term is the spectrum broadening due to the density fluctuation of the beam electrons and includes n_b^2 dependence. The magnitude of the density fluctuation is described by a spectral density function.

$\mathrm{d}I(\omega)/\mathrm{d}\Omega$ depends on the angular distribution of radiation. The directivity depends on the relative direction of the dipole moment of the caviton electric field to the beam direction. For relativistic beam, the radiation should be relativistically beamed [11]. We note that when the dipole moment is transverse to the direction of the beam, the single-particle spectrum has flat part [11]. The cutoff frequency of the single-particle spectrum is determined by $\gamma^2 c/\pi D$, where γ is Lorenz factor and c is the light speed. The cutoff frequency is estimated to be a few tens THz in our experiment.

In the experimental results, some tendencies of the parameter dependence of the spectrum appeared. The increment of I_b causes the increase of the power of the radiation. This may be explained by Equation (1), since as shown in Figure 2, the increase of I_b causes the increase of n_b.

In the measurement of the directivity, the difference between the power observed axially and that observed radially is approximately only 10 dB or less, and the spectrum observed axially is slightly different from the spectrum observed radially in low frequency region. According to the collective Compton boosting model, the radiation power observed axially should be higher about 30 dB than that observed radially, while the spectrum should not be changed in each observation direction. If the radiation is originated from the accelerated electrons, some mechanisms which make the directivity broad must exist.

The cutoff frequency of the observed spectra does not depend on the plasma density. Here we define the cutoff frequency as the frequency of the 3 dB power down point in the experiments. This tendency cannot be explained by the model, because according to the model the spectrum should be affected by the plasma density.

The observed radiation power depends on n_p. But in our experiment the power depends on n_b/n_p, too [6]. Because we could not fix n_b/n_p in this experiment, we cannot recognize whether the n_p variation causes the power variation or not. It can be seen from the above results that some tendencies in the spectrum variation accompanied with the change of the parameters are not explained with the collective Compton boosting model.

Shape of the spectrum We calculated some spectrum shapes according to the collective Compton boosting model for some of the spectral density functions and the relative directions of the dipole moment of the cavitons to the beam direction. The values of the parameters in the calculation and in the experiment were approximately the same. The calculation was done in the following manner: (1) only the frequency dependence was calculated, (2) the term of the plasma line emission was neglected because the estimation of its relative power to the power of the broadband emission was difficult and the plasma line emission did not appear in each of the observation spectrum. Figures 10 (a) and (b) show an experimentally obtained spectrum and an example of calculated spectrum, respectively. Here we assumed Gaussian as the spectral density function and the transverse orientation of the dipole moment of the cavitons to the beam direction. The experimental and calculated spectra resemble each other in shape qualitatively, but quantitatively they are very different. We have not yet had agreement between calculated and experimental spectra.

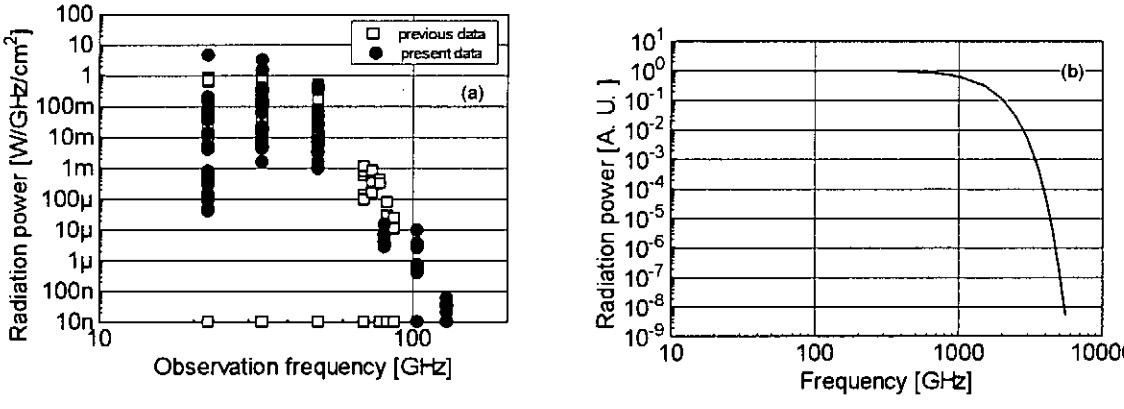

Figure 10: A comparison of the experimental and calculated spectra.

Concluding Remarks

In order to investigate the radiation mechanism, we prepared a new spectrometer to measure high frequency spectra (60 - 140 GHz) in addition to the filter bank spectrometer covering 18 -60 GHz. Measurements of radiation spectra were made for three parameters: the beam current, the observation direction, and the plasma density. The obtained spectra and the power were compared with the theoretical model proposed by Benford and Weatherall in dependence on each parameter and in the spectrum shape. The results show that the Compton boosting model does not explain our experimental results well. We cannot yet explain these disagreement and do not have a model to describe our experiment. The development of a new model is difficult but we must do it.

References

[1] K. G. Kato, G. Benford, and D. Tzach, Phys. Fluids 26, 12 (1983)

[2] M. S. DiCapua, J. F. Camacho, E. S. Fulkerson, and D. Meeker, IEEE Trans. Plasm 16, 2 (1988)

[3] M. Masuzaki *et al.*, Proc. of the 8th International Conference on High Power Particle Beams, 1991, Novosibirsk, USSR, vol. 2, p. 683.

[4] M. Masuzaki *et al.*, Proc. of the 9th International Conference on High Power Particle Beams, 1992, Washington, DC., vol. 2, p. 1227.

[5] R. Ando *et al.*, Proc. of the 10th International Conference on High Power Particle Beams, 1994, San Diego, California, vol. 2, p. 933

[6] R. Ando *et al.*, J. Phys. Soc. Jpn. 65 (1996) 2518.

[7] M. Masuzaki *et al.*, Proc. of the 11th International Conference on High Power Particle Beams, 1996, Prague, Czech., vol. 1, p. 339.

[8] P. A. Robinson, and D. L. Newman, Phys. Fluids B2 (1990) 3120.

[9] M. Yoshikawa, M. Masuzaki, and R. Ando, J. Phys. Soc. Jpn. 64 (1994) 3303.

[10] G. Benford, and J. C. Weatherall, Phys. Fluids, B4 (1992) 4111.

[11] J. C. Weatherall, and G. Benford, Astrophys. J. 378 (1991) 543.

Microwave Radiation Process in an Axial Virtual Cathode Oscillator

Mitsuru Tanigawa, Mitsuyasu Yatsuzuka and Sadao Nobuhara
Himeji Institute of Technology
2167 Shosha, Himeji, Hyogo 671-22

Abstract

The cross-section of pinched electron beam was measured by an X-ray pinhole camera to determine the electron beam density. The radiation pattern of microwave emission is confirmed to be TM_{01} mode in the output circular waveguide. The observed radiation frequency is in good agreement with the theoretical frequency of trapped reflecting electrons between the real and virtual cathodes, and almost consistent with the frequency of TM_{01} mode. The maximum power emission is observed at the A-K gap length for which the frequency of reflecting electrons satisfies the dispersion relation of TM_{01} mode. The frequency of virtual cathode oscillation, which is determined with the beam cross-section and beam current, is less than the observed radiation frequency.

1. Introduction

The virtual cathode oscillator (vircator) has been attracted as one of promising high-power microwave sources, because of simple structure and high-power output capability.[1,2] In vircators the axial electric field driven by reflecting electrons between the real and virtual cathodes or oscillation of virtual cathode itself couples with axially symmetric transverse magnetic waveguide mode (TM_{0m}).[3] However, there is little direct experimental observation on these radiation mechanisms.

In this paper, the radiation frequency from an axially extracted vircator is compared with theoretical frequency estimated with the experimental parameters. The frequency of reflecting electrons is determined with the beam energy and the anode-cathode (A-K) gap length, while the virtual cathode frequency is estimated with the beam density that is determined with the beam cross-section on the anode and the beam current at the downstream. The dependence of radiation frequency on cathode diameter, output waveguide diameter, and A-K gap length is

also studied experimentally. In section 2, theoretical microwave frequencies from vircators are described. Experimental apparatus is described in section 3. In section 4, results and discussion are presented. Conclusions are given in section 5.

2. Radiation Frequency from a Vircator

The dispersion relation of TM_{0m} mode in a circular waveguide is given by

$$(k_z c)^2 = \omega^2 - \omega_c^2 \tag{1}$$

where ω_c is the cutoff frequency given by $\omega_c = x_{0m} c / R_w$, x_{0m} is the solution of Bessel function $J_n(x)=0$, c is the speed of light, k_z is the wavenumber, R_w is the radius of circular waveguide. If $k_z = \pi / R_c$, where R_c is the cathode radius, the frequency of TM_{0m} modes is written as

$$f = \left[\frac{1}{(2R_C)^2} + \left(\frac{x_{0m}}{2\pi R_w} \right)^2 \right]^{1/2} c \tag{2}$$

In a virtual cathode device, there are two possible sources of microwave radiation; one from oscillating electrons between the real and virtual cathode or oscillation of virtual cathode formed by electrons itself. The radiation frequency due to trapped electron reflecting is given by[2)]

$$f_r = \frac{c\beta}{4d} \approx 7.5 \frac{\beta}{d(cm)} \quad \text{(GHz)} \tag{3}$$

where d is the A-K gap length.

On the other hand, the oscillating frequency of the virtual cathode itself is given by the relativistic plasma frequency as follows:

$$f_p = \frac{1}{2\pi} \left(\frac{ne^2}{\gamma m \varepsilon_0} \right)^{1/2} \tag{4}$$

Then the virtual cathode frequency can be written in practical units as[2)]

$$f_{vc}(\text{GHz}) = 4.08 \left(\frac{J(\text{kA/cm}^2)}{\beta\gamma} \right)^{1/2} \tag{5}$$

where J is the beam current density.

3. Experiment

Figure 1 shows a schematic of vircator diode consisting of an annular cathode with its diameter of 2.0 - 3.5 and thickness of 1 mm and an aluminum foil anode of 15 μm in thickness. The A-K gap length d was varied from 2.0 to 7.0 mm. Electron beam currents were measured by a ns-response Rogowski coil at the upstream (1.1 cm away from the anode in the cathode direction) and downstream (0.1 cm away from the anode in the drift space). The diode voltage was measured by a resistive divider at the location close to the anode. The microwave radiation traveled along a circular waveguide (radius R_w=2.25 cm and 2 m in length) and was emitted into a free space through a conical horn. The microwave signals were picked up by an open-end rectangular waveguide antenna (WRJ-10) at the position of 1 m from the circular horn. This antenna could be rotated by 90° and was swept radially to measure radiation power and mode patterns. The microwave frequency was determined by a long waveguide dispersive delay line (WRJ-10, cutoff frequency f_c=6.55 GHz, and length L =105.7 m). The X-rays radiated from the anode due to electron beam bombardment were measured by an X-ray pinhole camera (Polaroid XR−7 and Polaroid film 57) to determine electron beam cross-section on the anode. The distance between the anode and camera was 2 m, and the P_b plate having the pinhole of 2 mm in a diameter and its thickness of 8 mm was set at the middle of anode and camera. Then, the spatial resolution for X-ray measurement was ±7 mm that is less than the cathode radius.

4. Results and Discussion

4.1 Microwave emission and radiation pattern

The typical time histories of diode voltage, electron beam current in the diode region (upstream), electron beam current in the drift tube region (downstream), and microwave emission are shown for R_c=1.5 cm and d=5 mm in Fig. 2. As seen in Fig. 2, the microwave emission with the maximum peak power of approximately 10 MW and the pulse duration of 15 ns appears at the diode voltage of 350 kV and beam currents of 31.8 kA at the upstream and 12.4 kA at the downstream. The microwave frequency was found to be 11.3 GHz by the measurement of propagation time in the 105.7-m dispersive delay line. The

power density profiles in the radial and azimuthal directions are shown for R_c=1.5 cm and d= 5 mm in Fig. 3. As seen in Fig.3, the radially polarized microwave with a peak in the radial direction is dominant and symmetrical to the axis, indicating the radiation pattern of TM_{01} mode. The total microwave power is estimated to be approximately 10 MW by integrating the radiation pattern in Fig. 3.

4.2 Beam cross-section and beam density

The typical beam cross-section and the radial beam profile for the case of R_c=1.0 cm and d= 4.5 mm are shown in Figs. 4 (a) and (b), respectively. An outer ring indicates the circular waveguide, while a dark spot at the center results from the beam bombardment on the anode. As seen in Fig. 4 (b), the X-ray strength is maximum at the center of axis, indicating that the annular electron beam initially is strongly pinched and then the beam radius is 0.52 cm (F.W. H.M.). Here, since the beam cross-section is not a perfect circle, the average beam radius was estimated with the F.W.H.M of radial beam profile in the six directions. The microwave emission appeared simultaneously with the strong electron pinching.[4,5] Then, the electron beam density at the instant of microwave emission can be determined with the pinched-beam radius and beam current at the downstream.

The electron beam radius, diode voltage and beam current at the downstream are shown as function of A-K gap length in Figs. 5 for (a) R_c=1.0 cm, (b) 1.25, and (c) 1.5 cm, where the diode voltage and beam current are obtained at the instant of maximum microwave emission. As seen in Fig. 5, both beam radius and beam current at the downstream decrease almost linearly with the A-K gap length, but the diode voltage slightly increases with the gap length.

4.3 Microwave frequency

Figure 6 shows (a) the typical initial microwave pulse and (b) the delay pulse through the 105.7-m dispersive delay line. Since the propagation time is 437 ns in Fig. 6, the frequency is found to be 11.1 GHz.[5] The microwave pulse widths before and after propagating through the delay line remains unchanged, so that the radiation frequency is considered to be a single frequency. The experimental frequency and microwave power are plotted as a function of A-K gap length for (a) R_c=1.0 cm, (b) 1.25 cm, and (c) 1.5 cm in Fig. 7 together with the theoretical frequencies from eqs. (2), (3) and (5), where a dashed line is the frequency of reflecting electrons, a solid line is the frequency of virtual cathode oscillation, and the chained lines are the frequency of TM_{0m} mode. Here we assumed that the beam radius, diode voltage, and beam current were given by a linear equation shown by a solid line in Fig. 5. As seen in Fig. 7, the observed frequency is in good agreement with the frequency of reflecting electrons and almost consistent with the frequency of TM_{01} mode. However,

the frequency of virtual cathode oscillation is less than the observed frequency except the case of R_c=1.5 cm. In Fig. 7, the relative power of microwave emission is also shown as a function of A-K gap length. The maximum power emission is observed at the A-K gap length for which the frequency of reflecting trapped electrons is equal to the frequency of TM_{01} mode.

5. Conclusion

(1) The cross-section of pinched electron beam was measured by an X-ray pinhole camera. Typical beam radius is approximately 0.4 - 0.9 cm less than the cathode radius and decreases with the A-K gap length.

(2) The measurement of power density profile in the radial and azimuthal directions shows the radiation pattern of TM_{01} mode.

(3) The observed radiation frequency is in good agreement with the theoretical frequency of trapped reflecting electrons between the real and virtual cathodes, and almost consistent with the frequency of TM_{01} mode in the output circular waveguide. The frequency of virtual cathode oscillation, which is determined with the beam cross-section and beam current at the downstream, is less than the observed frequency except a case of cathode radius of 1.5 cm.

(4) The maximum power emission is observed at the A-K gap length for which the frequency of reflecting electrons is equal to the frequency of TM_{01} mode.

References

1. V. L. Granatstein and I. Alexeff : *High-Power Microwave Sources* (Artech House, Boston, 1987) Chaps.13 and 14.

2. J. Benford and J. Swegle : *High-Power Microwaves* (Artech House, Boston, 1992) Chap.9.

3. S. C. Burkhart, R. D. Scarpetti and R. L. Lundberg: J. Appl. Phys. **58** (1985) 28.

4. M. Yatsuzuka, K. Nagakawa, Y. Hashimoto, K. Aoki, S. Nobuhara and O. Ishihara: *Proc of 10th Inter'l Conf. on High Power Particle Beams* (San Diego, 1994) 869.

5. M. Yatsuzuka, K. Nagakawa, Y. Hashimoto, O. Ishihara, and S. Nobuhara: IEEE Trans. Plasma Sci., **22** (1994) 939.

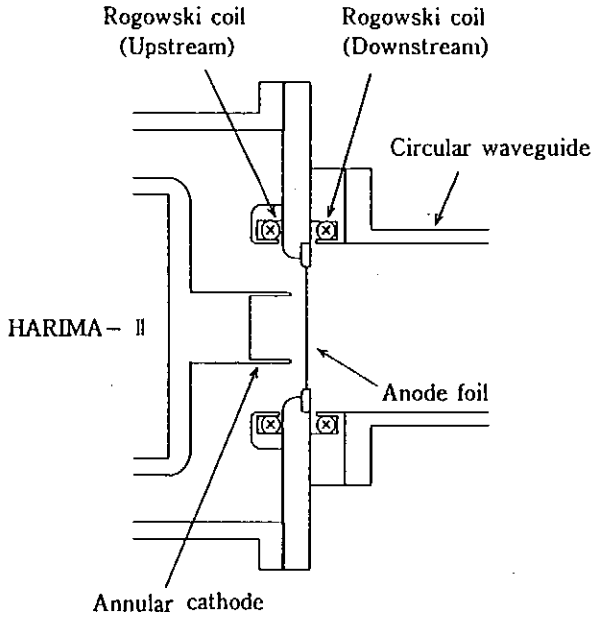

Fig. 1. The schematic of vircator diode.

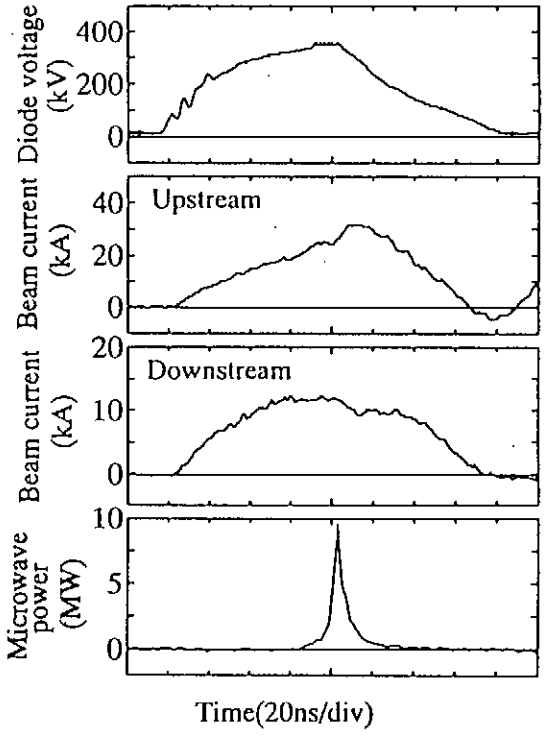

Fig. 2. The typical time histories of diode voltage, electron beam current in the diode region (upstream), electron beam current in the drift tube region (downstream), and microwave emission for R_c=1.5 cm and d=5 mm.

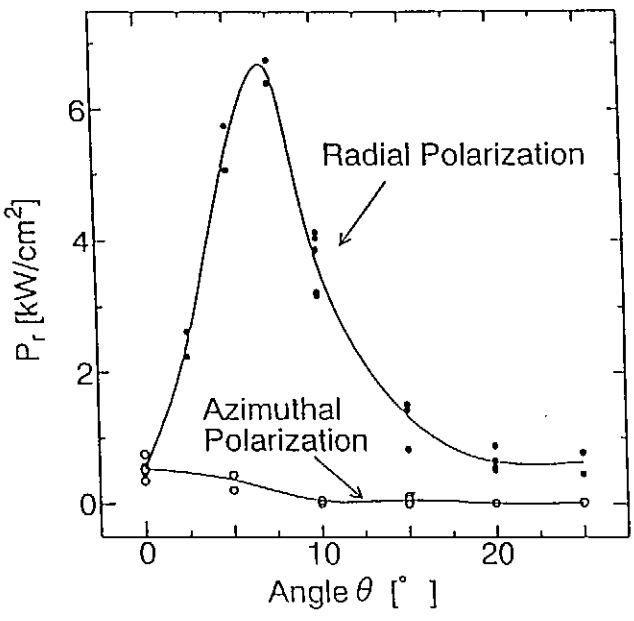

Fig. 3. The power density profile in the radial and azimuthal directions for R_c=1.5 cm and d =5 mm.

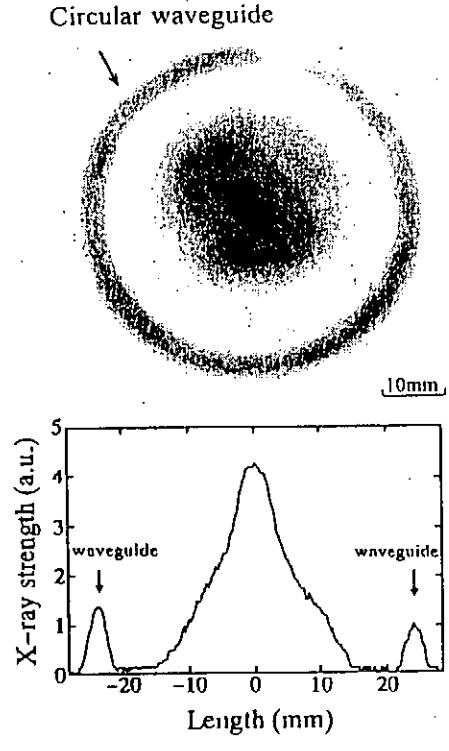

Fig. 4. The typical beam cross-section and the radial beam profile for the case of R_c=1.0 cm and d=4.5 mm.

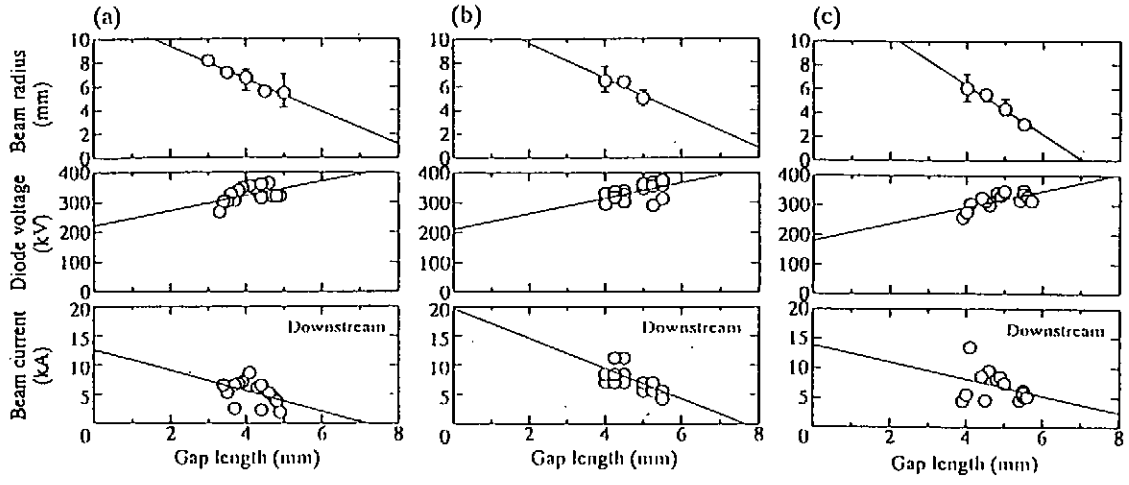

Fig. 5. The electron beam radius, diode voltage and downstream beam current at the time of maximum microwave emission as function of A-K gap length for (a) R_c=1.0 cm, (b) 1.25, and (c) 1.5 cm.

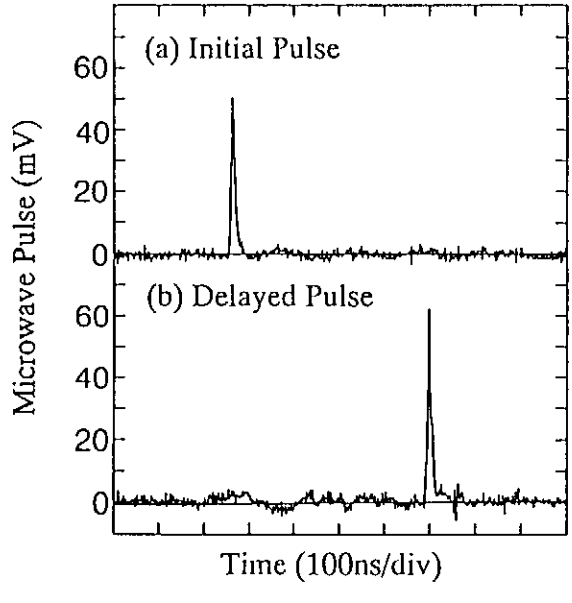

Fig. 6. (a) The typical initial microwave pulse and (b) the delay pulse through the 105.7-m dispersive delay line.

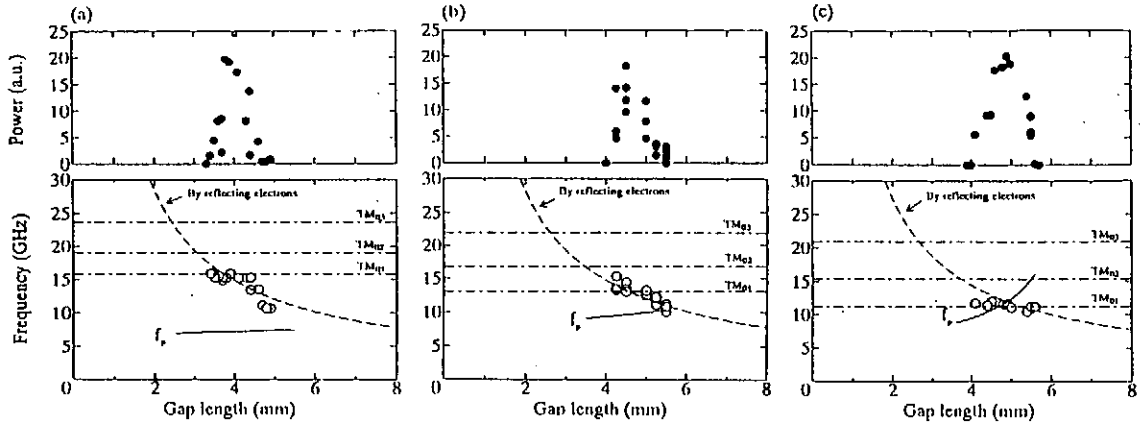

Fig. 7. The experimental frequency and microwave power as a function of A-K gap length for (a) R_c=1.0 cm, (b) 1.25 cm, and (c) 1.5 cm together with the theoretical frequencies from eqs. (3) and (5) and the frequency of TM_{0m} mode, where a dashed line is the frequency of reflecting electrons, a solid line is the frequency of virtual cathode oscillation, and a chained line is the frequency of TM_{0m} mode.

Dynamics of Fast Capillary Z-discharge and Prospect for Laser Operation in Shorter Wavelength Region

Tomonao HOSOKAI, Hikaru HANAJIMA, Mitsuo NAKAJIMA, Takayuki AOKI, Masao OGAWA and Kazuhiko HORIOKA

Department of Energy Sciences, Tokyo Institute of Technology, 4259 Nagatsuta , Midori-ku, Yokohama 226 Japan

Abstract

We have studied the dynamics of fast capillary Z-discahrge to obtain prospects for laser operation in shorter wavelength range. The recent results of our studies indicate that, by preionized fast discharge, the column can implode stably in a wide initial pressure range of 200-1000 Pa of argon. These results also suggest that the final plasma parameters and their spatial distributions can be controlled in the stable implosion range.

If we can avoid destructive magneto-hydrodynamic (MHD) instabilities over a wide range of implosion parameters, we can make Z-scaling to shorter wavelengths by extrapolation from that of classical (conventional) discharge lasers. In order to obtain accurate prospects for the operation in shorter wavelengths, the Z-scaling should be carried out based on a proper modeling including the Z-discharge dynamics and radiation transport.

1. Introduction

If a compact, low-cost, and energy-rich laser functioning in the X-ray region is developed, its applications would result in great progress not only in basic science but also in industrial fields. The required pumping power for production of population inversion approximately increases with $\sim\lambda^{-4}$, where λ means wavelength. Thus a large amount of power more than scale of TW must be put into a small region less than a few cm^{-2} to produce a high energy density plasma; the inversion for X-ray laser. [1] Until recently, it was considered that only a huge high-power optical laser can produce such high power density. [2,3]

Recently, a new development have been made in X-ray laser research. It was reported that a fast capillary discharge could collisionally pump *3p-3s* line of Ne-like Ar (469 Å), and achieved a saturated amplification. [4,5] Although the wavelength is still longer than that of 'laser-driven X-ray laser', its low-cost, compactness and high-efficiency look very attractive for the applications. Naturally, the next stage of study is extending these techniques to the shorter wavelength operational range.

For collisionally pumped X-ray lasers, both high temperatures of more than 100 eV and high electron density of more than 10^{19} cm^{-3} are generally required. [6,7] In the case of the capillary discharge pumped soft X-ray laser, plasma column is contracted to obtain such

high plasma parameters by Z pinch discharge. However the plasma parameters have, to date, not been stably met with the requirements using conventional Z pinch. The final plasma parameters are strongly dependent on the dynamics of the Z pinch. Thus it is necessary, for the laser operation in shorter wavelength range, to clarify of the discharge dynamics including the stabilizing mechanism of the plasma column.

In order to realize the discharge-pumped laser functioning in the shorter wavelength range, we have studied the dynamics of the fast capillary discharge with experiments and MHD simulations. [8] Here we discuss some problems on Z-scaling to shorter wavelength range based on the results of our recent studies.

2. Experiment and 1D-MHD simulations

The detailed results of our previous studies on the dynamics of capillary Z-discharge plasma are shown in Ref.8. The typical experimental setup is shown in Fig.1. We have driven capillary discharges through a uniformly preionized argon gas by a fast pulse power generator LIMAY-I, which enabled direct discharge drive with complete suppression of pre-pulse. We observed the radiation from the discharge column with temporal and spatial resolution, using a fast streak camera and X-ray detectors. We have also carried out 1D-MHD simulations to discuss the discharge dynamics in details. Figure 2 and 3 show the typical streak image of the discharge and the typical flow diagram of the discharge obtained by the MHD simulation. These results indicated consistently that the plasma column can implode stably within a pressure range of 200-1000 Pa under preionized operations, and it has a complex internal structure including a shock wave and current sheet. These results also suggest that the final plasma parameters satisfy the lasing condition for collisionally pumped Ne-like Ar with a sufficient margin of stability.

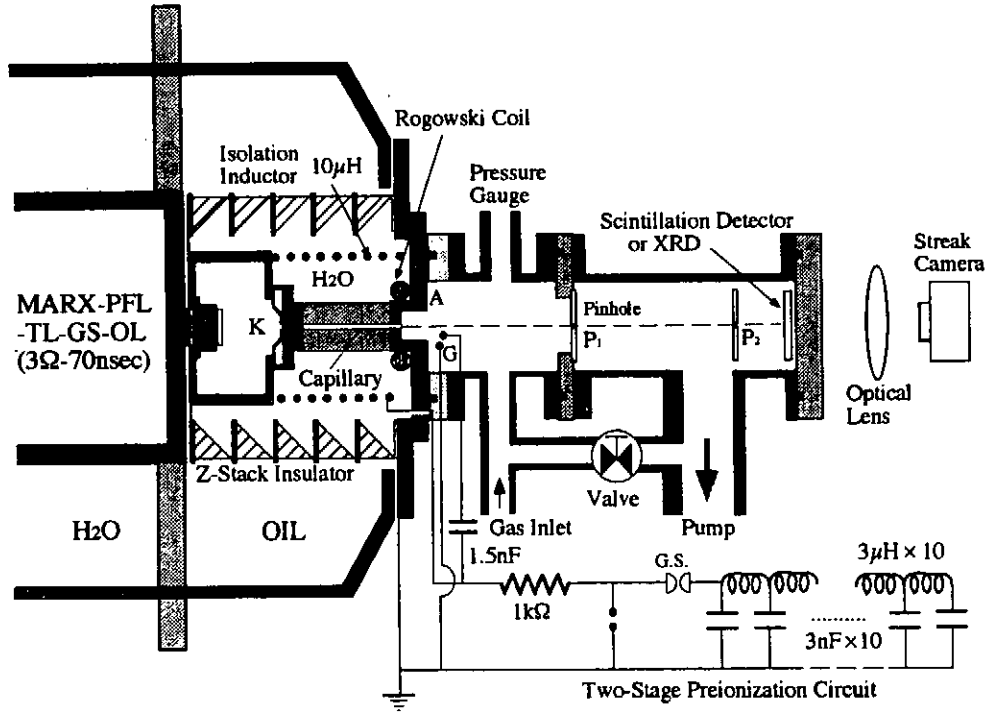

Fig.1 Typical set-up for capillary discharge experiment.

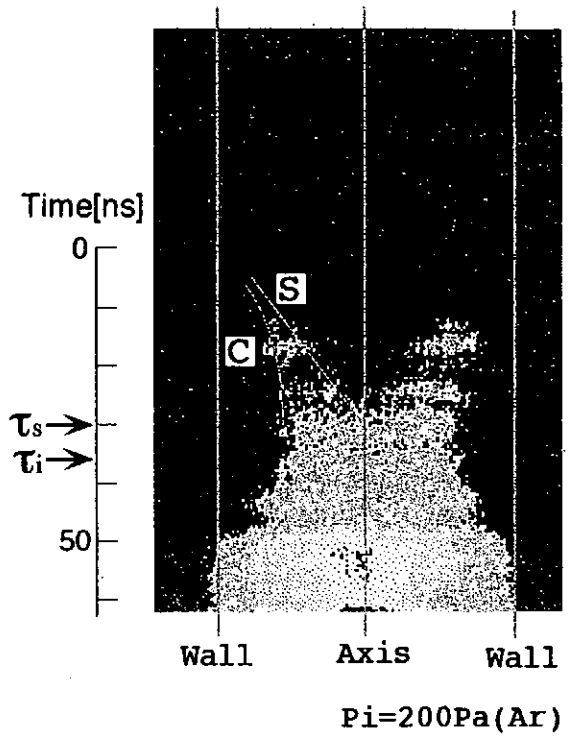

Fig.2 Streak images of capillary discharge (Pi=200 Pa)
Implosion time (τi) and shock wave arrival time (τs) are indicated by arrows.

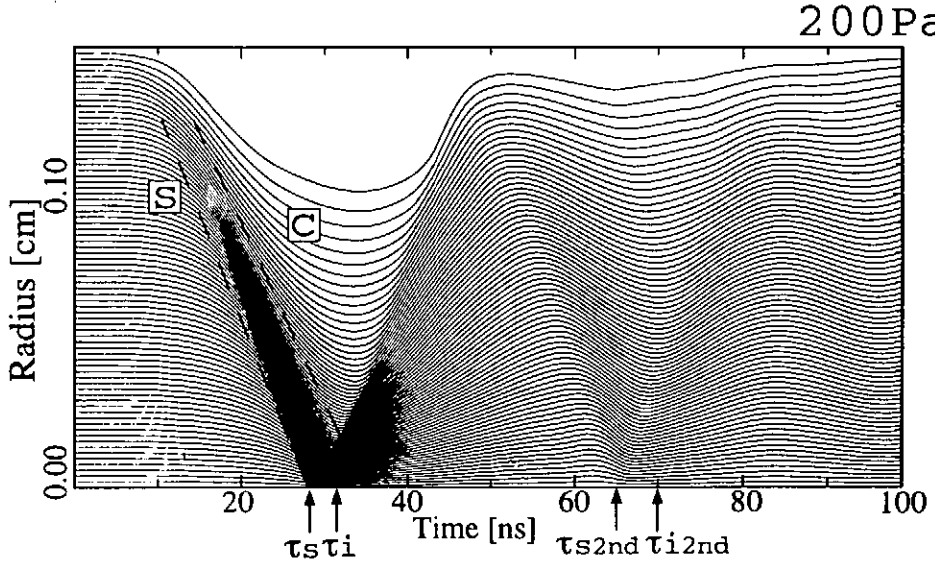

Fig.3 Flow diagram of capillary discharge obtained by 1D-MHD simulation.

τs : Implosion time of shock wave (S: shock wave)

τi : Implosion time of current sheet (C: Current sheet boundary).

τi2nd : Implosion time of current sheet in second phase

τs2nd : Implosion time of shock wave in second phase

3. Z-scaling

Shorter wavelengths can be obtained using isoelectronic sequence such as Ne-like or Ni-like sequences of higher-Z atoms (Z-scaling). The most important issue for collisionally pumped X-ray lasers is to satisfy the required parameters (density and temperature). If the lasing condition can be maintained enough time, in principle, it is possible to obtain quasi-CW-operation. The excitation in the discharge pumping is a pure thermal heating process, which does not contain any anomalous enhanced pumping factors such as superthermal electrons. Thus Z-scaling to shorter wavelengths should be taken place by extrapolation from that of classical (conventional) discharge lasers.

At present, there is only Z-scaling using a simple analytical model. [9] As shown in table 1 both quite high electron density and temperatures are required for the laser operation in shorter wavelength region. [9]

	λ (Å)	Ne (cm^{-3})	Te (eV)
Ne-like Ar	469	$0.5\text{-}2 \times 10^{19}$	60-90
Ne-like Kr	~170	$2\text{-}5 \times 10^{20}$	500-700
Ni-like Xe	~90	$2\text{-}5 \times 10^{20}$	300-600

(Table 1 Examples of required plasma parameters
for collisionaly pumped soft X-ray lasers.)

In the capillary Z discharges, if stable implosion without destructive magneto-hydrodynamic (MHD) instabilities is assumed, Z-scaling to shorter wavelengths can be made simply by increasing the discharge current. The result of this Z-scaling is shown in Fig.4. The required currents were estimated by Bennet codition for confinement of the plasma column. Here, the diameter of plasma column was assumed to be ~100μm. A current of ~10 kA for Ne-like Ar (λ~469 Å), ~200 kA for Ne-like Kr (λ~170 Å) or ~200 kA for Ni-like Xe (λ~90 Å) is required, and they are well within the operational range of recent pulse power generators. But they are only tentative values because the imploding plasma column exhibits complex internal structure. Thus, Z-scaling should be done with taking the dynamics into account.

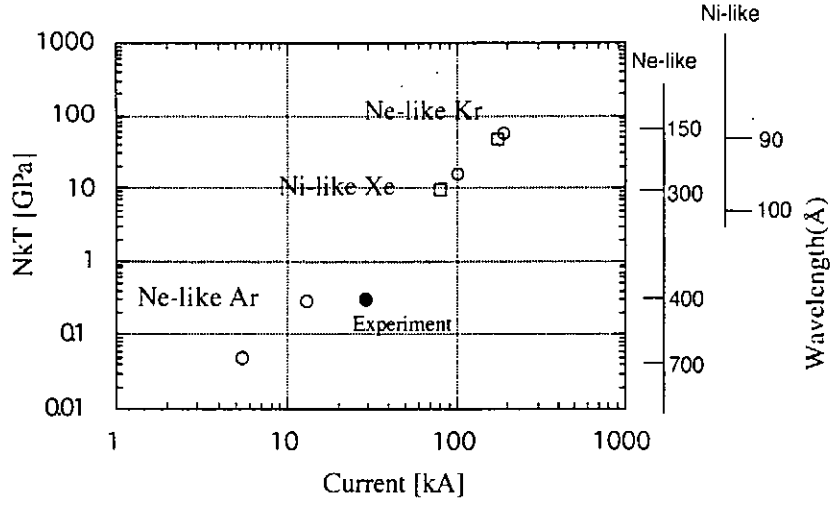

Fig.4 Z-scaling using simple analytical model.

4. Discussion

In this section, from the point of view of the laser medium for shorter wavelengths, we consider some problems which should be taken into account in the Z-scaling. Figure 5 shows the typical time-space distribution of electron density obtained by the MHD simulation, which could explain well the experimental results. Our results have suggested that it is possible to control the final plasma parameters, their spatial distributions and confinement time of the high-energy density within the stable implosion range by the discharge parameters; radius of capillary, initial pressure of filled gas, wave form of drive current and magnitude of peak current. [8] It also means that the time-space distribution of the gain region, the region satisfying lasing conditions, can be controlled by tailoring of the implosion.

As shown in Fig.5, the difference of initial pressure caused obvious difference in the density profiles. We have to consider which profile is better for the laser medium. The available output energy seems to be increased with enlargement of gain volume. However, in a relatively thick gain layer produced in the present capillary discharges, the reabsorption of *3s-2p* radiation depleting the lower laser level could be a serious problem for achieving amplification. [1] In our Z pinch, the layer implodes inward with a radial velocity of ~1.5×10^7 cm/s. For operation at shorter wavelengths, the implosion velocity should be larger than this value. Thus, we can expect considerable reduction of opacity at the line center because of Doppler shift of the line due to the fast ion traveling. On the other hand, the ion temperature increases at the stagnation phase which results in gain drops due to Doppler broadening of lasing lines. These effects should be quantitatively estimated for the wavelength shortening.

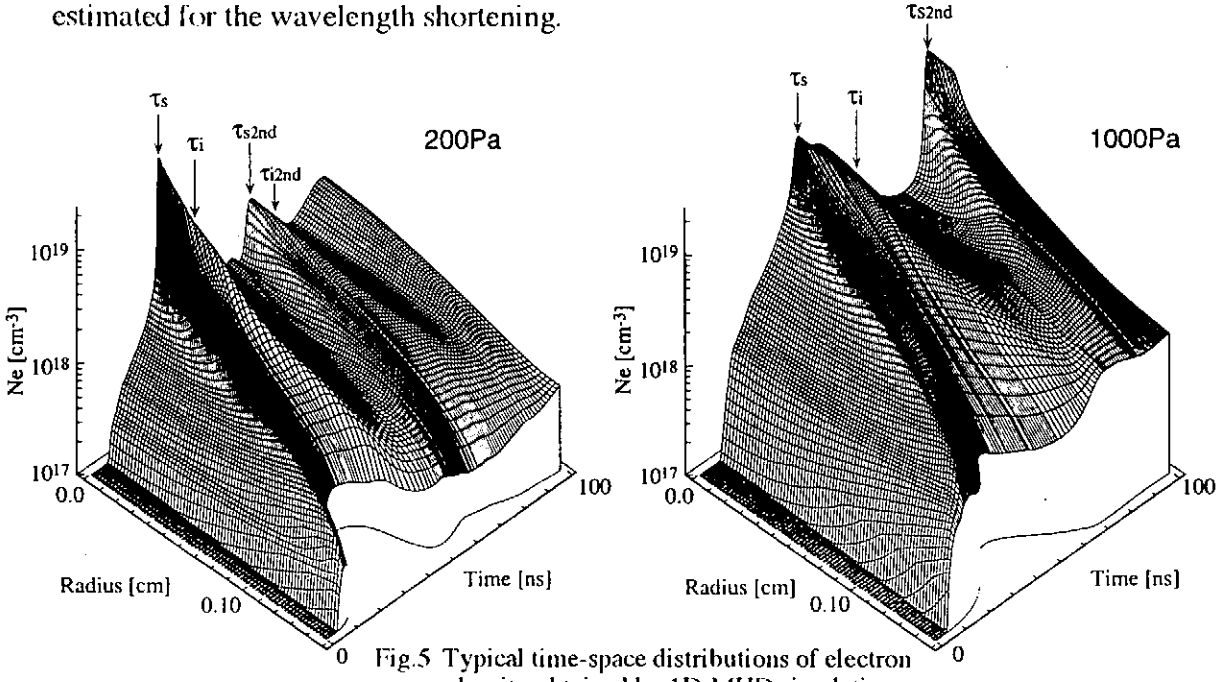

Fig.5 Typical time-space distributions of electron density obtained by 1D-MHD simulation.

τs: Implosion time of shock wave

τi: Implosion time of current sheet

τs2nd: Implosion time of shock wave in second phase

τi2nd: Implosion time of current sheet in second phase

For collisional excitation, high-density plasma is required. Generally, the transport of the radiation down the length of the medium is subject to refraction out of the gain channel by the high transverse electron density gradient. [10,11] The refraction effect becomes more serious in the shorter wavelength range because the transverse electron density gradient increases with the lasing requirements. Then, we have carried out calculations of the X-ray transport in high density plasma to estimate the refraction effect. Figure 6 shows the calculated ray traces (469Å) in a parabolic density profile of ~100μm thickness, which is the satisfying lasing condition of Ne-like Ar. Almost the whole radiation refracted out of the narrow gain channel. While, Figure 7 shows the ray traces (469Å) in a double peaked density profile of ~100μm thickness. The electron density was ~2×10^{19}cm^{-3} conditions of Ne-like Ar. As shown in Fig.5, actually the radial distribution of electron density has a dip on the axis just before the maximum compression phase in which we can expect population inversion. The radiation can be confined and transported in the long and narrow gain region similar to in an optical fiber cable. It may be only the solution for the coherent radiation transport through the long and narrow gain region to obtain a sufficient amplification.

For the wavelength shortening of the capillary discharge X-ray laser, there are many unknown factors at the present stage. If an accurate Z-scaling based on proper modeling can be taken place, we can obtain the laser operation in shorter wavelength range.

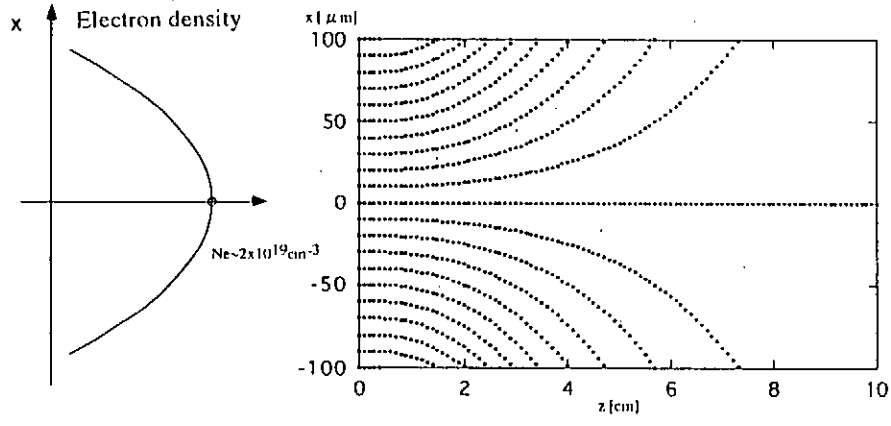

Fig.6 Ray transport in parabolic density distribution. (λ=469Å)

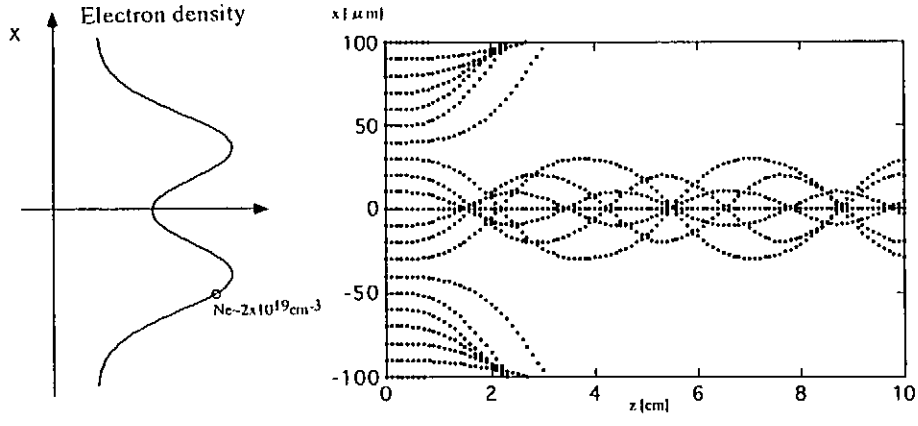

Fig.7 Rray transport in double peaked density distribution. (λ=469Å)

5. Summary

The laser operation by collisional excitation depends on whether the plasma can satisfy the required plasma parameters (density and temperature). In case of the capillary discharge, the final plasma parameters and their distribution are strongly dependent on the dynamics of the discharge. Thus we have studied the dynamics of capillary discharges to obtain the discharge pumped soft X-ray laser functioning in the shorter wavelength range. The results we have already obtained suggested that the plasma column was imploded to a higher energy density free from destructive hydrodynamic instabilities. In other words, we can expect that the final plasma parameters and their spatial distributions can be controlled in the stable implosion range.

According to Z-scaling using a simple analytical model, even for lasing of Ne-like Kr or Ni-like Xe the magnitude of required currents are well within the operational range of recent pulse power generators. However, to estimate the discharge condition accurately, we need to take into account some factors related with the discharge dynamics such as spatial gain distribution, radiation trapping or the radiation transport in the plasma column.

References

1) R.C.Elton: *X-ray Lasers* (Academic Press, New York, 1990).

2) D.L.Matthews,P.L.Hagelstein:Phys.Rev.Lett.**54**(1985) 110.

3) S.Suckwer,C.H.Skinner,H.Milchberg,C.Keane and D.Voorhees: Phys.Rev.Lett.**55**(1985) 1753.

4) J.J.Rocca, V.Shlyaptsev, F.G.Tomasel, O.D.Cortazar,D.Hartshorn and J.L.A.Chilla: Phys.Rev.Lett.**73**(1994) 2192.

5) J.J.Rocca, M.C.Marconi, F.G.Tomasel, V.N.Shlyaptsev, J.L.A.Chilla and D.P.Clark : *SPIE 2520* (1995) 209.

6) A.V.Vinogradov and V.N.Shlyaptsev: Sov.J.Quantum.Electron.**10** No.6 (1980) 754.

7) A.V.Vinogradov and V.N.Shlyaptsev: Sov.J.Quantum.Electron.**13** No.3 (1983) 303.

8) T.Hosokai, M.Nakajima, T.Aoki, M.Ogawa and K.Horioka : Jap.J.Appl.Phys.**36**.No.4.Part1 (1997) :to be published in

9) V.N.Shlyaptsev, A.V.Gerusov, A.V.Vinogradov, J.J.Rocca, U.D.Cortazar, M.C.Marconi, F.G.Tomasel, F.G.Tomasel and B.Szapiro: *SPIE 2012* (1993) 99.

10) Richard A.London : Phys.Fluids.**31** No.1 (1988) 184.

11) V.A.Chirkov:Sov.J.Quantumn Electron.**14**(1984)1497.

Publication List of NIFS-PROC Series

NIFS-PROC-1 "*U.S.-Japan on Comparison of Theoretical and Experimental Transport in Toroidal Systems Oct. 23-27, 1989*", Mar. 1990

NIFS-PROC-2 "*Structures in Confined Plasmas –Proceedings of Workshop of US-Japan Joint Institute for Fusion Theory Program–* "; Mar. 1990

NIFS-PROC-3 "*Proceedings of the First International Toki Conference on Plasma Physics and Controlled Nuclear Fusion –Next Generation Experiments in Helical Systems– Dec. 4-7, 1989*" Mar. 1990

NIFS-PROC-4 "*Plasma Spectroscopy and Atomic Processes –Proceedings of the Workshop at Data & Planning Center in NIFS–*"; Sep. 1990

NIFS-PROC-5 "*Symposium on Development of Intensed Pulsed Particle Beams and Its Applications February 20 1990*"; Oct. 1990

NIFS-PROC-6 "*Proceedings of the Second International TOKI Conference on Plasma Physics and Controlled Nuclear Fusion , Nonlinear Phenomena in Fusion Plasmas -Theory and Computer Simulation-*"; Apr. 1991

NIFS-PROC-7 "*Proceedings of Workshop on Emissions from Heavy Current Carrying High Density Plasma and Diagnostics*"; May 1991

NIFS-PROC-8 "*Symposium on Development and Applications of Intense Pulsed Particle Beams, December 6 - 7, 1990*"; June 1991

NIFS-PROC-9 *"X-ray Radiation from Hot Dense Plasmas and Atomic Processes"*; Oct. 1991

NIFS-PROC-10 "*U.S.-Japan Workshop on "RF Heating and Current Drive in Confinement Systems Tokamaks" Nov. 18-21, 1991*, Jan. 1992

NIFS-PROC-11 "*Plasma-Based and Novel Accelerators (Proceedings of Workshop on Plasma-Based and Novel Accelerators) Nagoya, Japan, Dec. 1991*"; May 1992

NIFS-PROC-12 "*Proceedings of Japan-U.S. Workshop P-196 on High Heat Flux Components and Plasma Surface Interactions for Next Devices*"; Mar. 1993

NIFS-PROC-13 『NIFS シンポジウム
「核燃焼プラズマの研究を考える－現状と今後の取り組み方」
1992 年 7 月 15 日、核融合科学研究所』
1993 年 7 月

NIFS Symposium
"Toward the Research of Fusion Burning Plasmas -Present Status and Future strategy-", 1992 July 15, National Institute for Fusion Science"; July 1993 (in Japanese)

NIFS-PROC-14 "*Physics and Application of High Density Z-pinches*", July 1993

NIFS-PROC-15 岡本正雄、講義「プラズマ物理の基礎」
平成 5 年度　総合大学院大学
1994 年 2 月
M. Okamoto,
"Lecture Note on the Bases of Plasma Pysics"
Graduate University for Advanced Studies
Feb. 1994 (in Japanese)

NIFS-PROC-16 代表者　河合良信
平成 5 年度　核融合科学研究所共同研究
研究会報告書
「プラズマ中のカオス現象」
"Interdisciplinary Graduate School of Engineering Sciences"
Report of the meeting on Chaotic Phenomena in Plasma
Apr. 1994 (in Japanese)

NIFS-PROC-17 平成 5 年度 NIFS シンオジウム報告書
「核融合炉開発研究のアセスメント」
平成 5 年 11 月 29 日-30 日　於　核融合科学研究所
"Assessment of Fusion Reactor Development"
Proceedings of NIFS Symposium held on November 29-30, 1993 at National Insitute for Fusion Science" Apr. 1994
(in Japanese)

NIFS-PROC-18 *"Physics of High Energy Density Plasmas Produced by Pulsed Power"* June 1994

NIFS-PROC-19 K. Morita, N. Noda (Ed.),
"*Proceedings of 2nd International Workshop on Tritium Effects in Plasma Facing Components at Nagoya University, Symposion Hall, May 19-20, 1994*", Aug. 1994

NIFS-PROC-20 研究代表者　阿部　勝憲　（東北大学・工学部）
所内世話人　野田信明
平成 6 年度　核融合科学研究所共同研究［研究会］
「金属系高熱流束材料の開発と評価」成果報告書
K. Abe and N. Noda (Eds.),
"Research and Development of Metallic Materials for Plasma Facing and High Heat Flux Components" Nov. 1994
(in Japanese)

NIFS-PROC-21 世話人：森田　健治（名大工学部）、金子　敏明（岡山理科大学理学部）
「境界プラズマと炉壁との相互作用に関する基礎過程の研究」

研究会報告
K. Morita (Nagoya Univ.), T. Kaneko (Okayama Univ. Science)(Eds.)
"*NIFS Joint Meeting "Plasma-Divertor Interactions" and "Fundamentals of Boundary Plasma-Wall Interactions" January 6-7, 1995 National Institute for Fusion Science*"
Mar. 1995 (in Japanese)

NIFS-PROC-22
代表者　河合　良信
プラズマ中のカオス現象
Y. Kawai,
"*Report of the Meeting on Chaotic Phenomena in Plasma,* 1994"
Apr. 1995 (in Japanese)

NIFS-PROC-23
K. Yatsui (Ed.),
"*New Applications of Pulsed, High-Energy Density Plasmas*";
June 1995

NIFS-PROC-24
T. Kuroda and M. Sasao (Eds.),
"*Proceedings of the Symposium on Negative Ion Sources and Their Applications, NIFS, Dec. 26-27, 1994*", Aug. 1995

NIFS-PROC-25
岡本　正雄
新古典輸送概論（講義録）
M. Okamoto,
"*An Introduction to the Neoclassical Transport Theory" (Lecture note)*, Nov. 1995 (in Japanese)

NIFS-PROC-26
Shozo Ishii (Ed.),
"*Physics, Diagnostics, and Application of Pulsed High Energy Density Plasma as an Extreme State*"; May 1996

NIFS-PROC-27
代表者　河合　良信
プラズマ中のカオスとその周辺非線形現象
Y. Kawai ,
"*Report of the Meeting on Chaotic Phenomena in Plasmas and Beyond, 1995*", Sep. 1996 (in Japanese)

NIFS-PROC-28
T. Mito (Ed.),
"*Proceedings of the Symposium on Cryogenic Systems for Large Scale Superconducting Applications*", Sep. 1996

NIFS-PROC-29
岡本　正雄
講義「核融合プラズマ物理の基礎 - I」
平成 8 年度　総合研究大学院大学　数物科学研究科　核融合科学専攻
1996年 10月
M. Okamoto
"*Lecture Note on the Fundamentals of Fusion Plasma Physics - I" Graduate University for Advanced Studies;* Oct. 1996 (in Japanese)

NIFS-PROC-30

研究代表者　栗下　裕明（東北大学金属材料研究所）
所内世話人　加藤　雄大
平成 8 年度核融合科学研究所共同研究
「被損傷材料の微小体積強度評価法の高度化」研究会
1996年 10月　9日　於：核融合科学研究所

H. Kurishita and Y. Katoh (Eds.)

NIFS Workshop on Application of Micro-Indentation Technique to Evaluation of Mechanical Properties of Fusion Materials, Oct. 9, 1996, NIFS

Nov. 1996 (in Japanese)

NIFS-PROC-31

岡本　正雄
講義「核融合プラズマ物理の基礎 - II」
平成 8 年度　総合研究大学院大学　数物科学研究科　核融合科学専攻
1997年 4月
M. Okamoto
"Lecture Note on the Fundamentals of Fusion Plasma Physics - II" Graduate University for Advanced Studies; Apr. 1997 (in Japanese)

NIFS-PROC-32

代表者　河合　良信
平成8年度　核融合科学研究所共同研究
研究会報告「プラズマ中のカオスとその周辺非線形現象」

Y. Kawai (Ed)

Report of the Meeting on Chaotic Phenomena in Plasmas and Beyond, 1996; Apr. 1997 (mainly in Japanese)

NIFS-PROC-33

H. Sanuki,
Studies on Wave Analysis and Electric Field in Plasmas; July 1997

NIFS-PROC-34

プラズマ対向機器・PSI・熱・粒子制御合同研究会報告
平成 9 年 6 月 27 日（金）9:00 ～16:20
核融合科学研究所・管理棟 4 F 第 1 会議室
1997年　10月
T. Yamashina (Hokkaido University)
Plasma Facing Components, PSI and Heat/Particle Control
June 27, 1997, National Institute for Fusion Science
T. Yamashina (Hokkaido University)
Oct. 1997 (in Japanese)

NIFS-PROC-35

T. Watari,
Plasma Heating and Current Drive; Oct. 1997

NIFS-PROC-36

T. Miyamoto and K. Takasugi (Eds.)
Production and Physics of High Energy Density Plasma; Production and Physics of High Energy Density Plasma; Oct. 1997